MINISTÉRIO DA CIÊNCIA, TECNOLOGIA, INOVAÇÕES E COMUNICAÇÕES
INSTITUTO NACIONAL DE PESQUISAS ESPACIAIS

sid.inpe.br/mtc-m21c/2019/08.17.01.06-TDI

THE IMPACT OF PHOTOIONIZING FEEDBACK IN STAR FORMING MOLECULAR CLOUDS

Nina Sanches Sartorio

Doctorate Thesis of the Graduate Course in Astrophysics, guided by Dr. Diego Antonio Falceta Gonçalves, approved in September 13, 2019.

URL of the original document:
<http://urlib.net/8JMKD3MGP3W34R/3TRNE3L>

INPE
São José dos Campos
2019

PUBLISHED BY:

Instituto Nacional de Pesquisas Espaciais - INPE
Gabinete do Diretor (GBDIR)
Serviço de Informação e Documentação (SESID)
CEP 12.227-010
São José dos Campos - SP - Brasil
Tel.:(012) 3208-6923/7348
E-mail: pubtc@inpe.br

DIGITAL LIBRARY:
Dr. Gerald Jean Francis Banon
Clayton Martins Pereira - Serviço de Informação e Documentação (SESID)
DOCUMENT REVIEW:
Simone Angélica Del Ducca Barbedo - Serviço de Informação e Documentação (SESID)
André Luis Dias Fernandes - Serviço de Informação e Documentação (SESID)
ELECTRONIC EDITING:
Ivone Martins - Serviço de Informação e Documentação (SESID)
Cauê Silva Fróes - Serviço de Informação e Documentação (SESID)

MINISTÉRIO DA CIÊNCIA, TECNOLOGIA, INOVAÇÕES E COMUNICAÇÕES
INSTITUTO NACIONAL DE PESQUISAS ESPACIAIS

sid.inpe.br/mtc-m21c/2019/08.17.01.06-TDI

THE IMPACT OF PHOTOIONIZING FEEDBACK IN STAR FORMING MOLECULAR CLOUDS

Nina Sanches Sartorio

Doctorate Thesis of the Graduate Course in Astrophysics, guided by Dr. Diego Antonio Falceta Gonçalves, approved in September 13, 2019.

URL of the original document:
<http://urlib.net/8JMKD3MGP3W34R/3TRNE3L>

INPE
São José dos Campos
2019

Cataloging in Publication Data

Sartorio, Nina Sanches.
Sa77i The impact of photoionizing feedback in star forming molecular clouds / Nina Sanches Sartorio. – São José dos Campos : INPE, 2019.
xxii + 180 p. ; (sid.inpe.br/mtc-m21c/2019/08.17.01.06-TDI)

Thesis (Doctorate in Astrophysics) – Instituto Nacional de Pesquisas Espaciais, São José dos Campos, 2019.
Guiding : Dr. Diego Antonio Falceta Gonçalves.

1. Turbulence. 2. Stars massive. 3. photoionization. 4. star formation. 5. methods numerical. I.Title.

CDU 524.338.2

Aluno (a): ***Nina Sanches Sartorio***

Título: "THE IMPACT OF PHOTOIONIZING FEEDBACK IN STAR FORMING MOLECULAR CLOUDS"

Aprovado (a) pela Banca Examinadora em cumprimento ao requisito exigido para obtenção do Título de ***Doutor(a)*** em ***Astrofísica***

Dr. Francisco Jose Jablonski

Presidente / INPE / SJCampos - SP

( ) Participação por Video - Conferência

(X) Aprovado ( ) Reprovado

Dr. Diego Antonio Falceta Gonçalves

Orientador(a) / EACH/USP / São Paulo - SP

( ) Participação por Video - Conferência

(X) Aprovado ( ) Reprovado

Dr. João Braga

Membro da Banca / INPE / São José dos Campos - SP

( ) Participação por Video - Conferência

(X) Aprovado ( ) Reprovado

Dr. Grzegorz Kowal

Convidado(a) / EACH/USP / São Paulo - SP

( ) Participação por Video - Conferência

(X) Aprovado ( ) Reprovado

Dra. Elisabete Maria de Gouveia Dal Pino

Convidado(a) / IAG/USP / São Paulo - SP

( ) Participação por Video - Conferência

(X) Aprovado ( ) Reprovado

Dr. Alex Cavaliéri Carciofi

Convidado(a) / IAG/USP / São Paulo - SP

( ) Participação por Video - Conferência

(X) Aprovado ( ) Reprovado

Este trabalho foi aprovado por:

( ) maioria simples

(X) unanimidade

São José dos Campos, 13 de setembro de 2019

“If people do not believe that mathematics is simple, it is only because they do not realize how complicated life is."

John Von Neumman

To my first Physics teachers, Airton Algozini Junior and Mike Sabberton, the people who inspired me to dive into the Physics universe

ACKNOWLEDGEMENTS

I have to thank first of all my supervisor Diego Falceta Goncalves for all the help and support throughout my PhD. I would also like to say my deep thanks to the people in the St Andrews group, specially to Dr. Kenneth Wood and Dr. Bert Vandenbroucke for all their teaching, support and insightful conversations, without which this work would not have been possible. Finally, I would like to thank my mother Magali Duran, for her relentless support and wisdom, which made me the person I am today.

ABSTRACT

Molecular clouds are imperative to Astronomy as the sites of all known star formation. These clouds are constantly exposed to strong emission of ionizing radiation incoming from the most massive stars. This photoionizing feedback dramatically alters the molecular cloud by ionizing and heating the gas and creating shock fronts, which accelerate and compress gas in the cloud. Thus, this mechanism has important consequences to the chemistry and the dynamics of the environment around the source stars. The goal of this work is to improve our understanding of the role photoionizing feedback from massive stars plays in their own formation and in the dynamics of turbulent gas of molecular clouds. In order to carry out this study, we perform a series of high-resolution radiation hydrodynamics grid simulations. The radiation transfer uses a Monte Carlo scheme, which was coupled to an existing magnetohydrodynamics grid code (AMUN). This new combined code, presented as part of this work, was tested against a number of benchmarks in order to ensure that the coupling between radiation and hydrodynamics was robust. Simulations of turbulent molecular clouds were run with the aim to analyse how the turbulence statistics changed once ionizing feedback was present. We find that this feedback mechanism does not present significant changes to the statistics of the molecular clouds. This, in turn, implies that observational data can be compared with simulations that do not include photoionizing feedback. We also run simulations of massive star formation models with the code CMacIonize. We simulate massive stars accreting through a torus or disk and probe which scenarios the ionizing radiation from the star will lead to a dissipation of the disk and, thereby, a cessation of accretion. We show that ionized regions in this accretion mode take a number of distinct configurations and we establish limiting values for luminosities for which accretion is allowed to proceed for distinct stellar masses and ambient densities. We also find that, if a forming massive star has companions, then it is harder for the photoionizing feedback to lead a stop in accretion and, therefore, that a multiplicity may facilitate massive star formation.

Keywords: turbulence. stars: massive. photoionization. star formation. methods: numerical.

O IMPACTO DA FOTOIONIZAÇÃO NA FORMAÇÃO ESTELAR NA ESCALA DE NUVENS MOLECULARES

RESUMO

Nuvens moleculares são de extrema importância, já que representam o local onde toda a formação estelar ocorre. Essas nuvens estão constantemente expostas a uma forte emissão de radiação ionizante provinda das estrelas mais massivas. Esse *feedback* fotoionizante muda drasticamente a nuvem molecular, ionizando e aquecendo o gás e criando frentes de choque que aceleram e comprimem o gás na nuvem. Portanto, esse mecanismo tem consequências marcantes na química e na dinâmica do ambiente ao redor das estrelas fonte da radiação. O objetivo deste trabalho é melhorar nosso entendimento do papel do *feedback* fotoionizante das estrelas massivas na sua própria formação e na dinâmica do gás turbulento das nuvens moleculares. Visando esta meta, fizemos uma série de simulações de alta resolução de hidrodinâmica radiativa. A transferência radiativa usa o método de Monte Carlo e foi acoplada a um código já existente de magnetohidrodinâmica (AMUN). Esse novo código combinado, que constitui parte deste trabalho, foi validado em casos teste a fim de nos certificarmos de que o acoplamento da radiação com a hidrodinâmica era robusto. Simulações de nuvens moleculares turbulentas foram realizadas com o intuito de analisar o efeito da fotoionização na estatística da turbulência. Mostramos que esse mecanismo de *feedback* não apresenta mudanças significativas na turbulência da nuvem molecular. Isso implica que os dados observacionais podem ser comparados com simulações que não incluam os efeitos de fotoionização. Além disso, também realizamos simulações de formação de estrelas massivas com o código CMacIonize. Simulamos uma estrela massiva acretando material via um torus ou um disco de acreção e testamos em quais cenários a radiação ionizante da estrela causa a destruição/dissipação do disco e, portanto, determina o fim da acreção de gás. Mostramos que, nesse modo de acreção, as regiões ionizadas têm uma série de configurações possíveis e estabelecemos valores de luminosidade limite para os quais a acreção pode prosseguir em diversos casos distintos. Também constatamos que, se a estrela massiva tem companheiras (ou seja, é um sistema de duas ou mais estrelas), torna-se mais difícil para a radiação fotoionizante cessar a acreção à estrela. Portanto, a multiplicidade pode ser uma facilitadora na formação de estrelas de alta massa.

Palavras-chave: turbulência. estrelas massivas. fotoionização. formação estelar. códigos numéricos.

LIST OF FIGURES

Page

LIST OF TABLES

CONTENTS

1 INTRODUCTION

1.1 Motivation

It is hard to think of something more central to Astrophysics than the study of stars as, arguably, almost everything of interest in the field are (stars, clusters, galaxies), were (neutron stars, black holes), will be (proto-stars) or depends on (planets) stars. Unsurprisingly, for many decades the topic of how stars came to be or star formation has been in the limelight of research. Both observations and theory have undergone great advances in recent years. In the latter, they were driven largely by improved numerical simulations (which have been able to incorporate an increasingly large number of physical processes at higher resolutions) and, in the former, by the advent of large-scale surveys with new telescopes capable of probing details of star-forming regions previously out of reach (ALMA, Spitzer, etc).

Despite the recent progress and the attention it has received, star formation is not yet completely understood. Part of the difficulty lies on the fact that star formation depends on a hierarchy of physical processes acting on a wide range of length scales: Galactic dynamics (kpc scales) determine the characteristics of the molecular clouds (10s-100s pc scales) whose cold gas then collapses and fragments to form clumps (pc scales) containing cores (0.1 pc scales) which eventually may contract to form stars (AU scales). As a result, a thorough understanding of star formation would require the ability to correctly account for the inter-dependence of these scales, which is still not clear.

Within this hierarchy, gravity clearly plays a central role in the processes of transforming gas onto stars. However, the observed star formation rate is much slower than one would expect from the action of gravity alone (MACLOW; KLESSEN, 2004; KRUMHOLZ, 2014). This indicates that some mechanism that opposes the gravitational forces is at play. Turbulence was invoked as such a mechanism in the gravo-turbulent model (MACLOW; KLESSEN, 2004; MCKEE; OSTRIKER, 2007; HOPKINS, 2013). This model predicted that star formation can only be explained when supersonic turbulence in the interstellar medium re-structures the gas within the molecular clouds. Turbulence would be responsible to establish a complex network of interacting shocks, where regions of high-density build up at the stagnation points of convergent flows. In other words, star formation would be controlled by an interplay between supersonic turbulence and self-gravity: while turbulence is strong enough to counterbalance gravity on global scales, on sub-parsec scales it may create dense enough structures that are locally Jeans unstable and thus able to collapse to form stars (MACLOW; KLESSEN, 2004; SCALO; ELMEGREEN, 2004). The processes that drive the turbulence within molecular clouds (MCs) are still highly debated. MCs likely inherit their initial turbulence from the interstellar medium (ISM), but these motions are expected to decay quickly. Feedback mechanisms, that is, any process by which a star injects matter, momentum and/or energy in its neighbouring gas, may be able to sustain the turbulent state of the MCs. While observational and numerical studies indicate that energy associated with feedback processes (protostellar outflows, winds and radiation, etc) is comparable to the cloud energy, it has not yet been shown if the feedback plays a role in the turbulent cascade or if it only affects the immediately surrounding gas.

Feedback itself is thought to have a close relation to star formation. Many studies claim that stellar feedback processes may reduce the overall star formation efficiency, while also triggering star formation in specific locations where gas is thought to accumulate as a byproduct of these processes (LUCAS et al., 2017; REY-RAPOSO et al., 2017). Thus, it is often stated that star formation is a self-regulating process, with one generation of stars determining the subsequent one (HAYWARD; HOPKINS, 2017). In addition, feedback from the earliest stages of stellar evolution may play a key role in how mass is added onto an accreting proto-star.

In this thesis we are going to focus on a single feedback mechanism: the photoionization feedback. This type of feedback is intrinsically correlated to massive stars (stars with masses superior to around eight times that of the Sun), as these stars are the only ones able to emit large enough amounts of UV radiation capable of ionizing their surroundings. The ionizing luminosity from less massive stars is indeed much smaller than the ones from massive stars despite the number of the former being significantly larger than the latter. We will investigate the relation of the ionizing feedback to the turbulence present in the molecular clouds and how that may affect star formation. We will also probe the effect the photoionization of a massive star has on its own acquisition of mass during the early stages of their formation.

1.2 Scientific aims

The investigation of the impact of photoionizing radiation from massive stars on star formation is done both via analytical and numerical studies. The numerical simulations required the ability of recreating, as well as possible, the sites where star formation occurs and of performing the radiation transfer in order to correctly address the impact of photoionization. Thus, it is essential that the code used possesses the following capabilities:

- Perform hydrodynamics
- Include the effect of turbulence
- Do radiative transfer

In this thesis we used two codes. One of them, CMacIonize (VANDENBROUCKE; WOOD, 2018a), could perform efficiently radiation-hydrodynamic simulations, but did not include turbulent forcing. The other, AMUN (KOWAL, 2007–2016), had the hydrodynamics as well as turbulent forcing, however, did not include radiation transfer. During the course of the PhD we added both radiation transfer to the latter as well as turbulent forcing to the former.

CMacIonize was first used, without the turbulent module, to study accretion onto forming massive stars both in a spherically symmetric fashion and via a disk. The AMUN code was used, after the incorporation of a module of Monte Carlo radiative transfer, to study the expansion of HII regions in turbulent media and to investigate if photoionization feedback altered the statistics of the turbulence in the simulated molecular clouds. Finally, CMacIonize is being used with the new turbulent module to study spectral hardening of photons escaping HII region, as well as studying the driving of turbulence by radiative feedback.

The specific questions we endeavour to address with these studies were:

- Can photoionizing feedback cease accretion onto a forming massive proto-star? In what conditions does this occur?

- Does the photoionizing feedback from massive stars affects the statistics of the turbulence around it? If so, to what extent? What impact that may have to star formation?

This thesis is divided as follows. Chapter 2 aims at providing a review of the current knowledge of star formation, presenting some fundamental concepts which provide a basis for the material later explored in the thesis. Chapters 3 and 4 are related to the theory behind numerical simulations. Chapter 3 presents a brief review of hydrodynamics and how it is approached numerically in grid-based codes used for this work. In this chapter we report how we incorporate turbulence within the CMacIonize code. Chapter 4 presents how radiative transfer can be done by using Monte Carlo techniques and the advantages and disadvantages of such a method. Chapter 4 also explains how Monte Carlo radiative transfer (MCRT) was incorporated into the magneto-hydrodynamic code AMUN and some benchmark tests that were run in order to validate the coupling of radiation to the hydrodynamics. Chapters 5 to 7 present the result of the research done with the MCRT - hydrodynamical codes. Each chapter contains a a brief introduction to content pertaining to the topic to be discussed. This aims to include any information which has not been addressed in Chapter 2, due to it being needlessly detailed for a review of star formation, but which is required to be laid out in order to give a self contained explanation of the research undertaken in this thesis.

In Chapters 5 and 6 we focus on the study of accretion onto massive stars. We first review the idealized scenario on which accretion happens in a symmetrical manner (a Bondi accretion) in Chapter 5 and derive an analytical solution for this scenario. We then progress in Chapter 6 to a more complicated (but more realistic) scenario in which accretion occurs via a disk aiming to probe how does this mode of accretion changes the interaction between the star's ionizing feedback and its surroundings.

Chapter 7 lays out the relevant statistical description of turbulence for this work and its relation to star formation. We present an analysis of the impact that ionizing radiation has to the turbulence in our simulations.

Finally, in Chapter 8 we present the main conclusions of this thesis and future projects.

2 ZOOMING IN ON STAR FORMATION

2.1 Introduction

The interstellar medium (ISM) is the nomenclature given to all the gas and dust that lies in the space between stars. For the Milky Way, it accounts for $\sim 15\%$ of the mass of the galactic disk (FERRIERE, 2001), most of which is concentrated around spiral arms. The ISM is often described by being “mutiphased", depending on the typical temperatures and ionization state of the gas. Three phases are defined: the Cold Neutral Medium (CNM), the DIG (Diffuse Ionized Gas), often referred as the Warm Ionized Medium or WIM when regarding the Milky Way, and the Hot Ionized Medium (HIM).

Within the CNM are located the sites where star formation takes place: the molecular clouds. These clouds have typical average number densities of 100 cm^{-3} and mean temperatures are normally just a few tens of Kelvin (WOLFIRE et al., 2003), though local values for these quantities can be much higher (HENNEBELLE; FALGARONE, 2012). In fact, the cloud’s gas is far from being uniformly spread throughout interstellar space; instead, it shows pronounced density and temperature contrasts. When observed at sufficient sensitivity and a large enough dynamic range, clouds exhibit a highly structured framework, with filamentary structures comprising dense cores being the most common (ANDRE et al., 2010; MOLINARI et al., 2010). It is only in the densest, coldest regions, where a myriad molecules can easily form, that star formation takes place.

The most abundant molecule within molecular clouds is the hydrogen one, H_2. Thus, to find molecular clouds and the sites of ongoing star formation, we have to trace the H_2. Molecular hydrogen cannot, however, be directly observed. One of the reasons is that H_2 is extremely stable: as it is a homonuclear molecule (containing only one type of atom), it does not posses a permanent dipole moment (STERNBERG, 1989). In addition, its rotational transitions are very weak and occur at mid-infrared wavelengths, which are too energetic to be collisionally excited by the low temperatures of the clouds (HABART et al., 2005). As a result, the amount of H_2 and the associated estimate of masses of molecular clouds have to be found by some other measurement.

One good tracer of molecular gas is dust. The gas-to-dust ratio seems to be invariable within interstellar clouds (PREDEHL; SCHMITT, 1995). Measurements of the absorption and scattering of background light, known as dust extinction, are particularly useful, as they are independent of dust temperature and directly proportional to the column density of the dust. Another commonly used tracer is the CO isotopes ^{12}CO and ^{13}CO, as carbon monoxide is the second most abundant molecule found in molecular clouds and they are easily excited.

As the capability of performing sensitive CO molecular-line observations increased, we were able to measure total gas surface densities in external galaxies. Simultaneously, improvements in infrared and ultraviolet observations made the detection of ongoing star formation easier and led to significant progresses in the measurements of star formation rates. Since then, a lot of work was expended in order to systematically measure star formation rates and total gas surface densities in increasingly large samples of galaxies, culminating in the study of Kennicutt (1998), who compiled galaxy-averaged measurements for a wide sample of galaxies. He derived a scaling relation between the SFR surface density and total gas surface density, which is characterised by a power-law index of $n \approx 1.4$.

In addition to tracing H_2, CO emission lines, as well as other molecules', can be used to measure the velocity dispersion, which is obtained from their line widths. Using this method, in a seminal paper, Larson (1981) plotted the velocity dispersion as a function of size for a number of cloud complexes, individual clouds and clumps or density enhancements in larger clouds. In Figure 2.1, we plot the same original data used by Larson. As it can be seen, a correlation between the line widths and the velocity dispersion seems to exist.

This power-law form was taken to be indicative of the turbulence cascade that encompasses molecular cloud scales. Within molecular clouds, velocity dispersion values are of order σ_v (L) $\approx$ 20 km s^{-1} down to 1 km s^{-1} over the entire projected cloud (ZUCKERMAN; EVANS, 1974). Considering that the isothermal sound speeds (c_s) for the temperatures mentioned earlier in this section are of order of a few hundred meters per second, the sonic Mach number ($M_S = \sigma_v / c_s$) is greater than one, indicative that the turbulence is supersonic.

The power law observed by Larson also demonstrates that, as we go towards smaller scales, the velocity dispersion decreases. This, in turn, implies that at some scale (the sonic scale) the flow will transition from being supersonic to being subsonic. This scale is useful because it separates the larger scales, where turbulence is dominant, from scales where the typical velocity fluctuations are small compared to the thermal motions of the gas. Therefore, in these scales, turbulence support against gravitational collapse becomes less important than the thermal support. For this

Figure 2.1 - Illustration of Larson's law.

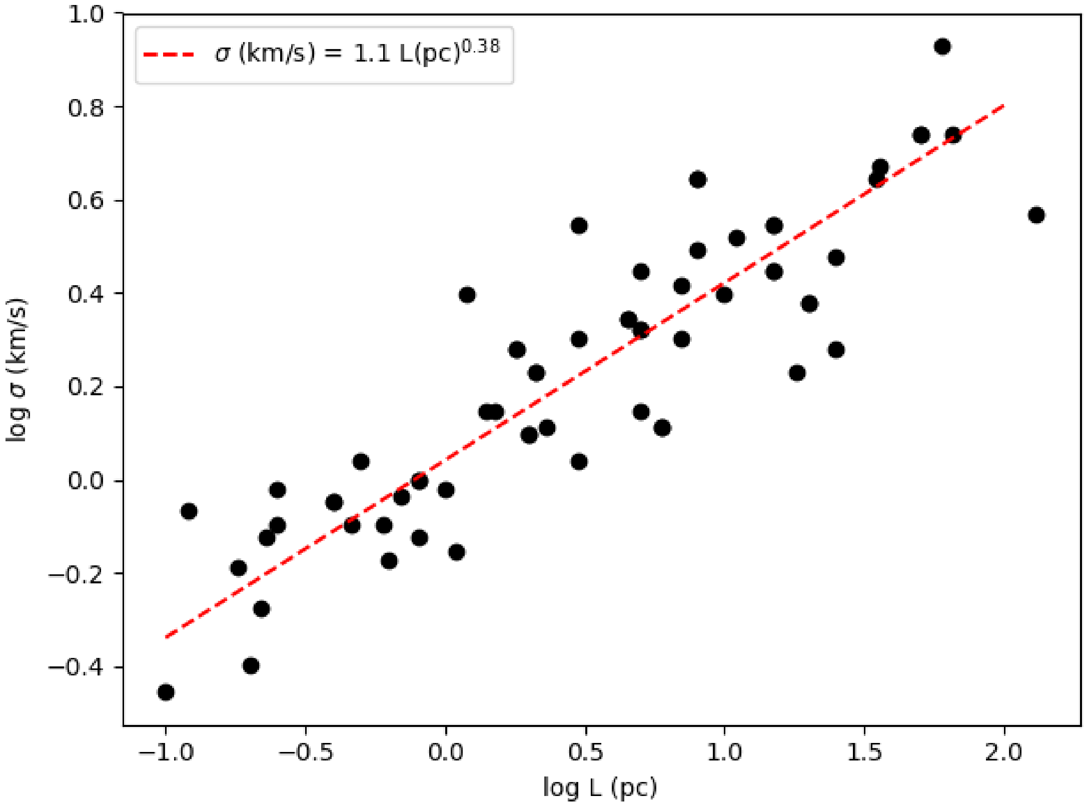

Illustration using the original data released by Larson (1981), who discovered the empirical relationship between the size of a molecular cloud and its internal velocity dispersion. Larson found that the average velocity dispersion within a cloud is proportional to its size raised to a power n. This relation holds for clouds ranging in size from about 0.1 to 100 parsecs and is indicative that turbulence is pervasive in the diffuse gas spawning molecular clouds.

reason, the sonic scale is thought to be linked to the size of the dense cores which bear the formation of stars.

This idea of turbulent interstellar matter was not a new one. As early as the 1950s, vonWeizsäcker (1951) outlined a theory for interstellar matter (ISM) that is similar to what we believe today: cloudy objects with a hierarchy of structures form in interacting shock waves by supersonic turbulence that is stirred on the largest scale by differential galactic rotation and dissipated on small scales by atomic viscosity. But it wasn't until evidence of the ubiquity of turbulent motions by Larson, and the fact that turbulence seemingly dictates the distribution of the gas content in molecular clouds, that turbulence became a key ingredient in star formation.

2.1.1 Turbulence and star formation theory: the gravo-turbulent model

One of the central topics within star formation is the rate at which available molecular gas is converted into stars. This is not only important for the understanding of the process of star formation, but also for galaxy evolution (AGERTZ et al., 2013). The star formation rate is directly related to what is referred to the star formation efficiency (ξ), defined as the fraction of a molecular cloud's mass that is converted into stars per free-fall time at the mean density of the cloud. That is:

$$\xi = \frac{\dot{M}_\star}{M_{MC}(\rho_{mean})/t_{ff}(\rho_{mean})} \tag{2.1}$$

where $\dot{M}_\star$ is the star formation rate, M_{MC} is the mass of the cloud in question and t_{ff} is the free-fall time for a uniformly dense sphere ($t_{ff} = \sqrt{\frac{3\pi}{32G\rho}}$).

In the Milky Way, the giant molecular clouds (GMCs) have the bulk of the mass contained within molecular clouds. GMCs have typical masses of $10^6 M_\odot$ and altogether their masses exceed $10^9\ M_\odot$ (WILLIAMS; MCKEE, 1997). If we consider the earliest models of molecular clouds (for instance that of Goldreich e Kwan (1974) in which molecular clouds are considered to be gravitationally bound spheres of gas that are in free-fall collapse), we would expect, using the average densities mentioned above, the free-fall time is $t_{ff} \approx 5 \times 10^6$ yr. Thus, as $M_{MC}/t_{ff} \approx 200 M_\odot/\mathrm{yr}$, for the observed star formation rate of $\sim 1 M_\odot/\mathrm{yr}$, we have an efficiency of only 0.01% (BIGIEL et al., 2011; LEROY et al., 2013).

This very low star formation rates, first noticed by (ZUCKERMAN; EVANS, 1974), was posteriorly confirmed by repeated observation using many different density tracers (KRUMHOLZ; TAN, 2007; MURRAY; RAHMAN, 2010), and remains one of the major unsolved conundrums in star formation theory (ZUCKERMAN; PALMER, 1974; WILLIAMS; MCKEE, 1997; KRUMHOLZ; TAN, 2007; FEDERRATH, 2013).

The first attempt to explain such low star formation rates was to argue that, due to the presence of strong magnetic fields, the collapse of dense regions would be hindered by magnetic pressure support within clouds. This support can be estimated by the ratio of magnetic to gravitational binding energy, which is proportional to the mass to magnetic flux ratio M/ϕ. The minimum value of this ratio, needed to support molecular cloud collapse, is given by the critical value $(M/\phi)_{crit}$. Magnetically dominated cores have sub-critical to trans-critical values $(M/\phi)/(M/\phi)_{crit} \leq 1$. In ideal MHD, the field is frozen into the gas and ϕ remains constant. This implies that, as a cloud contracts, the gravitational energy decreases, but the magnetic one remains the same because of flux freezing. Consequently, for sub-critical clouds, collapse is not possible. The only way of the cloud to collapse is to change the magnetic critical mass, which requires changing the magnetic flux through the cloud. This can only happen through non-ideal MHD phenomena, one possible solution being the ambipolar drift (the drift of neutral matter with respect to ions and the magnetic field). This ambipolar diffusion, originally suggested by (MESTEL; SPITZER L., 1956), would act as a way of magnetic flux to leak out of interstellar clouds and induce collapse and fragmentation. If this were the case, the star formation rate would be controlled by ambipolar drift. A reevaluation of this process was presented by Mouschovias (1976), who pointed out that ambipolar diffusion led primarily to the gravitational redistribution of mass and magnetic flux within the magnetic flux tubes of a cloud. This implicates that the formation and collapse of cores should occur in magnetically supported envelopes.

However, Zeeman spliting measurements of magnetic field lines (PADOAN; NORDLUND, 1999) have demonstrated that mean magnetic fields in the molecular clouds were much weaker than the ones required to offer the proper support gravitational collapse. McKee e Ostriker (2007) gathered a number of observational works to show that molecular clouds are mostly supercritical instead of subcritical, in which case the ambipolar-drift time cannot be the solution to the SFR problem (see also (CRUTCHER et al., 2009).

Another scenario that could solve the low star formation rate is if clouds are in fact not gravitationally bound and are more transient entities (BABA et al., 2017; DOBBS; PRINGLE, 2013; DOBBS, 2015). In this case, the free-fall time is no longer the characteristic timescale for molecular cloud evolution and it should not be surprising that our simple calculation above leads to low star formation efficiency as we are modelling the problem wrongly. Dobbs et al. (2011) considers this scenario in simulations of spiral galaxies, including some feedback mechanisms from star formation, but excluding magnetic fields effects. During cloud collisions, material was found to be reallocated, with some clouds being dispersed. Feedback acted as the main mechanism for removing large amounts of gas from a cloud, such that, besides very massive clouds, the majority of clouds changed dramatically over a few Myr. In this picture, the low efficiency mirrors the fact that only a small fraction of molecular gas is found in bound structures.

Testing this theory is, however, non-trivial, as there is no accurate way of observationally verifying if clouds are bound, especially when they have a complex filamentary structure. Observational results often have conflicting conclusions, with some having mostly bound molecular clouds (ROMAN-DUVAL et al., 2010), some having almost exclusively unbound cloud complexes (NGUYEN-LUONG et al., 2016) and some claiming there is a mass threshold clouds must have to be bound (more massive clouds being bound) (HEYER; DAME, 2015).

Interestingly, turbulence plays an important, yet slightly different role, for both bound and unbound star forming clouds. In the case of bound clouds, as magnetic fields are not capable of containing the cloud collapse, turbulence is invoked to do it. This is arguably the most popular star formation theory which started gaining popularity in early 2000s. This so called gravo-turbulent model predicts that star formation can only be explained when the turbulence in the interstellar medium re-structures the gas within the molecular clouds, creating high density regions that then become unstable and collapse into stars (KRUMHOLZ; MCKEE, 2005). The underlying assumption is, thus, that star formation is controlled by interplay between supersonic turbulence and self-gravity. By this account, turbulence plays a dual role in star formation. While it is strong enough to counterbalance gravity on global scales, it may provoke collapse locally (KLESSEN, 2011). Turbulence establishes a complex network of interacting shocks, where regions of high-density build up at the stagnation points of convergent flows. These gas clumps can be dense and massive enough to become gravitationally unstable and collapse when the local Jeans' length becomes smaller than the size of the fluctuation.

In unbound clouds, turbulence does not need to contain the gravitational collapse of the cloud, however, it is responsible again for the formation of gravitationally bound substructures of the clouds, which are also ultimately responsible for the star formation.

Therefore, it seems that turbulence is an ingrained characteristic of molecular clouds and has fundamental importance in the formation of stars. However, the mechanism throughout which turbulence is generated is still question of debate. Some say it is gravitationally created (WADA et al., 2002; KRUMHOLZ; BURKHART, 2016), some say it is mainly due to supernova feedback (GENT et al., 2019; PADOAN et al., 2016). Other advocate that supernovae are important, but not enough to explain all turbulence within clouds (SEIFRIED et al., 2018). It is also said that other types of feedback are required to pump energy into other scales in order to maintain turbulence, as otherwise it seems to quickly decay and disappear (STONE et al., 1998). The concept that turbulence can be sustained by feedback of existing and forming stars has been currently a topic of intense study. As the molecular clouds are turbulent, a given region within it exhibits sub-patches with a range of surface densities. The high-density patches would be jostled around by feedback mechanism, thereby locally driving turbulence and regulating star formation (HAYWARD; HOPKINS, 2017; KRUMHOLZ et al., 2014). Observational and numerical studies alike often find that energy associated with stellar outflows, winds and radiation is of comparable energy to that of cloud energy. Nevertheless, disentangling the turbulent flows generated by feedback from the initial cloud turbulence is challenging, and the extent that feedback from young sources contribute to the local turbulent cascade is yet to be ascertained.

2.1.2 Massive stars: their formation and importance

If feedback effects are indeed important for star formation, then massive stars are most likely the major players in shaping molecular clouds and controlling the formation of the next generation of stars (MASSEY, 2003; HARRIES et al., 2017; KUIPER; HOSOKAWA, 2018; OFFNER; LIU, 2018). These stars are typically differentiated from low mass stars by the way they end their lives, namely in energetic supernovae explosions(MAUND et al., 2017). This usually imposes a definition that massive stars are stars with masses of order 8 solar masses or more. As it is well known, supernovae explosions have dramatic consequences not only to the star immediate environment but to the entire galaxy. Supernovae alter the gas dynamics to kiloparsec scales and they are thought to be essential to create the diffuse layer of gas found above the galactic disk plane, also known as the diffuse ionized gas or DIG. Furthermore, supernovae are thought to be a main driver of turbulence at large scales. Chemically, these powerful explosions managed to synthesise most of the heavy elements found in the universe today, which dramatically changed the way gas heats and cools and allowed for the sub-sequential formation of planets and eventually life. Even before their deaths, massive stars play important roles in molecular cloud dynamics and chemistry. Through feedback processes such as photoionization, winds and jets, they heat and stir the surrounding gas. If we analyse the mass distribution of newly formed stars - the Initial Mass Function (IMF) - of different regions, it is clear that the number of massive stars is a small percentage of total number of stars forming (see Figure 2.2).

Figure 2.2 - Mass function of different regions

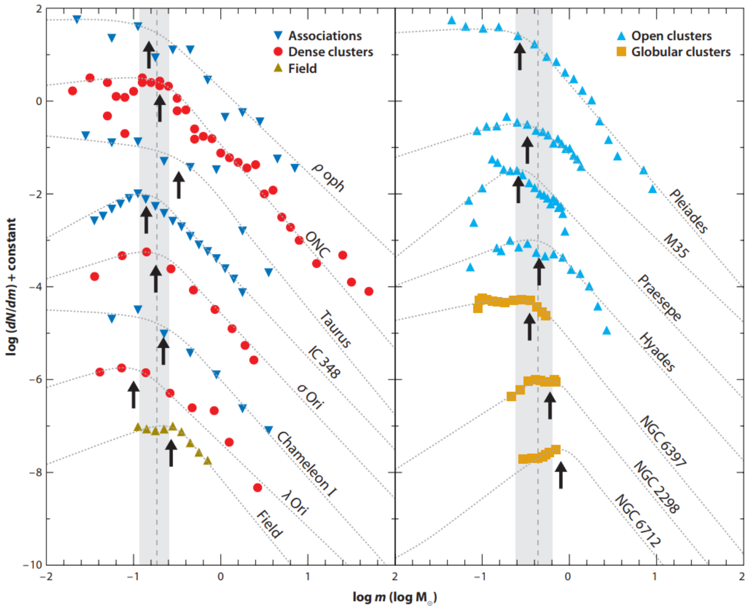

The present-day mass function of a sample of young star-forming regions, open clusters spanning a large age range, and old globular clusters from the compilation of G. de Marchi, F. Parsesce, and S. Portegies Zwart. The dashed grey lines represent the predicted IMFs for each scenario.
Source: (BASTIAN et al., 2010).

On average, only one star of 30 $M_\odot$ forms for every hundred stars with mass similar to our Sun's. These stars also live a factor 10^{-3} less than solar type stars, as they have to fuse elements at a much larger rate to keep their enormous mass from collapsing onto themselves. This implies that, at any point in time, the present number of these stars would be a factor 10^5 less than solar-like stars. Yet, a typical 30 $M_\odot$ is more 10^6 times more luminous than a 1 $M_\odot$ star and, thus, massive stars dominate the luminosity of the universe. Furthermore, if we consider ionizing radiation, the preponderance of massive stars is even more marked (see Figure 2.3). Clearly, throughout their short lives (and their death), massive stars have a disproportionate effect on the ISM.

Despite the clear pivotal role that these stars play, their formation is, in many ways, poorly understood. Radiation feedback is thought to have an important impact during the formation of these stars, however, the extent and quantification of this impact is not yet clear.

Figure 2.3 - Emission of ionizing radiation per stellar mass

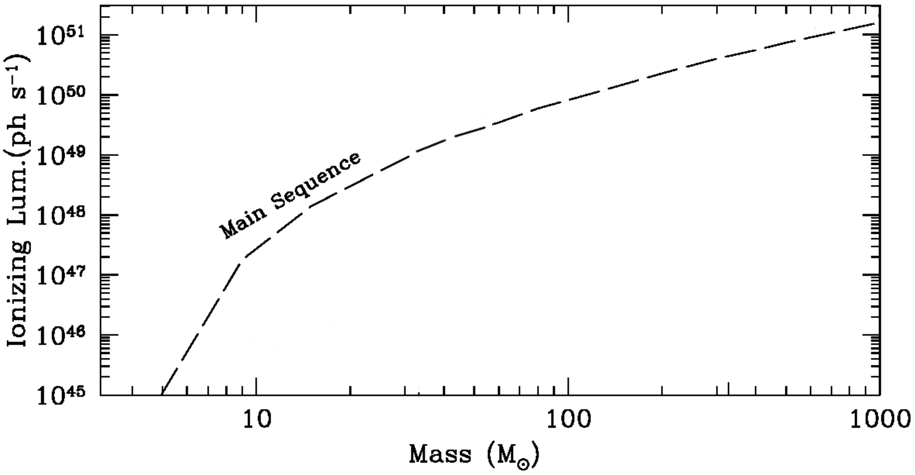

Figure, modified from Tan e McKee (2004) showing the amount of hydrogen-ionizing radiation for stars depending on the stellar mass.

2.2 Rationale of the thesis

As we have seen, massive stars and turbulence have tremendous importance to molecular clouds properties. In the work presented in this thesis we are going to analyse star formation with a concern for the impact exerted by radiative feedback from massive stars. First, we are going to concentrate on the smaller scales of star formation by considering the means by which a massive star can form and the effect of photoionization resulting from the radiation emitted by the forming massive stars themselves. We then endeavour to quantify the impact massive stars have on the turbulence of molecular clouds in which they are born by analysing the influence photoionizing radiation has on the statistics of turbulence.

3 ANALYTICAL AND NUMERICAL HYDRODYNAMICS

3.1 Introduction

From a numerical stand point, the topics relevant to this thesis rely on two cornerstones: how the gas moves and how the radiation propagates. In this chapter, we are concerned with the first: how does the material moves within molecular clouds. We keep the explanation of how the radiative transport is implemented to the following chapter.

In order to model the interstellar gas, we assume that it behaves as a fluid. The fluid dynamics can be described from two distinct points of view: one from a point of reference that moves with the fluid (Lagrangian) and one in which the fluid moves with respect to a static reference frame (Eulerian). In Section 3.2 these two points of view are presented, as well as the most common numerical models (particle and grid base methods) which use either approach. We present, then, the criteria we used to choose the codes employed on this thesis.

In Section 3.3, we review the basic concepts of hydrodynamics, deriving the most important equations from first principles. We proceed to show how the derived equations can be translated into a computational description of a fluid. This is required because, although an analytical description can offer many insights, complex problems often do not have analytical solutions and need to be studied by means of numerical simulations. Throughout Section 3.4, we review the standard Eulerian approach, used by both codes (AMUN and CMacIonize) to numerically approach the fluid dynamics, referred as the Finite Volume Method (FVM). Because we cannot trace the properties of our fluid at every point in space, hydrodynamic modelling requires discretizing physical quantities. During this discretization process, the continuum, or a quantity which has the property of being continuous, is replaced by number of individual data points. In the case of the FVM, these are small volume elements, typically referred to as cells. Each volume element stores the relevant cell-averaged hydrodynamic quantities which are of interest to a particular simulation. These quantities have to be evolved according to the equations of hydrodynamics presented in the preceding section. A short outline of how the hydrodynamics is solved on this discretized representation of our physical domain is given, demonstrating how the fluid equations are solved by computing the flux of the mass, momentum, and energy across cell boundaries.

Lastly, we give a general outline on how turbulence is added in our simulation and how it compares to other ways of creating turbulent media in Section 3.5.

3.2 Eulerian and Lagrangian descriptions

In order to simulate the dynamics of molecular clouds and accretion flows, we assume that they can be treated as a single fluid. This fluid and its motions can be, then, described by standard hydrodynamic equations, which may be approached in two ways: by using the Eulerian or the Lagrangian descriptions of the flow.

The Eulerian description regards the analysis of a fluid flowing through a volume fixed in space, whereas the Lagrangian description regards a volume co-moving with the fluid itself. Clearly, these two descriptions simply represent the same problem analysed through different points of view and are, therefore, equivalent. These two views can be brought together by realising that the time derivative of a fluid volume in the Lagrangian scheme $\frac{D}{Dt} = \frac{\partial}{\partial t}$ has an analogue in the Eulerian scheme $\frac{D}{Dt} = \left[\frac{\partial}{\partial t} + v\boldsymbol{\nabla}\right]$, referred as the convective derivative. That is, the Lagrangian time derivative of a variable Q has a term due to the rate of change of this variable at a fixed point in space (the Eulerian time derivative $\frac{\partial Q}{\partial t}$) plus a term $(\boldsymbol{u} \cdot \boldsymbol{\nabla} Q)$ that incorporates the movement of the fluid volume to a new position in space where that variable has a distinct value.

Hydrodynamical codes can use either Eulerian or Lagrangian descriptions. Each numerical scheme has certain advantages and disadvantages, which we now present. Given the characteristics of each scheme we, then, justify our choice of codes.

3.2.1 Particle codes and SPH

The most common Lagrangian method is that of particle codes. Particle codes split the fluid into a number of particles, each of which has a given mass. These particles are moving fluid elements with a certain fluid velocity, which naturally cluster at regions of high densities and are spread apart at regions of low density. Because the number of particles in a region is directly proportional to the resolution of that region, high density areas are straightforwardly better resolved. In other words, the Lagrangian character gives particle codes the advantage of following the geometry of the simulation with adaptive spatial resolution. In addition, it turns out that the particle based codes have excellent conservation properties. Energy, linear momentum, angular momentum, mass, and entropy (if no artificial viscosity operates) are all simultaneously conserved. The main advantage of particle codes is their strict Galilean-invariant property.

The most common particle based codes use Smoothed Particle Hydrodynamics (SPH), created by Lucy (1977) and largely extended by works of Gingold e Monaghan (1977) thereafter. In this method, fluid properties are determined by averaging or "smoothing" over a fixed number of neighbouring particles. The radius of the circle (in a 2D simulation) or sphere (in 3D) encompassing these neighbours is referred to as the "smoothing length". This averaging makes SPH techniques unsuitable for solving very sharp density contrasts and thus unable to correctly resolve shocks and instabilities (AGERTZ et al., 2007), unless some artificial viscosity is added to the problem. However, the addition of artificial viscosity broadens shocks by several smoothing lengths, degrading the resolution.

As the topics explored on this thesis involve working with turbulent media, which in turn rely strongly on our ability to resolve shocks and density gradients, we opted to use grid based codes (see next subsection). It should be pointed out that SPH is able to reproduce comparable results of grid codes for volumetric statistics of turbulence (PRICE; FEDERRATH, 2010). However, this is only achieved by using a number of particles equal to the number of cells in a grid based code. For this reason, SPH codes are not well suited to quantify such properties since, for this kind of problem, a SPH code will be significantly more expensive than a uniform-grid implementation at similar numbers of computational elements.

3.2.2 Grid codes

The standard approach to Eulerian methods is to discretize the problem and solve the fluid equations on a grid by computing the flux of mass, momentum, and energy across adjacent grid cell boundaries. In conservative schemes, the flux of a given quantity that leaves one cell is added to the neighbouring cell, guaranteeing the correct propagation of the quantities, and proper identification of shocks. Conversely to the Lagrangian schemes, this approach has a large dynamic range in mass, but not in length. In general, Eulerian algorithms are easily parallelized, which makes it straightforward to obtain a significant gain in speed in the code.

In the Eulerian-based codes used in this thesis, we choose a Cartesian grid with evenly spaced cells of identical size. This has the disadvantage that regions of high and low density have equal resolution. This could have been circumvented by using an adaptive mesh refinement (AMR), which increases the resolution in certain areas by breaking down a of the existing cells into smaller subcells, according to some pre-stablished criterium (FRYXELL et al., 2010; TEYSSIER, 2002). Adaptive mesh refinement is already implemented and tested in one of our codes, AMUN.

However implementing a Monte Carlo method for radiation transfer (described in the next chapter) in such a grid is non-trivial. Since we did reach convergence for the simulated scenarios at 256^3 and 512^3 cells with a uniform fixed grid for the 3D simulations (which was also tractable with the computational resources at hand), we opted to use Eulerian fixed grid codes. There are many such codes available. We opted to use the codes familiar to our research groups which made the codes AMUN and CMacIonize more suitable for this project. Both codes are grid codes that make use of the Eulerian Finite Volume Method (laid out later in the chapter) to solve the hydrodynamic equations on a Cartesian grid. AMUN is able to perform relativistic MHD simulations and has turbulent forcing implemented. In this thesis, we only use the hydrodynamics capability of the AMUN code, adding to it the ability to perform radiative transfer by using the Monte Carlo method (described in the next chapter). We intend to use magneto-hydrodynamics capability of AMUN in future work to perform radiative-magnetohydrodynamic calculations. CMacIonize is a radiation hydrodynamics code which can be used as a moving mesh or as a fixed grid code. We incorporate the turbulent forcing (described at the end of this chapter) to CMacIonize.

3.3 Euler equations

The state and motion of a single neutral fluid can be described by using the following properties: density ρ, velocity $\boldsymbol{u}$ and pressure p. Given the pressure and density, we can also obtain the internal energy and the temperature through an equation of state (EOS). These properties can be used to write a set of equations, collectively known as Euler equations, which describe the conservation of mass, momentum and energy. Below we derive each one of this conservation laws (subsections 3.3.1. 3.3.2 and 3.3.3) and show how closure is achieved by the use of an EOS (3.3.4). In subsections 3.3.4 and 3.3.5, we also derive a relation of the properties above to other quantities of interest, such as the temperature and the sound speed.

3.3.1 Conservation of mass

The mass of a fluid element of density $\boldsymbol{\rho}$ and volume V can be expressed as $\int \rho dV$. Thus, the change in mass of the element over time can be expressed as:

$$\frac{\partial}{\partial t} \int_V \rho dV \tag{3.1}$$

If we subdivide the surface area of our fluid element into many smaller elements $d\boldsymbol{S}$, which lie along the normal to the surface at that point, the flow through the surface element can be described as:

$$\rho \boldsymbol{u} \cdot d\boldsymbol{S} \tag{3.2}$$

Therefore, the total mass gained is $-\int_S \rho \boldsymbol{u} \cdot d\boldsymbol{S}$ or, by the divergence theorem:

$$-\int_V \boldsymbol{\nabla} \cdot (\rho \boldsymbol{u}) dV \tag{3.3}$$

Hence, from 3.1 and 3.3 we have that :

$$\frac{\partial}{\partial t} \int_V \rho dV = -\int_V \boldsymbol{\nabla} \cdot (\rho \boldsymbol{u}) dV \tag{3.4}$$

and consequently, as this applies to all fluid elements:

$$\frac{\partial \rho}{\partial t} + \boldsymbol{\nabla} \cdot (\rho \boldsymbol{u}) = 0 \tag{3.5}$$

This is known as the conservation of mass equation or the continuity equation in Eulerian form. The Lagrangian form is easily obtained by using the convective derivative introduced earlier and can be written as:

$$\frac{D\rho}{Dt} = \rho \boldsymbol{\nabla} \boldsymbol{\cdot} \boldsymbol{v} \tag{3.6}$$

3.3.2 Conservation of momentum

Here let us start with the Lagrangian view. Let V be a volume co-moving with the fluid. We can write Newton's second law simply as:

$$\rho V \frac{D\boldsymbol{u}}{Dt} = \boldsymbol{F} \tag{3.7}$$

Where $\boldsymbol{F}$ is any force (gravitational, pressure, viscous, eletromagnetic, etc) acting on the fluid.

Now, in order to expand this equation, we first need to find an expression the forces of interest to our problem. At the present moment, we will only consider the pressure and the gravitational forces.

Pressure Force

The pressure force pushes inwards into the fluid element, allowing us to write it as:

$$\begin{aligned} \boldsymbol{F}_P &= \int (-p d\boldsymbol{S}) \\ &= \int -\boldsymbol{\nabla} p dV \\ &= -V \boldsymbol{\nabla} p \end{aligned} \tag{3.8}$$

Gravitational Force

Since gravity is a conservative force (the work done by or against it depends only on the starting and ending points of a motion and not on the path taken), it can be written as the gradient of a scalar potential. In the case of gravity, we define a (scalar) gravitational potential ϕ, such that the gravitational acceleration g is $\boldsymbol{\nabla}\phi$. Then, the gravitational force itself is:

$$\boldsymbol{F}_G = (\rho V)(-\boldsymbol{\nabla}\phi) \tag{3.9}$$

Thus, a complete version of the momentum conservation equation is obtained from 3.7, 3.8 and 3.9:

$$\rho \frac{D\boldsymbol{u}}{Dt} = -\boldsymbol{\nabla} p - \rho \boldsymbol{\nabla}\phi \tag{3.10}$$

Now, to get the Eulerian expression, we apply the definition of the convective derivative to obtain:

$$\rho \left[\frac{\partial \boldsymbol{u}}{\partial t} + (\boldsymbol{u} \cdot \boldsymbol{\nabla})\boldsymbol{u} \right] = -\boldsymbol{\nabla} p - \rho \boldsymbol{\nabla}\phi \tag{3.11}$$

Summing and subtracting $u\boldsymbol{\nabla}\cdot(\rho\boldsymbol{u})$ on the left hand side:

$$\rho\frac{\partial\boldsymbol{u}}{\partial t}-\boldsymbol{u}\boldsymbol{\nabla}\cdot(\rho\boldsymbol{u})+\rho(\boldsymbol{u}\cdot\boldsymbol{\nabla})\boldsymbol{u}+\boldsymbol{u}\boldsymbol{\nabla}\cdot(\rho\boldsymbol{u})=-\boldsymbol{\nabla}p+(\rho)(-\boldsymbol{\nabla}\phi) \tag{3.12}$$

Now, note that $\frac{\partial\rho\boldsymbol{u}}{\partial t}=\boldsymbol{u}\frac{\partial\rho}{\partial t}+\rho\frac{\partial\boldsymbol{u}}{\partial t}=-\boldsymbol{u}\boldsymbol{\nabla}\cdot(\rho\boldsymbol{u})+\rho\frac{\partial\boldsymbol{u}}{\partial t}$; where we made use of the mass conservation Equation 3.5. Further note that $\rho(\boldsymbol{u}\cdot\boldsymbol{\nabla})\boldsymbol{u}+\boldsymbol{u}\boldsymbol{\nabla}\cdot(\rho\boldsymbol{u})=\boldsymbol{\nabla}\boldsymbol{\cdot}(\rho\boldsymbol{u}^2)$. So, the momentum equation can be written as:

$$\frac{\partial(\rho u)}{\partial t}+\boldsymbol{\nabla}\boldsymbol{\cdot}(\rho\boldsymbol{u}^2)=-\boldsymbol{\nabla}p+\rho(-\boldsymbol{\nabla}\phi) \tag{3.13}$$

3.3.3 Conservation of energy

The momentum and the continuity equations do not form a closed set of equations. In order to have closure, we require another expression linking ϕ and p to ρ and u. The gravitational potential can be found from the Poisson relation:

$$\boldsymbol{\nabla}^2\phi=4\pi GM \tag{3.14}$$

The relationship between p and other hydrodynamic properties of the system is called the equation of state.

From the first law of thermodynamics we have that the internal energy of a fluid parcel U is related to the energy gained or lost, Q, and to the work done, $dW=pdV=\frac{pM}{d\rho}$ (M being the mass of a fluid parcel). In the absence of heat transfer $Q=0$, the law can be written as:

$$\frac{DU}{Dt}=\frac{DW}{Dt}. \tag{3.15}$$

As:

$$\frac{DW}{Dt}=-pM\frac{D(1/\rho)}{Dt}=\frac{pM}{\rho^2}\frac{D\rho}{Dt}, \tag{3.16}$$

we have simply that:

$$\frac{De}{Dt} = \frac{p}{\rho^2}\frac{D\rho}{Dt} \tag{3.17}$$

where the internal energy was replaced by the internal energy per unit mass ($e = U/M$). Let us define the total energy (in this case internal, gravitational and kinetic) per unit volume as E:

$$E = \rho\left(\frac{u^2}{2} + \phi + e\right) \tag{3.18}$$

Then:

$$\frac{DE}{Dt} = \frac{E}{\rho}\frac{D\rho}{Dt} + \rho\left(\boldsymbol{u}\cdot\frac{D\boldsymbol{u}}{Dt} + \frac{D\phi}{Dt} + \frac{p}{\rho^2}\frac{D\rho}{Dt}\right) \tag{3.19}$$

Using the Lagrangian form of the continuity equation ($\frac{D\rho}{Dt} = \rho\boldsymbol{\nabla}\boldsymbol{\cdot}\boldsymbol{u}$) and of the momentum equation ($\frac{D\boldsymbol{u}}{Dt} = -\boldsymbol{\nabla}p/\rho - \boldsymbol{\nabla}\phi$), we can re-write (3.19) as:

$$\begin{aligned}\frac{DE}{Dt} &= E\boldsymbol{\nabla}\boldsymbol{\cdot}\boldsymbol{u} + \boldsymbol{u}\cdot(-\boldsymbol{\nabla}p - \rho\boldsymbol{\nabla}\phi) + \rho\frac{\partial\phi}{\partial t} + \rho\boldsymbol{u}\cdot\boldsymbol{\nabla}\phi + p\boldsymbol{\nabla}\boldsymbol{\cdot}\boldsymbol{u}\\ &= (E+p)\boldsymbol{\nabla}\boldsymbol{\cdot}\boldsymbol{u} - u\cdot\boldsymbol{\nabla}p + \rho\frac{\partial\phi}{\partial t}\end{aligned} \tag{3.20}$$

We consider that, for most situations of interest here, we want a gravitational potential that is a function of space only and not of time ($\frac{\partial\phi}{\partial t} = 0$). Using the definition of the convective derivative:

$$\frac{\partial E}{\partial t} + \boldsymbol{u}\cdot\boldsymbol{\nabla}E = (E+p)\boldsymbol{\nabla}\boldsymbol{\cdot}\boldsymbol{u} - u\cdot\boldsymbol{\nabla}p \tag{3.21}$$

Finally, rearranging, we have the energy equation:

$$\frac{\partial E}{\partial t} + \boldsymbol{\nabla}\boldsymbol{\cdot}[(E+p)u] = 0 \tag{3.22}$$

3.3.4 Equation of state

So far we have six quantities (ρ, p, E and the three components of $\boldsymbol{u}$), which have their time evolution described by five equations (if we break down the momentum equation into its three components). Therefore, we still lack an extra equation to obtain closure of the system. This additional equation is known as the equation of state (EOS), which links the internal energy of the fluid parcel to its density and pressure. In its most simple form, for an ideal gas, it is:

$$p = e\rho(\gamma - 1) \tag{3.23}$$

where γ is the adiabatic index given by the ratio of the specific heats. The internal energy e can also be written as a function of temperature, T, in order to provide a more intuitive grasp of the system's state:

$$e = \frac{1}{\gamma - 1}\frac{kT}{m} \tag{3.24}$$

where k is the Boltzmann constant and m is the mass of the particles in the ideal gas. In turn, the EOS can be written as:

$$p = \frac{\rho}{m}kT \tag{3.25}$$

3.3.5 Sound Speed

In the next Section 3.4, we will demonstrate that the hydrodynamics of non-viscous fluids (given by the Euler equations) is, in fact, purely a matter of the propagation of signals. If we consider the propagation of a fluid in one dimension (here we will use x), we can illustrate the propagation of these signals in the (x, t) plane, and the signals propagate along lines called characteristics. In this subsection, we will derive another thermodynamic variable of interest: the sound speed c_s. The speed of propagation of sound waves is modelled as a small perturbation that moves in space.

The density of the problem can be written as the background density (ρ_0) plus perturbative term dependant on x and t (ρ_1), which is our sound wave :

$$\rho(x, t) = \rho_0 + \rho_1(x, t) \tag{3.26}$$

Similarly, the speed can be written as:

$$u(xt) = u_0 + u_1(x,t) \tag{3.27}$$

The mass and momentum conservation equations in 1D are:

$$\begin{aligned} \frac{\partial \rho}{\partial t} + \frac{\partial(\rho u)}{\partial x} &= 0 \\ \frac{\partial(\rho u)}{\partial t} + \frac{\partial(\rho u u)}{\partial x} + \frac{\gamma P}{\rho}\frac{\partial \rho}{\partial x} &= 0 \end{aligned} \tag{3.28}$$

Where we used $p = K\rho^{\gamma}$, which applies for adiabatic compression of an ideal gas where K is a constant. We also already used the perturbed mass conservation equation within the momentum conservation equation to get rid of terms that summed to zero. A first order perturbation to the above gives:

$$\begin{aligned} \frac{\partial \rho_1}{\partial t} + \rho_0\frac{\partial u_1}{\partial x} + u_0\frac{\partial \rho_1}{\partial x} &= 0 \\ \rho_0\frac{\partial u_1}{\partial t} + \rho_0 u_0\frac{\partial u_1}{\partial x} + \frac{\gamma P_0}{\rho_0}\frac{\partial \rho_1}{\partial x} &= 0 \end{aligned} \tag{3.29}$$

If we consider momentarily that $u_0 = 0$ (ie the fluid where the sound wave is travelling is static), the equations above can be combined to obtain a wave equation:

$$\frac{\partial^2 \rho_1}{\partial t^2} + \frac{\gamma P_0}{\rho_0}\frac{\partial^2 \rho_1}{\partial x^2} = 0 \tag{3.30}$$

which is a wave with travelling velocity $u = +\sqrt{\frac{\gamma P_0}{\rho_0}}$ or $u = -\sqrt{\frac{\gamma P_0}{\rho_0}}$. Thus, the square of the speed of sound is $c_s^2 = \frac{\partial P}{\partial \rho} = \frac{\gamma P}{\rho}$. Going back to the less trivial case of $u_0 \neq 0$, we can define a convective derivative $\frac{D}{Dt} = \frac{\partial}{\partial t} + u_0\frac{\partial}{\partial x}$, such that we are now working in the frame comoving with the fluid. Clearly, this gives rises to an equation identical in shape to 3.30 but with $\frac{D}{Dt}$ instead of $\frac{\partial}{\partial t}$:

$$\frac{D^2 \rho_1}{Dt^2} + \frac{\gamma P_0}{\rho_0}\frac{\partial^2 \rho_1}{\partial x^2} = 0 \tag{3.31}$$

Thus, we have two waves: one propagating to the left at velocity $u_0 - \gamma P_0/\rho_0$, and another propagating to the right at $u_0 + \gamma P_0/\rho_0$. Clearly, if $u_0 > \gamma P_0/\rho_0$, the left wave is also moving to the right, as it is dragged along with the background flow and u_0 is supersonic. We can plot the movement of the perturbation in the (x, t) plane (Figure 3.1).

Figure 3.1 - Fan diagram for the propagation of sound waves

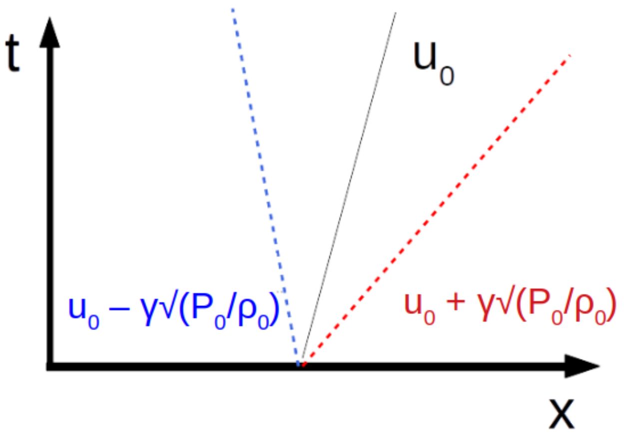

The characteristics lines for sound wave propagation (red and blue lines) and a discontinuity (black solid line). The slope of the curves are the inverse of the “characteristic speed" which shows how quickly the information carried by these waves travels over time.

The lines in this figure are called characteristics. These lines not necessarily have to be defined emerging from a same point. In fact, every line in the (x, t) diagram following the possible trajectory of a signal is called a characteristic. In this case, we have plotted the sound-characteristics in blue and red. There is still a third family of characteristics (the black line on the figure) which represent information that just propagates with the background flow speed u_0. One can think of a uniformly moving fluid that suddenly changes colour at $x = 0$. Let this property by traced by a function $\xi(x, t)$, then:

$$\begin{gathered}\frac{\partial \xi}{\partial t} + u\frac{\partial \xi}{\partial x} = 0 \\ \frac{\partial \xi}{\partial t} + u_0\frac{\partial \xi}{\partial x} = 0\end{gathered} \tag{3.32}$$

Again the term containing u_1 is negligible. Thus the full set of characteristics are:

- $\lambda_- = u_0 - \sqrt{\frac{\gamma p_0}{\rho_0}}$

- $\lambda_0 = u_0$
- $\lambda_+ = u_0 + \sqrt{\frac{\gamma p_0}{\rho_0}}$

This example demonstrates that the hydrodynamics equations amount to the propagation of signals at three different speeds. We will now use the Euler equations to numerically simulate the dynamics of a fluid and this knowledge of characteristics will be an important illustration tool.

3.4 Finite Volume Method

Eulerian methods have now been a popular choice in computational fluid dynamics. Given their widespread use in computational astrophysics, understanding the fundamental limitations of such codes is important for interpreting the astrophysics of hydrodynamical simulations.

The standard Eulerian approach to computational fluid dynamics is to discretize time into discrete steps (the time steps) and space into finite volumes or cells, where hydrodynamical quantities are stored. In the simplest case, the integral Euler equations are solved on a Cartesian cubical lattice by computing the flux of mass, momentum, and energy across cell boundaries at each time step. When modelling the conservative form of Euler's equations, the flux of quantities corresponds to the change in those quantities integrated over cell units of size Δx in the discretized mesh over a time step Δt.

In this section, we are going to present the Finite Volume Method (FVM) and, by doing so, illustrate all the concepts mentioned above. We subdivide the scheme into the following steps:

- Discretization
- Reconstruction
- Solution at the cell boundary (the Riemann Problem)
- Updating of the variables

Before we delve into details of FVM, it is important to notice that the choice of timestep is not arbitrary as, if we use too long a timestep, it is possible that all the material in a cell will be advected through to neighbouring cells in a single timestep. This could lead to errors, such as negative pressures and densities. In order to avoid this, it is necessary that the timestep obeys what is known as the Courant–Friedrichs–Lewy (CFL) condition (COURANT et al., 1928):

$$\Delta t_{CFL} < \frac{\Delta x}{u_{max}} \tag{3.33}$$

where u_{max} is the maximum speed in the simulation domain. In the case of a 3D simulation, the y and z cell sizes must also be considered.

3.4.1 Discretization

We start to numerically describe our fluid by discretizing the spatial domain into cells; thus, let us set a uniform mesh with Nx, Ny and Nz cells in the x, y and z direction of width Δx. Henceforth, subscripts refer to spatial location, with cell centres denoted by integer subscripts $i = 1, ..., Nx$ (e.g. x_i) and interfaces denoted by half integers (e.g. $x_{i\pm 1/2}$), such that $x_{i\pm 1/2} = x_i \pm \Delta x/2$, as illustrated in Figure 3.2. In a similar way, we discretize the time, such that the temporal increment is given by Δt and reference to the 'nth' time step is indicated by a superscript 'n'. We have that $t^{n+1} = t^n + \Delta t$.

Figure 3.2 - Illustration of the 3D grid.

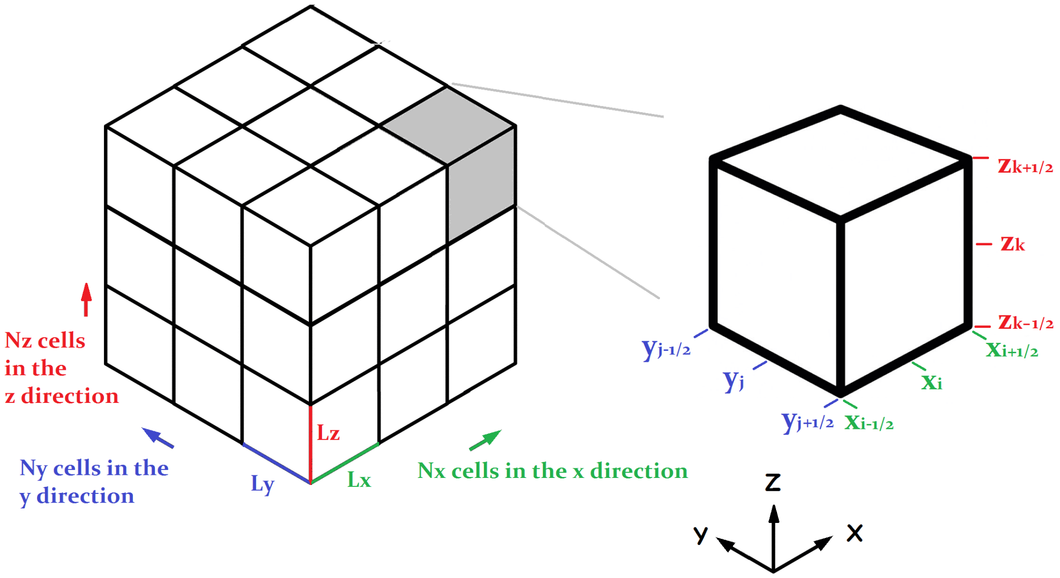

We now need to find a way to solve the equations of hydrodynamics for this discrete set of cells.

Firstly, consider the Euler equations without the gravity term. We have the following set:

$$\begin{aligned} \frac{\partial \rho}{\partial t} + \boldsymbol{\nabla} \cdot (\rho u) = 0 \\ \frac{\partial (\rho u)}{\partial t} + \boldsymbol{\nabla} \cdot (\rho u u + p) = 0 \\ \frac{\partial E}{\partial t} + \boldsymbol{\nabla} \cdot [(E + p) u] = 0 \end{aligned} \tag{3.34}$$

All these equations can be written in what is called conservative form:

$$\frac{\partial U}{\partial t} + \boldsymbol{\nabla} \cdot F(U) = 0 \tag{3.35}$$

with

$$U = \begin{bmatrix} \rho \\ \rho u \\ E \end{bmatrix}$$

and

$$F(U) = \begin{bmatrix} \rho u \\ \rho u u + p \\ (E + p) u \end{bmatrix}$$

If we integrate these equations in this form, over an arbitrary volume, we have:

$$\begin{aligned} \int_V \left(\frac{\partial U}{\partial t} + \boldsymbol{\nabla} \cdot F(U) \right) dV = 0 \\ \frac{\partial}{\partial t} \int_V U dV + \int_V \boldsymbol{\nabla} \cdot F(U) dV = 0 \\ \frac{\partial}{\partial t} \int_V \begin{pmatrix} \rho \\ \rho u \\ E \end{pmatrix} dV + \oint_{S(V)} F(U) dS = 0 \\ \frac{\partial}{\partial t} \begin{pmatrix} m \\ m u \\ E_{tot} \end{pmatrix} + \oint_{S(V)} F(U) dS = 0 \end{aligned} \tag{3.36}$$

Note that the time differential is now acting on quantities that we know need to be conserved: mass, momentum and total energy. These are ‘conserved variables’ as opposed to the ‘primitive variables’ we used before (density, velocity and pressure). It can be seen, from the last equation, that the change in these quantities in a cell over time is going to depend on the fluxes $F(U)$ over the surfaces delimiting the cell.

Each of the cells on the grid holds a single value for fluid properties (density, pressure and velocity), which are given by the cell averaged values. These can be expressed as:

$$\bar{U}_i^n = \frac{1}{\Delta x} \int_{x-1/2}^{x+1/2} U(x, t^n) dx \tag{3.37}$$

We want to know how this average evolves over time. By integrating our conservation law over the length of the cell, we have that:

$$\begin{aligned} \frac{\partial}{\partial t} \int_{x-1/2}^{x+1/2} U(x, t^n) dx &= - \int \frac{\partial}{\partial x} f(U(x, t)) \\ &= f(U(x_{i-1/2}, t)) - f(U(x_{i+1/2}, t)) \end{aligned} \tag{3.38}$$

We can use the cell average 3.37 alongside 3.38 to obtain the change in an average value over time:

$$\frac{\partial \bar{U}_i}{\partial t} = \frac{f(U(x_{i-1/2}, t)) - f(U(x_{i+1/2}, t))}{\Delta x} \tag{3.39}$$

If we further integrate in time, we can find an expression for the average value at a certain time step (say $n + 1$), as a function of the fluxes and the averaged value at the previous time step:

$$\bar{U}^{n+1} = \bar{U}^n + \int_{t^n}^{t^{n+1}} \frac{f(U(x_{i-1/2}, t)) - f(U(x_{i+1/2}, t))}{\Delta x} dt \tag{3.40}$$

We can simplify this by writing it in terms of the average fluxes $F_{i-1/2}^n \approx \frac{1}{\Delta t} \int_{t^n}^{t^{n+1}} f(U(x_{i-1/2}, t)) dt$. We have that discretely, the Euler equation evolve in time according to:

$$\bar{U}^{n+1} = \bar{U}^{n} - \frac{\Delta t}{\Delta x}\left[F^{n}_{i+1/2} - F^{n}_{i-1/2}\right] \tag{3.41}$$

It is clear, from the last equation, that our problem reduces to an evaluation of a given flux function at the cell edges. However, we only have access to the data stored locally, which are the volumetric average values in each cell. We, therefore, require a means of obtaining values at the cell edges, a process called reconstruction.

3.4.2 Reconstruction

Reconstruction entails taking the cell averaged values of the hydrodynamics quantities and returning a local (within each cell) distribution of values of those quantities. One can use any monotonic function to perform the reconstruction. For instance, modern approaches use reconstruction schemes, which, depending on their order, take several neighbouring cells into account to reconstruct the local flow. Figure 3.3 illustrates three different reconstruction schemes, with increasing order of accuracy can be approximated by piecewise constant (GODUNOV, 1959), linear (VANLEER, 1977), parabolic (COLELLA; WOODWARD, 1984) interpolations on the discrete grid (see Figure 3.3). Both codes used apply linear reconstruction methods. .

Figure 3.3 - Distinct reconstructions methods

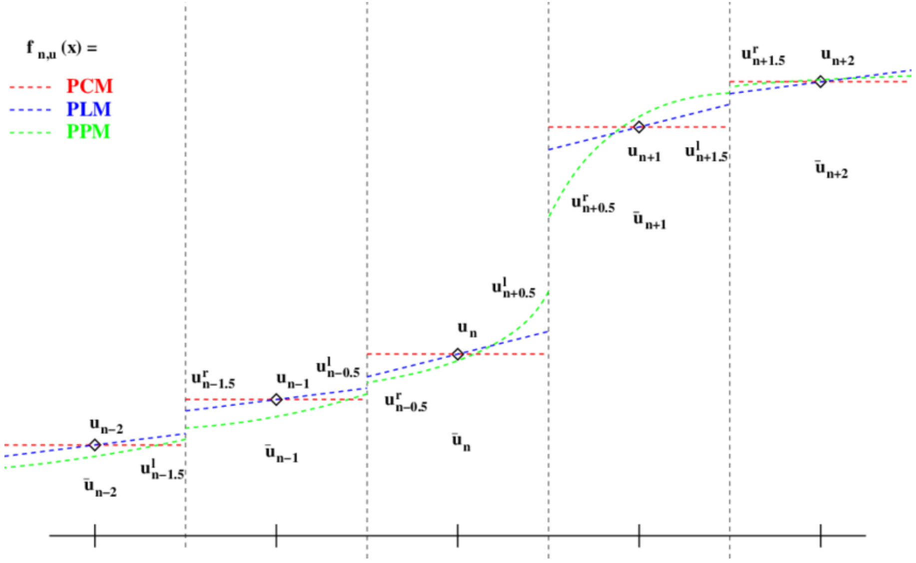

Reconstruction of the principal variables (u_n) on the grid using different methods: piecewise constant (PCM), piecewise linear (PLM) and piecewise parabolic (PPM). The reconstruction scheme permits us to determine the left and right-hand sided values at the cell boundaries ($u^l_{n-0.5}, u^r_{n+0.5}$).
Source: Dolag et al. (2008).

Once reconstruction has been done, we have a cell interface with a discontinuity in value of the quantities across the cell boundaries. Based on this quantities, we have to compute the flow. This is the so called Riemann Problem and is a key piece of any numerical hydrodynamical code.

3.4.3 Riemann Problem

The Riemann Problem is illustrated in Figure 3.4. It consists of a piecewise initial data of two constant states (which we will refer as left and right states) U^l and U^r, separated by a jump discontinuity. That is, it can be expressed as the following initial value problem:

$$U = \begin{cases} U^l, & \text{if } x \leq x_{i+1/2} \\ U^r, & \text{if } x \geq x_{i+1/2} \end{cases} \tag{3.42}$$

Figure 3.4 - An illustration of the Riemann problem at the boundary between two cells

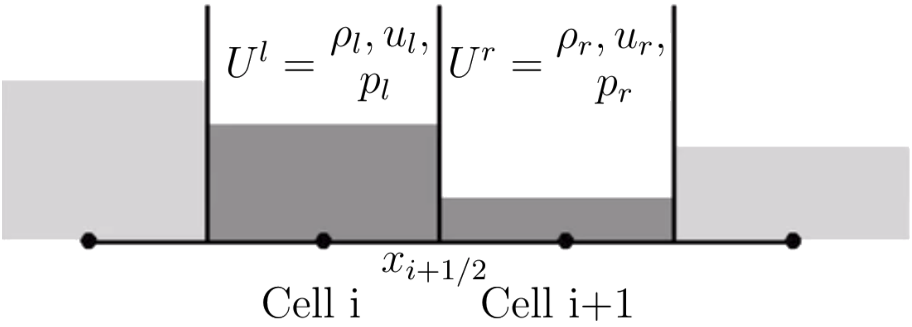

In other words, we allow for the movement of fluid between the left and right cells and we are concerned with finding the middle ground between U^l and U^r, U^*, at the boundary at time Δt later.

In order to try to grasp the problem, we can manipulate the Euler equations written in conservative form, recall:

$$\frac{\partial U}{\partial t} + \nabla \cdot F(U) = 0 \tag{3.43}$$

with

$$U = \begin{bmatrix} U_1 \\ U_2 \\ U_3 \end{bmatrix}$$

and

$$F(U) = \begin{bmatrix} F_1 \\ F_2 \\ F_3 \end{bmatrix} = \begin{bmatrix} U_2 \\ (\gamma - 1)U_3 + \frac{3-\gamma}{2}\frac{U_2^2}{U_1} \\ \gamma\frac{U_3 U_2}{U_1} + \frac{1-\gamma}{2}\frac{U_2^3}{U_1^2} \end{bmatrix}$$

Where we have re-written the equations in terms of $U_1 = \rho$, $U_2 = \rho u$ and $U_3 = E$. Note that, for that, we have used 3.24 ($\rho e = p/(\gamma - 1)$) to rewrite the energy flux $E = \rho(e + 0.5u^2) = p/(\gamma - 1) + 0.5\rho u^2$, such that the pressure can be expressed in terms of U_i as $p = (\gamma - 1)(U_3 - 0.5U_2^2/U_1)$.

We can further expand 3.43, using the chain rule as:

$$\frac{\partial U}{\partial t} + J\boldsymbol{\nabla} \cdot U = 0 \tag{3.44}$$

where we call J the flux Jacobian $\frac{\partial F}{\partial U}$. For the Euler equations, these are:

$$J = \begin{bmatrix} \frac{\partial F_1}{\partial U_1} & \frac{\partial F_1}{\partial U_2} & \frac{\partial F_1}{\partial U_3} \\ \frac{\partial F_2}{\partial U_1} & \frac{\partial F_2}{\partial U_2} & \frac{\partial F_2}{\partial U_3} \\ \frac{\partial F_3}{\partial U_1} & \frac{\partial F_3}{\partial U_2} & \frac{\partial F_3}{\partial U_3} \end{bmatrix}$$

$$J = \begin{bmatrix} 0 & 1 & 0 \\ \frac{\gamma-3}{2}\frac{U_2^2}{U_1^2} & (3-\gamma)\frac{U_2}{U_1} & \gamma - 1 \\ -\frac{\gamma U_3 U_2}{U_1^2} + (\gamma+1)\frac{U_2^3}{U_1^3} & \frac{\gamma U_3}{U_1} + \frac{3(1-\gamma}{2}\frac{U_2^2}{U_1^2} & \frac{\gamma U_2}{U_1} \end{bmatrix}$$

or in terms of primitive variables:

$$J = \begin{bmatrix} 0 & 1 & 0 \\ \frac{\gamma-3}{2}\rho u^2 & (3-\gamma)u & \gamma - 1 \\ -\gamma\frac{Eu}{\rho} + (\gamma+1)u^3 & \frac{E}{\rho} + \frac{3(1-\gamma}{2}u^2 & \gamma u \end{bmatrix}$$

As J is diagonalizable, we can write it in the form $J = R\Lambda R^{-1}$ with $JR^i = \lambda R^i$. That is, J is given by a set of eigen-vectors (with $R = [v_-, v_0, v_+]$) with real eigenvalues (λ) (with $\Lambda = diag(\lambda_-, \lambda_0, \lambda_+)$). Physically, eigenvalues represent speeds of propagation of information. In other words, they describe characteristic lines, as seen in subsection 3.3.5. For the Euler equations we get:

$$\begin{bmatrix} \lambda_- \\ \lambda_0 \\ \lambda_+ \end{bmatrix} = \begin{bmatrix} u - c_s \\ u \\ u + c_s \end{bmatrix}$$

$$v_- = \begin{bmatrix} 1 \\ u - c_s \\ H - c_s u \end{bmatrix}, v_0 = \begin{bmatrix} 1 \\ u \\ 0.5u^2 \end{bmatrix}, v_+ = \begin{bmatrix} 1 \\ u + c_s \\ H + c_s u \end{bmatrix}$$

where H is the specific enthalpy $H = (E + p)/\rho$.

We can use these to illustrate the solution to the Riemann Problem 3.42 by using the eingenvalues to express the problem in the $x - t$ plane. This is depicted in Figure 3.5.

Figure 3.5 - Fan diagram of the Riemann problem

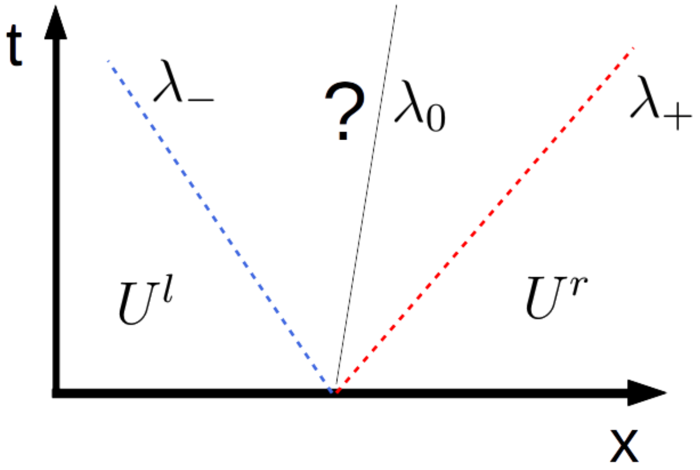

Characteristic lines arising from the Euler equations. We want to know the middle state lying in between U^l and U^r. Due to its shape this representation of the solution is often referred to as the Riemann Fan.

The structure of the Riemann solution then consists of 3 waves emanating from the origin, one for each eigenvalue λ_i. Each wave i carries a jump discontinuity in U, propagating with speed λ_i . Naturally, the solution to the left of the λ_+ wave is simply the initial data U^l and to the right of the λ_- wave is U^r. The task at hand is therefore to try to find the solution in the wedge between the λ_- and λ_+ waves.

Because the characteristic speed λ is a function of U, the characteristic the left and right states have different characteristic waves. As an example, consider Figure 3.6. If the eigenvalue for λ_i from the left state is less than the equivalent eigenvalue for the right state ($\lambda_i^l < \lambda_i^r$), the information travelling with λ_i^r has a region where it cannot catch up with the information travelling with λ_i^l . This gives rise to a rarefaction wave. Similarly, if the eigenvalue for λ_i from the left state is larger than the equivalent eigenvalue for the right state ($\lambda_i^l > \lambda_i^r$), the information travelling with λ_i^l will not only catch up but also, if it were possible, it would “overtake" the information travelling with λ_i^r . This is illustrated by the overlapping of characteristic lines in the figure. Physically, because characteristic cannot truly overlap, this give rise to a shock. Lastly, characteristics from either side may have the same eigenvalues (and thus same propagation speeds) giving rise to contact discontinuities.

Figure 3.6 - Possible scenarios arising from the Riemann problem

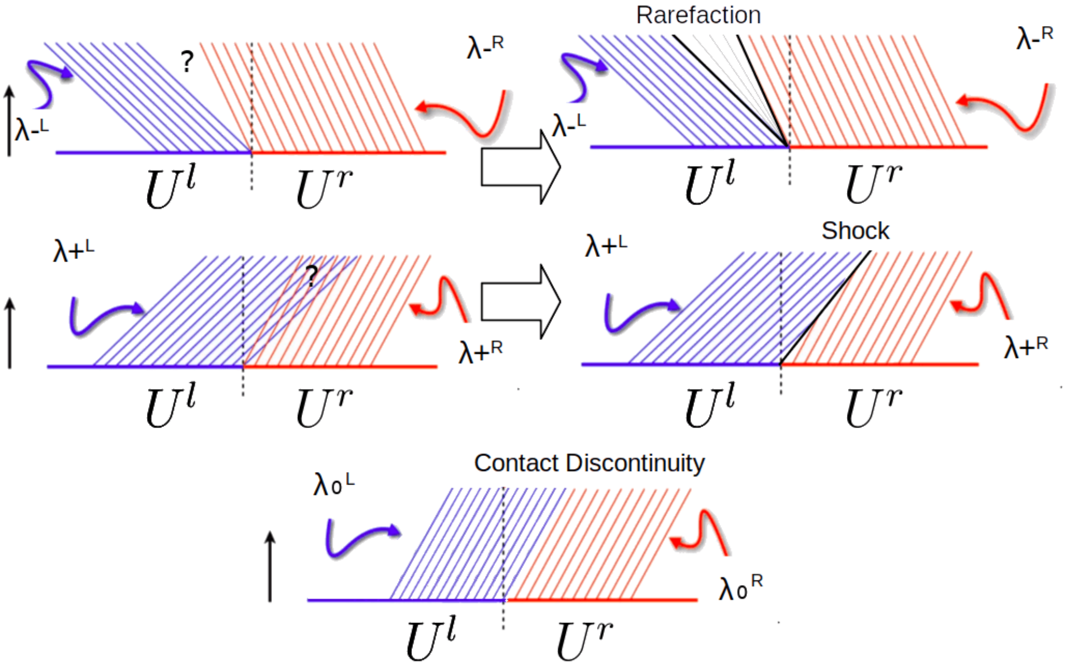

Characteristics of the left and right states showing the emergence of rarefaction (top), shock (middle) and contact discontinuities. The black arrow show the time direction. In rarefactions characteristics fail to cover a region in the $x-t$ plane (top left). The solution in this region needs to be calculates and is represented by a rarefaction fan (black lines on top right plot). In shocks characteristics overlap (middle left). The solution is a characteristic (black line) with propagation speed in between the left and right states (the shock per se).

Thus, the Riemann Problem reduces to a combination of contact discontinuities, shocks and rarefaction waves. It can be shown that, for the cell boundary, the middle wave (λ_0) is always a contact discontinuity and that λ_- and λ_+ are either shocks or rarefaction waves. We can re-think our Riemann Problem as being composed of different regions:

a) Initial left state (not altered yet by shock or rarefaction)

b) Wave travelling to the left (may be a shock or a rarefaction)

c) Region between wave travelling to the left and contact discontinuity ($U*_l$)

d) Region between wave travelling to the right and contact discontinuity ($U*_r$)

e) Wave travelling to the right (may be a shock or a rarefaction)

f) Initial right state (not altered yet by shock or rarefaction)

Numerically, the Riemann Solver takes the knowledge of the left and right states and builds up the middle states by calculating the jumps represented by the eigenvalues and eigenvectors of the Euler equation, accounting, in its solution, for rarefactions and shocks. For a full account on how a Riemann Solver computes the solutions across the distinct regions of the problem see Toro (1997).

Riemann Solvers can be exact, solving the problem analytically, but because we have to solve the Riemann Problem at each cell boundary for every cell, this is usually too computationally expensive. Instead, most codes use an approximate Riemann solver. Both AMUN and CMacIonize use a HLL-type (Harten, Lax and van Leer) (HARTEN et al., 1983) approximate Riemann Solver, due to its lower computational cost.

The HLL solver is based on a 2 wave approximation of the Riemann Fan, requiring estimates for the fastest signal velocities emerging from the initial discontinuity at the cell interface. In other words, the Riemann solver ignores the middle wave that represents the contact discontinuity, giving rise to a configuration that consists of the righmost and leftmost λ_- and λ_+ waves separating three constant states: left state, the middle state and the right state. Assuming that the wave speeds are given by some algorithm, we can apply the conservation laws to get an approximate expression for the flux which will be:

- $F(U^l)$ for $\lambda_- \geq 0$
- $F(U^r)$ for $\lambda_+ \leq 0$
- $F^* = \frac{\lambda_+ F(U^l) - \lambda_- F(U^r) + \lambda_- \lambda_+ (U_r - U_l)}{\lambda_+ - \lambda_-}$, otherwise.

A more accurate method is the HLLC, introduced by Toro and collaborators (TORO et al., 1994). This method restores the contact discontinuity in the HLL solver and, thus, assumes a three–wave model, resulting in higher resolution of intermediate waves. This solver is known as HLLC where the extra ‘C’ refers to the the inclusion of the contact discontinuity.

3.4.4 Updating the variables

Once we have the conditions determined at the boundary, we can update our variables. As a simple example, we could feed the Riemann Solver $U^l = (\rho_l, u_l$ and $p_l)$

and $U^r = (\rho_r, u_r$ and $p_r)$ and get the resulting values at the interface $U^* = \rho^*, u^*$ and p^*. For a constant reconstruction, we would have:

$$U^*_{x+1/2} = RP\left[U^n_i, U^n_{i+1}\right] \tag{3.45}$$

where the RP here represents the Riemann Problem solution given for the states fed to it. This defined the so called Godunov flux:

$$F^{n+1/2} = F(U^*_{i+1/2}) \tag{3.46}$$

In this case, the flux of mass, momentum and energy:

(F(U)) are then:

- flux mass $= \rho^* v^*$
- flux momentum $= \rho^* v^* v^* + p^*$
- flux energy $= \left(p^* \frac{\gamma}{\gamma - 1} + 0.5\rho^* v^* v^*\right)$

So that, we could update the hydrodynamic variables using 3.41. We can update the primitive variables as:

- mass$(t + \Delta t)$ = mass$(t) + \rho^* v^* \Delta x A$
- momentum$(t + \Delta t)$ =momentum$(t) + \rho^* v^* v^* + p^*$
- energy$(t + \Delta t)$ =energy$(t) \left(p^* \frac{\gamma}{\gamma - 1} + 0.5\rho^* v^* v^*\right)$

Once the variables are updated, the time-step is complete and the code moves on the the following time-steps, repeating the same processes described previously.

3.5 Turbulence in CMacIonize

The many experiments regarding turbulence take the “turbulence-in-a-box” approach: we assume we have a infinitely repeating box with periodic boundary conditions and a random driving force, $\boldsymbol{f}$, is added to the momentum equation:

$$\frac{\partial(\rho u)}{\partial t} + \boldsymbol{\nabla} \cdot (\rho \boldsymbol{u}^2) = -\boldsymbol{\nabla} p + \rho(-\boldsymbol{\nabla}\phi) + f \tag{3.47}$$

This force used to accelerate the numerical fluid up to the point the statistical properties of the fluid do not vary, reaching a state regarded as “fully developed” turbulence. The resulting turbulence is often set to be isotropic (statistically invariant under rotation and reflection of the axis) and homogeneous (statistically invariant under translation of the axis). The forcing may vary between two extreme scenarios: solenoidal or divergence-free forcing (when $\boldsymbol{\nabla} \cdot \boldsymbol{f} = 0$) and compressive or curl-free forcing (when $\boldsymbol{\nabla} \times \boldsymbol{f}$). Each of these have different statistical characteristics. In reality, we probably have a bit of both. For a comprehensive comparison of these turbulent forcing types see Federrath et al. (2010).

The turbulence added to CMacIonize follows the same general outline of the one included in the AMUN code, both of which are based in the paper by Alvelius (1999). The turbulence is purely solenoidal and is set to be also isotropic and homogeneous. He considers the discrete nature of time in numerical simulations and demonstrates that power input during a time step has two contributing terms, one from the force-force correlation and one from the velocity-force correlation. He shows how to make the former zero and how to make the force uncorrelated with itself in time.

In the code, the power input for the force-force (P_{ff}) correlation is calculated in spectral space:

$$P_{ff} = \Delta t 2\pi \int_0^\infty k^2 < \hat{f}\hat{f}* > (k) dk = \Delta t \int_0^\infty F(k) dk \tag{3.48}$$

where Δt is the timestep, f is a known random force per unit mass, $\hat{}$ represents the Fourier transform, $<> (k)$ represents the average of a spherical shell in Fourier space with a radius at a wavenumber k. Finally, $F(k)$ defines the force spectrum, which we choose to be Gaussian like:

$$F(k) = \frac{P_{ff}}{\Delta t \sum_{k_{min}}^{k_{max}} \exp\Big\{\Big(-\frac{(k-k_f)^2}{c}\Big)\Big\}} exp\left(-\frac{(k-k_f)^2}{c}\right) \tag{3.49}$$

Note that as c is equivalent to the variance of the Gaussian it determines the width of our spectrum and as k_f is on the role of the mean it gives the scale at which the forcing is peaked. Both c and k_f are input parameters in the simulations.

The force is set to be only active in range of pre-established wave numbers from k_{min} to k_{max}. Thus, we need to calculate all possible wave modes, k, between k_{min} and k_{max} ($k_{min} < k < k_{max}$), considering the wavenumber for each axis, i.e. $k = \sqrt{k_x^2 + k_y^2 + k_z^2}$. Because the force is set to be divergence free in spectral space we also require that $k_n \hat{f}_n = 0$, we write the force in spectral space as:

$$\hat{f}_n = A_{ran}(k,t)\mathbf{e}_n^1 + B_{ran}(k,t)\mathbf{e}_n^2 \tag{3.50}$$

where e^1 and e^2 are unit vectors orthogonal to one another and to k and A_{ran} and B_{ran} are complex random numbers.

For each wave number within the specified range we calculate the unit vectors, which are chosen as in the Alvelius (1999) paper:

$$\begin{aligned}
\mathbf{e}^1 = [e_x^1, e_y^1, e_z^1] &= \left[\frac{k_y}{\sqrt{k_x^2 + k_y^2}}, \frac{-k_x}{\sqrt{k_x^2 + k_y^2}}, 0\right] \\
\mathbf{e}^2 = [e_x^2, e_y^2, e_z^2] &= \left[\frac{k_x k_z}{k\sqrt{k_x^2 + k_y^2}}, \frac{k_y k_z}{k\sqrt{k_x^2 + k_y^2}}, \frac{\sqrt{k_x^2 + k_y^2}}{k}\right]
\end{aligned} \tag{3.51}$$

We, then, require from Equation (3.48) that:

$$F(k) = 2\pi k^2 \left[< A_{ran} A_{ran}* > + < B_{ran} B_{ran}* >\right]. \tag{3.52}$$

This is satisfied if we define the complex random numbers as:

$$\begin{aligned}
A_{ran} &= \left(\frac{F(k)}{2\pi k}\right)^{1/2} e^{i\theta_1} sin(\phi) \\
B_{ran} &= \left(\frac{F(k)}{2\pi k}\right)^{1/2} e^{i\theta_2} cos(\phi)
\end{aligned} \tag{3.53}$$

with θ_1, θ_2 and ϕ being random numbers, such that $0 < \theta_1, \theta_2, \phi < 2\pi$.

Thus, explicitly if we divide $\hat{f}$ into a real and an imaginary part, $\hat{f}_r$ and $\hat{f}_i$ respectively, we have that:

$$
\begin{aligned}
\hat{f}_r &= \sqrt{\frac{F(k)}{2\pi k}}\left[cos(\theta_1)sin(\phi)\mathbf{e}^1 + cos(\theta_2)cos(\phi)\mathbf{e}^2\right] \\
\hat{f}_i &= \sqrt{\frac{F(k)}{2\pi k}}\left[sin(\theta_1)sin(\phi)\mathbf{e}^1 + sin(\theta_2)cos(\phi)\mathbf{e}^2\right]
\end{aligned}
\tag{3.54}
$$

or substituting $F(k)$ in:

$$
\begin{aligned}
f_r &= \underbrace{\sqrt{\frac{P}{\Delta t}\frac{\exp\left\{\left(-\frac{(k-k_f^2)}{c}\right)/2\pi k\right\}}{\sum_{k_{min}}^{k_{max}}\exp\left\{\left(-\frac{(k-k_f^2)}{c}\right)\right\}}}}_{A_{for}}\left[\underbrace{cos(\theta_1)sin(\phi)}_{\text{RealRand[0]}}\times\mathbf{e}^1 + \underbrace{cos(\theta_2)cos(\phi)}_{\text{RealRand[1]}}\times\mathbf{e}^2\right] \\
f_i &= \underbrace{\sqrt{\frac{P}{\Delta t}\frac{\exp\left\{\left(-\frac{(k-k_f^2)}{c}\right)/2\pi k\right\}}{\sum_{k_{min}}^{k_{max}}\exp\left\{\left(-\frac{(k-k_f^2)}{c}\right)\right\}}}}_{A_{for}}\left[\underbrace{sin(\theta_1)sin(\phi)}_{\text{ImRand[1]}}\times\mathbf{e}_1 + \underbrace{sin(\theta_2)cos(\phi)}_{\text{ImRand[1]}}\times\mathbf{e}^2\right]
\end{aligned}
\tag{3.55}
$$

The values of A_{for} and the unit vectors above are always the same and, thus, are only computed once at the beginning of every simulation. The values of random real and imaginary parts $RealRand$ and $ImRand$ are computed at each timestep based on the random numbers $\theta_1.\theta_2$ and ϕ created from a random number generator.

Once we compute f_r and f_i we can find the force per unit mass in real space by doing an inverse Fourier transform and use it to update the hydrodynamic variables, therefore introducing the turbulence.

For more details on the turbulent forcing refer to (ALVELIUS, 1999). The code itself is available online as a part of the github repository that holds the rest of the CMacIonize code `https://github.com/bwvdnbro/CMacIonize/blob/pmacionize/src/AlveliusTurbulenceForcing.hpp`

This code is now being used to analyse escape fractions of photons from molecular clouds, in order to better quantify the impact pf photoionization to the formation and temperature structure of the DIG (3.7).

Figure 3.7 - Difference in ionization between a turbulent and a uniform medium

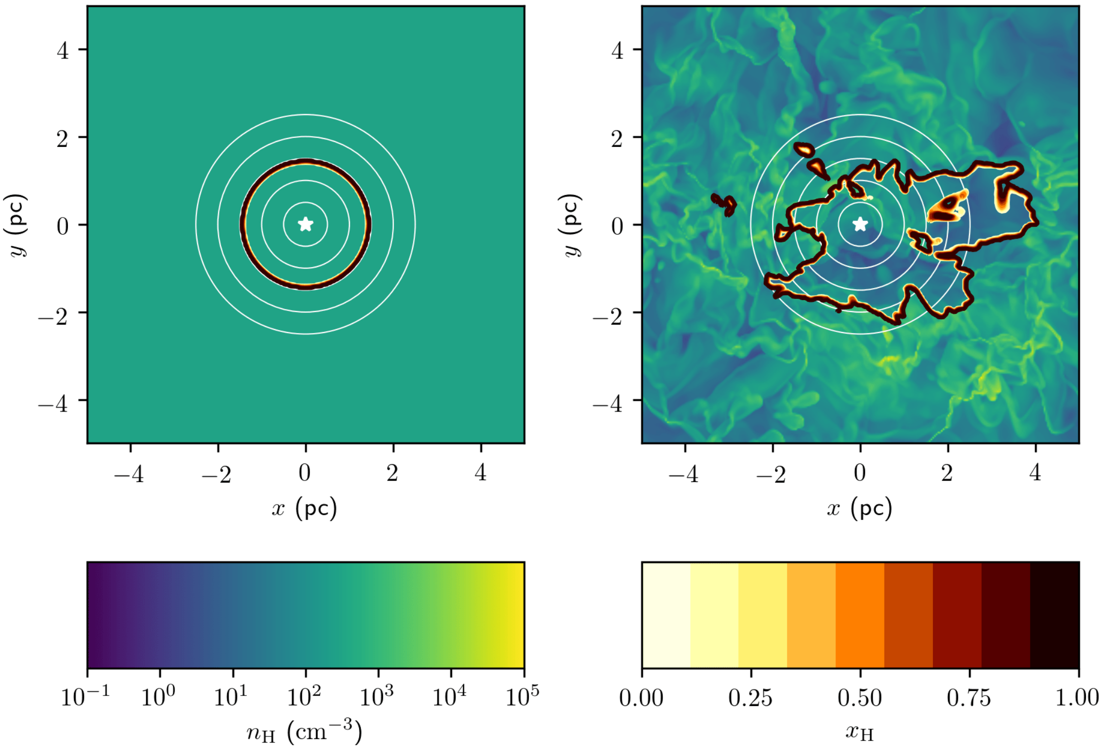

Density slices of a 256 cube turbulent simulation with the ionized region (fraction of neutral hydrogen atoms shown as x_H). On the left the region ionized by a source emitting photons isotropically in a uniform medium and on the right the same source placed in a turbulent medium (with average density equal to the density of the uniform medium on the left) modelled by the code described in this chapter using CMacIonize. It is clear that the ionization manages to reach locations much farther from the source in the turbulent case. It is also interesting to note the existence of apparently disconnected pockets of ionized material. These pockets are in fact connected to the rest of the ionized region and appear due to radiation that ionized low density channels that happen to cross this slice only at specific regions.

4 ANALYTICAL AND NUMERICAL RADIATIAVE TRANSFER

4.1 Introduction

In the last chapter we delved into the hydrodynamic equations and developed an intuition of how the problem is approached numerically. This chapter will follow a similar layout, except that presently we are going to concentrate in the propagation of radiation. We start the chapter by reviewing some theoretical concepts of radiation transfer and the most important equations. We then give an introduction to the technique of solving mathematical problems by stochastic sampling (or by the simulation of random variables). This technique had been used in science before, but is wasn't until the mid 1940s that it came into widespread use and received its name: the“Monte Carlo" method. This term, coined by Nicolas Metropolis, refers to a famous casino, making an allusion to how the random nature of the method is similar to a gamble or a game of chance. It was, indeed, by playing a card game that Stanislaw Ulam had the idea of the Monte Carlo method. He was trying to calculate the probability that a set of 52 cards in a game of solitaire would come out successfully. He realised that it would be easier to get a computer to lay down the cards multiple times and count how many times successes were obtained than actually go through the trouble of estimating the probability by combinatorial calculations. At the time, the very first electronic computers were coming into operation. Those machines allowed this almost brute force method to become a very efficient and an easy way of obtaining accurate results without having to solve analitically the complicated equations underlying the problem. The application of the Monte Carlo method shown in here is very similar to the one used by John von Neumann in the study of neutron reaction chains to calculate the rate at which reactions within the chain would occur (these were necessary calculations for the making of nuclear weapons). It was, perhaps, the success of these calculations that popularised the method and lead to its widespread in Physics and other areas of science. Although the idea behind Monte Carlo may seem intuitive and simple to us today, there is a subtlety in realising that exact physical problems can be solved by a suitably chosen random process. In the light of its inner workings, we then proceed to use the Monte Carlo technique to show how photoionization is handled numerically and workings of the code we developed to couple to AMUN.

We end the chapter by doing the validation of our coupled code to a few simple scenarios. One of studied scenarios, the expansion of an ionized region onto a uniform medium, will be a stepping stone for the two chapters that follow in which we investigate the accretion of a material by a massive star surrounded by an ionized region in 1D (Chapter 5) and 3D (Chapter 6).

4.2 The physical background

The problem we are tackling consists on analysing how radiation from a star propagates through a medium and, by interacting with it, changes the medium's properties (temperature, ionization level, pressure, etc). In order to quantify these changes, we have to first understand in which ways and how often the source photons interact with the gas they encounter in their paths. This, in turn, requires a knowledge of cross-sections, optical depths and ionization and recombination rates. In this section, we shall swiftly review these concepts.

4.2.1 Change in intensity

The whole concept of radiation transfer can be resumed in the following: a photon is emitted by a source, it travels a certain distance within a medium and then, by means of an interaction, something happens to it (absorption/scattering).

We define the specific intensity or brightness of a star as the radiative energy, dE, due to photons with frequency within the interval, $d\nu$, travelling within a solid angle, $d\Omega$, and traversing an area, dA, normal to its direction of motion for every interval of time, dt. That is:

$$I_\nu = \frac{dE}{dA dt d\Omega d\nu}. \tag{4.1}$$

Now, suppose the photons that undergo an interaction no longer contribute to the intensity. The decrease in intensity will depend on the density of particles and the likelihood of those to interact with a photon. Assume that we have a homogeneous medium with number density n of particles, that are randomly distributed in space. The probability that a given interaction (absorption, scattering, etc) will occur is expressed in terms of a cross section σ. This cross section has units of area and is defined in a way that an interaction will occur only if an incoming photon passes perpendicularly through a circle, centred around the particle, of area equal to the cross section. The linear scale of the cross section is, for the astrophysical situations of interest here, much smaller than mean inter-particle distance and, in addition, particles are roughly randomly distributed through space. These conditions imply that the area in which interactions can occur is roughly the number of particles

Figure 4.1 - Absorption of light in a a volume

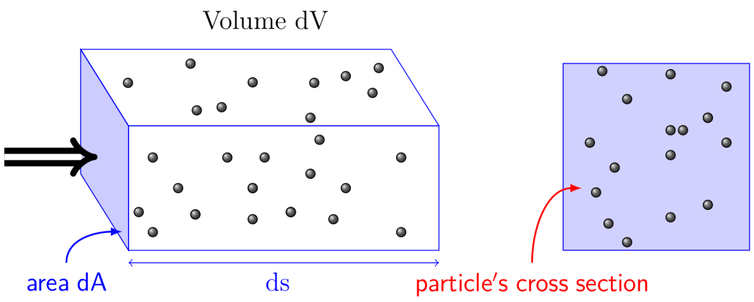

A number of photons incident on a volume, dV, with particle density n will perceive potential area of interaction $A_{int} = ndV\sigma$; as ndV is the number of particles in that volume each of which has a cross section σ. If the area perpendicular to the travel direction of the photons is dA and the length of the volume is ds, we can use our expression for intensity to estimate the energy being absorbed.

($ndV = ndsdA$) times the cross sectional area (as particles cross sections will rarely overlap) as schematised in Figure 4.1.

From the fact that $A_{int} = n\sigma dsdA$ and Equation 4.1, we can quantify the energy being absorbed by:

$$\begin{aligned}\text{Energy absorbed} &= I_\nu \; A_{int} dt d\Omega \; d\nu \\ &= I_\nu \; ndsdA\sigma dt d\Omega \; d\nu \\ &= dI_\nu dA dt d\Omega d\nu\end{aligned} \tag{4.2}$$

Which implies:

$$dI_\nu = -I_\nu dsn \; \sigma \tag{4.3}$$

So that the change in intensity with distance travelled is:

$$\frac{dI_\nu}{ds} = -I_\nu \; n \; \sigma \tag{4.4}$$

Integrating along the path distance s, we obtain the radiative transfer equation:

$$
\begin{aligned}
I_\nu(s) &= I_\nu(0)e^{-\int_0^s n\sigma ds} \\
&= I_\nu(0)e^{-n\sigma s} \\
&= I_\nu(0)e^{-\tau}
\end{aligned} \tag{4.5}
$$

where $I_\nu(0)$ is the initial intensity and the dimensionless quantity $\tau = n\sigma s$ is the so called optical depth. The larger the number of particles, the cross sectional area or the distance travelled, the higher is the probability of absorption. Thus, for large optical depths, the chance of an interaction occurring increases and the medium is called optically thick. Conversely, for small optical depths, or equivalently an optically thin medium, the photon will, on average, travel a longer distance before it interacts with any particle. It is, then, also clear that the mean free path, l_ν, travelled by a photon, has an inverse relation to the optical depth. Indeed, the optical depth can be understood as the average number of mean free paths that needs to be travelled before an interaction.

Equation 4.5 clearly shows the intensity exponentially diminishes with distance, with $I_\nu(s)$ being the remaining fraction of intensity that can be observed at a distance s from the source. Because the intensity is proportional to the energy which in turn is proportional to the number of photons, we can say that the portion of the initially emitted photons that still haven't interacted after travelling s is:

$$
\frac{N_{phot}(s)}{N_{phot}(total)} = \frac{I_\nu(s)}{I_\nu(0)} \tag{4.6}
$$

Therefore, the probability of a photon travelling a certain distance s before interaction is $I_s/I_0 = e^{-n\sigma_\nu s} = e^{-\tau}$. We will later use this probability density function to calculate the distance a photons will travel in Monte Carlo simulations.

4.2.2 Mean intensity and the energy density

Photons carry energy. Therefore, a volume will encompass a certain amount of energy due to the photons contained within it. Let us define the specific energy density of some region to be the energy within some volume of space due to photons with some small range of wavelengths between λ and $\lambda + d\lambda$. Any photon will only contribute to the energy density for a time dt in which it finds itself within the defined volume. Consider Figure 4.2. It is clear that, for photons with normal incidence to the area dA, dt will be simply ds/c. Thus, we can rewrite the volume as $dV = dA \times c \times dt$. Hence, the specific energy density, u_ν, of the block is:

Figure 4.2 - Energy density

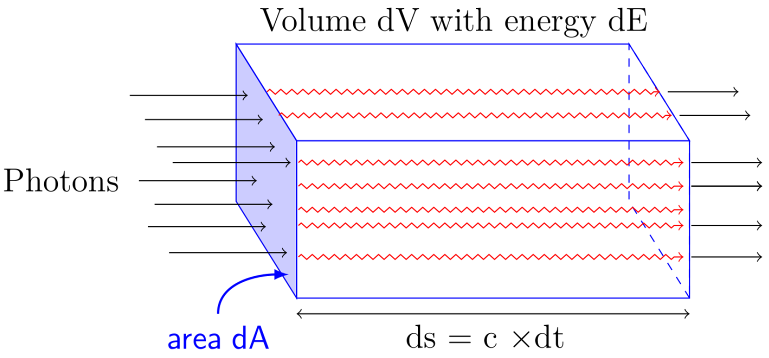

Photons traversing a cuboid volume, dV, travelling perpendicular to the face dA through which they enter the volume. As the photons travel at the speed of light c they will remain in the volume for a time $dt = ds/c$ where $ds = dV/dA$ is the cuboid's length during which they will contribute to the volume's energy density.

$$\begin{aligned} u_\nu &= \frac{dE}{dV d\nu} \\ &= \frac{dE}{\mathrm{dA\ c\ dt\ d}\nu} \end{aligned} \tag{4.7}$$

The right hand side of the equation is very similar to the expression for the specific intensity (4.1) we have derived earlier if it were integrated in solid angle. We thus define "mean intensity", J_ν, as the intensity averaged over all solid angles:

$$\begin{aligned} J_\nu &= \frac{\int I_\nu d\Omega}{\int d\Omega} \\ &= \frac{1}{4\pi} \int I_\nu d\Omega \end{aligned} \tag{4.8}$$

such that $4\pi J_\nu = \frac{dE}{dAdtd\nu}$ and thus we can use our definition of mean intensity to write a more compact form of the energy density equation:

$$u_\nu = \frac{4\pi J_\nu}{c} \tag{4.9}$$

4.2.3 Equations for photon packets

In Monte Carlo simulations, it would impractical to follow individual photons; instead, we use bundles of photons, all at a certain frequency (ν), which we refer as "photon packets". The energy of each packet is:

$$\epsilon = \frac{Qh\nu\Delta t}{N} \tag{4.10}$$

Where Q is the number of photons being emitted per unit time, Δt is our Monte Carlo timestep and N is the number of packets. It is, therefore, necessary to rewrite the equations derived in the last section in terms of quantities associated with the photon packet.

The photon packets are travelling in a 3D Cartesian grid formed by a number identical of cells of volume ΔV. A packet contributes for the energy density of a particular cell during the time it is inside that cell. If the photon travels a distance l within the cell, it will spend a fraction $\frac{l}{c\Delta t}$ of the time (Δt) inside the cell, therefore contributing with an energy of $\epsilon\frac{l}{c\Delta t}$ to the cell.

Because ϵ, c and Δt are constant, the energy density of a cell will only depend on the path length, l, taken by the photon packet within the cell. The energy density within a cell expressed as the sum of path length of the photons that crossed that cell.

$$u_\nu = \frac{[\epsilon \sum l/c\Delta t]}{\Delta V} = \frac{Qh\nu}{N}\frac{1}{c\Delta V}\sum l \tag{4.11}$$

Because the energy density can be written in terms of the mean intensity ($u_\nu = \frac{4\pi J_\nu}{c}$), we have that:

$$J_\nu = \frac{Qh\nu}{4\pi\Delta V N}\sum l \tag{4.12}$$

This equation is called the “Path length Formula" and was first derived by Lucy (1999). As we are going to see in Section 4.4 this is a key expression for Monte Carlo Radiative Transfer codes.

4.3 General Monte Carlo approach

The main idea behind the Monte Carlo Method is to approach a deterministic problem in a probabilistic way by making use of random numbers. Consider, for instance, a dart board made of a circle of radius R inside a square of radius 2R.

If we throw darts randomly at the board, we would expect (assuming that no darts completely miss the board) that the ratio of the number of darts that hit the circle, N_c, to the total number of darts, N_{tot}, to be equal to the area of the circle divided by the area of the square:

$$\frac{N_C}{N_{tot}} = \frac{\text{Area Circle}}{\text{Area Square}} = \frac{\pi R^2}{4R^2} = \frac{\pi}{4} \tag{4.13}$$

Thus, we can express π as:

$$\pi = \frac{4 \times N_C}{N_{tot}} \tag{4.14}$$

Therefore, by throwing darts at a board and measuring the proportion of them that are a hit, we can find an estimate for the number pi.

Figure 4.3 - Calculation of the number π using Monte Carlo

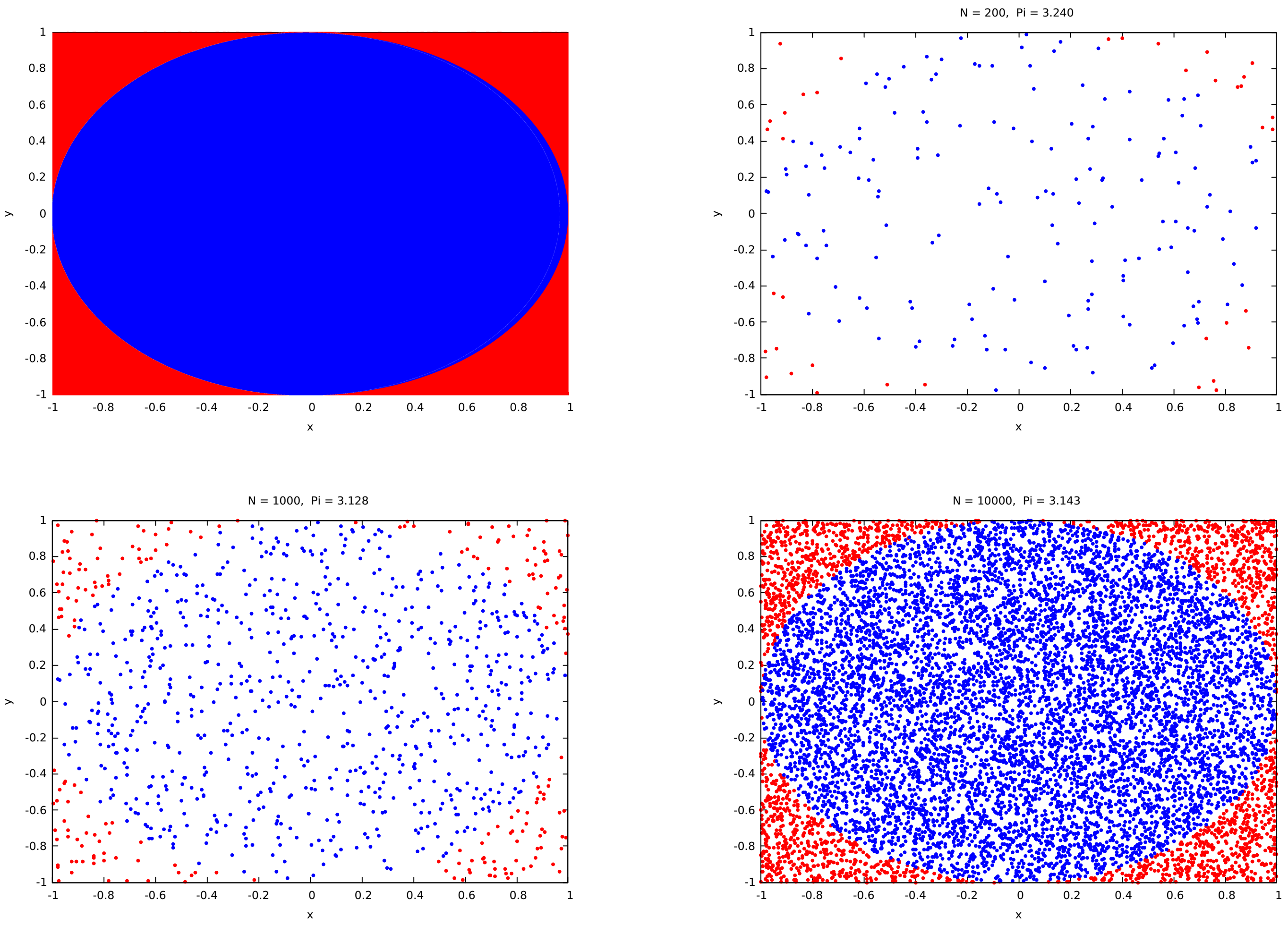

N = 200, Pi = 3.240

N = 1000, Pi = 3.128

N = 10000, Pi = 3.143

A Monte Carlo simulation used to determine the value of π by computing how many random points in a square also lie in a circle of diameter equal to the square's side. From top to bottom and left to right: the illustration of the true areas of the square and the circle, the Monte Carlo method with 200, 1000 and 10000 random points respectively and the associated estimate of π.

Figure 4.3 mimics such a situation: blue dots are darts that hit the circle and red darts the ones that missed it. Note that the more darts we throw on the board the better is our estimation of pi. Thus, the strength here lies in numbers. Moreover, we can see how important it is to ensure that the numbers are truly random. If we had a professional dart player, all darts would fall inside the circle and we would arrive to the conclusion that $\pi = 4$. It is therefore paramount that we are able to create reliable random numbers in order to use the Monte Carlo method. If we are able to generate such random numbers, Monte Carlo is an easy to set up method that allows us to obtain a quick and reliable solutions to complicated equations. But, (as in the case for the calculation of π) we need to know in advance what are the probabilities of an outcome taking place (like hitting the circle or not). This is the information conveyed by the probability distribution function or PDF. For any given interval of values, the area underneath the PDF between those values will be the probability one gets a result within the interval. This implies two things. Firstly, the area under the entire PDF must be one (as the probability of you hitting any value at all is of 100%). Secondly, the probability of a single discrete value occurring in the PDF is zero as it doesn't define an area. The reasoning behind this is that there are an infinite amount of values that could occur to begin with and the chance that one value will be obtained exactly is, thus, infinitely small.

Consider a PDF, $P(x)$ which only has non-zero values for the interval $a < x < b$. If we were to plot the integral of $\int_a^{x_0} P(x)dx$ against x_0 for all x_0 lying between a and b, we would obtain the so called cumulative distribution function (CDF).

The CDF evaluated at x_0 is the probability that the random variable x will have a value smaller or equal to x_0, that is, it gives the area under the PDF enclosed by the lower bound and x_0. As a visual example, see Figure 4.4.

$$CDF = \int_a^{x_0} P(x)dx = \text{ Area under the PDF from } a \text{ to } x_0 \tag{4.15}$$

Now consider the variable ξ, defined as:

$$\xi = \frac{\int_a^{x_0} P(x)dx}{\int_a^b P(x)dx} = \int_a^{x_0} P(x)dx \tag{4.16}$$

As x_0 goes from a to b, the ξ, goes from 0 to 1 smoothly. Thus, to sample a 'random variate' x_0 , we can simply call a random number generator that samples uniformly

Figure 4.4 - PDF and CDF example

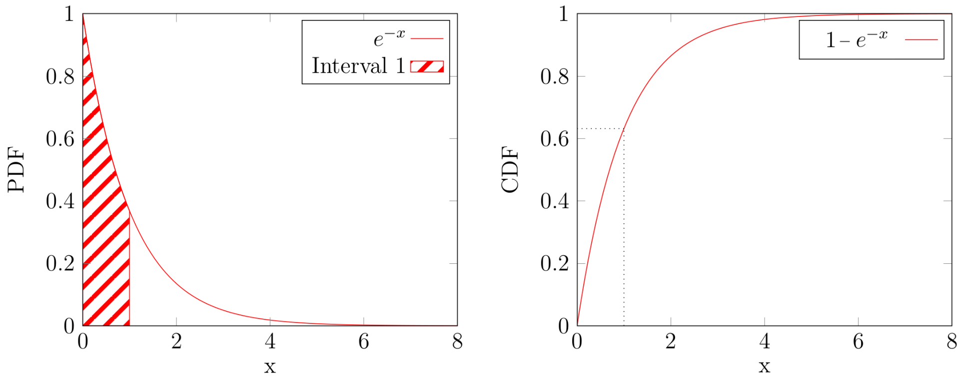

Right: the PDF of a function which is given by e^{-x}. The hashed area under the curve reprensents the value for the CDF at $x = 1$. Left: The CDF of the same function, the value of $x = 1$ is shown corresponding to the value of the area under the PDF curve on the figure to the left between 0 and 1.

from 0 to 1 (giving us the value of ξ) and then invert the equation above to get a value x_0.

This “sampling of the PDF” is the key idea used in the Monte Carlo technique and it is sometimes referred to as the ‘Fundamental Principle’ . It allows us to reproduce the correct statistics of a physical system from simple random numbers.

In order to obtain x_0, it is necessary to first solve the integral. This poses a problem, since, in many cases, the PDF is not well behaved and integrating it may be a non-trivial task. Therefore, we need alternative ways of sampling the PDF in these cases. One possible way of solving the problem is by tabulating the CDF and then linearly interpolate this table according to ξ to get the value of x_0. Another solution is to use the so called “rejection method". This method consists of finding the maximum value of the PDF, PDF_{max}, and using it to form a rectangle of dimension $PDF_{max} \times (b-a)$, which encloses the PDF completely. Then we sample the point coordinates within the rectangle from two random numbers: $x = \xi_1 \times (b-a) + a$ and $y = PDF_{max}\xi_2$. If the point is underneath the curve, that is, if $y < P(x)$, then the point is accepted, otherwise the point is rejected. By sampling enough points, we accurately sample the different values of x appropriately as, in regions of the plot where $P(x)$ is low, we sample those values of x less frequently than in regions where $P(x)$ is large. It is worth noting that the rejection method is less efficient for highly peaked PDFs because the rectangle enclosing the PDF will have a lot more area above the PDF than underneath it and, therefore, most points will be rejected.

4.4 The code

The Monte Carlo technique described in the last Section 4.3 can be used to simulate the radiative transfer situations described in the second Section 4.2. The code used in this work does exactly that and thus we refer to it as the Monte Carlo Radiative Transfer Code (MCRT code).

This code is run in conjunction with the AMUN hydrodynamics code being called within AMUN at every hydrodynamical timestep. For that reason, the MCRT code cannot be too computationally expensive. We achieve that by using a very elementary model for the interstellar medium which contains only hydrogen. In addition, a two frequency model is used: we only classify the frequency as being either capable of ionizing hydrogen or not. We show, later in this section, that these approximations are justifiable for the problems we are tackling in this work.

The code framework consists of emitting photons from a source and tracking them as they travel across a Cartesian grid until they are terminated. Photons are terminated in two ways: either they exit the grid or they are absorbed by a hydrogen and re-emitted as a non-ionizing photon.

4.4.1 The grid

The MCRT code inherits the Cartesian grid used in AMUN. All axis have the same length and are subdivided into the same number of segments, so that our cells are cubic and identical. Figure 4.5 shows photons travelling through a 2D analogue of the grid and their possible fates.

4.4.2 Isotropic emission

The first step of the simulation is to emit the photons from the source points we define. We assume that sources emit photons isotropically, which implies that they are randomly distributed in solid angle. From the definition of solid angle, we have that $d\Omega = sin(\theta)d\theta d\phi$, where two angles $0 < \theta < \pi$ and $0 < \phi < 2\pi$ are as in Figure 4.6. We then have the normalized probability distributions are:

$$P(\phi) = \frac{1}{2\pi} \tag{4.17}$$

$$P(\theta) = \frac{sin(\theta)}{2} \tag{4.18}$$

Figure 4.5 - Possible photon paths through the grid

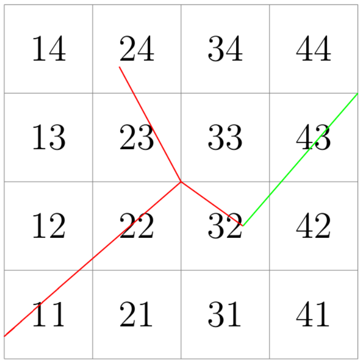

Three different possibilities for a photon emitted at the centre of a sample 2D grid: i) It ionizes a hydrogen atom, getting re-emitted as a non-ionizing photon and it is terminated (photon represented by red line traversing cells 23 and 24); ii)It ionizes a hydrogen atom and gets re-emitted as an ionizing photon which keeps being traced by the simulation (source photon represented by red line traversing cell 32 and re-emitted photon represented by the green line) or iii) photon does not interact and simply leaves the computational domain, being then terminates (red line through 22,12 and 11).

Figure 4.6 - Representation of the solid angle (grey area) as given by the angles θ and ϕ.

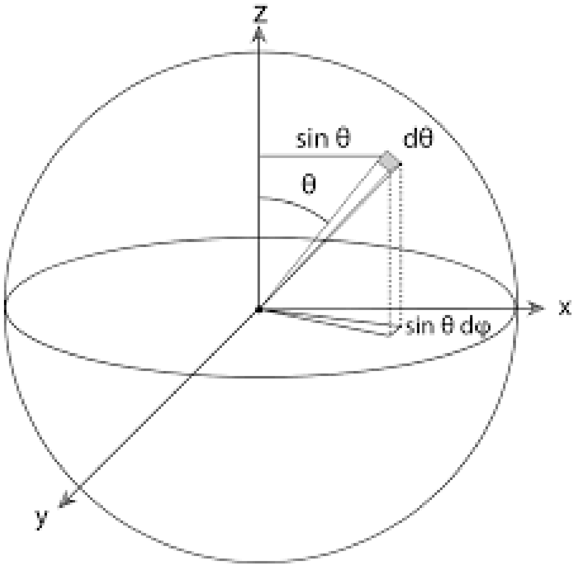

which, following the Monte Carlo technique described before, can be sampled as follows:

$$\phi = 2\pi\xi \tag{4.19}$$

$$\theta = acos(2\xi - 1) \tag{4.20}$$

As we are working in a Cartesian grid, it is useful to express the direction in terms of a unit vector n such that:

$$\hat{n} = n_i + n_j + n_k \tag{4.21}$$

where $n_i = sin\theta cos\phi$, $n_j = sin\theta sin\phi$ and $n_k = \cos\theta$ are the components in the x, y and z directions.

4.4.3 Optical depth travelled

We know now that our photon will travel in the direction $\hat{n}$ until it either interacts or it escapes the grid. Thus, we have to figure out if and where a photon will interact and this will naturally depend on the optical depth of the medium.

We have seen that the probability of a photon travelling a distance s is $P(\tau) = e^{-\tau}$ where $\tau = n\sigma s$. Following the Monte Carlo method, we adopt a number, ξ that lies between 0 and 1 such that:

$$\xi = \int_0^{-\tau_R} P(\tau) d\tau = \int_0^{-\tau_R} e^{-\tau} d\tau \tag{4.22}$$

such that:

$$\xi = 1 - e^{-\tau_R} \tag{4.23}$$

Which can be rewritten as:

$$\tau_R = -ln(1 - \xi) \tag{4.24}$$

Thus, we can obtain a value for τ_R by assigning a random value to ξ. Consider, for

Figure 4.7 - Photon attenuation

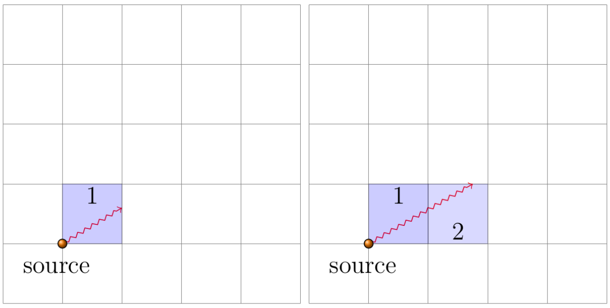

$\tau_1 < \tau_R$?
No, proceed to next cell

$\tau_{total} + \tau_2 = \tau_1 + \tau_2 > \tau_R$?
No, proceed to next cell

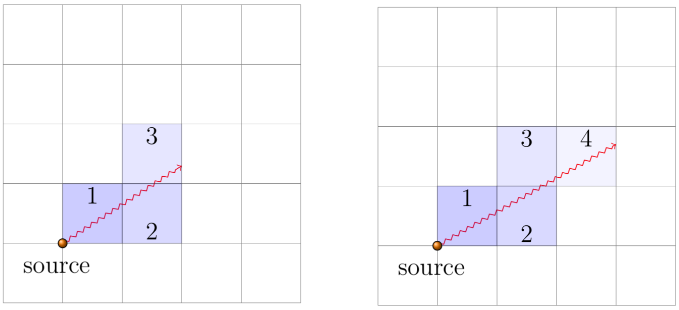

$\tau_{total} + \tau_3 = \tau_1 + \tau_2 + \tau_3 > \tau_R$?
No, proceed to next cell

$\tau_{total} + \tau_4 = \tau_1 + \tau_2 + \tau_3 + \tau_4 > \tau_R$?
Yes. Find interaction location

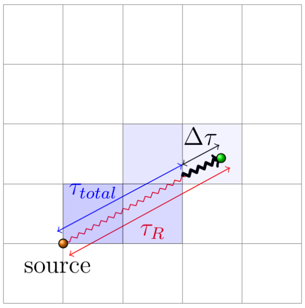

● interaction point
$\Delta\tau = \tau_R - \tau_{total}$

Illustration of a photon travelling through a grid a certain optical depth τ randomly selected by the Monte Carlo method. One cell is crossed at a time and the total optical depth is compared to the randomly selected one. Once the required optical depth is reached the photon undergoes an interaction.

instance, a photon that has just been emitted from the source travelling on our grid as in Figure 4.7.

The photon has to travel τ_R before interacting. Because each cell has a distinct absorption coefficient, $\alpha_{cell} = n_{cell}\sigma_{cell}$, we need to calculate the individual cell contributions to the optical depth as the the photon travels through them. Suppose the photon finds itself in a position (x_p, y_p, z_p) inside a cell and it is travelling in direction defined by the unit vector $\hat{n} = n_i\hat{x} + n_j\hat{y} + n_k\hat{z}$.

In order to calculate the optical depth travelled in the cell, we need to know from which of the cells faces (x_{face}, y_{face} or z_{face}) the photon will escape the cell. As the sign of n_i, n_j and n_k gives us the information of whereas we are travelling in positive or negative axis directions, we can already determine which face from each axis the photon is approaching. So, for instance, if $n_i < 0$, the photon will be travelling in the negative x direction and will be approaching the left x-face of the cell (the "-x-face"). We can calculate the number of times the photon would have to travel the unit vector $\hat{n}$ to get to each of face by:

$$\begin{aligned} dx &= \text{steps to x-face} = \frac{x_{face} - x_p}{n_i}, \\ dy &= \text{steps to y-face} = \frac{y_{face} - y_p}{n_j}, \\ dz &= \text{steps to z-face} = \frac{z_{face} - z_p}{n_k} \end{aligned} \tag{4.25}$$

Where x-face, y-face and z-face are the positions of the x, y and z faces towards which the photon is travelling.

The direction for which the number of steps is the least is going to be the first one to be reached. Thus, by finding the minimum of dx, dy and dz, we find the number of steps we need to move to hit a face. After moving this distance, the photon position and the optical depth is updated, taking into account the optical depth travelled in the cell, which can be calculated from $\tau_{cell} = min(dx, dy, dz) \times n_{cell}\sigma_{cell}$.

Imagine a photon that has just been emitted. It first travels to the edge of the first cell at which point it will have covered an optical depth $\tau_1 = n_1\sigma_1 s_1$, with s_1 being the distance from the source to the cell edge. In the case that $\tau_1 < \tau_R$, we set $\tau_{total} = \tau_1$, and the photon proceeds to the next cell. In the second cell, the photon travels again to the cell edge. Now it has covered in total an optical depth $\tau_{total}^{new} = \tau_{total}^{old} + \tau_2 = \tau_{total}^{old} + n_2\sigma_2 s_2$. The updated total optical depth is again compared to the value of τ_R and, once more, if it is smaller ($\tau_{total} < \tau_R$), the photon is moved to the next cell along. The process is repeated until the optical depth travelled, $\tau_{total} + \tau_{i+1} = \sum_{i=1}^{i=N}(n_i\sigma_i s_i) + n_{N+1}\sigma_{N+1}s_{N+1})$ is larger than the random optical depth. When this occurs, we know the photon must have interacted while it travelled through that last cell (that is, cell N+1). Thus, instead of adding the optical depth τ_{N+1}, we add the distance that lacks for us to reach the random optical depth $\Delta\tau$, that is:

$$\Delta\tau = \tau_R - \tau_{total} \tag{4.26}$$

We reached the point where an interaction will happen, thus we have to determine what is happening next to the photon.

4.4.4 The interaction

The photon in our code has now travelled a certain optical depth the way described above and now it will interact with a hydrogen atom, ionizing it and being later re-emitted either as an ionizing or as a non-ionizing photon. If it is re-emitted as an ionizing photon, a new optical depth and direction will be sampled, and the photon will continue travelling the grid. The probability of a photon being re-emitted as an ionizing photon is simply given by the probability it will recombine to the ground level, which is given by the division of the recombination rate to the ground level α_1 by the recombination rate to all excited states, α_A:

$$P_{ION} = \frac{\alpha_1}{\alpha_A} \tag{4.27}$$

4.4.5 Photoionization

When the photon interacts with a hydrogen atom, since the photon from the source has an ionizing frequency, the latter will be ionized. Given enough time, however, the H nuclei will recombine again. Thus, when considering photoionization, there are two rates which are of interest: firstly, how often does a hydrogen atom gets ionized and, secondly, how often do electron and protons recombine together. The former is, unsurprisingly, referred to as the ionization rate, t_i, and the latter as the recombination rate, t_r. It is the equilibrium between these two rates that will dictate how much of the hydrogen will maintain an ionized state.

The photoionization rate will depend on:

- the frequency: the photon has to have enough energy to ionize H
- the density of the medium: the more atoms there are, the greater the chance a photon reaches one of them

- the cross section: the larger the area of interaction with an atom, the more likely it is to interact with a photon

- the intensity: the more photons are emitted, the higher the chance each atom has to be ionized

Thus t_i is represented by:

$$t_i = \int_{\nu_0}^{\infty} n(H_0)\sigma_\nu(H_0)\frac{4\pi J_\nu}{h\nu}d\nu \tag{4.28}$$

The recombination rate will depend on:

- number of hydrogen nuclei (protons/HII) and number of recombining species ($n_e n_p$)

- the recombination coefficient α, which gives the probability the electron and the nucleus will recombine. Note that we use a recombination rate $\alpha_B = \alpha_A - \alpha_1$, as photons that are re-emitted at ionizing frequency should not be counted as contributing to the ionizing equilibrium.

At the equilibrium point, $t_i = t_r$, we have that:

$$\int_{\nu_0}^{\infty} n(H_0)\sigma_\nu(H_0)\frac{4\pi J_\nu}{h\nu}d\nu = n_e n_p \alpha \tag{4.29}$$

Now, from our path-length formula, we can re-write the left hand side as:

$$n(H_0)\frac{Q}{\Delta V N}\sum l\sigma_\nu(H_0) = n_e n(H^+)\alpha \tag{4.30}$$

But because $n_e = n(H^+)$ and $n(H_0) = n(H) - n(H^+)$, we can get to a quadratic:

$$n(H^+)^2\alpha + \Big[\frac{Q}{\Delta V N}\sum l\sigma_\nu(H_0)\Big]n(H^+) - \Big[\frac{Q}{\Delta V N}\sum l\sigma_\nu(H_0)\Big]n(H) = 0 \tag{4.31}$$

$$n(H^+)^2 + \left[\frac{Q}{\Delta V N \alpha} \sum l\sigma_\nu(H_0)\right] n(H^+) - \left[\frac{Q}{\Delta V N \alpha} \sum l\sigma_\nu(H_0)\right] n(H) = 0 \tag{4.32}$$

By solving the quadratic, we can obtain the number of ionized hydrogen atoms.

$$\begin{aligned} n(H^+) &= \frac{-b + \sqrt{b^2 + 4b^2 n(H)}}{2} \\ &= \frac{b(-1 + \sqrt{1 + 4n(H)})}{2} \end{aligned} \tag{4.33}$$

where $b = \frac{Q}{\Delta V N} \sum l\sigma_\nu(H_0)$.

4.4.6 Temperature and pressure

Since we aim to quantify the dynamical effect resulting from the ionization, we also need to calculate the extra pressure and temperature arising in the system due to the photoionization. We assume that ions and electrons are perfectly coupled and, following the photoionization, they reach the same temperature and pressure very rapidly. As when we ionize hydrogen we double the number of particles ($H^0 \longrightarrow H^+ + e$), the pressure is also doubled. We here use a two temperature approximation (which will be tested in the next section). We set all the fully ionized cells to a temperature T_i and all the neutral cells to a temperature T_n. Partially ionized cells' temperatures are fond by linearly interpolating between these two values. Doing this approximation speeds up the Monte Carlo method significantly because it means we do not require to trace ionization states of any element other than hydrogen (if we were to compute the heating and cooling self-consistently we would need to require the knowledge of ionic fractions of many other elements).

Given the ionized fraction of a cell $n(H^+)$, its temperature and pressure are now given by:

$$\begin{aligned} T_{cell} &= T_0 + T_i n(H^+) \\ P_{cell} &= P_0(1 + n(H^+)) \frac{T_{cell}}{T_0} \end{aligned} \tag{4.34}$$

Where T_0 and P_0 are the temperature and pressure of the neutral state.

These updated values of the temperature and density are then returned to the hydrodynamic code which otherwise operates as before.

4.5 Testing the code

Now that we have seen how the MCRT code works, we have to test if it is behaving adequately and giving the correct physical results when coupled to AMUN. In order to verify it is working as expected, we run two tests comparing the MCRT + AMUN with other codes.

The first test is the expansion of an ionized region and tests the coupling between the MCRT and the hydrodynamics in AMUN. The second test checks, against another Monte Carlo Radiative Transfer code, that the two temperature approximation is appropriate for the cases being studied here.

4.5.1 STARBENCH: D-type expansion

The D-type expansion of H_{II} regions is a well studied benchmark for coupled radiative hydrodunaamical codes. In fact, this problem was used to contrast and compare a number of radiation hydrodynamics codes in the StarBench paper (BISBAS et al., 2015). In this subsection, we will pose the D-type expansion problem and then compare the outcome of our simulations to the results of other numerical schemes from the StarBench.

4.5.2 The formation and expansion

Massive stars emit copious amounts of UV radiation capable of ionizing hydrogen ($E_{photon} = h\nu \geq 13.6eV$). The UV photons ionize the gas surrounding their source star giving rise to a region where the hydrogen content is almost fully ionized, known as an H_{II} region. The region can maintain itself ionized because the number of ionizing photons being emitted per unit time is of the same order as the recombination rate of ions back into neutral hydrogen. This equilibrium between the ionization and recombination rates is referred as the ionization balance. The kinetic energy of the photoelectrons ejected as a result of the ionization can then heat up the surrounding gas by collisions. The gas inside the H_{II} regions can also cool efficiently owing to collisionally excited line radiation of metal ions, which leads to an equilibrium temperature of approximately $10,000K$.

In what follows, we will treat a toy model of H_{II} regions formation and expansion. Among the simplifying assumptions for the problem at hand are:

a) The star emits monochromatic photons with energy $h\nu = 13.6eV$ in a spherically symmetric manner

b) the background medium has (initially) uniform density and temperature

c) the gas is composed solely of atomic hydrogen

This scenario was first studied by Strömgren (1939). His work showed that, in this spherically symmetric scenario, an ionized sphere would form around the emitting star. This sphere was later dubbed as the Stromgren sphere. Once a star generates the ionized region, it will expand quickly in what is dubbed as a rarefied or R-type expansion. This expansion leaves the gas relatively unaffected and ends when the sphere reaches ionization balance at a radius, R_{St}:

$$R_{St} = \left(\frac{3N_\gamma m_p^2}{4\pi\alpha\rho_0^2} \right) \tag{4.35}$$

where N_γ is the number of ionizing photons, m_p is the proton mass, α is the recombination rate and ρ_0 is just the initial background density.

Furthermore, Stromgren demonstrated that the transition between the almost fully ionized gas and the surrounding neutral medium happens over a very small spatial range in comparison to the size of the ionized sphere's radius. This transition region is known as the ionization front and can be treated as a sharp discontinuity.

However, the evolution of an H_{II} region does not end when it reaches the Stromgren radius. Although the H_{II} region has a number density that is only twice that of the neutral gas, its temperature will be around two orders of magnitude higher. This large temperature difference between these two regions implies a large difference in thermal pressure, triggering further expansion of the ionized region. In this expansion second phase, which is called D-type (D=Dense), the ionization front propagates at supersonic speeds with respect to the neutral gas. As a result, it sweeps up the surrounding gas in a thin dense neutral shell. As the ionized region expands, its density decreases, as no material crosses the front. Therefore, the recombination rate falls, meaning that the ionizing luminosity of the star is able to ionize out to a larger radius. The expansion will continue until the ionized bubble is able to re-establish a pressure equilibrium with the adjacent neutral region.

The D-type expansion was first modelled by Spitzer (1978). Following Raga et al.

(2012), by assuming that the expanding H_{II} region is in pressure balance with the shocked, neutral material and that the shock is isothermal, it can be shown that the expansion rate of the ionized region can be given by:

$$\frac{1}{c_{s_i}}\frac{dR(t)}{dt} = \left(\frac{R_{St}}{R(t)}\right)^{3/4} - \frac{c_{s_0}^2}{c_{s_i}^2}\left(\frac{R_{St}}{R(t)}\right)^{-3/4} \tag{4.36}$$

where c_{s_i} and c_{s_0} are the sound speeds of the ionized and neutral medium respectively. Because the temperature in the ionized region is so much higher, the sound speed is a lot higher as well. Thus, to first order, one can ignore the second term in 4.36, which gives the so called Sptizer solution:

$$R_{Sp}(t) = R_{St}\left(1 + \frac{7}{4}\frac{c_{s_i}t}{R_{St}}\right)^{4/7} \tag{4.37}$$

However, this method does not account for the inertia of the shocked neutral gas, which is created during the expansion of the H II region. Inclusion of inertia leads to:

$$\frac{1}{c_{s_i}}\frac{dR(t)}{dt} = \sqrt{\frac{4}{3}\left(\frac{R_{St}}{R(t)}\right)^{3/2} - \frac{c_{s_0}^2}{2c_{s_i}^2}} \tag{4.38}$$

Again ignoring the term with $\frac{c_{s_0}^2}{c_{s_i}^2}$, we get:

$$R_{HI}(t) = R_{St}\left(1 + \frac{7}{4}\sqrt{\frac{4}{3}}\frac{c_{s_i}t}{R_{St}}\right)^{4/7} \tag{4.39}$$

This equation was first presented by Hosokawa e Inutsuka (2006) and we will refer to it as the Hosokawa-Inutsuka solution.

4.5.3 Benchmarking our code

Now we compare both the Spitzer 4.37 and the Hosokowa-Inutsuka 4.39 analytic solutions as well as the the average results from the codes from the StarBench paper to the numerical result from our coupled code. The initial conditions are set as on the StarBench paper and are resumed on Table 4.1.

Table 4.1 - Initial conditions for the simulations of early D-type expansion of an H II region.

Variable	Value
N_γ	10^{49}
T_0	10^2 K
c_{s_0}	$0.91\ km\ s^{-1}$
α_B	$2.7 \times 10^{-13}\ cm^3\ s^{-1}$
ρ_0	$5.21 \times 10^{-21}\ g\ cm^{-3}$
T_i	10^4 K
c_{s_i}	$12.85\ km\ s^{-1}$
Resolution	256^3
Boundary Conditions	Zero Gradient
Equation of State	Isothermal

The Monte Carlo radiative transfer was performed with 10 iterations with 10^6 photon packets each, in order to obtain reliable ionization fractions. Once all the photon packets are propagated, the ionic fractions are updated at the end of the iteration, based on the photon packet trajectories. At the first iteration, the code assumes that all cells are fully ionized . This way, photons can travel longer distances and probe the grid much better than if the simulations had started with a fully neutral medium. We find that, by using this strategy, convergence is found with fewer iterations.

Figure 4.8 shows cross-section plots through the centre of our simulation box for the density and temperature of our simulations. It is clear that the general behaviour of H_{II} region expansion is as expected: a spherical region is expanding rapidly and sweeping up a shell of shocked gas.

In order to estimate the rate of expansion of the ionized bubble, we measure the radius from the sphere where at least 50% of the gas is ionized and use this radius as being representative of the beginning of the ionization front. We trace the evolution of this radius from the Stromgren sphere ($t = 0$) first 0.14 Myrs. In Figure 4.9 we plot the evolution of our ionization front with time and compare it to the analytical models of Spitzer and Hosokawa-Inutsuka, presented earlier in this chapter. We also plot the average of the codes which participated from the StarBench paper. As it can be seen, our code follows very well the Hosokawa-Inutsuka solution, specially at later times, behaving better than the average of the codes. It should, however, be pointed out that other codes participating in StarBench have similar behaviour to our code.

Figure 4.8 - Pressure driven (D-type) expansion of an ionized region

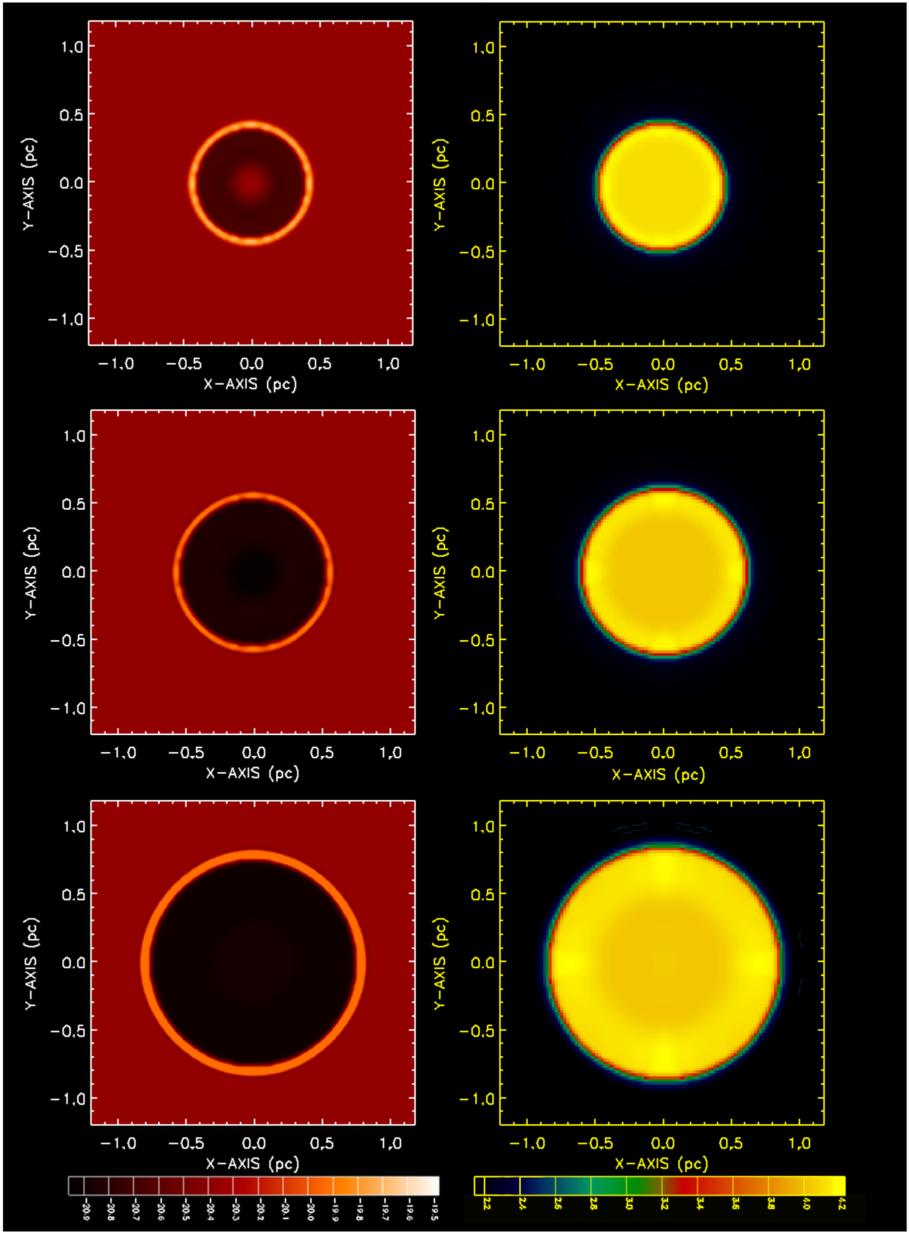

Cross section of the density (left) and temperature (right) through the middle of our simulation box at times (from top to bottom) $t = 0.01$, 0.02 and 0.04 Myr . The logarithmic colour bars shows gas density in gcm^{-3} and the temperature in K.

Figure 4.9 - Comparison between the analytical solution and the code results for the expansion of an HII region

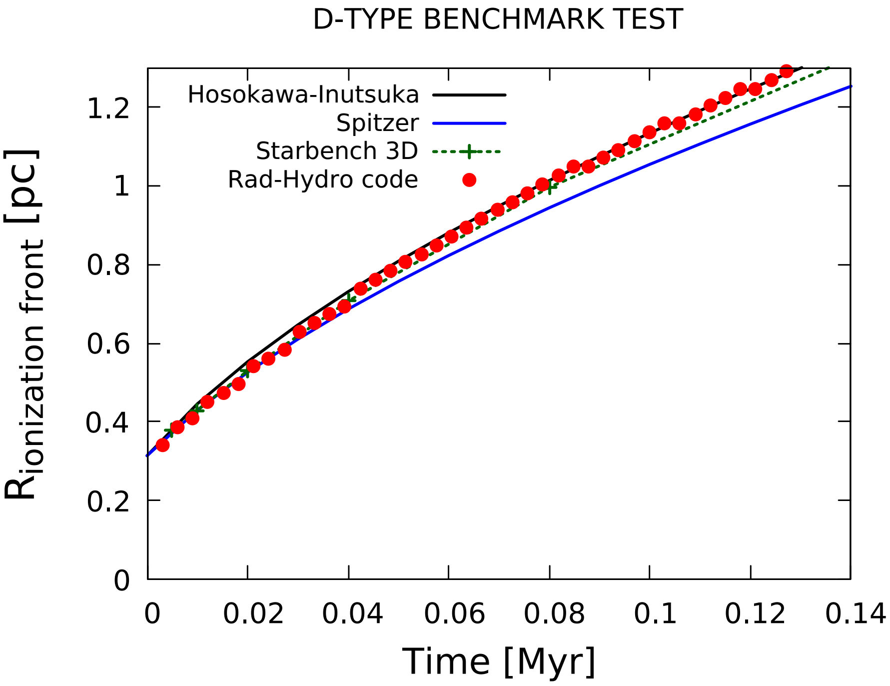

Comparison between the expansion of our ionized region over time in comparison with the average for the 3D codes used in StarBench (BISBAS et al., 2015). In order to quantify the rate of expansion, we track the radius at which the ionization fraction is 50%. We additionally plot the Spitzer and the Hosokawa-Inutsuka analytical expressions for reference.

We therefore conclude that our code does succeed in coupling the Monte Carlo Radiation Transfer to the hydrodynamics.

4.5.4 Testing the two temperature approximation

As pointed out earlier in Section 4.4 we use a two temperature approximation for our Monte Carlo code, much similar to the one used in the StarBench benchmark problem. Every fully ionized cell is set a temperature of $8000K$ and every cell that is fully neutral has a temperature of $500K$. Partially ionized cells' temperatures are a linear interpolation between these two extremes. We test our Monte Carlo code against the Monte Carlo code of Wood et al. (2004) (MC-W) that does trace the cooling in H_{II} regions via a few mechanisms: collisionally excited forbidden lines, recombination and free-free emission. The code does so by tracing the ionization structure of a number of coolants, namely. C+, C++, N0 , N+, N++, O0, O+, O++, Ne+, Ne++, S+, S++, and S+++. These chemical elements are chosen

Figure 4.10 - Comparison with other codes: size of the ionized region for H and He

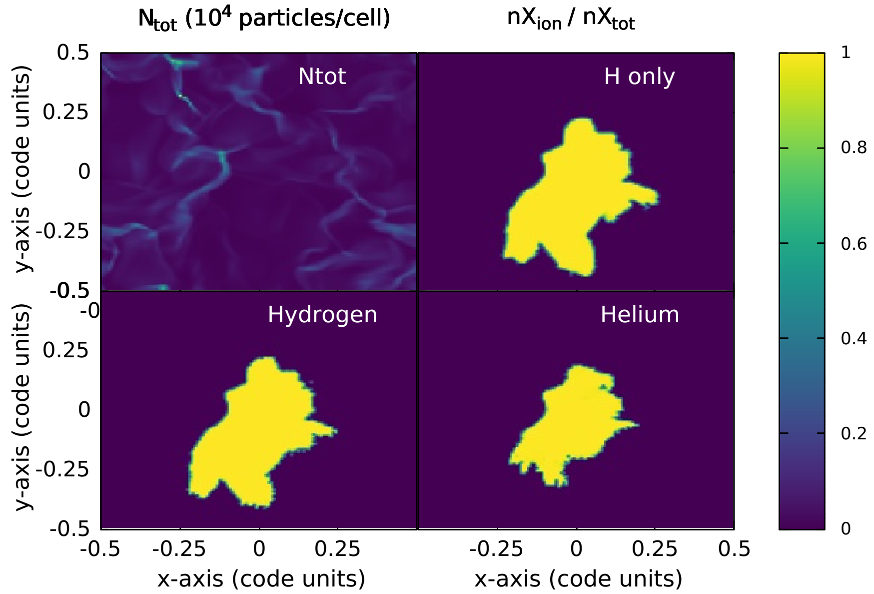

Middle slices of the simulation box. From left to right, top to bottom: i) original density structure of the turbulent grid, ii) the ionized fraction resulting from our code, iii) the region with ionized hydrogen obtained from the MC-W code, iv) as in (iii) but for helium.

because some of their ions are important for the heating and cooling rates. Other elements should not appreciably affect the H ionization structure or contribute to the heating or cooling and, thus, are not included (for further detail please refer to the code paper (WOOD et al., 2004)).

Figures 4.10 and 4.11 show the ionization structure for a density slice of a 3D simulation of a turbulent grid. For this test, we have output a turbulent density structure resulting from a simulation from AMUN and post-processed it with MC-W or performed a single Monte Carlo time-step with our coupled code (being also effectively a post processing in this case). We can see that our code results in an ionized region with shape and size much similar to the one obtained from the more complete model. We also see that the ionized region from other elements is either smaller or equal in size to the hydrogen ionized region.

We can also compute the free electron fraction (number of electron per initial particle density) which is therefore 1 for fully ionized regions and 0 for fully neutral regions (as then there are no free electrons). This is shown in Figure 4.12, which shows that our approximation also leads to a satisfactory result with the largest error being

Figure 4.11 - Comparison with other codes: size of the ionized region for O, C, N and S

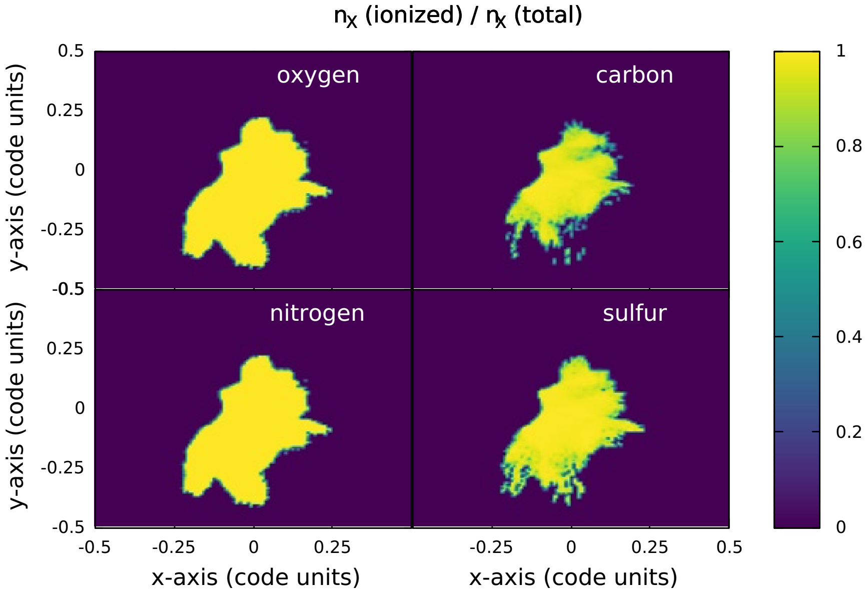

Ionized fraction for oxygen, carbon, nitrogen and sulfur obtained from the MC-W code for the turbulent grid in Figure 4.10.

10% in a few cells.

Finally, we compare the temperature structure to two cases with the MC-W code: one in which we switch off the cooling by all elements other than hydrogen (Hydrogen Only Complete Model) and one in which we have all the cooling as used for the other tests (Complete Model). This is illustrated in Figure 4.13. We can see that only tracing the hydrogen ionization state there is not enough cooling and the temperatures of the HII regions are artificially very high. Using the two temperature approximation we get comparable temperatures for each cell between our code and the MC-W with proper cooling.

We thus conclude that our methods should give reliable results for the study of H_{II} regions. Note that, however, the code as it is presented at the moment may not be suitable for other situations where other types of cooling may be relevant.

Figure 4.12 - Comparison with other codes: electron density

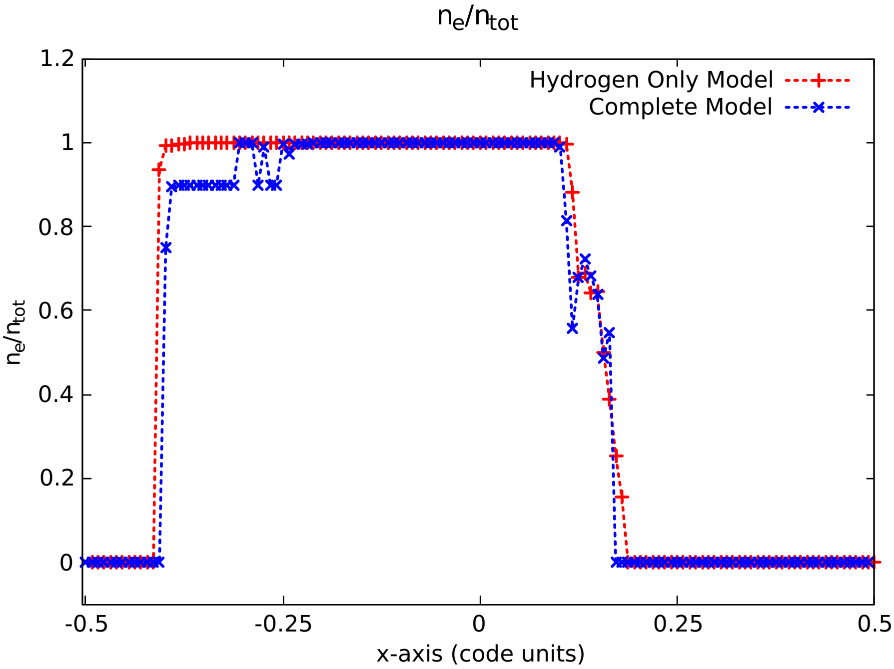

Electron fractions (for the slice shown in Figures 4.10 and 4.11) obtained in our code (red line) and in the MC-W code (blue).

Figure 4.13 - Comparison with other codes: temperature of the ionized region

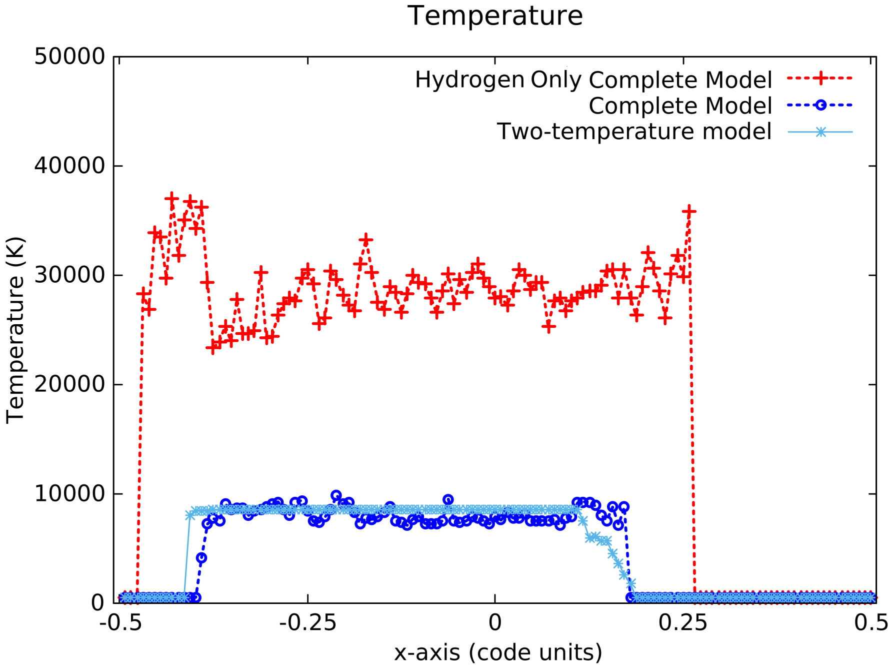

Temperatures for the slice shown in Figures 4.10 and 4.11 obtained with the complete code using only hydrogen cooling (red line) and using the complete cooling (dark blue) and our two temperature approximation (light blue).

5 SPHERICAL ACCRETION ONTO A MASSIVE PROTO-STAR

5.1 Introduction

In the last chapter, we have seen how massive stars emit enough UV radiation create, in a spherically symmetric case, an ionized sphere of gas commonly referred as an H_{II} region. In the present and the following chapters we are going to consider how a star that is massive enough to create such a region may simultaneously be able to accrete material. In this chapter, we are going to study a virtually one dimensional scenario where accretion onto the star takes place in a spherically symmetric manner. In the next chapter, we are going to study a more realistic 3D scenario.

We begin the chapter by giving a concise review of massive star formation 5.2. We, then, introduce the equation, describing the spherical accretion onto a point mass M, resulting solely from the gravitational attraction due to M. This is known as the Bondi Problem 5.3 Bondi (1952). In the following Section (5.4), we derive expressions that link the hydrodynamics quantities on either side of an ionization front. Thereafter, in Section 5.5 we join the expressions from the two previous sections to determine the profile we expect for the hydrodynamics variables (here density, velocity and pressure) for a star that has an ionizing region and is accreting. This analytical derivation had not yet been done before and it has been published as part of our group (VANDENBROUCKE et al., 2019) and used as a comparison solution in another paper from our collaboration (LUND et al., 2019). Finally, in Section 5.6, we compare both codes used in this thesis with the derived analytical solution. We finish by giving a semi-analytic account that shows the H_{II} region is unstable to small perturbations in the ionization front in this 1D scenario.

5.2 Massive star formation

Massive stars (from 10 up to above 100 solar masses) represent a minority of the stars in the stellar initial mass function (MASSEY, 2003). They have, however, a profound impact on their environment as their feedback mechanisms (winds, outflows, radiation pressure, photoionization, supernovae) inject vast amounts of energy and momentum, leading to dynamical and chemical changes in the surrounding gas (KENNICUTT, 1998).

Despite their importance, the formation of massive stars remains, in many ways, unclear. One of the reasons modelling massive star formation is challenging is that, in comparison with low mass stars, there is very little observational information

(BELTRÁN; DEWIT, 2016). This is due to the fact that massive stars form quickly and, hence, the sites where ongoing massive star formation can be observed are rare. As a consequence of their rapid formation, massive proto-stars do not have time to clear out their surroundings and are, therefore, deeply concealed in the innermost region of an infalling envelope of gas and dust (CESARONI et al., 2007). This makes mm and sub-mm wavelength observations the only way to probe deep into the core region (BELTRÁN; DEWIT, 2016). Observations are further complicated by the fact that the closest massive proto-stars are at least a kiloparsec away (ZINNECKER; YORKE, 2007; TAN et al., 2014). These large distances imply that sub-arcsecond resolution is required in the measurements if we are to resolve, for instance, disk structures. The first models for massive star formation consider simple accretion scenarios. The case study of a spherically symmetric accretion flow onto a massive star, including a rigorous treatment of the hydrodynamics, was pioneered by Bondi (1952), and is, consequently, often referred to as the Bondi problem. Mestel (1954) studied the effect of ionizing radiation on the original Bondi problem, using an approximation whereby both the neutral and the ionized regions are assumed to follow an isothermal equation of state, with distinct isothermal sound speeds (due to the expected difference in temperature and number density in the two regions). Is is also assumed, as in the D-type expansion, that there is a sharp transition from the ionized to the neutral regime, with the transition region being regarded as the ionization front. The works of Keto (2002), Keto (2003)) showed that Mestel's analysis implies the existence of a steady state solution in which an ionized region is trapped inside the accreting flow. This can be understood simply by considering the problem as a struggle between the gravitational force and the pressure gradient force at the ionization front (Figure 5.1). If the pressure differential force is small, compared to the gravitational force, the H_{II} region cannot expand in a D-type expansion as seen in the last chapter. Instead, this ionized region will remain confined at a certain distance from the star and it is traditionally referred as a "trapped H_{II} region". This explains the existence of trapped compact and ultracompact H_{II} regions observed around massive accreting stars, with typical radii varying from $\sim 10^3$ au (CHURCHWELL, 2002) to as small as ~ 10 au (ILEE et al., 2016).

Figure 5.1 - Toy model of an H_{II} region.

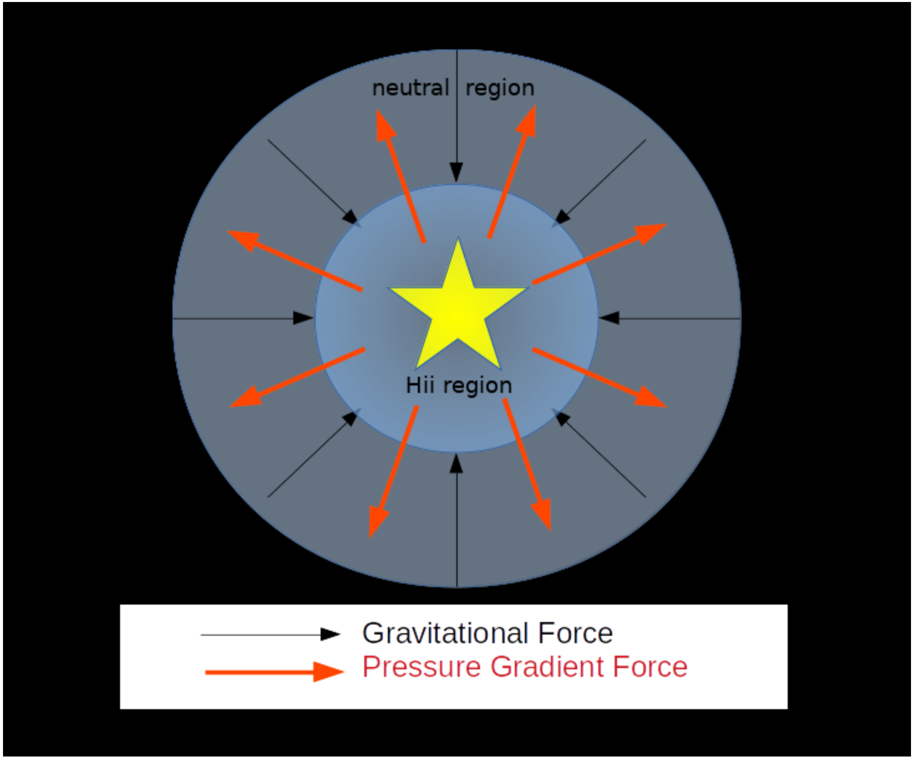

Schematic showing an ionized region around a massive star. The H_{II} region around a star will be trapped if the gravitational force is larger than the pressure force or will expand otherwise.

Therefore, pressure driven expansion may only occur if the ionization front of the H_{II} region finds itself at a radial distance from the central mass where the gravitational attraction is less than the pressure force. Another way to describe the problem is considering the sound speed (c_s) relation to the escape velocity (v_{esc}). As c_s reflects the changes in temperature and number density in the ionized region compared to the neutral one, and v_{esc} is related to the gravitational attraction from the star, if the sound speed of the ionized gas exceeds the escape velocity, pressure driven expansion may take place. By this account, the transition to D-type expansion occurs just before the sonic point R_s of the ionized accretion flow, that is:

[redacted]

$$H_{II} \text{ region is } \begin{cases} \text{Trapped,} & R_{IF} \leq R_s \\ \text{in Pressure Driven (D-type) Expansion,} & R_{IF} > R_s \end{cases}$$

Recall that, throughout the pressure expansion phase, material in the neutral region is swept up by the ionization front as it expands in a shock. In this case, no gas can cross the ionization front and accretion onto the central star, clearly, is terminated. Contrastingly, a star with a trapped ionized region may still accrete material. Gas can cross the front, get ionized and accelerate under gravity until it is eventually accreted onto the star. Deriving a new analytical solution for this last scenario is the main aim of this chapter.

5.3 Bondi accretion

We want to analytically study a continuous, spherically symmetric flow onto a point of mass M, which here represents our massive star. In order for the flow to be steady, we require that the rate at which mass flows through any spherical shell around the star has to be the same. In other words, we require that:

$$\frac{d\dot{M}}{dr} = 0 \tag{5.1}$$

where r represents the radial distance from the point mass and '$\cdot$' the time derivative.

The flow of mass through a spherical shell at radius r is simply the area of the shell multiplied by the density and velocity at that radius, thus:

$$\dot{M} = 4\pi r^2 \rho u \tag{5.2}$$

Substituting 5.2 into 5.1, we have:

$$4\pi \frac{d(r^2\rho u)}{dr} = 4\pi \left[2r\rho u + r^2 \rho \frac{du}{dr} + r^2 u \frac{d\rho}{dr} \right] = 0 \tag{5.3}$$

Such that (dividing by $r^2\rho u$), this is the form the conservation of mass takes for our problem:

$$\frac{2}{r} + \frac{1}{u}\frac{du}{dr} + \frac{1}{\rho}\frac{d\rho}{dr} = 0 \tag{5.4}$$

Recall the momentum equation is:

$$\frac{\partial \rho u}{\partial t} + \boldsymbol{\nabla} \cdot \rho u^2 = -\left[\boldsymbol{\nabla} p + \rho \boldsymbol{\nabla} \phi \right] \tag{5.5}$$

A steady solution implies that the time derivative is zero. From the mass conservation equation $\frac{\partial \rho}{\partial t} + \boldsymbol{\nabla} \cdot (\rho u) = \boldsymbol{\nabla} \cdot (\rho u) = 0$. We also have the gravitational force enters as a term $\rho \boldsymbol{\nabla} \phi = \rho g = \rho \frac{GM}{r^2}$. Rearranging, we have:

$$u \cdot \boldsymbol{\nabla}(u) + \frac{1}{\rho} \boldsymbol{\nabla} P + \frac{GM}{r^2} = 0 \tag{5.6}$$

Using the chain rule to expand $\boldsymbol{\nabla} P$ and the fact that $c_s^2 = \frac{dP}{d\rho}$, we can rewrite the momentum equation as:

$$u \cdot \boldsymbol{\nabla}(u) + \frac{1}{\rho} \frac{dP}{d\rho} \frac{d\rho}{dr} + \frac{GM}{r^2} = u \cdot \boldsymbol{\nabla}(u) + \frac{c_s^2}{\rho} \frac{d\rho}{dr} + \frac{GM}{r^2} = 0 \tag{5.7}$$

Note also that, due to this being a spherically symmetric problem, $\boldsymbol{\nabla} = \frac{\partial}{\partial r} \hat{\mathbf{r}} + \frac{1}{r} \frac{\partial}{\partial \theta} \hat{\boldsymbol{\theta}} + \frac{1}{r \sin\theta} \frac{\partial}{\partial \phi} \hat{\boldsymbol{\phi}} = \frac{\partial}{\partial r} \hat{\mathbf{r}}$. Thus, we use the gradient symbol interchangeably with the radial derivative.

Substituting 5.4 in the above:

$$\begin{aligned}
u \cdot \boldsymbol{\nabla}(u) - c_s^2 \left[\frac{2}{r} + \frac{1}{u} \frac{du}{dr} \right] + \frac{GM}{r^2} &= 0 \\
\implies u \cdot \boldsymbol{\nabla}(u) - c_s^2 \left[\frac{2}{r} + \frac{1}{u^2} (u \cdot \boldsymbol{\nabla}(u)) \right] + \frac{GM}{r^2} &= 0 \\
\implies u \cdot \boldsymbol{\nabla}(u) \left[1 - \frac{c_s^2}{u^2} \right] - \frac{2c_s^2}{r} + \frac{GM}{r^2} &= 0
\end{aligned}$$

Because $u \cdot \boldsymbol{\nabla}(u) = \frac{1}{2} \boldsymbol{\nabla}(u^2)$:

$$\frac{1}{2} \boldsymbol{\nabla}\left(u^2\right) \left[1 - \frac{c_s^2}{u^2} \right] = -\frac{GM}{r^2} + \frac{2c_s^2}{r}$$

Which gives us the Bondi equation:

$$\boldsymbol{\nabla}\left(u^2\right) \left[1 - \frac{c_s^2}{u^2} \right] = -\frac{2GM}{r^2} \left[1 - \frac{2c_s^2 r}{GM} \right] \tag{5.8}$$

The Bondi radius, R_B , is defined such that, at this radius, right hand side of the

Equation 5.8 is zero, that is:

$$R_B = \frac{GM}{2c_s^2} \tag{5.9}$$

With this definition, the Equation 5.8 can be expressed as:

$$\boldsymbol{\nabla}\left(u^2\right)\left(1 - \frac{c_s^2}{u^2(r)}\right) = -\frac{4c_s^2 R_B}{r^2}\left(1 - \frac{r}{R_B}\right), \tag{5.10}$$

At $R = R_B$, we have, by definition, that:

$$\boldsymbol{\nabla}\left(u^2\right)\left[1 - \frac{c_s^2}{u^2}\right] = 0 \tag{5.11}$$

So, possible solutions are:

- $\boldsymbol{\nabla}(u^2) = 0$ at the Bondi radius
- $c_s = |v|$, that is, the Bondi radius is a sonic point

These solutions can be divided into 3 groups of solutions, namely:

a) $u(R_s) = c_s$ and as $u \to 0$ either $r \to 0$ or $r \to \infty$

b) $\boldsymbol{\nabla}(u^2) = 0$ and either $u > c_s$ (always supersonic) or $u < c_s$ (always subsonic)

c) $u(R_s) = c_s$ and either $r < R_s$ or $r > R_s$ (unphysical solutions)

These solutions are illustrated in Figure 5.2. It is easy to see from the figure that the only solution that fits our proposed problem is solution 1 with $u \to 0$ as $r \to \infty$ (since we want the gas to be at rest at infinity; with increasing speed as it approaches $r = 0$). Note that, for this solution, the Bondi radius is the sonic radius $R_B = R_s$.

Figure 5.2 - Bondi equation solutions

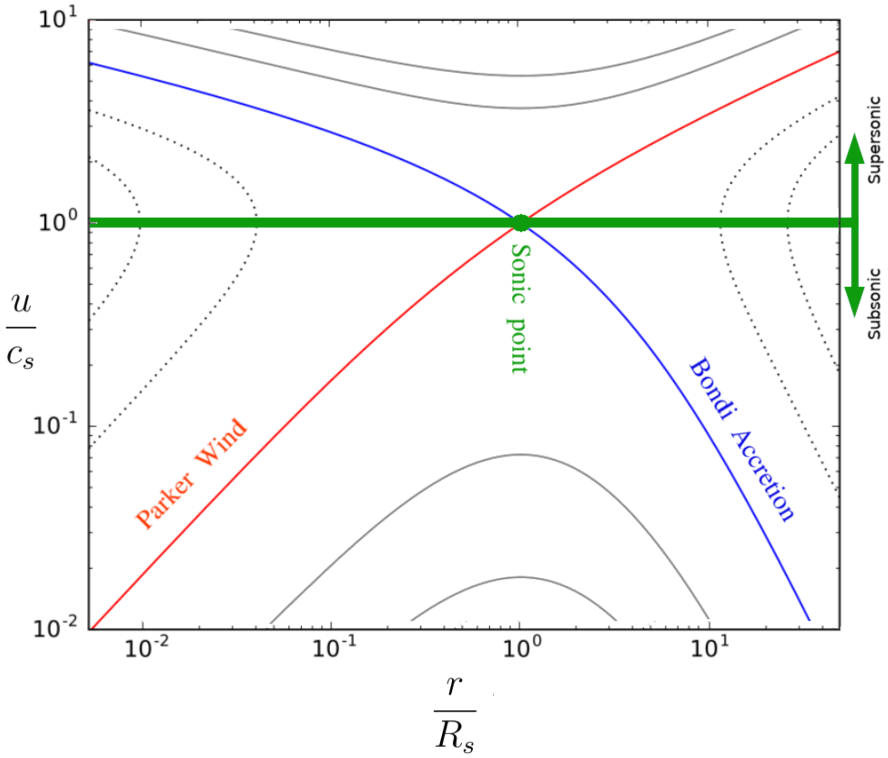

Graphical representation of the solutions to the Bondi equation. The solutions represented by the dashed lines are doubled valued and, thus, unphysical. The black continuous lines represent solutions where the flow that is everywhere subsonic (top of image) or everywhere supersonic (bottom of image). Finally, there are two solutions which go through the sonic point (blue and red lines). These transonic solutions represent either the Parker stellar wind (for increasing velocity with radius) solution or the Bondi accretion (for decreasing velocity with radius).

With this solution in mind, we now want to find the profiles of how velocity and density vary with radius.

5.3.1 Solution for the velocity

We start to find the solution for the velocity by integrating the momentum Equation (5.6) to obtain the Bernoulli equation:

$$\frac{u^2}{2} + \int \frac{dP}{\rho} - \frac{GM}{r} = C_1 \tag{5.12}$$

where C_1 is a constant Assuming an isothermal equation ($P = c_s^2 \rho$) of state, we have:

$$\begin{aligned} C_1 &= \frac{u^2}{2} + c_s^2 \int \frac{d\rho}{\rho} - \frac{GM}{r} \\ &= \frac{u^2}{2} + c_s^2 ln(\rho) - \frac{GM}{r} \\ \implies C_2 = \frac{C_1}{c_s^2} &= \frac{u^2}{2c_s^2} + ln(\rho) - \frac{GM}{rc_s^2} \\ &= \frac{u^2}{2c_s^2} + ln(\rho) - \frac{2R_B}{r} \end{aligned} \tag{5.13}$$

Since at $r \to \infty$, we have $(1/r, u) \to 0$, the constant C_2 has to be simply $ln(\rho(\infty))$. The full Bernoulli equation is then:

$$ln(\rho(\infty)) = \frac{u^2}{2c_s^2} + ln(\rho) - \frac{2R_B}{r} \tag{5.14}$$

Analysing the Bernoulli equation at the Bondi radius, where $u^2 = c_s^2$:

$$\begin{aligned} ln(\rho(\infty)) &= \frac{1}{2} + ln(\rho(R_B)) - 2 \\ ln(\rho(\infty)) &= -\frac{3}{2} + ln(\rho(R_B)) \end{aligned} \tag{5.15}$$

This means that the density at the Bondi radius is directly linked with the background density far away from the accreting point mass.

We also have from the steady flow assumption that:

$$4\pi R_B^2 \rho_B u_B = 4\pi r^2 \rho u \tag{5.16}$$

where the B subscript indicate the value of a quantity at the Bondi radius. Note that the left hand side is a known value, since $R_B = \frac{GM}{2c_s^2}$, $u_B = -c_s$ and $\rho_B = e^{ln(\rho_\infty)+\frac{3}{2}}$, depending only on the initial conditions for the problem.

Using the definition of the Bondi radius and 5.15, 5.16 becomes:

$$-c_s \frac{G^2 M^2}{4c_2^4} e^{\left(ln(\rho_\infty)+\frac{3}{2}\right)} = r^2 \rho u \tag{5.17}$$

Using this equation, we obtain an expression for ρ in terms of u and r:

$$\rho = \frac{-R_B^2 c_s}{r^2 u} e^{\left(ln(\rho_\infty)+\frac{3}{2}\right)} \tag{5.18}$$

which we substitute in the Bernoulli Equation (5.14), to find:

$$\frac{u^2}{2c_s^2} + ln\left(\frac{-R_B^2 c_s}{r^2 u}\right) + \left(ln(\rho(\infty)) + \frac{3}{2}\right) - \frac{2R_B}{r} = ln(\rho(\infty)) \tag{5.19}$$

Cancelling the ρ_∞ terms and multiplying by 2:

$$\frac{u^2}{c_s^2} - ln\left(\frac{r^4 u^2}{R_B^4 c_s^2}\right) + 3 - \frac{4R_B}{r} = 0 \tag{5.20}$$

Calling $U = \frac{u^2}{c_s^2}$:

$$U - \ln(U) - \ln\left(\frac{r^4}{R_B^4}\right) + 3 - \frac{4R_B}{r} = 0 \tag{5.21}$$

Which is of type:

$$x - \ln(x) + c = 0 \tag{5.22}$$

with solution:

$$x = -W(-e^c) \tag{5.23}$$

where W is the Lambert W function.

Thus, for our case, the solution is:

$$U = \frac{u^2}{c_s^2} = -W\left(- e^{-4\ln\frac{r}{R_B} + 3 - \frac{4R_B}{r}}\right) \tag{5.24}$$

or :

$$u = -c_s\sqrt{-W\left(- e^{4\ln\frac{R_B}{r} - \frac{4R_B}{r} + 3}\right)} \tag{5.25}$$

The negative root is justified by the fact that we want the star to be accreting (i.e. material has to be moving inwards).

5.3.2 Solution for the density

Once we have the velocity, the expression for the density follows naturally from Equation 5.18:

$$\rho(r) = \frac{R_B^2 \rho_B c_s}{r^2(-v)} \tag{5.26}$$

or:

$$\rho(r) = \frac{R_B^2 \rho_B}{r^2 \sqrt{W(-e^{4\ln\frac{R_B}{r} - \frac{4R_B}{r} + 3})}} \tag{5.27}$$

5.3.3 A note on Lambert W function

The Lambert W function is a general complex valued function that has many branches. However, two of these branches, called $W_0(x)$ and $W_{-1}(x)$, have the interesting property that they are real valued in the range $[-\frac{1}{e}, 0]$ with $W_{-1} < -1$ and $W_{-1} > -1$. The two branches meet at $W_0(-\frac{1}{e}) = W_{-1}(-\frac{1}{e}) = -1$, which we refer to as the turning point.

Since we require a real solution for the velocity, we see that we can indeed restrict ourselves to the real valued versions of the Lambert W function. The real part of the two branches is illustrated on Figure 5.3.

Figure 5.3 - Lambert-W function.

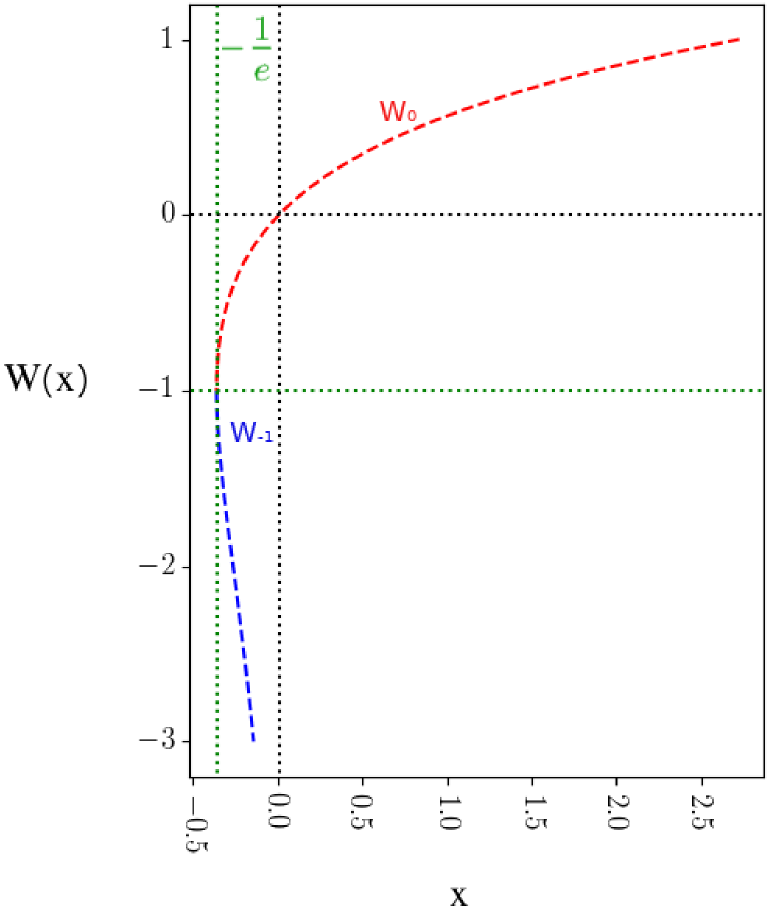

The two branches of the Lambert W function used in the solution of the Bondi problem with an ionized region. The W function is multivalued (except at 0). If we restrict ourselves to real-valued W(x), with x also being real, the function is defined for $x \geq -1/e$ and is double-valued on the interval $[-1/e, 0]$. For $W \geq -1$ we define the single-valued function W_0, while for $W \leq -1$ we define the single-valued function W_{-1} with the two functions meeting at $W_0(x = -1/e) = W_{-1}(x = -1/e)$.

Note that in our solutions $x = -e^{4\ln\frac{R_B}{r} - \frac{4R_B}{r} + 3}$ and, therefore the transition point between the two solutions ($x = -1/e$) is the Bondi radius. Therefore, as a sanity check, at $W_0(-\frac{1}{e}) = W_{-1}(-\frac{1}{e}) = -1$, we expect to have that the solution for our velocity is $u(r) = -c_s$, which indeed is the case.

5.3.4 Summary of the solution for the ionization front profile

We have

$$\rho(r) = \begin{cases} \frac{R_B^2 \rho_B}{r^2 \sqrt{W_{-1}(\omega)}}, & r \leq R_B, \\ \frac{R_B^2 \rho_B}{r^2 \sqrt{W_0(\omega)}}, & r > R_B, \end{cases} \tag{5.28}$$

and

$$u(r) = \begin{cases} -c_s \sqrt{-W_{-1}(\omega)}, & r \leq R_B, \\ -c_s \sqrt{-W_0(\omega)}, & r > R_B. \end{cases} \tag{5.29}$$

For $\omega = -e^{4 \ln \frac{R_B}{r} - \frac{4R_B}{r} + 3}$.

5.4 Solution across an ionization front

Now consider only a star emitting enough ionizing photons to create an H_{II} region surrounding it. The resulting scenario consist of two distinct regions:

- A hot ionized region, forming a bubble around the star
- A cold neutral region outside the ionization bubble

In order to find what is happening at the boundary dividing the two regions, we have to solve the hydrodynamic equations across the ionization front. Thus, what we have is another Riemann problem:

$$U = \begin{cases} \rho_1, u_1, p_1 \ ; \text{for} & r > R_{IF} \\ \rho_2, u_2, p_2 \ ; \text{for} & r < R_{IF} \end{cases} \tag{5.30}$$

From here onward the index 1 refers to the neutral region and the index 2 refers to the ionized region. Values with a bar on top refer to conditions at the ionization front itself, for instance $\bar{\rho}_1$ would be the density just on the neutral side of the ionization front.We also adopt an isothermal equation of state, applicable on either side of the ionization front (such that $p_1 = \rho_1 c_1$ and $p_2 = \rho_2 c_2$; where we dropped the 's' subscript for the speed of sound for simplicity).

Assuming that the ionization front (located at a radius R_{IF}) is also the (only) place where a discontinuous jump in density (and thus pressure) and velocity occurs, we have that the conditions on either side of the front obey the Rankine-Hugoniot jump conditions:

$$\bar{\rho}_1\bar{u}_1 = \bar{\rho}_2\bar{u}_2 \tag{5.31}$$

$$\bar{\rho}_1(\bar{u}_1^2 + c_1^2) = \bar{\rho}_2(\bar{u}_2^2 + c_2^2) \tag{5.32}$$

which basically entail the application of conservation of mass and momentum, respectively, across the front.

Using (5.31) to get an expression for $\bar{u}_2$ and substituting in (5.32):

$$\frac{\bar{\rho}_1}{\bar{\rho}_2}(\bar{u}_1^2 + c_1^2) = \left(\bar{u}_1^2\frac{\bar{\rho}_1^2}{\bar{\rho}_2^2} + c_2^2\right)$$

Defining $\Gamma = \frac{\bar{\rho}_2}{\bar{\rho}_1} = \frac{\bar{u}_1}{\bar{u}_2}$:

$$\begin{aligned}\frac{1}{\Gamma}(\bar{u}_1^2 + c_1^2) =& (\bar{u}_1^2\frac{1}{\Gamma^2} + c_2^2)\\ c_2^2\Gamma^2 - \Gamma(\bar{u}_1^2{+}c_1^2) + \bar{u}_1^2 =& 0\end{aligned}$$

Which is a quadratic with roots:

$$\Gamma = \frac{(\bar{u}_1^2 + c_1^2) \pm \sqrt{\left[(\bar{u}_1^2 + c_1^2)^2 - 4\bar{u}_1^2c_2^2\right]}}{2c_2^2} \tag{5.33}$$

As Γ needs to be real, we have also to satisfy the following condition:

$$(\bar{u}_1^2 + c_1^2)^2 - 4\bar{u}_1^2c_2^2 > 0 \tag{5.34}$$

This condition is again a quadratic, now in u_1^2. We have two possible roots u_R and u_D:

$$u_R = -\left(c_2 + c_2\sqrt{1-(c_1/c_2)^2}\right) \tag{5.35}$$

$$u_D = \left(c_2 - c_2\sqrt{1-(c_1/c_2)^2}\right) \tag{5.36}$$

Because $c_2 >> c_1$, we can expand the square root term,which to first order gives:

$$u_R = -2c_2 \tag{5.37}$$

$$u_D = -\frac{c_1^2}{2c_2} \tag{5.38}$$

We find that solutions exist for:

$$\bar{u}_1 > u_R \text{ or } \bar{u}_1 < u_D \tag{5.39}$$

These are referred as R and D type solutions respectively. At the points where $\bar{u}_1 = u_R$, the solution is termed R-critical. Likewise, if $\bar{u}_1 = u_D$, the solution is D-critical.

Two modes exist within each type solution, depending on which sign we take for the square root on Equation (5.33). One of the D-type solutions is nothing less than the D-type (pressure driven) expasion considered in the last chapter. In this chapter, however, we are interested in the R-type solutions. Here we consider only the negative root of (5.33) as it has a smaller jump in the density and velocities and, thus, it will be the one that will form, if initially we have a simple neutral Bondi profile. Thus:

$$\Gamma = \frac{\bar{\rho}_2}{\bar{\rho}_1} = \frac{\bar{u}_1}{\bar{u}_2} = \frac{(\bar{u}_1^2 + c_1^2) - \sqrt{\left[(\bar{u}_1^2 + c_1^2)^2 - 4\bar{u}_1^2 c_2^2\right]}}{2c_2^2} \tag{5.40}$$

5.5 Bondi problem with an ionized region

In this section we present the first analytical expression for a star accreting material in a Bondi-like fashion and that has an ionized region around it (VANDENBROUCKE et al., 2019).

Consider that initially we have a neutral Bondi profile just like in Section 5.3 and then the star, by some means, begins to emit a sizeable amount of ionizing photons and the medium around the star is ionized almost instantaneously.

We know the shape of the neutral region from the simple Bondi problem and thus the value of $\bar{u}_1$ and $\bar{\rho}_1$. If we know the speed of sound for the ionized gas (which depends only on temperature), we can calculate Γ and therefore $\bar{u}_2$ and $\bar{\rho}_2$. Values for the pressure on either side of the front can be easily obtained using the equation of state, as we are considering an isothermal scenario on either side of the ionization front.

Having the values for the hydrodynamical quantities on the ionized side of the front, we want now to find how these quantities change with radius.

5.5.1 Finding the velocity profile

Analysing the hydrodynamic equations on the ionized side, we have from the Bernoulli Equation 5.14:

$$\frac{u_2^2}{2c_2^2} + \ln \rho_2 - \frac{GM}{c_2^2 r_2} = \frac{\bar{u}_2^2}{2c_2^2} + \ln \bar{\rho}_2 - \frac{GM}{R_{IF} c_2^2} = B \tag{5.41}$$

and from the conservation of mass (steady state condition) 5.18:

$$r_2^2 u_2 \rho_2 = R_{IF}^2 \bar{u}_2 \bar{\rho}_2 \tag{5.42}$$

Substituting (5.42) in (5.41):

$$\frac{u_2^2}{2c_2^2} + \ln \frac{R_{IF}^2 \bar{u}_2 \bar{\rho}_2}{r_2^2 u_2} - \frac{GM}{c_2^2 r_2} = \frac{\bar{u}_2^2}{2c_2^2} + \ln \bar{\rho}_2 - \frac{GM}{R_{IF} c_2^2} \tag{5.43}$$

Cancelling $\ln \bar{\rho}_2$ on either side and multiplying through by 2:

$$\frac{u_2^2}{c_2^2} + 2 \ln \frac{R_{IF}^2 \bar{u}_2}{r_2^2 u_2} - \frac{2GM}{c_2^2 r_2} = \frac{\bar{u}_2^2}{c_2^2} - \frac{2GM}{c_2^2 R_{IF}} \tag{5.44}$$

Because u is always negative (accretion):

$$\frac{u_2^2}{c_2^2} - 2ln(-u_2) + 2 \ln \frac{-R_{IF}^2 \bar{u}_2}{r_2^2} - \frac{2GM}{c_2^2 r_2} - \frac{\bar{u}_2^2}{c_2^2} + \frac{2GM}{c_2^2 R_{IF}} = 0 \tag{5.45}$$

Rearranging:

$$\frac{u_2^2}{c_2^2} - \ln\left(u_2^2\right) + 2\ln\frac{-R_{IF}^2\bar{u}_2}{r_2^2} - \frac{2GM}{c_2^2 r_2} - \frac{\bar{u}_2^2}{c_2^2} + \frac{2GM}{c_2^2 R_{IF}} = 0 \tag{5.46}$$

Adding and subtracting $ln(c_2^2)$

$$\frac{u_2^2}{c_2^2} - \ln\left(\frac{u_2^2}{c_2^2}\right) + \ln\frac{R_{IF}^4\bar{u}_2^2}{r_2^4 c_2^2} - \frac{2GM}{c_2^2 r_2} - \frac{\bar{u}_2^2}{c_2^2} + \frac{2GM}{c_2^2 R_{IF}} = 0 \tag{5.47}$$

Call $U = \frac{u_2^2}{c_2^2}$ and using the definition for the Bondi radius for the ionized quantities ($R_{B2} = \frac{GM}{2c_2^2}$):

$$U - \ln(U) + \ln\frac{R_{IF}^4\bar{u}_2^2}{r_2^4 c_2^2} - \frac{4R_{B2}}{r_2} - \frac{\bar{u}_2^2}{c_2^2} + \frac{4R_{B2}}{R_{IF}} = 0 \tag{5.48}$$

Which, like in the original Bondi problem, is of the type:

$$x - ln(x) + c = 0 \tag{5.49}$$

with solution:

$$x = -W(-e^c) \tag{5.50}$$

So we have:

$$U = \frac{u_2^2}{c_2^2} = -W\left(-e^{\ln\frac{R_{IF}^4\bar{u}_2^2}{r_2^4 c_2^2} - \frac{4R_{B2}}{r_2} - \frac{\bar{u}_2^2}{c_2^2} + \frac{4R_{B2}}{R_{IF}}}\right) \tag{5.51}$$

$$u_2 = -c_2\sqrt{-W\left(-e^{\ln\frac{R_{IF}^4\bar{u}_2^2}{r_2^4 c_2^2} - \frac{4R_{B2}}{r_2} - \frac{\bar{u}_2^2}{c_2^2} + \frac{4R_{B2}}{R_{IF}}}\right)} \tag{5.52}$$

Compare this with what the simple Bondi solution would be:

$$u_2 = -c_2\sqrt{-W\Big(-e^{4\ln\frac{R_{B2}}{r_2}-\frac{4R_{B2}}{r_2}+3}\Big)} \tag{5.53}$$

We see the overall format is the same, but the argument of the Lambert W function differs and, thus, we can expect a different turning point between the W_0 and W_{-1} branches.

Turning point for the Lambert-W function

We saw that, for the simple Bondi, the Lambert-W function switches branches from 0 to -1 at the Bondi radius. For the ionized solution, this is not the case. We now have to find the turning point by finding where the argument of the W function for the velocity is $-e^{-1}$, which is equivalent to:

$$\ln\frac{R_{IF}^4\bar{u}_2^2}{r_2^4c_2^2} - \frac{4R_{B2}}{r_2} - \frac{\bar{u}_2^2}{c_2^2} + \frac{4R_{B2}}{R_{IF}} = -1 \tag{5.54}$$

It is clear that, in the case the ionization front is at the Bondi radius for the ionized quantities, the equation above is satisfied.

At a general ionization front position, we have:

$$\ln\frac{R_{IF}^4\bar{u}_2^2}{R_{IF}^4c_2^2} - \frac{4R_{B2}}{R_{IF}} - \frac{\bar{u}_2^2}{c_2^2} + \frac{4R_{B2}}{R_{IF}} = \ln\frac{\bar{u}_2^2}{c_2^2} - \frac{\bar{u}_2^2}{c_2^2} \tag{5.55}$$

which is of type $\ln(y) - y$. This value is always less or equal to -1 and, hence, the ionization front solution is always at the W_{-1} branch. As the radius decreases (we get closer to the star), we want the velocity to become more negative (as the gas is accelerating under the gravitational force). Therefore, we require W to become more negative with smaller radii. Looking back at Figure 5.3 it is clear that we want the whole solution for the ionized region to W_{-1} branch.

5.5.2 Finding the density profile

The density profile can be easily obtained by the steady accretion condition:

$$\rho_2 = \frac{R_{IF}^2\bar{v}_2\bar{\rho}_2}{r^2v_2}$$

$$\rho_2 = \frac{R_{IF}^2 \bar{v}_2 \bar{\rho}_2}{-r^2 c_2 \sqrt{-W\Big(- e^{\ln \frac{R_{IF}^4 \bar{v}_2^2}{r_2^4 c_2^2} - \frac{4R_{B2}}{r_2} - \frac{\bar{v}_2^2}{c_2^2} + \frac{4R_{B2}}{R_{IF}}}\Big)}}$$

5.5.3 Summary

Neutral Region:

For $\omega_1 = -e^{4\ln \frac{R_{B1}}{r} - \frac{4R_{B1}}{r} + 3}$.

- velocity

$$u(r) = \begin{cases} -c_1\sqrt{-W_{-1}\left(\omega\right)}, & r \leq R_{B1}, \\ -c_1\sqrt{-W_0\left(\omega\right)}, & r > R_{B1}. \end{cases} \tag{5.56}$$

- density

$$\rho(r) = \begin{cases} \frac{R_B^2 \rho_B}{r^2 W_{-1}(\omega)}, & r \leq R_{B1}, \\ \frac{R_B^2 \rho_B}{r^2 W_0(\omega)}, & r > R_{B1}, \end{cases} \tag{5.57}$$

Ionized region: For $\omega_2 = -e^{\ln \frac{R_{IF}^4 \bar{u}_2^2}{r_2^4 c_2^2} - \frac{4R_{B2}}{r_2} - \frac{\bar{u}_2^2}{c_2^2} + \frac{4R_{B2}}{R_{IF}}}$

- velocity

$$u(r) = \begin{cases} -c_2\sqrt{-W_{-1}\left(\omega_2\right)}, & r \leq r_{turn}, \\ -c_2\sqrt{-W_0\left(\omega_2\right)}, & r > r_{turn}. \end{cases} \tag{5.58}$$

- density

$$\rho_2 = \begin{cases} \frac{R_{IF}^2 \bar{u}_2 \bar{\rho}_2}{-r^2 c_2 \sqrt{-W_{-1}(\omega_2)}}, & r \leq r_{turn}, \\ \frac{R_{IF}^2 \bar{u}_2 \bar{\rho}_2}{-r^2 c_2 \sqrt{-W_0(\omega_2)}}, & r > r_{turn}. \end{cases} \tag{5.59}$$

With ionized variables at the I.F. determined by:

$$\Gamma = \frac{\bar{u}_1}{\bar{u}_2} = \frac{\bar{\rho}_2}{\bar{\rho}_1} = \frac{(\bar{u}_1^2 + c_1^2) \pm \sqrt{\left[(\bar{u}_1^2 + c_1^2)^2 - 4\bar{u}_1^2 c_2^2\right]}}{2c_2^2} \tag{5.60}$$

5.6 Testing the codes against the analytical solution

Once we have the analytical solution for the Bondi accretion through an ionization front, we can test our codes against it. The analytical solution derived is entirely fixed by specifying the neutral Bondi parameters, ionization front radius and pressure contrast between the neutral ans ionized regions. Similarly, the numerical solution should be entirely determined by the inflow boundary conditions, the mass of the external point mass,the ionization front position and pressure contrast. We start the simulations with a constant density and velocity, and set a constant ionization front radius. As in the previous chapter we use a two temperature approximation. Other general conditions of the simulations are resumed in Table 5.1. We can see on Figure 5.4 that, under these conditions, both codes settled into the derived steady state solution.

Figure 5.4 - Numerical and analytical comparison of the ionized region quantities

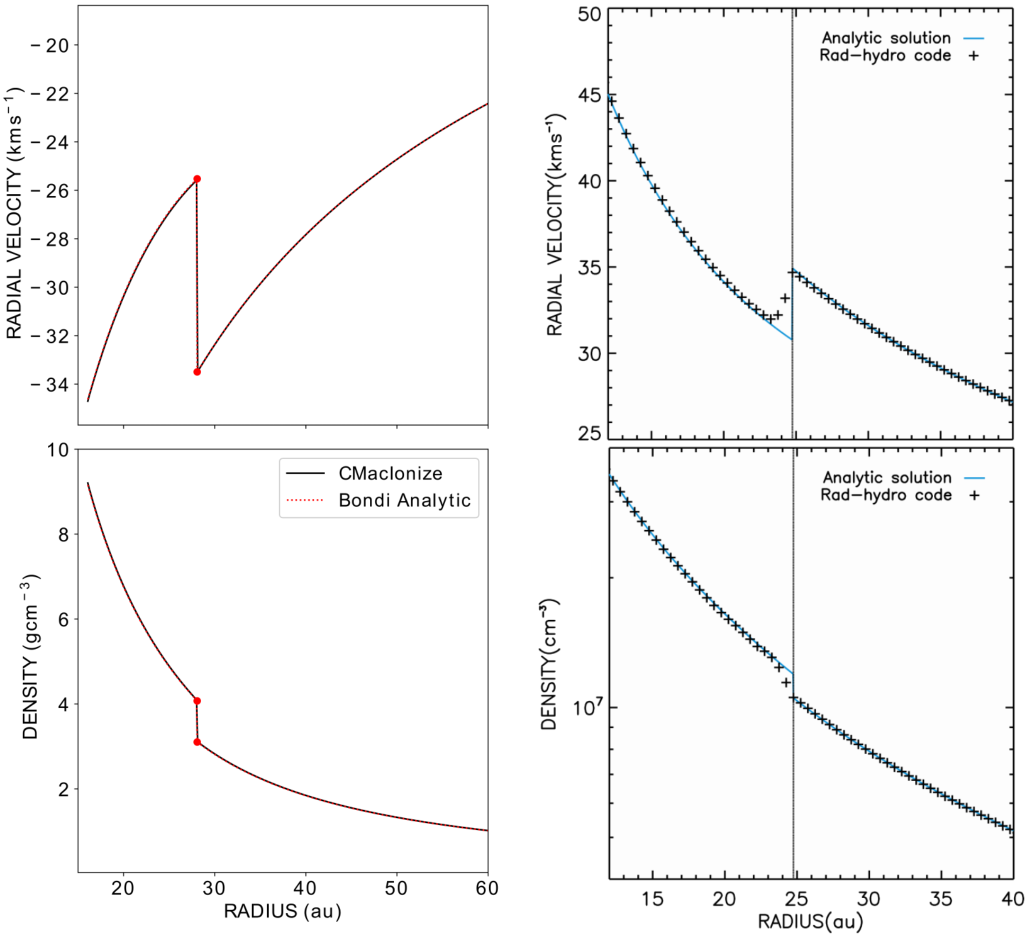

(a) CMacIonize

(b) AMUN + MCRT

(a) Simulation against analytical solution for CMacIonize (VANDENBROUCKE et al., 2019).The ionization front radius is set to the fixed radius $R_{IF} = 30$ au (b)Simulation against analytical solution for AMUN + MCRT (LUND et al., 2019). The ionization front radius is set to the fixed radius $R_{IF} = 24.75$ au

5.7 Stability analysis

The derivation above did not make any assumptions about how the ionization happens, it just assumed ionization leads to a constant ionization radius R_{IF}. However, in general, the ionization radius $R_{IF}(t)$ will vary with time, and the time evolution will be linked to the hydrodynamical quantities, $\rho(r,t)$ and $u(r,t)$. In order to find

Table 5.1 - Initial parameter of the simulations compared with the analytical solution.

Simulation Parameters		
Parameter	CMacIonize	AMUN + MCRT
Dimensions	1D	3D
Resolution	2700 cells for 90 au	128^3 cells for 28 au
$M(M_\odot)$	18	17.87
$\rho\ (g/cm^3)$	10^{-19}	5×10^{-20}
$R_{IF}(au)$	30	24.75
$T_1(K)$	500	500
$T_2(K)$	8000	8000
$Q\ (s^{-1})$	10^{48}	2.5×10^{46}

out if the steady-state solution obtained in Section 5.5 is actually stable, we have to include this effect.

First let us assume that the dynamical time scale t_{dyn} over which the hydrodynamical quantities evolve is much larger than the recombination time scale, $t_{rec} = (n_H \alpha_B)^{-1}$, where n_H is the number density of hydrogen atoms and α_B is the recombining ionizations to the ground state (the so-called on-the-spot approximation). Under this assumption, the ionization structure of the system instantaneously adapts to any change in density, and we can model ionization by simply changing the equation of state. To get the ionization radius R_{IF}, we assume that all material inside the ionization region is completely ionized and the ionization front is a sharp discontinuity. In this case, the ionization balance equation is given by:

$$Q(t) = \frac{4\pi\alpha_B}{m_H^2} \int_{R_\star}^{R_{IF}} \rho^2(r,t) r^2 dr \tag{5.61}$$

Applying the Leibniz rule:

$$\frac{dR_{IF}(t)}{dt} = \frac{1}{\rho^2(R_{IF},t)R_{IF}^2(t)} \left[\frac{m_H^2}{4\pi\alpha_B} \frac{dQ(t)}{dt} - 2\int_{R_\star}^{R_{IF}} \rho(r,t) \frac{\partial \rho(r,t)}{\partial t} r^2 dr \right] \tag{5.62}$$

For what follows, we will assume a constant source luminosity $Q(t)$, and assume we already have a steady state solution as derived in 5.5.

We will now perturb this solution by introducing a small density perturbation outside the ionization radius. As shown by 5.62, this will not affect the ionization radius, and the perturbation will accrete until it reaches the ionization front radius.

Once the perturbation reaches the ionization front and crosses it by a small distance ζ, the ionization front radius will change according to:

$$\frac{dR_{IF}}{dt} = 2\int_{R_{IF}-\zeta}^{R_{IF}} \rho(r,t)\frac{\partial\rho(r,t)}{\partial t} r^2 dr \tag{5.63}$$

since this is the only part of the integral that is non trivial.

This expression does not lend itself to a rigorous linear perturbation analysis because of the presence of an integral in a differential equation, so that, we will restrict ourselves to a semi-analytic analysis below.

What happens next depends on the sign of $\partial\rho(r,t)/\partial t$. If this sign is positive (a positive perturbation), the value of the integral will be positive and the ionization front will move inwards. For a negative perturbation, the ionization front will move outwards.

In either case, the perturbation does not cause a restoring force that balances out the perturbation and restores the initial ionization front radius, as the perturbation will be further accreted inside the ionized region, and will keep contributing to 5.63.

Depending on the size of the perturbation, the ionization radius will either settle into a new dynamic equilibrium value, or will keep moving in the same direction. In the limit of a very large positive perturbation, the ionization front will move with the accreting bump and collapse entirely.

This qualitative behaviour of the ionization front radius constitutes a first important result: the change in ionization front caused by a perturbation cannot be undone while that perturbation is still present inside the ionized region.

The rate at which the ionization radius changes depends on the size and the shape of the perturbation. Once the initial perturbation leaves the ionized region, by accreting onto the star, the situation is nominally reset to the original two temperature situation.

However, since the profile behind the perturbation adjusted to a new ionization radius while the perturbation was still present, the amount of available material to ionize will now no longer match the initial stable two temperature solution. For a positive perturbation, the ionization front will have shrunk and the density will now be too low, while, for a negative perturbation, the reverse will have happened.

We now end up in the opposite scenario of what we started out with: the initially positive perturbation now results in a profile with a negative perturbation, while the initially negative perturbation is now a positive perturbation.

This is a second important result: once a perturbation leaves the ionized region, a new perturbation of opposite sign is created.

The new perturbation of opposite sign has to ensure the ionizing luminosity $Q(t)$ is exactly balanced by recombinations. Since the new perturbation will be created at a larger radius than the original perturbation, and since the traditional Bondi accretion profile for the density scales as $\sim r^{-1.4}$, a larger density perturbation is needed to achieve this.

This leads to the final important result: the newly created perturbation will always be larger than the original perturbation.

In conclusion, any initially small perturbation will lead to an oscillation of the ionization front radius on a time scale of the free fall time (the time a perturbation created at the ionization front needs to reach the inner cut off radius) and with a growing amplitude, until the amplitude is large enough to cause the ionization front to move at the same speed as the perturbation. Physically, there are four interesting scenarios, depending on the sign and the size of the initial perturbation:

a) A large positive perturbation will cause a collapse of the ionization front whereby the ionization front gets trapped inside the perturbation and collapses onto the central star.

b) A small positive perturbation will initially cause a collapse of the ionization front, but the ionization front will move at a slower pace than the accretion velocity of the perturbation. When the perturbation reaches the central cut off radius, the ionization front will go through a phase of expansion, followed by one or more subsequent oscillations with growing ionization front speed, until the ionization front gets trapped inside a perturbation, leading to the collapse of the ionization front.

c) A large negative perturbation will initially cause an expansion of the ionization front until the perturbation reaches the central cut off radius. At this point, a large positive perturbation will form and the ionization front will collapse..

d) A small negative perturbation will initially cause an expansion of the ionization front, followed by multiple oscillations with growing ionization front speed, until the ionization front gets trapped inside a perturbation, leading to the collapse of the ionization front.

In other words, regardless of the size or sign of the perturbation, once it occurs it will eventually lead to the collapse of the H_{II} region, which will repeat itself over the time accretion timescale.

This, indeed, is observed in numerical simulations, an example of which is shown in Figure 5.5. For a full numerical account of the cases above see (VANDENBROUCKE et al., 2019), which analysed all the types of initial perturbation mentioned above.

Figure 5.5 - Stability of ionization front

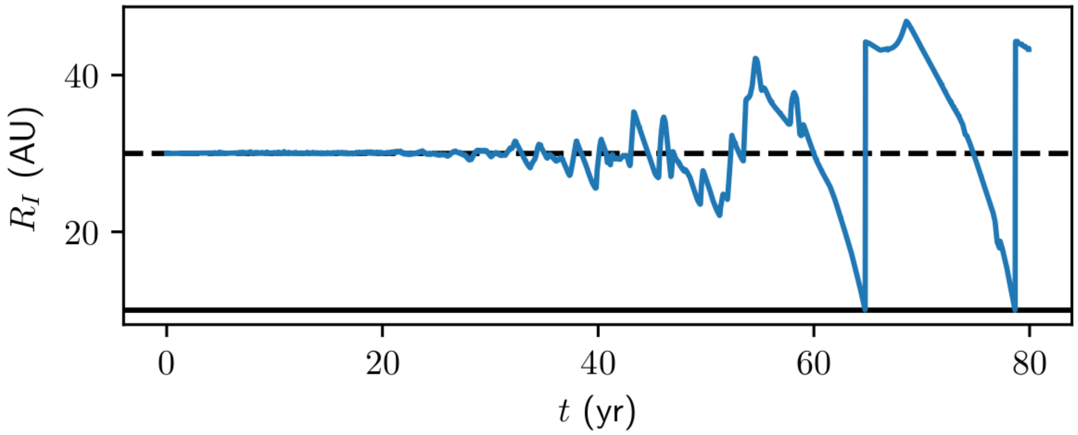

Ionization front radius as a function of time for the stability test run with the radiation hydrodynamics code CMacIonize (VANDENBROUCKE et al., 2019). The dashed horizontal line shows the initial ionization front radius, while the full horizontal line shows the inner outflow boundary radius of the simulation.

6 PHOTOIONIZATION EFFECT ON ACCRETION DISKS OF FORMING MASSIVE STARS

6.1 Introduction

We have seen, in the last chapter, how a massive star may be able to have both an ionized region and yet keep accreting material. We have not, however, discussed why that should be the case. After all, shouldn't a star ionize it's environment only after it starts fusion on its core? And, if a star is already fusing, why should it need to keep on accreting? In this chapter, we are going to first give an introduction to why massive stars require this simultaneity of accretion and ionization processes in Section 6.2. In Section 6.3, that follows, we show why spherical accretion is most likely not the method through which massive stars gain most of their mass. We are going to argue that an accretion via a disk scenario is a more likely configuration for massive star formation, given numerical and observational data from the last decades.We are also going to demonstrate that it is probable that massive stars only form with companion stars. We then present the results of 3D simulations ran with CMacIonize, which mimic a massive star accreting via a disk/torus and the effects that photoionization has on this scenario 6.4. The content presented in this last section has been published in Sartorio et al. (2019).

6.2 Massive Star Formation

A star's life is often thought to initiate once it first starts fusing hydrogen into helium on its core, as a means of stopping it collapsing onto itself due to gravity. After the onset of fusion, the star will enter a fairly stable evolution phase, where it is going to spend most of its life as a “Main Sequence" star.

Young, pre main sequence, stars evolve in different ways, depending on their mass. The evolution of these proto-stars up to the point where they first join the main sequence, known as the Zero Age Main Sequence (ZAMS), is theoretically and observationally fairly well understood and/or empirically tested for low-intermediate mass stars. The situation for more massive stars ($8M_\odot$ or more) is, however, still uncertain. Even basic parameters, such as the time they take to form, have been elusive. A very simple model that may give us a first approximation to the time an over-density might take to collapse into a star is the Kelvin-Helmholtz timescale, t_{KH}. It is simply the time it takes for a body of gas to radiate its gravitational energy away. From the virial theorem, only half the change in gravitational potential energy, δE_g, is available to be radiated away as the protostar contracts; the remaining potential energy supplies the thermal energy that heats up the proto-star's forming interior, thus:

$$t_{KH} = \frac{\delta E_g}{2L} = \frac{GM^2}{2RL} \tag{6.1}$$

Here, L is the luminosity of the proto-star in question. Taking some approximate relations of $L \propto M^{3.2}$ and $R \propto M^{0.6}$, we have that the Kelvin-Helmholtz timescale varies approximately as $t_{KH} \propto M^{-1.8}$. Using the fact that the Kelvin Helmholtz time for a star similar to the sun is of order 10^7 years, we have (assuming a homologous relation exists between stars with different masses) that, for another star of mass M:

$$t_{KH} \approx 10^7 \left(\frac{M}{M_\odot}\right)^{-1.8} \tag{6.2}$$

Figure 6.1 compares this expression for the Kelvin-Helmholtz timescale with the time that it would take a star to accrete its mass at a constant accretion rate of $10^{-3}, 10^{-4}$ or 10^{-5} solar masses per year. The point where an accretion rate line crosses the Kelvin-Helmholtz timescale line can be understood as representing the highest attainable mass (at that accretion rate) of a star before it joins the ZAMS. Thus, we see that, from the lowest to the highest accretion rate, the maximum mass of the stars would be of order 10, 25 and 60 solar masses. Thus, any star more massive than these values would have to accrete after the onset of fusion. Massive stars should, therefore, become truly massive stars after they start shining, evolving along the main sequence while accreting.

Figure 6.1 - Kelvin Helmholtz vs accretion timescale

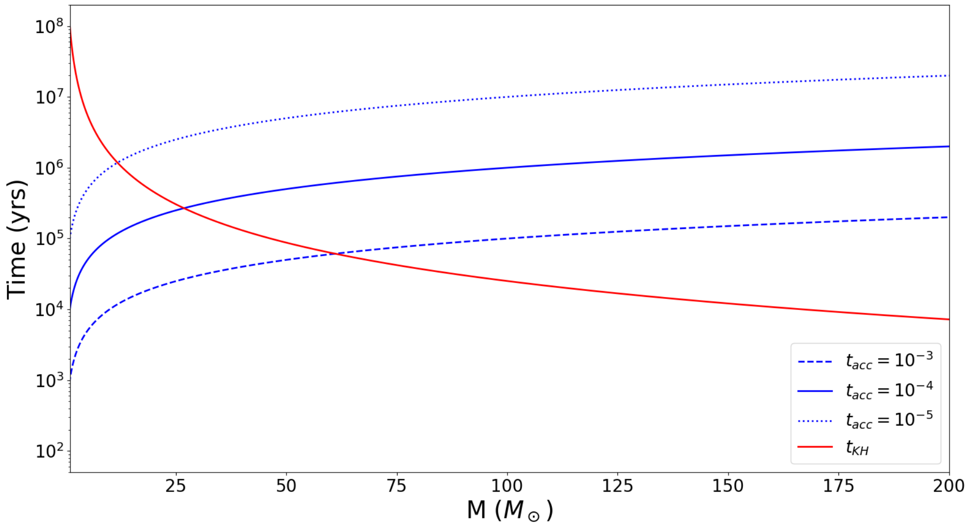

The Kelvin-Helmholtz timescale as a function of mass (red line) and the mass acquired by a body, with negligible initial mass, accreting at a constant rate of 10^{-3}(dashed blue line),10^{-4} (continuous blue line) or 10^{-5} (dotted blue line) solar masses per year.

This fact was first pointed out by Palla e Stahler (1993) and it implies that the stars closer to the upper limit of the IMF have to keep accreting while they are already emitting copious amounts of radiation.

Figure 6.2 - Kelvin-Helmholtz vs accretion time for a stellar evolution model

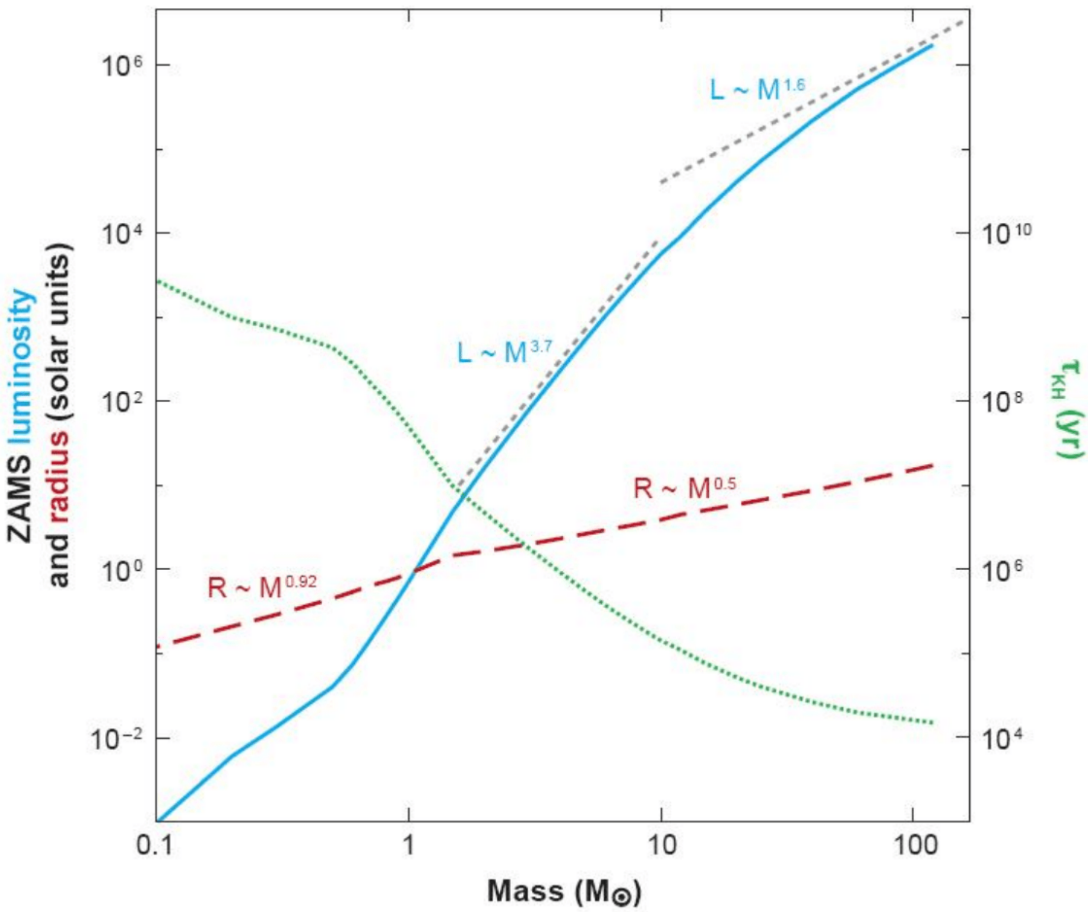

Figure showing the variation of radius and luminosity with protostellar mass, according to a stellar evolution model, and the resulting Kelvin-Helmholtz timescale. As it can be seen, the variation of our simplified Kelvin-Helmholtz timescale has a similar variation with mass for the most massive stars (which are the ones of interest for this study).
source: Zinnecker e yorke (2007)

Clearly, the estimates above are crude and serve only for the purpose of illustrating the problem. However, it turns out that, if you consider more accurate models for proto-stellar evolution (see Figure 6.2), the relation $t_{KH} < t_{acc}$ is still true for the most massive stars. The highest mass achievable at the ZAMS depends on the accretion rates and, thus, varies depending on if these rates are constant (HOSOKAWA; OMUKAI, 2009; HOSOKAWA et al., 2010) or increasing with stellar mass (BEHREND; MAEDER, 2001; HAEMMERLÉ et al., 2013; HAEMMERLÉ et al., 2016) or if accretion takes place in episodic events (MEYER et al., 2017). Regardless of the accretion mode, there is still no model that reproduces the tail of the IMF completely so as to allow for any star to accrete all its mass before joining the ZAMS. Therefore, it is essential that we find a way to conciliate accretion and radiative emission.

6.3 From spherical to disk accretion

If we assume that massive stars originate by accretion and not by other means, such as coalescence of other stars (see Bonnell e Bate (2002)), we have to take into account the effect of radiative emission on the star's surroundings during its formation. As we have seen in the last chapter, a star is indeed able to accrete via a spherically symmetric steady flow and still have an ionized region. The major conceptual problem in massive star formation via a spherically symmetric setting arises from the radiation pressure that massive stars exert on the surrounding dust and not from the photoionization (KAHN, 1974; WOLFIRE; CASSINELLI, 1987). This radiation pressure is sufficiently strong to halt further accretion. Consequently, a star cannot reach a mass higher than about $40 M_{\odot}$, although this mass ceiling depends marginally on the dust properties being invoked (WOLFIRE; CASSINELLI, 1987).

A natural solution to the issues brought up by radiation pressure is to assume that massive stars, as their low mass counterparts, accrete mainly via a disk (see Figure 6.3). This is due to the fact that the impact of radiative pressure strongly depends on the geometry of the accreting gas (NAKANO, 1989). In a spherical scenario, the radiation has no easy path through which it can escape, because all directions have virtually the same optical depth. As a result, radiation pressure is sufficiently high to stop accretion. In contrast, a disk is able to block the flux of UV and visible radiation in its dusty midplane due to the high optical depths. Conversely, polar regions are comparatively rarefied and let the radiation escape. Furthermore, radiation from the disk is re-emitted isotropically and, thus, a large fraction of it also escapes through the poles. This strong anisotropic feature of the thermal radiation field was first investigated in 2D by Yorke e Sonnhalter (2002), who called it the "flashlight effect". Because so much of the radiation escaped through the poles, the pressure on the disk at the midplane is no longer strong enough to reverse the accretion flow and the star may get to much higher masses (KUIPER et al., 2010).

Figure 6.3 - Spherical vs disk accretion models and the radiation pressure problem

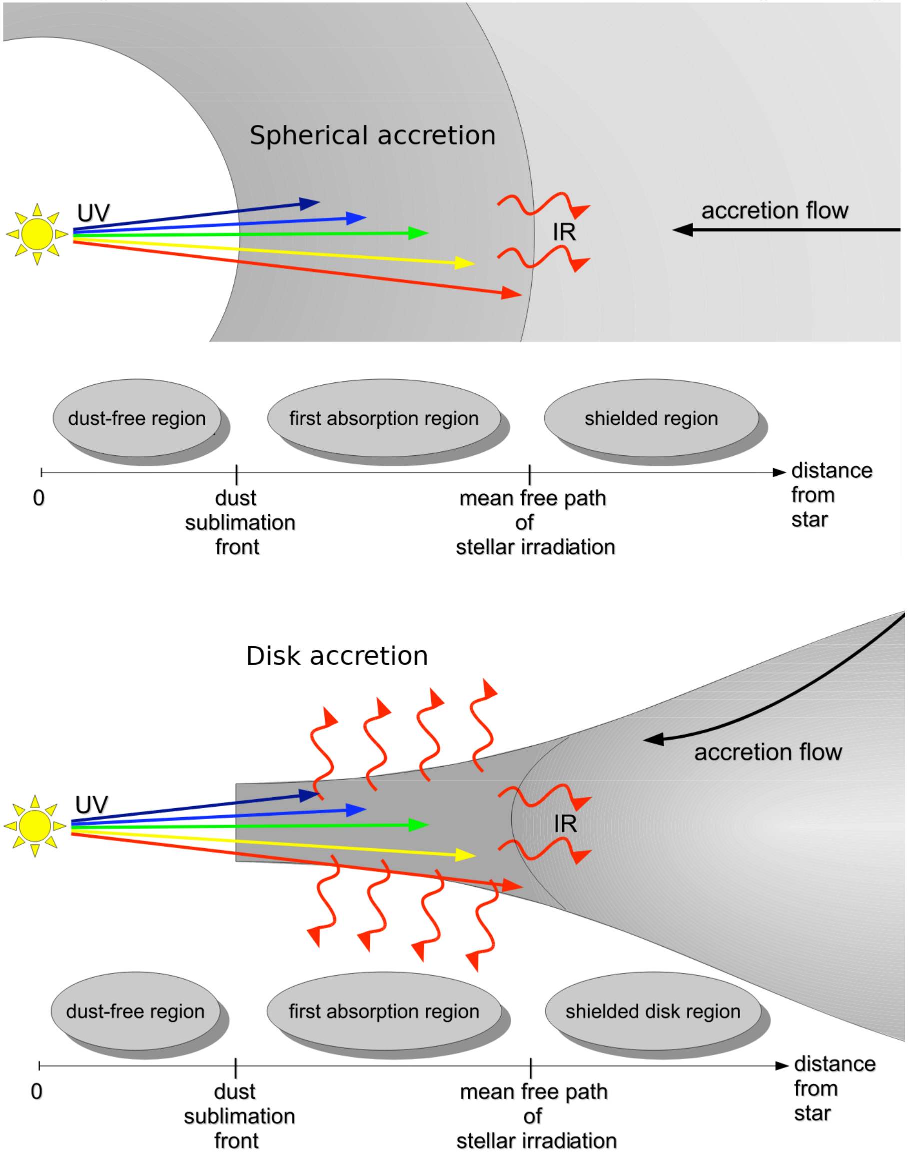

Schematic showing the radiation pressure problem in a spherical scenario (top) and on a disk accretion scenario (bottom). On the former the radiation exerts a strong radiative pressure on the dust, thereby stopping accretion. On the latter radiation can easily escape through the polar regions allowing the accretion to continue.
source: Kuiper et al. (2010)

Other reasons that denote that a disk is to be an expected accretion scenario is that accreting material is likely to have a tangential velocity component, and a disk is a natural mechanism that allows for the redistribution of angular momentum. Indeed, despite differing in the way large scale accretion occurs[1], both models, Core

---

[1] In the core collapse model, the maximum mass of the star is pre-determined by the size of

Accretion (MCKEE; TAN, 2003) and Competitive Accretion (BONNELL; BATE, 2006; BONNELL et al., 2001), seem to agree that accretion onto the protostar probably takes place via a disk (TAN et al., 2014).

Perhaps, however, the most compelling reason to favour disk accretion is the number of observational clues which started to build up in the last decade with the advent of new high resolution observational instruments, such as ALMA. Rotating structures, as disks and tori, have been observed around massive sources. The disks of these stars (early-B and late O-type) have been spatially resolved using line and continuum tracers, spanning wavelengths from the infrared to centimeter (ILEE et al., 2016; ILEE et al., 2018; JOHNSTON et al., 2015; CESARONI et al., 2014; CESARONI et al., 2005; PATEL et al., 2005). It should be noted, however, that current evidence for disks limits itself to stars around or below 30 solar masses (for a review (BELTRÁN; DEWIT, 2016)). Collimated outflows, which are thought to be the interplay of disk dynamics and magnetic fields, were also detected on several occasions in massive young stellar objects (BEUTHER et al., 2002; CODELLA et al., 2012; ZHANG et al., 2005). In the face of this set of data, massive star formation, at least with regards to the mode of accretion, can be seen in broad lines as "scaled up" version of low massive star formation. Clearly, however, massive stars should interact with their disk in a different manner, given the distinct feedback mechanisms at play and their strengths compared to their low mass counterparts.

Regarding the numerical efforts, there are several simulations of massive star formation, but due to the complex nature of the problem, they vary significantly in what Physics is included, usually containing one or more of the following factors: radiation pressure, photoionization, magnetic fields, outflows and stellar evolution models (see for instance (HARRIES et al., 2017; KUIPER; HOSOKAWA, 2018; ROSEN et al., 2016)). These simulations tend to focus on either the effect of one or two physical processes in 3D or they include the impact of many processes, but compromise in resolution and/or make the simulations 2D by assuming additional symmetries for the system. In this chapter, as in the previous one, we choose to focus only on the impact of ionization feedback on a massive star's environment, except now the star is accreting via a disk embedded in a torus. Shortcomings of our approach in the light of other feedback mechanisms that may be relevant to this life stage of a massive star (winds, jets, outflows, radiation pressure) are discussed at the end of

---

the parent clump, whereas in competitive accretion a number of stars form simultaneously in a common gravitational potential and stars located at the bottom of the potential can have much higher accretion rates.

the chapter.

In this simplified scenario of only photoionization feedback, Keto (2007) predicted the existence of three stages in the evolution of an ionized region in an accretion disk scenario: a fully trapped H_{II} region (similar to the ones considered in the last chapter), an H_{II} region trapped in the torus, but not in the poles, and an H_{II} region in expansion everywhere (see Figure 6.4).

Figure 6.4 - H_{II} region evolution around an accretion disk

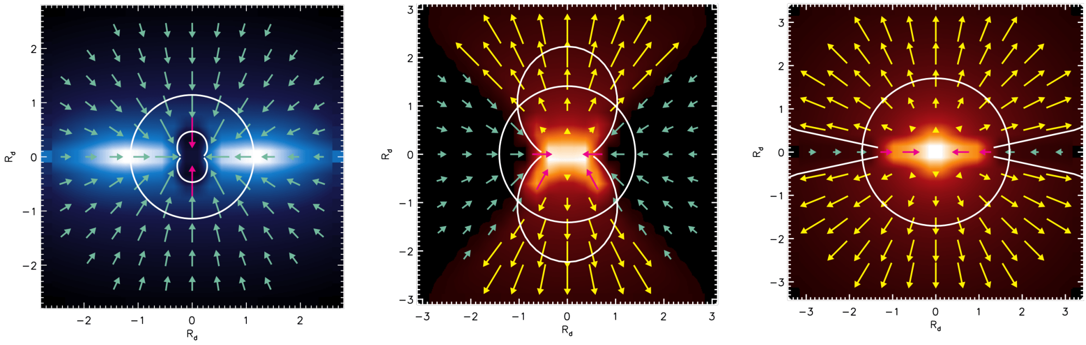

Fig. 1*a*

Fig. 1*b*

Fig. 1*c*

Schematic showing the different stages of an H_{II} region varying according to Keto (2007), from where this figure is. The white circle illustrates the largest radius at which an ionized region can be trapped by gravity. From the left to the right and as the star increases in ionizing luminosity: (1a) a fully trapped H_{II} region, (1b) an ionized region trapped at the disk, but not at the poles and (1c), as in the previous figure, but a higher luminosity causes a larger region being in pressure expansion and a smaller region being trapped. source: Keto (2007)

The H_{II} region would progress from one scenario to the next, as its central source gets more massive and starts emitting larger amounts of ionizing radiation, resulting in new regions entering the pressure expansion phase. We aim here to simulate this scenario and assert if and under which conditions trapped H_{II} regions can be expected.

6.4 3D simulation of accretion disks

In this section we present the results of 3D simulations of massive stars accreting via a disk while emitting ionizing radiation. We first lay out the methodology in Subsection 6.4.1. We then present the main results obtained in Subsection 6.4.2. Finally we discuss the results and their limitations in 6.4.3.

6.4.1 Method

The simulations are performed using the publicly available code CMacIonize[2] (VANDENBROUCKE; WOOD, 2018b). It uses a standard finite-volume method for the hydrodynamics with an HLLC Riemann solver and is coupled to a Monte Carlo radiation transfer module, similar to the one employed in (WOOD et al., 2004).

We use a static 3D cartesian grid with resolutions ranging from 64^3 to 256^3 cells to model an accretion torus around a star, for a range of stellar masses and ionizing luminosities. Both mass and luminosity are kept constant at any one simulation. This should not pose a problem, as the timescales for the development and evolution of the HII regions in these simulations are far shorter than the timescales in which the stellar properties change.

The size of our cubic simulation box is taken to be 0.1 pc, which is the same order of magnitude of the rotating cores seen around massive stars (BELTRÁN; DEWIT, 2016), but we can rescale the length unit of the simulation if required (see subsubsection 6.4.1.2). The boundaries of the simulation box were set to be open so material can flow in and out of the box. Gravity from the star is modelled through a source term in the momentum equation, as an external point mass located at the centre of the simulation box. In order to avoid numerical issues caused by the diverging gravitational force at small radii, as well as Cartesian grid induced boundary effects, we apply an inner spherical mask with a radius of 0.01 pc, corresponding to 10% of our box size in length. Within this masked region, we do not solve the hydrodynamics, meaning that material that flows into the mask is no longer tracked. Boundary conditions at the mask are set to inflow, but no specific conditions are set to be satisfied at the mask radius, such that it doesn't have any dynamical effects on the rest of the simulation box. Because we do not follow the material within the mask, we also do not account for the ionizing luminosity absorbed by the masked material. Therefore, the luminosity used in each of our simulations is simply a fraction of the true luminosity emitted by the star. We do, however, compute a luminosity correction (see subsubsection 6.4.1.7), which allows us to estimate the full luminosities emitted by the stars in our simulations.

We perform the simulations with an isothermal equation of state. Simulations are split in two types: hydrodynamical only (HD) simulations and simulations with both hydrodynamics and ionizing radiation (RHD). HD simulations start from a very

---

[2] `https://github.com/bwvdnbro/CMacIonize`

general initial setup, which is outlined in detail in subsubsection 6.4.1.1 and are let to evolve freely for 50,000 years in order to obtain a stable accretion scenario. The resulting accretion structure consists of a torus and models what we expect to find around a star that has just started emitting ionizing radiation. The torus may vary in shape and density, depending on the initial parameters. We discuss the impact that each of the input parameters has on the structure later, in the results section. Once a stable accretion structure is attained, the output of the HD simulation is used as the initial conditions for the RHD runs.

In the RHD runs, the mass at the centre also acts as a point source that emits ionizing photons isotropically. The photons can be either absorbed by the gas or re-emitted until they leave the grid (for more details see (VANDENBROUCKE; WOOD, 2018b)). The ionizing luminosities are set based on the expected value for the mass found at the centre of the simulation box. For simplicity, throughout the chapter, we use only ‘luminosity’ to refer to the ‘ionizing luminosity’, unless specified otherwise. At each Monte Carlo timestep, we emit 10^6 ionizing photon packets from the central source and iterate ten times to obtain sufficiently converged ionization fractions for each cell. The two temperature approximation, introduced in Chapter 4, is used: fully ionized gas has a temperature $T_i = 8,000$ K, whereas fully neutral gas has a temperature $T_n = 500$ K, see Lund et al. (2019). Partially ionized gas temperatures are calculated as a linear combination of the two cases based on the actual ionization fraction of a cell.

6.4.1.1 Initial setup

Recall the expression for the Bondi radius, R_B, is:

$$R_B = \frac{GM_\star}{2c_s^2}, \tag{6.3}$$

with G being the gravitational constant, $M_\star$ the mass of the star and c_s the sound speed, which itself is given by:

$$c_s = \sqrt{\frac{kT}{\mu_m m_p}}, \tag{6.4}$$

where k is Boltzmann’s constant, m_p is the proton mass and μ_m the mean molecular weight of the gas, such that $\mu_m = 1$ for fully neutral hydrogen and $\mu_m = 0.5$ for fully ionized hydrogen. Thus, our sound speed has a specific range of values under the two temperature approximation:

$$\sqrt{\frac{kT_n}{m_p}} \approx 2.0 \text{ km/s } < c_s < 12.8 \text{ km/s } \approx \sqrt{\frac{kT_i}{0.5m_p}} \tag{6.5}$$

The values for the density and tangential velocity are set as a function of their value at the Bondi radius, ρ_B and v_B:

$$\rho(r) = \rho_B \left(\frac{R_B}{r}\right)^{1.5} \tag{6.6}$$

and

$$\mathbf{v}(r) = v_B \left(\frac{R_B}{r}\right)^{0.5} \mathbf{e}_\theta, \tag{6.7}$$

Where $\mathbf{e}_\theta$ is the tangential unit vector in cylindrical coordinates:

$$\mathbf{e}_\theta = -\frac{y}{R}\mathbf{e}_x + \frac{x}{R}\mathbf{e}_y, \tag{6.8}$$

with $R = \sqrt{x^2 + y^2}$ the cylindrical radius.

The Bondi density, for a Bondi accretion scenario, is related to the density at infinity through the following relation:

$$\rho_B = \rho_\infty e^{3/2} \approx 4.48\rho_\infty \tag{6.9}$$

Assuming that, on scales larger than the size of our simulation box, the accretion flow is Bondi-like, the density at infinity would be representative of the density of the interstellar medium.

The tangential velocity has the same radial dependence as the keplerian velocity, defined as:

$$v_K = \left(\frac{GM_\star}{r}\right)^{0.5} \tag{6.10}$$

The keplerian velocity at the Bondi radius is simply:

$$v_B = \left(\frac{GM_\star}{R_B}\right)^{0.5} = \sqrt{2}c_s \tag{6.11}$$

and thus independent of the star's mass. For convenience, we start the hydrodynamical simulations with keplerian velocities at each cylindrical radius.

6.4.1.2 Hydrodynamics

Recollect that the hydrodynamic equations of conservation of mass and momentum for an isothermal equation of state, neglecting self-gravity of the accreting gas are:

$$\frac{\partial \rho}{\partial t} + \boldsymbol{\nabla}(\rho \mathbf{v}) = 0, \tag{6.12}$$

$$\frac{\partial \mathbf{v}}{\partial t} + \mathbf{v} \cdot \boldsymbol{\nabla} \mathbf{v} + \frac{c_s^2}{\rho} \boldsymbol{\nabla}(\rho) + \frac{G M_\star}{r^2} \mathbf{e}_r = 0, \tag{6.13}$$

where ρ, $\mathbf{v}$, t and r are the density, the velocity, the time and the distance, respectively, and $\mathbf{e}_r$ is the radial unit vector. One interesting aspect of the equations above is that they are scale invariant in density. In other words, we could multiply the density by any constant factor and this would not alter the qualitative results we get. Therefore, once we run a simulation for a star of a certain mass, we already have all the simulations for any value of the initial parameter ρ_B we might have chosen.

The HD runs are also scale invariant under the ratio $M_\star/r$. Suppose we were to re-scale in space and time, such that r becomes Cr and such that t becomes Ct, where C is a constant re-scaling factor. Then, the mass and momentum equation become:

$$C\left(\frac{\partial \rho}{\partial t} + \boldsymbol{\nabla}(\rho \mathbf{v})\right) = 0 \tag{6.14}$$

$$C\left(\frac{\partial \mathbf{v}}{\partial t} + \mathbf{v} \cdot \boldsymbol{\nabla} \mathbf{v} + \frac{c_s^2}{\rho} \boldsymbol{\nabla}(\rho) + \frac{C G M_\star}{r^2} \mathbf{e}_r\right) = 0 \tag{6.15}$$

Note that, if the mass of central star in the simulation were to be C times larger ($M_\star^{new} = C M_\star^{old}$), then the equations would not differ from our initial ones. This implies that simulations done in a simulation box of size L and stellar mass $M_\star$ will appear identical to one done with a box of size CL with stellar mass $CM_\star$, with the caveat that the latter will evolve a factor of C faster.

In other words, the accretion structures formed in simulations with higher central masses have the same density and velocity profiles we would expect to see in the smaller inner regions of simulations of a lower mass star. This re-scaling can be demonstrated to work numerically by re-scaling simulations with different masses and showing that the re-scaled hydrodynamical quantities follow a common profile.

This is done later in this section, in 6.4.1.4. However, it should be noted that this is only true if self-gravity is not included.

6.4.1.3 Radiation hydrodynamics

In the simulations that include radiation, in addition to the hydrodynamical equations, we need to take into account the balance between photoionization and radiative recombination, which is given by the photoionizing equilibrium equation:

$$Q_H(\star) = \frac{\alpha_A}{m_H^2} \int (1 - x_H(\mathbf{x}))^2 \rho^2(\mathbf{x}) dV, \tag{6.16}$$

where $Q_H(\star)$ is the photoionizing luminosity of the star (which, for each simulation, is considered a constant), α_A is the (constant) recombination rate to all excited states of hydrogen, m_H is the mass of hydrogen and x_H the neutral fraction of hydrogen and the integral is computed over the entire volume of the simulation box.

The recombination rate we use is given by the fit by Verner e Ferland (1996) which, for a temperature of 8000 K used in this work, is $\alpha_A = 4.896 \times 10^{-13}\text{cm}^3\ \text{s}^{-1}$. The diffuse radiation field is also taken into account by tracking the photons that are absorbed and re-emitted as ionizing ones. Photons recombine to the ground state at a recombination rate of $\alpha_1 = 1.773 \times 10^{-13}\text{cm}^3\text{s}^{-1}$ and thus the probability of a photon being re-emitted as an ionizing photon is $P_R = \alpha_1/\alpha_A \approx 0.36$.

We can obtain the volume that will be ionized for a given photoionizing luminosity by assuming a sharp transition from a completely ionized ($x_H = 0$) to a completely neutral ($x_H = 1$) gas, and by realizing that diffuse re-emission boosts the photoionizing luminosity with an additional factor $\frac{1}{1-P_R}$, such that the photoionizing equilibrium equation becomes:

$$Q_H(\star) = \frac{\alpha_B}{m_H^2} \int_{S_0}^{S_I} \rho^2(\mathbf{x}) dV, \tag{6.17}$$

where S_0 represents the inner boundary of the ionized volume, S_I represents the ionization front (which can have an arbitrary shape) and $\alpha_B = \alpha_A(1-P_R) = \alpha_A - \alpha_1$ is the total radiative recombination rate to all levels above the ground state (i.e., the total radiative recombination rate to levels 2 and higher).

Here, unlike in the HD runs, a particular density has to be chosen, as this will determine the number of recombinations occurring and, thus, the impact a certain luminosity will have on the torus. However, the RHD simulations are scale invariant

Table 6.1 - All these simulations are equivalent according to the scaling relation. Thus, we can model smaller radii within the masked regions by considering simulations of larger and larger masses

Scaling factor C	Central Mass ($M_\odot$)	Length
0.1	10	0.1 L
1	100	1 L
10	1000	10 L

Table 6.2 - Re-scaling factors that need to be applied for the different hydrodynamical variables of the simulations.

Quantity	Units	Re-scaling
Length	[L]	$\mathrm{L} \longrightarrow \mathrm{CL}$
Mass	[M]	$\mathrm{M} \longrightarrow \mathrm{CM}$
Time	[T]	$\mathrm{T} \longrightarrow \mathrm{CT}$
Density	$[\mathrm{M}]/[\mathrm{L}]^3$	$\rho \longleftrightarrow \rho/C^2$
Velocity	[L]/[T]	$\mathrm{v} \longrightarrow \mathrm{v}$
Angular Velocity	1/[T]	$\Omega \longrightarrow \Omega/C$

in the ratio ρ^2/Q_H, as the numerator determines the number of recombinations and the denominator the number of ionizations per unit time.

6.4.1.4 Testing the scalability

In Section 6.4.1.2, we have shown analytically that the length and mass units can be re-scaled such that there is no change to the hydrodynamical evolution of the system. We explore this in this chapter as a way of using one simulation to represent a number of different scenarios. We can see from Table 6.1 that a simulation with a central mass of 100 solar masses can be re-scaled to either represent the smaller scales of a simulation with a central mass of ten solar masses or to represent larger scale of a thousand solar mass simulation.

Clearly, re-scaling implies that the units of length, mass and time have changed and, therefore, the hydrodynamical properties need to change accordingly, as specified in Table 6.2

An alternative way to see this is by investigating the units for the hydrodynamical quantities and how they link to the simulation parameters. The velocity unit immediately links to the sound speed of the gas and hence its temperature, which we assume constant for all simulations. This means that the length unit and time unit will have a fixed ratio for all simulations. The mass unit of the system is clearly set by the choice of central point mass M. Once the mass and sound speed are chosen, the Bondi radius is also unequivocally fixed. In principle, this should fix the density unit, but, since the solution of the hydrodynamical equations does not depend on the density (as explained in subsubsection 6.4.1.2), this is not the case. Thus, we use a constant ρ_B, which defines the density at the Bondi radius, in order to fix the density. The only parameter left to choose is the box size, which will determine which part of the underlying general solution we sample.

As a result, we expect all simulations to have a general profile for each of the hydrodynamical quantities, which can be expressed in terms of Bondi units (Bondi radius, Bondi density, etc) and that can then be adjusted to represent any desired set of values.

In order to prove that this is indeed applicable numerically, we have re-scaled the simulations in order to show that a universal profile exists for each hydrodynamical quantity, as shown in Figure 6.5 . The description of the re-scaling procedure for each quantity is laid out below.

6.4.1.4.1 Width of the torus

We define the torus within our simulations to have a certain thickness based on where the majority of the gas within the simulation is concentrated. In order to compute the width of the torus, we plot a density profile from a simulation slice (perpendicular to the torus plane) for each radius from the central point mass. We, then, fit a Gaussian to the profile and define the material that represents the torus to be the material that lies in between the half maxima points. One such density slice with the Gaussian fitting is illustrated in Figure 6.6.

Figure 6.5 - Proof of scalability of the simulations

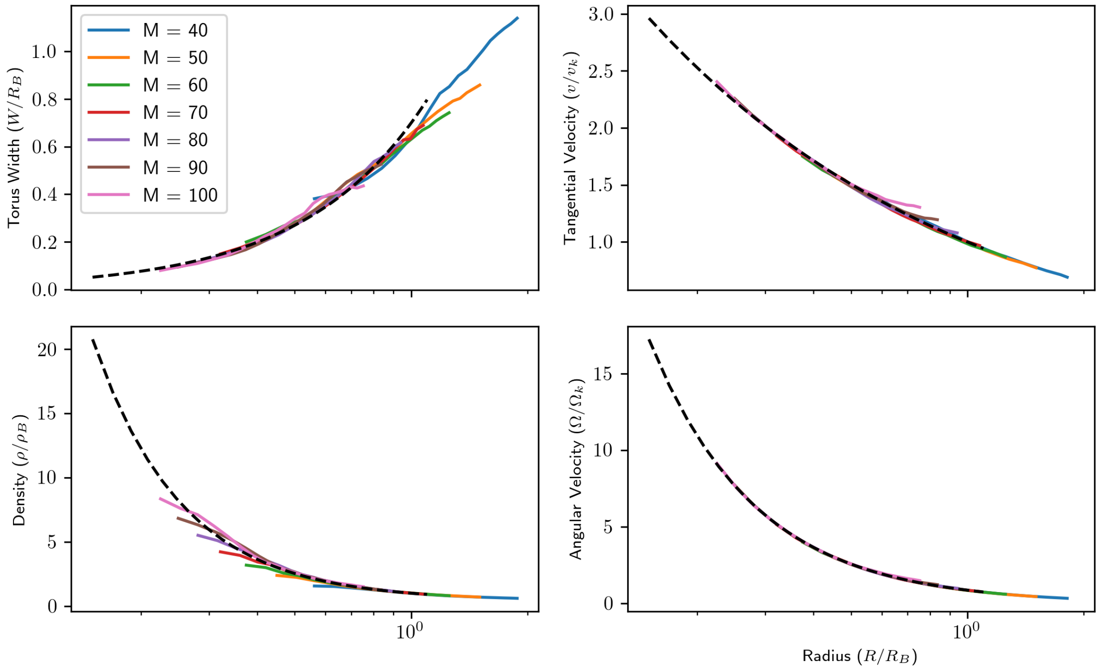

Basic hydrodynamical quantities re-scaled to Bondi units to show the existence of a common profile. The panels show, from top to bottom and left to right: the width of the torus, the density at the torus plane, the tangential velocity in respect to the keplerian velocity and the angular velocity in respect to the keplerian angular velocity. Every simulation had identical initial conditions, except for the mass, which is indicated by the colors: 40 $M_\odot$ (blue), 50 $M_\odot$ (yellow), 60 $M_\odot$ (green), 70 $M_\odot$ (red), 80 $M_\odot$ (purple), 90 $M_\odot$ (brown), 100 $M_\odot$ (pink). Power laws were fitted to each profile and are shown as dashed lines.

Figure 6.6 - Disk thickness measurement

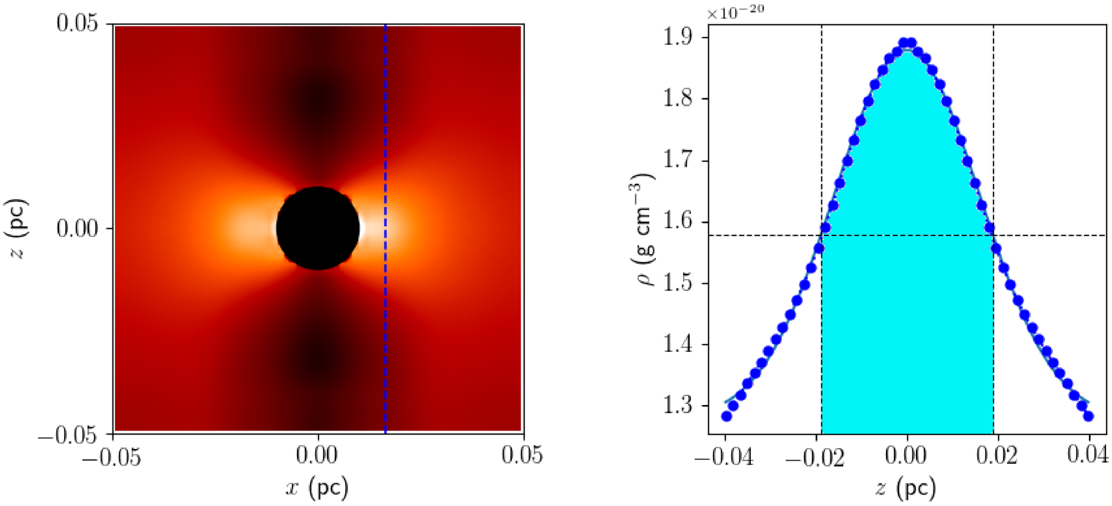

Left: A density plot of a simulation of a 35 solar mass star. The blue line shows the slice used for the density profile. *Right*: The density profile of the slice (blue dots) and the corresponding Gaussian fit (blue line). The dashed lines show the value for the half maximum and the heights (z) in the disk at which it occurs. The shaded light blue region shows the region that we consider to compose the torus.

This procedure is repeated for every simulation. These simulations are then re-scaled according to Table 6.1 and expressed in terms of Bondi units to show that their profile is the same. Finally, we fit a power law $y = c \times x^m$ to obtain an expression for the general profile. The final fitted parameters for the power law were $m = 1.51, c = 0.79$. In order to obtain the physical values for any particular simulation, we can simply multiply both the radius and the width of the torus by the Bondi radius of that particular simulation.

6.4.1.4.2 Density

Similarly to the torus width, we first re-scale the simulations in terms of the Bondi radius. The density values are then divided by the Bondi density found for this particular re-scaling, such that $\rho_{(r=R_B)} = 1$. Recall that the density can be re-scaled by a constant factor at will. By doing that, we obtain a universal profile to which we fit a power law $y = c \times x^m + c_0$, with parameters $m = -1.88, c = 0.57, c_0 = 0.43$. In order to adjust the profile to a particular simulation, we multiply the radius, R, by the desired Bondi radius R_B and the density by the correction factor, ρ_{corr}:

$$\rho_{corr} = \frac{1}{M^2 \rho_B} \tag{6.18}$$

6.4.1.4.3 Tangential and angular velocity

As discussed earlier in this section, the velocity does not change with the re-scaling of the simulations, as both the time and length units are re-scaled by the same factor. The angular velocity, however, does require re-scaling as it has units of inverse time. We divide each velocity and angular velocity value by their keplerian counterpart ($v_K = \sqrt{GM/R}$ and $\Omega = v_K/R$). The values are then expressed in Bondi units such that at the Bondi radius the values for the velocity and angular velocity equal one. We then fit a power law, as it was done for the density, to the obtained profiles. The fitting values obtained for the angular velocity, Ω, $m = -1.58, c = 0.99, c_0 = 0.01$ and for the tangential velocity, v, $m = -0.52, c = 1.17, c_0 = -0.17$.

The correction back to SI units is done by multiplying either simulation by their bondi counterparts:

$$v_{corr} = v_B = \sqrt{2} c_s \tag{6.19}$$

$$\Omega_{corr} = \Omega_B = \frac{\sqrt{2}c_s}{R_B} \tag{6.20}$$

6.4.1.5 Toomre Q calculation

As the models we are currently studying do not include self gravity, in order to have a consistent accretion scenario we need to check if we expect fragmentation to occur within the torus. Given a thin accretion disk, we can assess its local stability against fragmentation by calculating the Toomre Q parameter (TOOMRE, 1964), defined as:

$$Q = \frac{c_s \kappa}{\pi G \Sigma}, \tag{6.21}$$

where κ is the epicyclic frequency $\left(\kappa = \sqrt{r\frac{d\Omega^2}{dr} + 4\Omega^2}\right)$ and Σ is the surface density of our disk. In simple terms, the numerator of the Toomre parameter is representative of the thermal (c_s) and rotational (Ω) energies, whereas the denominator is representative of the gravitational energy. For instability, gravity must be dominant both over the rotational and the thermal energy. Thus, for $Q \gg 1$, the disk is stabilized by rotation and will not collapse, while for $Q \lesssim 1$ the disk is likely to fragment. Note that, as we use an isothermal equation of state, the value c_s is fixed for the HD simulations, and, thus, the thermal support is constant with radius. The rotational support, in contrast, is larger for smaller radii where the angular velocity is higher. Therefore, the stability of the disk is directly linked to the relative rate of increase in density and velocities as we approach smaller radii, such that we have two cases: 1) if the rate of increase in angular velocity is larger than the rate of increase in density, the rotational support increases more than linearly to the gravitational destabilizing effect, meaning that the torus would become more stable for smaller radii; 2) if the density increases more than linearly to the angular velocity, the torus gets more unstable for smaller radii. From our universal profiles obtained in the last subsubsection, we can see that, for our simulation, the second case applies and our disk will be more unstable with smaller radii. In order to determine if our simulations are or are not unstable, we require estimates for a disk surface density. Because the Toomre Q parameter only applies to a thin disk, for any point in the disk the scale height has to be much smaller than the radius. We use a height as 0.01 of the radius, which gives us the same error in the calculation of the Q parameter for every radius. The surface density $\Sigma = 0.01R \times \rho$, with both R and ρ being expressed in Bondi units. We compute the ratio $Q_B = \Omega/\Sigma$ in Bondi units based on the general profiles obtained in the last section in order to obtain a universal profile for the Toomre Q parameter shown in Figure 6.7. The Toomre Q in Bondi units (Q_B) is related to the true Toomre Q of any simulation by the following expression:

$$Q = \frac{c_s}{\pi G} * Q_B * F_{conv}, \tag{6.22}$$

where F_{conv} is the conversion factor to SI units defined as:

$$\begin{aligned} F_{conv} =& \frac{\Omega_{corr}}{\Sigma_{corr}} \qquad (6.23) \\ =& \left[\frac{\sqrt{2}c_s}{R_B}\right] \times \left[\frac{1}{M^2 \rho_B R_B}\right] \qquad (6.24) \\ =& \frac{\sqrt{2}c_s}{M^2 \rho_B R_B^2} \qquad (6.25) \end{aligned}$$

Figure 6.7 - Scale free Toomre Q

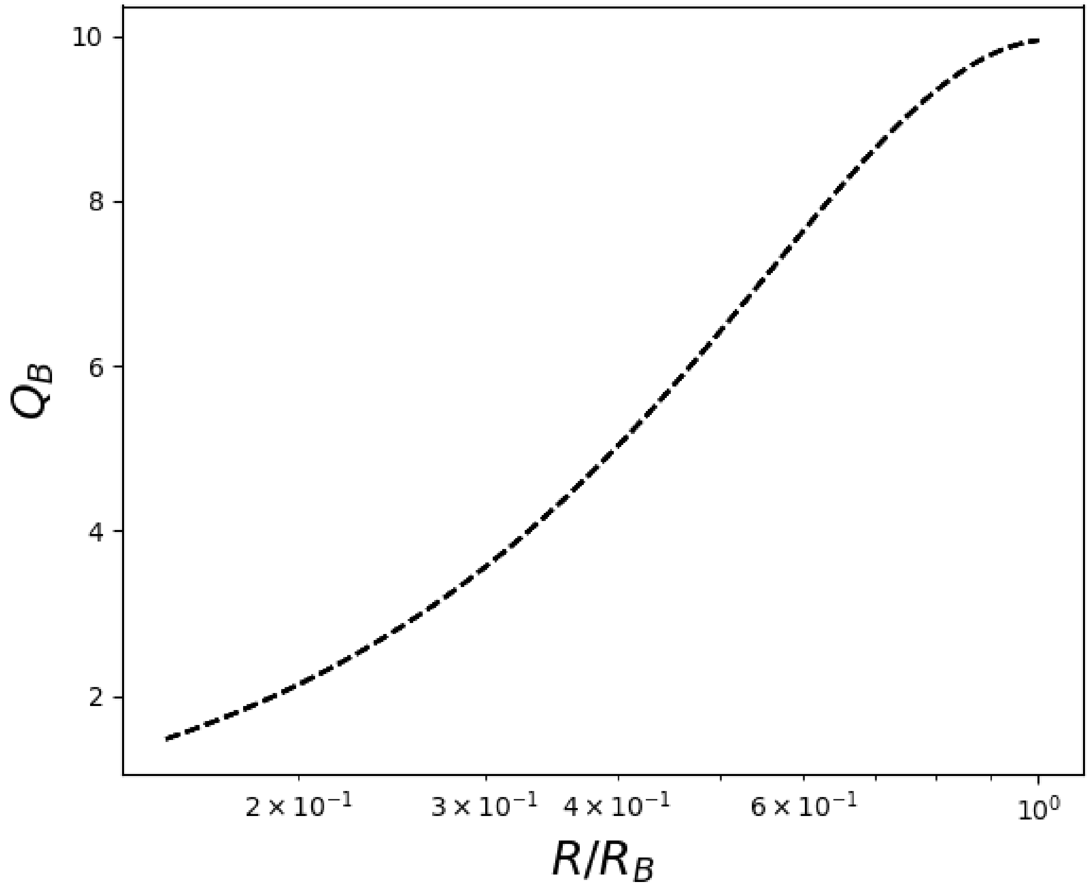

The profile for the Q_B in Bondi units, which can be re-scaled to find the Toomre Q profile of any simulation

Clearly the value of Q is going to differ significantly, depending on which densities and masses are considered, as illustrated in Figure 6.8. Nevertheless, the general trend is that the torus becomes more unstable for smaller radii.

Figure 6.8 - Toomre values for different masses.

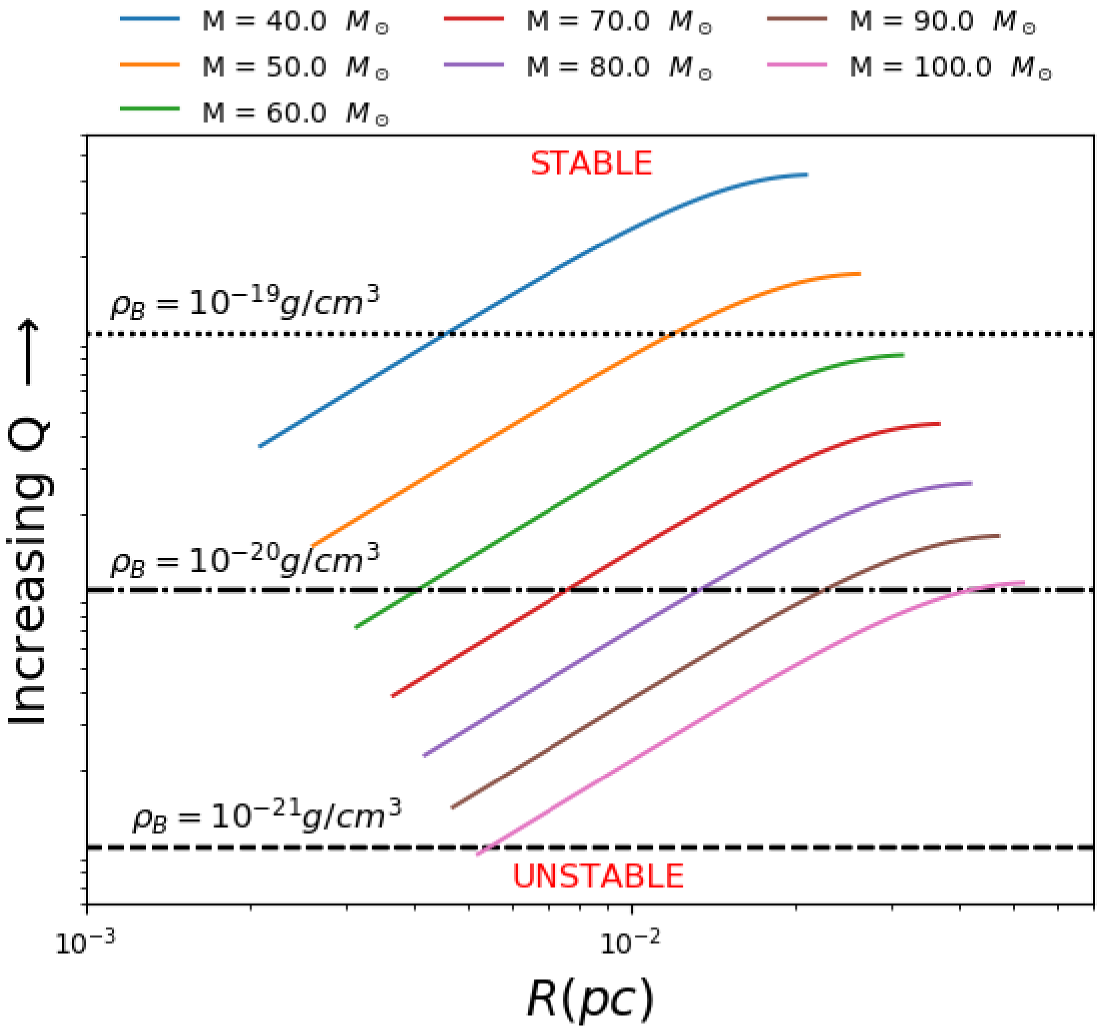

The colors associated with each mass are as in Figure 6.5. The horizontal lines show where $Q = 1$ for different Bondi densities. Anything below a particular horizontal line is Toomre unstable and anything above is Toomre stable.

6.4.1.6 Convergence

We ran the simulations at three different resolutions: 64^3, 128^3 and 256^3 cells. We found that, for most of the simulations, the three resolutions present little difference when compared to one another, as can be seen in Figure 6.9. The simulations in the remainder of this work have a resolution of 256^3. We do not consider using a higher resolution as this would demand too much computational time to run all required models and would make little difference to the qualitative results obtained.

Figure 6.9 - Convergence Test

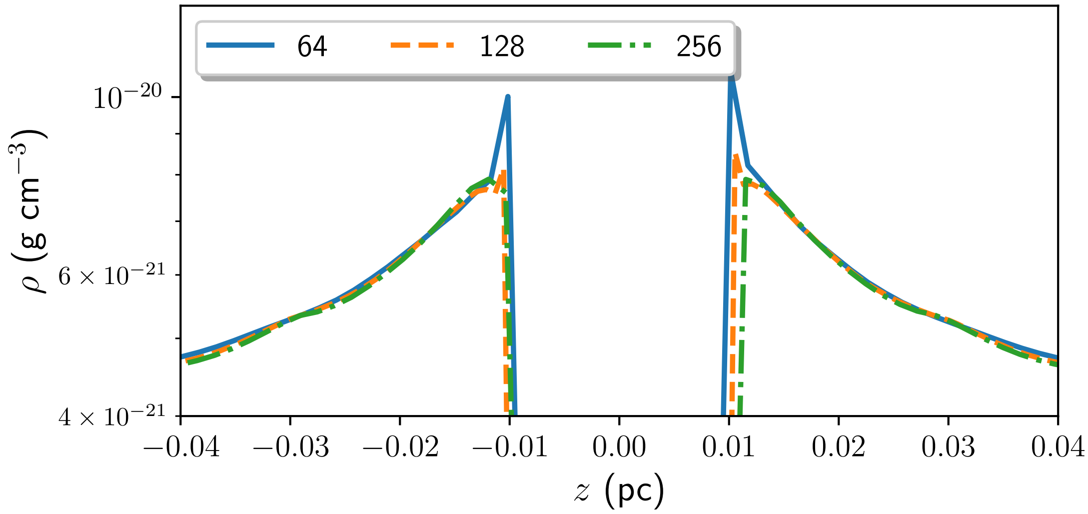

The density profile of for a 20 solar mass star through the torus axis for three different resolutions (64^3, 128^3 and 256^3 cells). The result for the two highest resolutions are clearly converged. The small difference at 0.01 pc is due to the fact our masked region has an integer number of cells which makes its edge slightly different for the three resolutions.

6.4.1.7 Ionizing luminosity correction

Our simulations use an internal mask of radius 0.01 pc. For the RHD runs, the region inside the mask is assumed to be ionized and, therefore, no radiation is absorbed. Therefore, the true luminosity of our central source is the value we set in the simulation plus an offset due to the number of photons we expect to have been absorbed inside our masked region.

In order to have an estimate of how much radiation has been absorbed within the masked region, we make use of the homology of the hydrodynamic simulations as discussed in 6.4.1.2. We can use the profiles obtained in Figure 6.5 to model the density and and shape of the torus for any simulation for the radii smaller than the one used for our mask. Given these values we can estimate the luminosity absorbed within the mask.

The homology implies that, for a specific choice of realization with density $\rho(\mathbf{x}) = \rho_B \rho'(\mathbf{x}')$, the ratio

$$Q_{H_B} = \frac{m_H^2 Q_H(\star)}{\alpha_B \rho_B^2 M_\star^4 R_B^3} = \int_{S_0'}^{S_I'} \rho'^2(\mathbf{x}') dV', \tag{6.26}$$

will be independent of that specific choice of realization of the general density profile, where all quantities in the integral have been replaced with their corresponding Bondi unit counterparts. To find a general expression for the Bondi luminosity that is absorbed within some sphere with radius S'_M (the radius of the mask in Bondi units), we will assume that this absorption can be reasonably approximated by absorption of the torus, with the width and density profiles following the fitted power-laws in 6.4.1.4. Assuming cylindrical symmetry, the Bondi luminosity is then:

$$Q_{H_B} = 2\pi \int_{r'_0}^{r'_M} \rho'^2(r')h'(r')r'dr' = 2\pi \left(f({r'}_M) - f({r'}_0)\right), \quad (6.27)$$

with

$$f(r') = f_0(r') + f_1(r') + f_2(r'), \quad (6.28)$$

$$f_0(r') = \frac{h_n}{h_e + 2\rho_e + 2}(r')^{h_e+2\rho_e+2}, \quad (6.29)$$

$$f_1(r') = \frac{2h_n\rho_0}{h_e + \rho_e + 2}(r')^{h_e+\rho_e+2}, \quad (6.30)$$

$$f_2(r') = \frac{h_n\rho_0^2}{h_e + 2}(r')^{h_e+2}, \quad (6.31)$$

6.4.2 Results

6.4.2.1 Hydrodynamical simulations

We first ran a number of HD simulations in order to obtain a torus to be used as initial conditions for the RHD runs. In these runs, the gravitational contraction in directions normal to the set rotation is halted by centrifugal forces, leading to a natural flattening of the system into a torus and to a rarefaction of the polar regions. Parameter space has been explored by changing the mass of the central star and the tangential velocity (keplerian, sub and super keplerian). Here we analyse how each of these affects the final torus structure.

6.4.2.1.1 Changing mass

Due to the larger gravitational force, larger central masses lead to higher centrifugal speeds at any given radius. In turn, this leads to a stronger flattening of the torus, making the torus thinner and denser. This is illustrated by Figure 6.10 where we plot the Gaussian fitting used to estimate the surface density of the torus for distinct stellar masses.

Figure 6.10 - Gaussian fit for the density for distinct masses

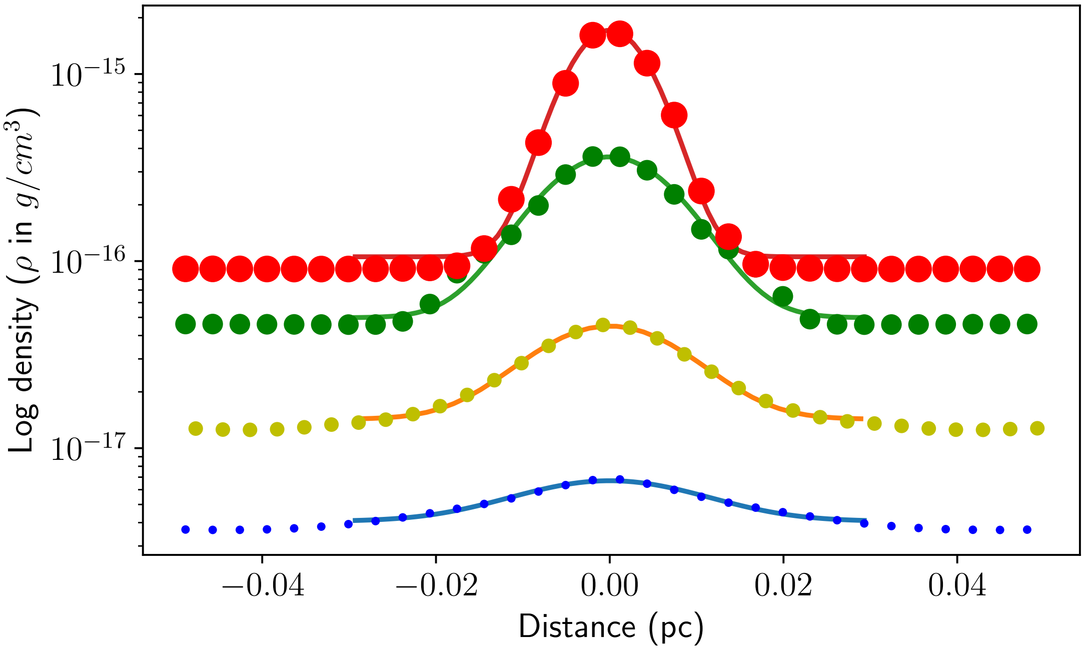

The Gaussian fit (as in Figure 6.6) for simulations with different central masses (20, 40, 60 and 80 solar masses). The dots are weighted according to the stars mass and show the simulation data, while the lines correspond to the fitted Gaussian. We can clearly see that as the mass increases the fitted Gaussian gets narrower and peaked at higher values indicative of a thinner, denser torus

Another effect is that polar regions become more rarefied. We quantify this by the parameter $\eta(x) = \rho_{\text{Torus}}(r = x)/\rho_{\text{Polar}}(z = x)$, where x is the distance from the central point mass. The value of $\rho_{\text{Torus}}(r)$ at each x is obtained by averaging the value of the density at a certain radius in the midplane of the torus $r = x$. For the $\rho_{\text{Polar}}(z)$ we average the densities along the torus normal at distance $|z = x|$ from the central point mass. We characterize the density contrast for the entire box with a single value $\eta = \langle \eta(x) \rangle$ obtained by averaging all the values $\eta(x)$ for x values ranging from just above the mask radius to the half the box size.

The values found are shown in Figure 6.11. The density contrast increases with mass and can be as low as $\eta = 2$ for a central mass of 10 solar masses and as high as $\eta = 16$ for the case with 80 solar masses.

Figure 6.11 - Ratio of polar to disk densities depending on mass

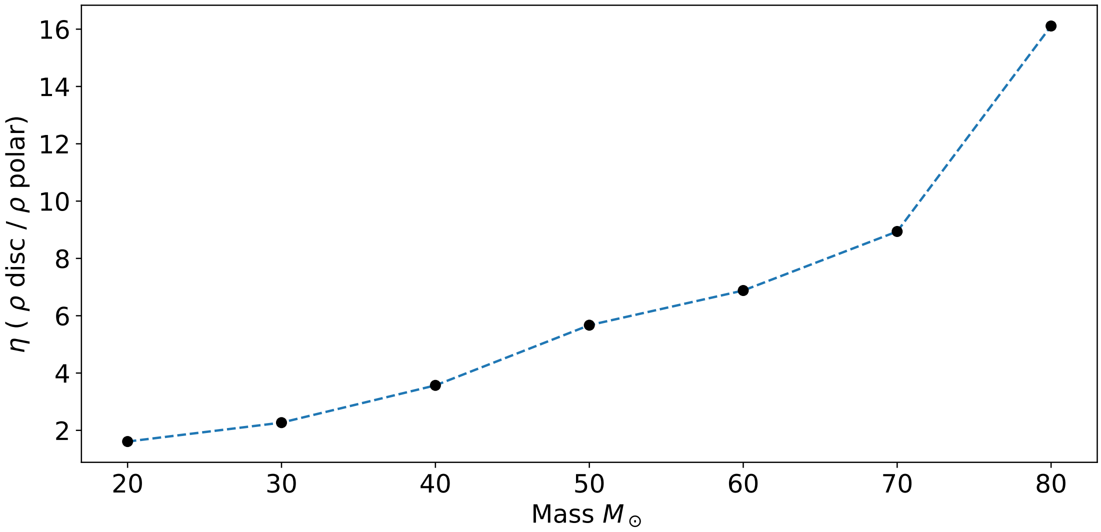

The evolution in the ratio of the torus and polar densities for different central masses. For lower masses the torus is only a couple of times denser than the polar regions. For higher masses the differences in density exceed an order of magnitude.

6.4.2.1.2 Changing tangential velocity

Throughout the simulations we use keplerian velocities as an initial condition for our torus. Since in the HD simulations the medium is completely neutral, the temperature of the gas is 500K, making the keplerian velocity at the Bondi radius 2.8 km s^{-1}. Using velocities lower than the keplerian velocity leads to a thicker, less dense torus whereas super-keplerian velocities lead to the opposite effect.

6.4.2.2 Radiation hydrodynamics simulations

The results of the RHD simulations can be broadly divided into three categories:

a) Fully trapped H_{II} region

b) H_{II} region trapped in the torus midplane but in pressure driven expansion in the polar axis

c) H_{II} region in pressure expansion at all axis

These are shown in Figures 6.12, 6.13 and 6.14, respectively. The outcome of each simulation is naturally dependant on the values of the density, which will regulate the recombination rate, and the luminosity, which will determine the number of hydrogen atoms being ionized (see Eq.6.17). The simulation results will also depend on the difference in density between the torus plane and the polar axis quantified by η. If η is close to one, there is no path through which the photons can escape more easily and a roughly spherical H_{II} region forms around the star. This is seen in simulations for stars around 10 solar masses or lower (Figure 6.12).

Figure 6.12 - Uniformly fully trapped H_{II} regions

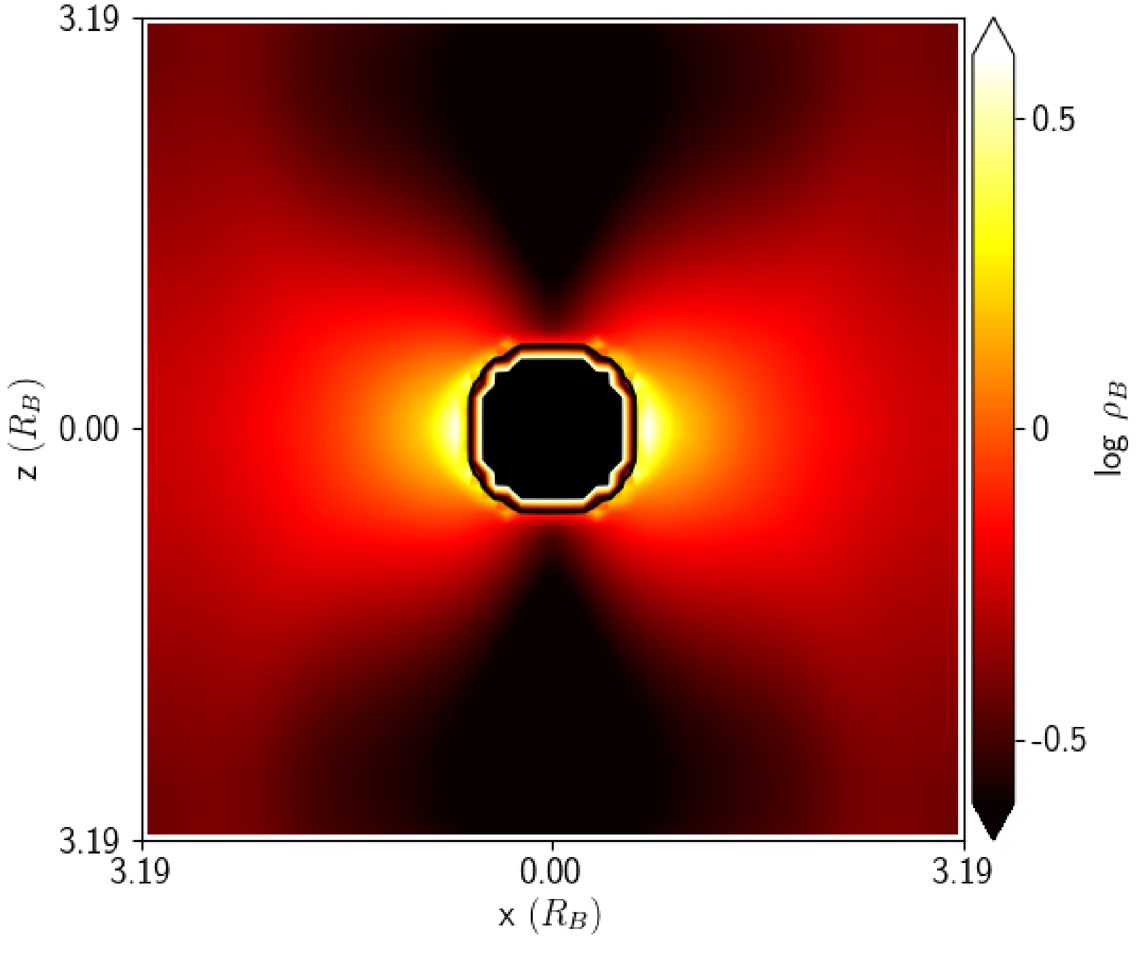

Density slice for a Bondi luminosity of 2.13×10^{-3}. The ionization contours are shown in yellow (75% ionized), red (50% ionized) and black (25% ionized). We can see from the ionization contours that the H_{II} region is completely trapped and almost spherical in shape.

For more massive stars the η parameter is larger, indicating that the photons will find more resistance when travelling in the torus midplane in comparison to the polar axis. As a result the polar regions get ionized to much larger radii than the torus; leading to a roughly hourglass shaped H_{II} region (see Figure 6.13).

Figure 6.13 - Hourglass fully trapped H_{II} regions

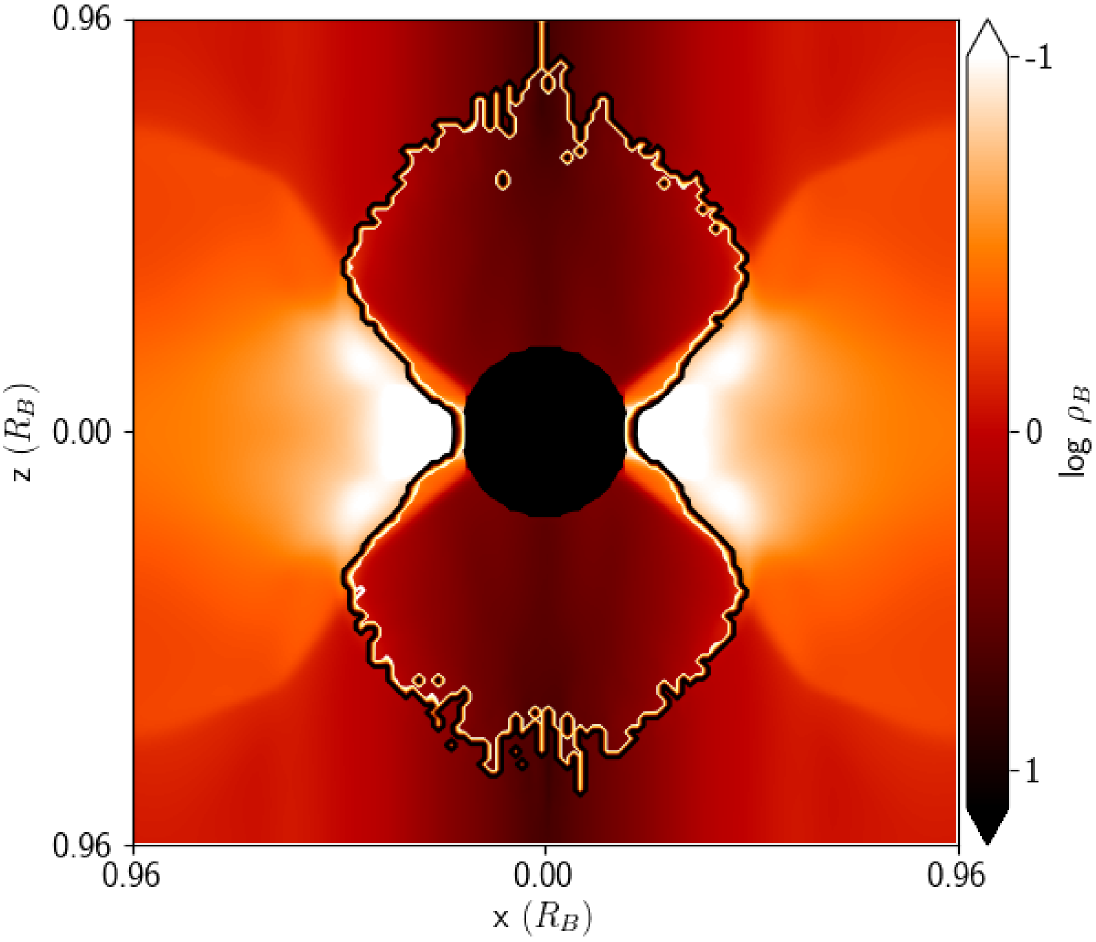

Density plot of a slice of an RHD simulation with a Bondi luminosity of 0.273. The contour lines show different ionization fractions (0.75, 0.5 and 0.25 for yellow, red and black respectively). Due to the reduced density the H_{II} region expands farther in the poles than in the torus, giving the ionized region an hourglass shape. The H_{II} region is not smooth due to the noise in the Monte Carlo method.

Because of this difference in density and consequently the extent of the H_{II} region we can expect that the transition from a trapped to an expanding ionized region will also happen distinctly in different directions. If we assume, as in the spherical scenario, that transition to the expansion phase happens at some critical radius, then some parts of the H_{II} region will enter the expansion phase before others.

Let the critical luminosity Q_H^{C} be the luminosity that is just large enough to ionize out to this critical radius. Owing to the fact that the density is different in different directions in our simulations, there will be a different critical luminosity for each direction. The lowest critical luminosity, $Q_H^{\mathrm{C_L}}$, is the one that will lead to an expanding ionized region at the line of lowest density: the polar axis. Conversely, the line of highest density through the torus midplane, will be hardest to fully ionize and will have the highest critical luminosity $Q_H^{\mathrm{C_H}}$. Whenever the set luminosity in the simulation in between these two extremes, $Q_H^{\mathrm{C_L}} < Q_H < Q_H^{\mathrm{C_H}}$, the resulting scenario will be a trapped H_{II} region in the torus plane and an expanding one at the poles (Figure 6.14). Because the ionizing luminosity is proportional to the density squared the range of values for which this scenario occurs also depends on the η parameter:

$$\frac{Q_H^{\mathrm{C_H}}}{Q_H^{\mathrm{C_L}}} \propto \left(\frac{\rho_{\mathrm{torus}}}{\rho_{\mathrm{Polar}}}\right)^2 \sim \eta^2 \tag{6.32}$$

From Figure 6.11 we can see that a larger stellar mass implies a larger value of η. As a result, the luminosity range that leads to case (ii) will increase with mass too.

Figure 6.14 - H_{II} region trapped on the disk plane only

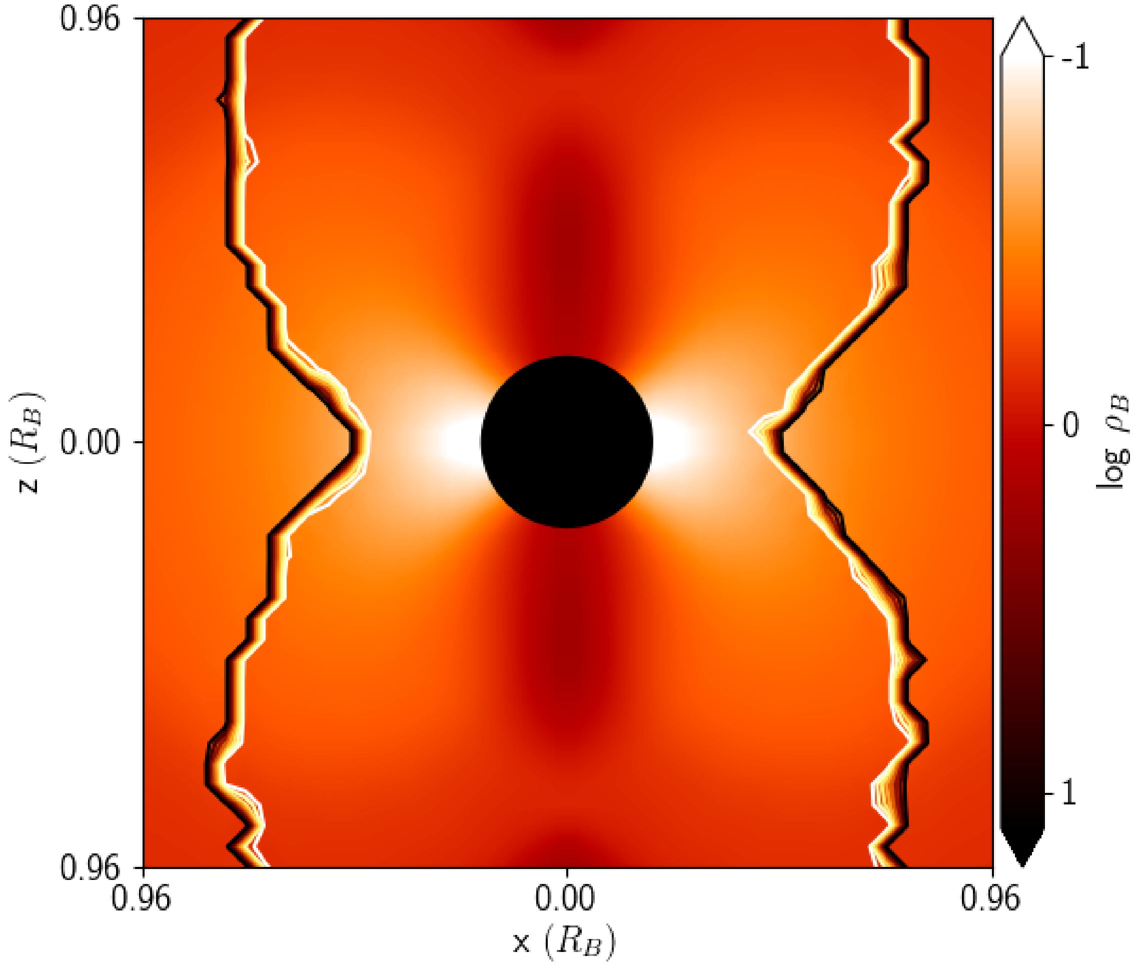

A 100 solar mass star simulation with luminosity of 2.73. Black, red and yellow contour lines are indicative of regions where 25%, 50% and 75% of the gas is ionized, respectively. As it can be seen, the H_{II} region is trapped in the torus plane but the polar regions, due to their much lower densities, have been completely ionized and have undergone pressure driven expansion.

Finally, there is the case where the luminosity is large enough to ionize both polar and torus axis out to a radius larger than their critical radii ($Q_H > Q_H^{\mathrm{C_H}}$), creating an expanding ionized bubble (Figure 6.15). One could, therefore, think of our three possible scenarios presented above as a natural evolution of the system. As the mass and, consequently, the ionizing luminosity increase, an initially fully trapped H_{II} region could get progressively larger, until it enters the expansion phase at the poles. The star would stop accreting through the poles but accretion would continue through the torus plane. Luminosity will continue rising until the star emits enough

Figure 6.15 - D-type expansion

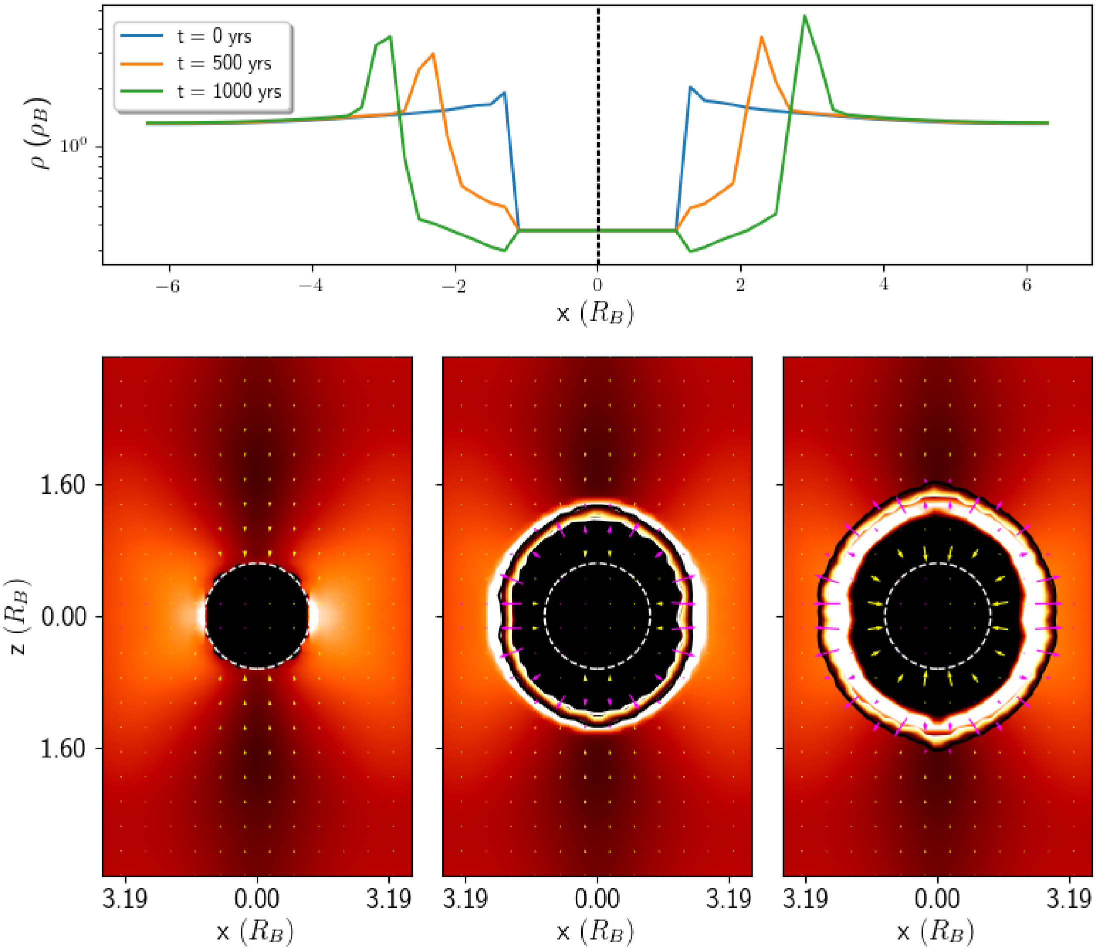

Top: Torus density profiles at different times showing the evolution of an expanding H_{II} region with Bondi luminosity 2.73. *Bottom*: Density slices of the simulation in the top panel. Degrees of ionization are shown by the black, red and yellow lines as in Figure 6.14. Pink and yellow arrows show outflows and inflows respectively. The whole H_{II} region is ionized past the critical radius and enters the expansion phase. In the last snapshot we can observe that the inside of the H_{II} region is drained as material inside the ionized region accretes to the star, but no more material traverses the ionization front.

luminosity to ionize the torus beyond the critical radius. This would halt accretion completely, setting the final mass of the star.

6.4.3 Discussion

As it was said in the introduction, massive stars need to be able to continue accreting after the onset of fusion, which leads to the emission of copious amounts of ionizing radiation. It is therefore essential that H_{II} regions remain trapped for timescales long enough to allow the required mass build up to occur. In respect to the factors under consideration in our simulation, the ability to trap the H_{II} region is going to depend on the following:

- Critical radius – set by the value of the central point mass
- Ionizing Luminosity – set by the source(s) at the centre
- Torus Density – set by the initial density and velocity and by the central point mass

In the rest of the section we discuss how the trapping of the H_{II} region might occur in light of our results as well as discussing limitations of our approach to the problem.

6.4.3.1 Luminosity Corrections

The results presented assume that the ionizing radiation incoming from the mask is isotropically emitted from its centre. Furthermore, the luminosity escaping the mask must be only a fraction of the one emitted by the star. We can, however, correct our luminosities using the method described in 6.4.1.7 which is based on the profiles obtained for the torus width and the density.

6.4.3.1.1 Testing the correction

In order to test this luminosity correction we first perform a mock correction to a known value. The scalability implies that for rescaled simulations, the size of the mask is inversely proportional to the mass. Thus, we may verify if we can reproduce the critical luminosity values obtained by a high mass (M_{large}) simulation by correcting the luminosity absorbed between its rescaled mask radius and the rescaled masked radius of an otherwise identical lower mass simulation, M_{small}:

$$Q_{HB}^{C_H}(M_{large}) = Q_{HB}^{C_H}(M_{small}) + 2\pi \int_{R_{Mask}(M_{large})}^{R_{Mask}(M_{small})} \rho^2 h r dr \tag{6.33}$$

Table 6.3 - Critical luminosities for different masses. These values are not corrected to account for luminosity absorbed within the mask.

Mass of Central Star ($M_\odot$)	Log of Critical Luminosity (s^{-1})
40	44
50	44.5
60	45
70	46
80	47
90	48.5
100	50

We use the the critical luminosity for expansion in the midplane $Q_{HB}^{C_H}$ for the $100M_\odot$ as a proxy and compare it to the critical values of simulations from 40 to 90 solar masses corrected for the radiation absorbed in the region between the re-scaled masked radii. The values we use for the critical luminosity are the lowest luminosity value which caused the midplane of the disk to enter pressure driven expansion for a simulation of a particular mass. The original values (before re-scaling) are laid out in Table 6.3 for reference, all for simulations with $\rho_B = 1 \times 10^{-20}$.

The test correction is illustrated in Figure 6.16. The top figure shows the relative size of the correction between the different simulations in Bondi units. The bottom plot shows the corrected value obtained for the critical luminosities. Should our values of the critical luminosity and corrections be exact, all critical luminosities should be the same. However, with the exception of the 90 and 80 solar mass simulations, the critical values obtained are larger than the expected value. This indicates that our correction provides an upper limit for the critical values. In other words, simulations for which the ionized region in the torus is in pressure driven expansion for our corrected simulations would also be in pressure driven expansion for a simulation run with a much smaller mask.

Figure 6.16 - Luminosity corrections

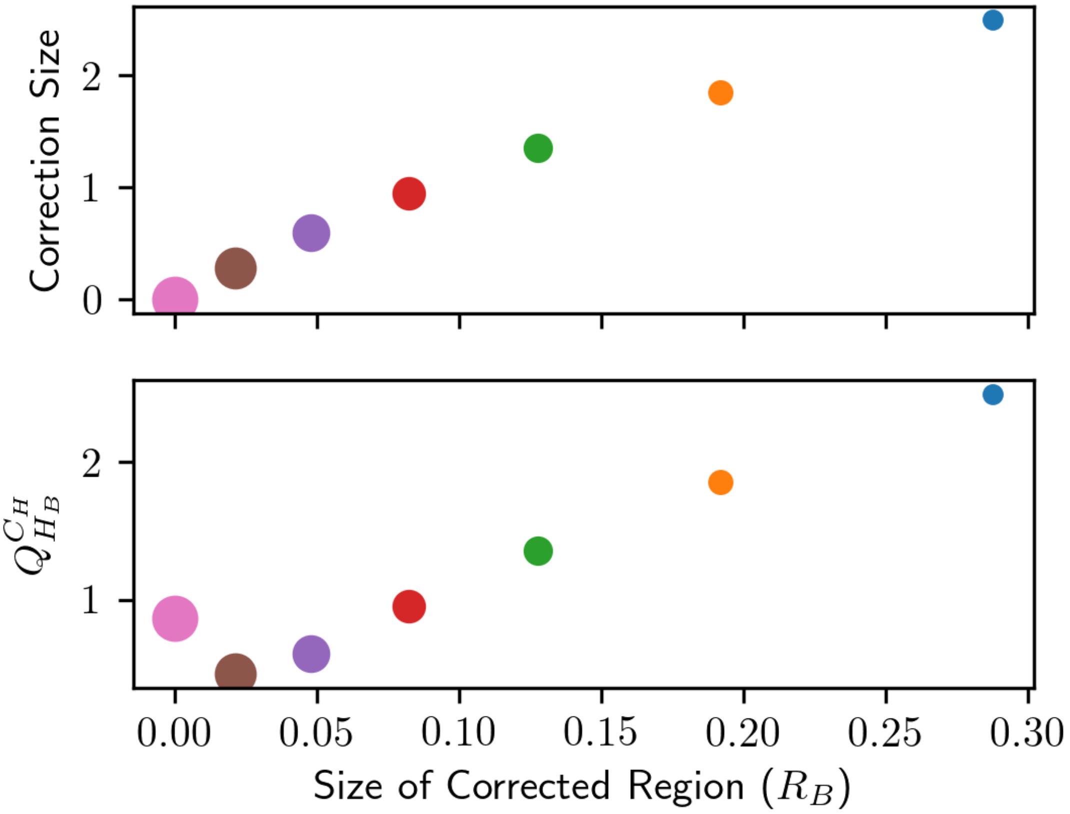

Top: Correction in Bondi luminosites for different masses as a function of the size of the corrected region (equivalent to the difference in radii of the re-scaled mask for the simulation in question and that of the 100 solar mass simulation). Colors are the same as in Figures 6.5 and 6.8 the and dot's size is scaled according to the mass it represents. By definition the correction to the 100 solar mass simulation is zero. *Bottom*: Critical Bondi luminosities for the 100 solar mass (uncorrected) and lower mass simulations (corrected to include radiation absorption from radii above the mask of the 100 solar mass simulation)

Hence, even though we cannot claim the sizes of the H_{II} region would be the same as the ones in our simulations, we are able to find an upper limit in the transition between the trapped and expanding scenarios within the torus midplane. Therefore, we can obtain an upper limit on the maximum luminosity a star can have while still being able to sustain an accretion disk from which it can keep accreting mass.

6.4.3.1.2 Luminosity comparison to models

We are interested in analysing which scenarios would create a suitable environment for a massive star to continue accreting via a disk given the large amount of ionizing radiation it emits. With that aim we correct the critical luminosity values obtained in our simulations to a radius of 1×10^{-4}pc and compare these values with ionizing luminosities given by stellar evolution models. This radius for the correction was chosen because all our simulations, except one, are unstable at this radius, such that all calculations of luminosities are overestimates of the true value. Here we use estimates of the true ionizing luminosities of massive stars which were obtained from the stellar evolution model of Sternberg et al. (2003). The values for the critical luminosities for different densities (dashed lines) plotted against model luminosities (continuous green line) are found in Figure 6.17. For Bondi densities of $\rho_B = 10^{-19}$g cm^{-3} and larger, we can expect the H_{II} region to always be trapped in the midplane. For Bondi densities of $\rho_B = 10^{-21}$g cm^{-3} and smaller we can expect the H_{II} region to be in expansion. For intermediate Bondi densities, $10^{-21} \leq \rho_B \leq 10^{-19}$g cm^{-3}, the H_{II} region starts expanding within the midplane for some particular mass.

6.4.3.2 Stability via multiplicity

As explained in the last subsubsection, the fate of the torus and H_{II} region is strongly dependant on the density. One aspect that might be of importance to the analysis of the disk resistance against the ionizing radiation is the stability of the disk itself. In Figure 6.18 we plot the radius at which we expect fragmentation to start taking place which is based on the data already shown in Figure 6.8. We can see that for a number of scenarios studied we expect fragmentation to occur.

Figure 6.17 - Limiting luminosities

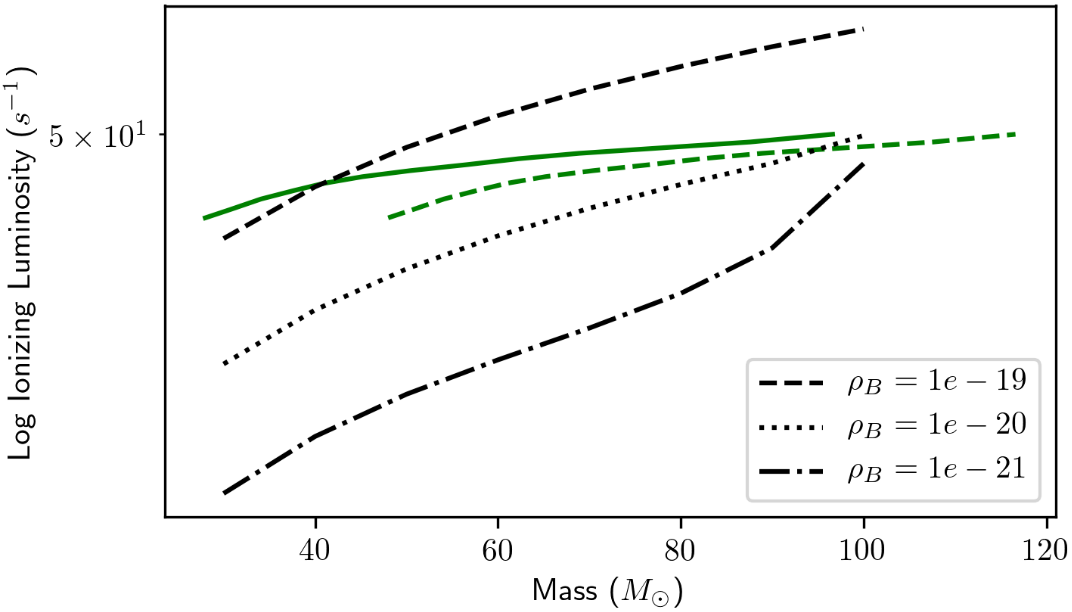

Dashed lines: critical luminosities for trapping H_{II} regions in the torus plane for different Bondi densities. Continuous green line: the expected luminosities for a each stellar mass according to the stellar model of Sternberg et al. (2003). If the expected values are above the critical luminosity the H_{II} region will enter the pressure expansion phase in the disk axis. Dashed green line: mimics the effect of having a massive star emitting at the expected values but also having companion stars with a combined mass of 20 solar masses. We can see that for this line the number of cases for which the H_{II} region is trapped increases

Figure 6.18 - Toomre unstable disk regions

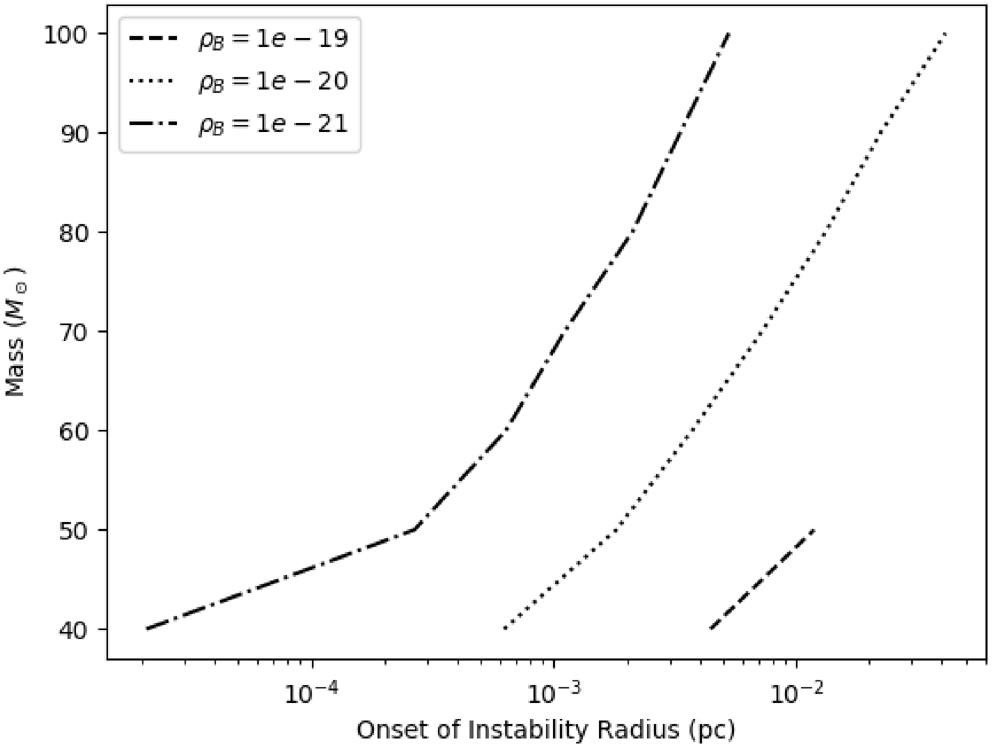

The radii bellow which the simulations would be Toomre unstable plotted for different stellar masses and Bondi densities. The curve for the $\rho_B = 10^{-19}$ only has values for masses between 40 and 50 solar masses because for all other masses it is completely unstable for every radius, as shown in Figure 6.7.

We speculate on the impact such fragmentation could have on our results. One of the effects fragmentation could have is on the interaction of radiation and the torus. Fragmentation implies that clumpy regions would form and, alongside them, lower density channels through which luminosity can escape (WOOD et al., 2013). This means that regions at larger radii in the torus might get more easily ionized than our simulations would suggest. In turn this might mean that the torus potentially enters D-type expansion for considerably lower luminosities than the upper limit found. Fragmentation could also lead to the formation of other proto-stars in the inner region of the torus. Interestingly, if other smaller proto-stars form, they could contribute to the gravitational potential more than they contribute to the increase in ionizing luminosity. As discussed previously, a larger gravitational attraction would imply that the torus would evolve to be denser and thinner and therefore more difficult to ionize. In order to model this effect we plot the model luminosities as if they were emitted by a star 20 solar masses larger than the true value. This mimics a massive star accompanied by a number of proto-stars with combined mass of 20 solar masses, but which do not emit significant amounts of ionizing radiation in comparison to the massive star. This is represented in Figure 6.17 by the dashed green line. As it can be seen, the increase in mass has a stabilizing effect: the masses that would enter the expansion phase for the 10^{-19}g cm^{-3} curve (portion for which the green line - true luminosity - is above the dashed line - critical luminosity values) are now all trapped (the green line is now fully bellow the dashed line). For the 10^{-20}g cm^{-3} curve this also implies that the trapped scenario would occur for lower masses than if we had a single star. Therefore if more than one star is forming simultaneously to a large mass star the torus/disk would be more stable against ionizing radiation and could keep feeding the stars for longer. This is interesting as O stars are found to be in a binary and multiple systems much more often than other types of stars (SANA et al., 2012). Perhaps, this high binarity is linked to the fact that maintaining a torus to form a massive star is more likely if there is core multiplicity. In this case, massive stars are not necessarily only competing for material, but actually need the other companion stars to form. However a verification if this is actually the case would require simulations with self-gravity that properly analyse the effect of fragmentation of the inner disk and its interaction with the incoming ionizing radiation which is beyond the scope of this work and is deferred to a later study.

6.4.3.3 Torus evolution

Although we do not simulate a self consistent evolution of the mass of our star and the corresponding torus changes it is important that we understand how the trapping of the H_{II} region would change as a star gets more massive. It was pointed out previously that for higher masses the torus in our simulations is found to be thinner and denser. As a star accretes, it is therefore reasonable to assume that its torus will try to adapt to the star's mass gain by following a similar trend. Clearly it takes time for the torus material to adapt to a new configuration dictated by the central mass. If the time taken by the torus to readjust is much longer than the accretion timescale the torus will not change dramatically its shape or density throughout the star's accretion history. Hence, it is likely the torus of the massive stars is going to be less dense and easier to ionize than what we consider in our simulations. If, conversely, the torus is able to conform quickly to the growth of the star then our simulations for different masses for a given Bondi density, can be thought of as snapshots through the evolution of a single star. We can use this extreme scenario as an upper limit for how much the torus can be expected to change throughout the stellar evolution. Figure 6.19 shows the relative increase in ionizing luminosity (based on the stellar evolution model by Sternberg et al. (2003)) and the torus surface density squared for this limiting case.

Recall that the size of the H_{II} region depends on the ionization balance and that the amount of ionizing photons required scales with the square of the density. We can see from Figure 6.19 that the rate of increase in density squared on the torus axis is much larger than the rate of increase in luminosity of the star as it evolves. We can conclude that, if a star were to evolve in such a way, once an H_{II} region is trapped in the torus it will either always be trapped, or it will quench as the luminosity coming from the star will be able to ionize up to progressively smaller radii in the torus plane. In this case the star's final mass needs to be halted by other means than ionizing feedback.

Figure 6.19 - Rate of increase of density and luminosity with stellar mass

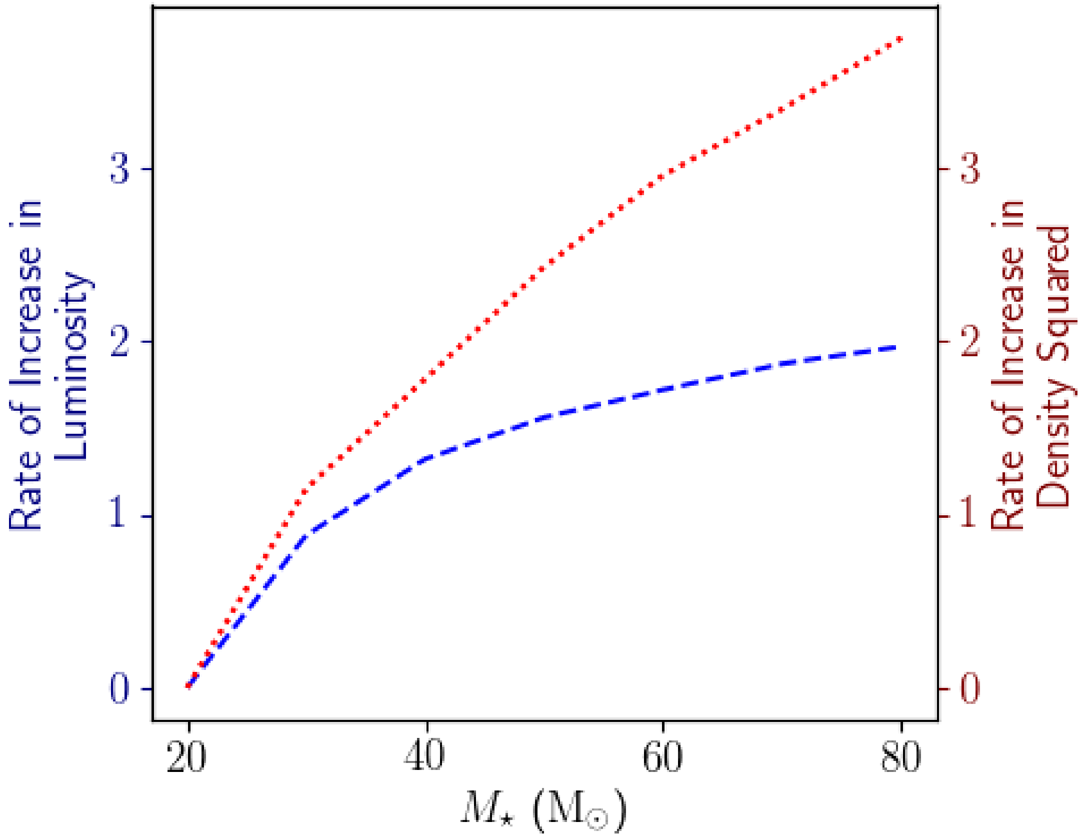

The rate of increase in torus density and ionizing luminosity as a star increases its mass. The values are normalized with respect to the torus density and ionizing luminosities of a 20 solar mass star.

6.4.3.4 Mass reservoir

Until now we have assumed that the mass of the torus and the star could keep increasing indefinitely, that is, we assumed an infinite mass reservoir. A more likely scenario would be to have a finite amount of mass that can be accreted. Material located at a distance R_{lim} from the central star for which the free-fall time is larger than the period for which the massive star accretes will clearly never be able to contribute to the star's mass. Therefore, it follows straightforwardly that the mass of the star will never be able to exceed the mass available within the boundaries of R_{lim}. In addition, limiting the amount of material available can limit the maximum density of the torus thus making the torus optically thinner and more prone to having an expanding H_{II} region.

6.4.3.5 Mask effects

As pointed out in section 2 we use an inner mask of 0.01 pc around our point mass. It is, therefore, reasonable to question how the results might change had we considered a smaller mask. It was already shown earlier in this section that the luminosity values corrected to include radiation absorbed in most of the masked region give a good estimate for the H_{II} region scenario (expanding or trapped) within the torus. The size of the mask does imply that for the the H_{II} region trapped within the first few cells from the mask could be more compact (trapped at smaller radii in the disk). It is however not the aim of this work to quantify the extent of the ionized region, but instead to obtain a general view of possible scenarios and constrain expected luminosities for which the ionized regions would no longer be trapped.

It is worth pointing out that any simulation of a torus or a disk has a masked region in the sense that accretion onto the stellar surface is not resolved. Even though some simulation resolve accretion to a single cell, this cell is still equivalent to a very small masked region in which the hydrodynamics and radiative transfer effects cannot be taken into account. The size of the mask used in our simulations was based on the fact that, at mask scales and below, a number of simulations (PETERS et al., 2010; KLASSEN et al., 2016) as well as observations (BEUTHER et al., 2017) indicate the existence of substructure and sometimes multiple accreting stars (PETERS et al., 2010; KRUMHOLZ et al., 2007). In light of the lack of self gravity in our simulation and, henceforth, our inability to evaluate such scales appropriately we have set a mask around these smaller scales and focused on the larger picture effect of ionizing radiation on the environment. In addition, should a disk truly exist around a single star at scales smaller than the mask used, we can still re-scale the simulations to these smaller scales. In other words, the qualitative results regarding the possible shapes of the H_{II} regions would still hold, albeit for slightly different luminosities and densities.

6.4.4 Other feedback effects

It is evident that other feedback effects will play important roles in the accretion disks around massive stars, and combined effects of different feedback mechanisms can have a very different impact from the effect of each mechanism acting individually. Citing a few examples from the literature:

- Outflows and jets: Kuiper e Hosokawa (2018) shows that the clearing of gas of the polar regions (perpendicular to the disk) by jets and outflows makes the impact of photo-ionization greater as it can more easily ionize these rarefied regions. The high pressure of the hot ionized poles may even push more material down to the disk plane, increasing accretion rates. However, these are 2D simulations and therefore ignore instabilities in accretion disks which could lead to the formation of companion stars. If companions exist, they could compete for material with the main star in their simulation and result in many less massive stars.

- Magnetic fields: (KRUMHOLZ et al., 2007) shows that HII (ionized) region evolution is altered by the existence of magnetic fields. This is to be expected as ionized gas can no longer flow freely in the directions perpendicular to the magnetic field lines, resulting in lower density contrasts and much weaker shocks for an expanding HII region than in the scenario without magnetic fields. Also, Seifried et al. (2011) showed that magnetic fields can have two almost opposite effects depending on the magnetic field strength. Strong fields make angular momentum transport efficient, via magnetic braking and can disrupt the disk entirely, whereas weak fields can support the disk against gravitational instabilities, making it less likely to fragment.
- Other feedback mechanisms such as line-driven winds (SUNDQVIST; OWOCKI, 2013; KEE et al., 2017)and the detailed impact of turbulence (SHAKURA et al., 1978; SEIFRIED et al., 2015) within these disks may also impact the disk structure and accretion rates.

As mentioned previously, including all of these feedback effects simultaneously in a simulation is impracticable, but by studying them in a simplified scenario will help us get insights into massive star formation until we are truly able to do a more all encompassing study.

7 TURBULENCE

7.1 Introduction

The preceding chapters have dealt with the impact of photoionization on the accretion environment around a forming massive star. However, the photoionization feedback from massive stars last most of these stars lives. In this last chapter, we are going to zoom out and analyse the impact that photoionization has on a scale of a few parsecs within a molecular cloud. First, we are going to overview some concepts about turbulence in Section 7.2, giving a summary of phenomenological approaches that have been developed since the pioneering studies of Reynolds (1883) and Richardson (1922). We are going to review the first successful analytical description of turbulence: the Kolmogorov model (KOLMOGOROV, 1941) and show that, despite being seemingly chaotic, turbulence can be described by considering its statistical behaviour (Section 7.3). In the ensuing Section 7.4, we are going to see what the statistics of turbulence may tell us about the molecular clouds and the local star formation. In the last Section 7.5, we will consider the effect photoionization from massive stars has on the statistics of turbulence and thus analyse the impact it may have on star formation by means of numerical simulations done with the AMUN code coupled to the radiative code disclosed in Chapter 4.

7.2 Turbulence: what is it?

The word ‘turbulence’ was coined by Leonardo Da Vinci to describe the chaotic motion of water flows. He identified that “Moving water strives to maintain the course pursuant to the power commenced by a circular and revolving movement...small eddies are almost numberless and large things are rotated by large eddies and not the small ones and small things are rotated by both small eddies and large”. This is a simple but insightful description; it identifies that the flow has a mean flow and a chaotic one. It also hints at a coherent structure for turbulence with large eddies being linked to the smaller ones (see Figure 7.1).

Figure 7.1 - Turbulence drawing by Da Vinci

A sketch of a turbulent flow by Leonardo Da Vinci showing the many different eddy sizes interacting with one another.

It took another four centuries until this picture of turbulence was improved. In the 19th century Navier (1823) added to the Euler equations the diffusion term that was able to describe the viscosity of a fluid. For an incompressible fluid, not subject to external forces, it reads:

$$\frac{\partial u}{\partial t} + u\boldsymbol{\nabla} u = -\frac{\boldsymbol{\nabla} P}{\rho} + \nu\boldsymbol{\nabla}^2 u \tag{7.1}$$

where ν is the kinematic viscosity of the fluid.

A few decades later, Osborne Reynolds (REYNOLDS, 1883) studied the transition from a laminar to a turbulent flow by injecting dye in the center-line of a pipe with water. For a laminar flow, the dye will mix with the surroundings only via molecular diffusion. As this process is inefficient, the dye forms a streak and does not mix with the water. As the injection speed of the dye is increased, the streak becomes more and more unstable and, as the flow gets progressively more turbulent, the dye quickly disperses across the whole pipe. This shows that turbulence is very effective in mixing fluids and that highly turbulent flows tend to restore the symmetries in a statistical sense.

Reynolds also proposed that the transition occurs due to the preponderance of the non-linear term ($u\boldsymbol{\nabla}u$), which causes the turbulence, over the viscous term ($\boldsymbol{\nabla}^2u$). This is illustrated in Figure7.2. Thereby, the transition point can be quantified by measuring the ratio of these terms. A dimensional analysis gives us the so called Reynolds number:

$$Re = \left[\frac{v\boldsymbol{\nabla}v}{\boldsymbol{\nabla}^2 v}\right] = \frac{lv}{\nu} \tag{7.2}$$

where l and v characterise the size and the velocity of the flow with turbulence occurring for high Reynolds numbers ($Re >> 1$). The cold ISM has Reynolds numbers of the order $10^5 - 10^7$ (ELMEGREEN; SCALO, 2004) and, thus, is very turbulent.

Figure 7.2 - Laminar to turbulent transition

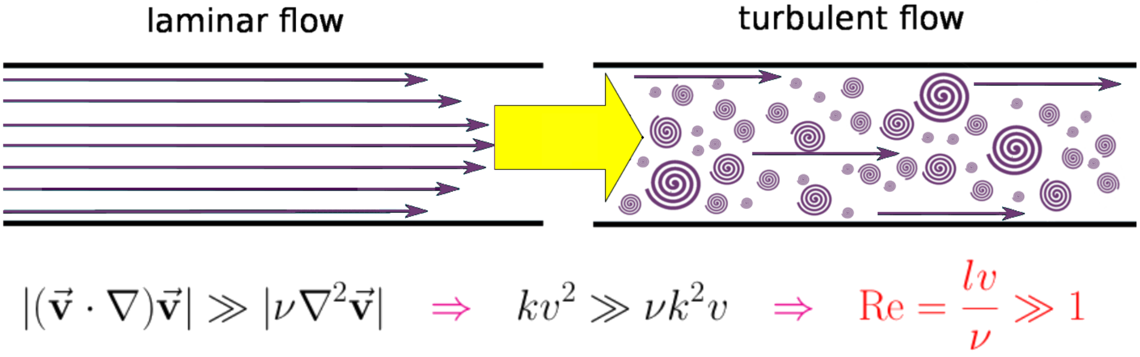

$$|(\vec{\mathbf{v}}\cdot\nabla)\vec{\mathbf{v}}| \gg |\nu\nabla^2\vec{\mathbf{v}}| \quad\Rightarrow\quad kv^2 \gg \nu k^2 v \quad\Rightarrow\quad \mathrm{Re} = \frac{lv}{\nu} \gg 1$$

The transition between a laminar and a turbulent flow depends on the preponderance of the inertial term of the Navier-Stokes equation in relation to the viscous term. The Reynolds number, obtained by a division of the former to the latter term gives a quantitative estimate for if the flow is turbulent or not, with turbulent flows having Reynolds numbers much larger than unity.

Since the pioneering Reynolds' experiments (REYNOLDS, 1883), there has been a continuous effort in elaborating a self-consistent theory of turbulence.

The concept of an energy cascade, which roots in the works of Richardson (1922), has been of particular importance. Richardson's breakthrough was to realise that the large eddies are unstable and break up, transferring their energy to somewhat smaller eddies. These smaller eddies themselves transfer their energy to yet smaller eddies and so on. This "energy cascade" carries on until the Reynolds number is sufficiently small that eddy motion is stable, and molecular viscosity is effective in dissipating the kinetic energy.

In order to understand this cascading, it is useful to think in frequency space or k-space. We can use Fourier transforms to express the hydrodynamical quantities into k-space. Imagine a region of space where the values for the velocity at each spacial point can be described at a single Fourier mode $v = sin(kx)$. Let us see what the non-linear term does to it:

$$(v\mathbf{\nabla})v \implies ksin(kx)cos(kx) \propto sin(2kx) \tag{7.3}$$

That is, one mode gives rise to another mode which has an effective wavenumber twice of that we started with. This new mode would give rise to yet another mode with an yet larger wavenumber and the process would repeat itself time and again. In other words, the inertial force drives progressively smaller scale movements, transferring kinetic energy from the largest to the tiniest scales, from wavenumber k to 2k, then from 2k to 4k, and so on.

It should be noted that, with the inclusion of compressibility, magnetic fields and/or self-gravity, all the related fields are distorted by the velocity field and vice-versa. Thus, one can have many flavours of turbulence: MHD turbulence, gravitational turbulence, or thermally driven turbulence, but they are all inherently connected to the $(v \cdot \mathbf{\nabla})v$ term. These additional effects add new globally conserved quantities and remove others (for instance, the kinetic energy is not conserved for compressible turbulence of an inviscid fluid), leading to behavioural changes. This may affect the way energy is distributed along the turbulent cascade.

In 1941, Kolmogorov added to this picture by proposing a self-similar cascade with a constant transfer rate of energy and proposing a statistical description of turbulence (KOLMOGOROV, 1941). This work is still the base upon which most of the turbulent theory was developed and we review it briefly in the next section. The topics introduced in this chapter can be found in a number of textbooks and review articles (POPE, 2001; FRISCH; KOLMOGOROV, 1995; FALCETA-GONCALVES et al., 2014) which deal with the theory of turbulence in more detail.

7.3 Kolmogorov

The "standard model" for description of turbulence was developed by Kolmogorov, who envisaged all turbulent eddies from the largest to the smallest are linked via a steady transfer of kinetic energy (KOLMOGOROV, 1941). The rate energy is fed to the largest scales, the 'injection scale' L_{inj}, is equal to the rate kinetic energy is lost at small scales, the 'dissipation scale' L_{dis}. The range of scales at which energy just cascades down with a constant mean rate ϵ is called the inertial range. The mean rate reads:

$$\epsilon = \frac{dE_k}{dt} = \text{ constant.} \tag{7.4}$$

Because $E_k \propto v^2$, from a dimensional analysis we have that:

$$\frac{v^2}{t} \sim \frac{v^3}{l} = \text{ constant,} \tag{7.5}$$

where we take the characteristic dissipation time for and eddy of size l to be $t \sim l/v$. This, then, results in the following scaling relation between the velocity, the length scale l and the wavenumber k:

$$v \sim l^{1/3} \sim k^{-1/3}. \tag{7.6}$$

which implies, for the injection and the dissipation scale, that:

$$v(L_{dis}) = v(L_{inj}) \left(\frac{L_{dis}}{L_{inj}}\right)^{1/3} \tag{7.7}$$

Since, at dissipation scales, the Reynolds number is approximately 1:

$$Re = \frac{v(L_{dis})L_{dis}}{\nu} = \frac{v(L_{inj})}{L_{inj}^{1/3}} \left(\frac{L_{dis}^{4/3}}{\nu}\right) = \epsilon^{1/3} \left(\frac{L_{dis}^{4/3}}{\nu}\right) = 1 \tag{7.8}$$

Follows immediately that the dissipation scale is:

$$L_{dis} = \left(\frac{\nu^3}{\epsilon}\right)^{1/4}. \tag{7.9}$$

We can also easily estimate the kinetic energy spectrum $E(k)$ by deriving the kinetic energy in k and using $E_k \sim v^2 \sim k^{-2/3}$:

$$E(k) = \frac{dE_K}{dk} \sim \frac{v^2}{k} \sim k^{-5/3}. \tag{7.10}$$

This is the famous Kolmogorov 5/3 law, which is illustrated in Figure 7.3

Figure 7.3 - Turbulent Cascade

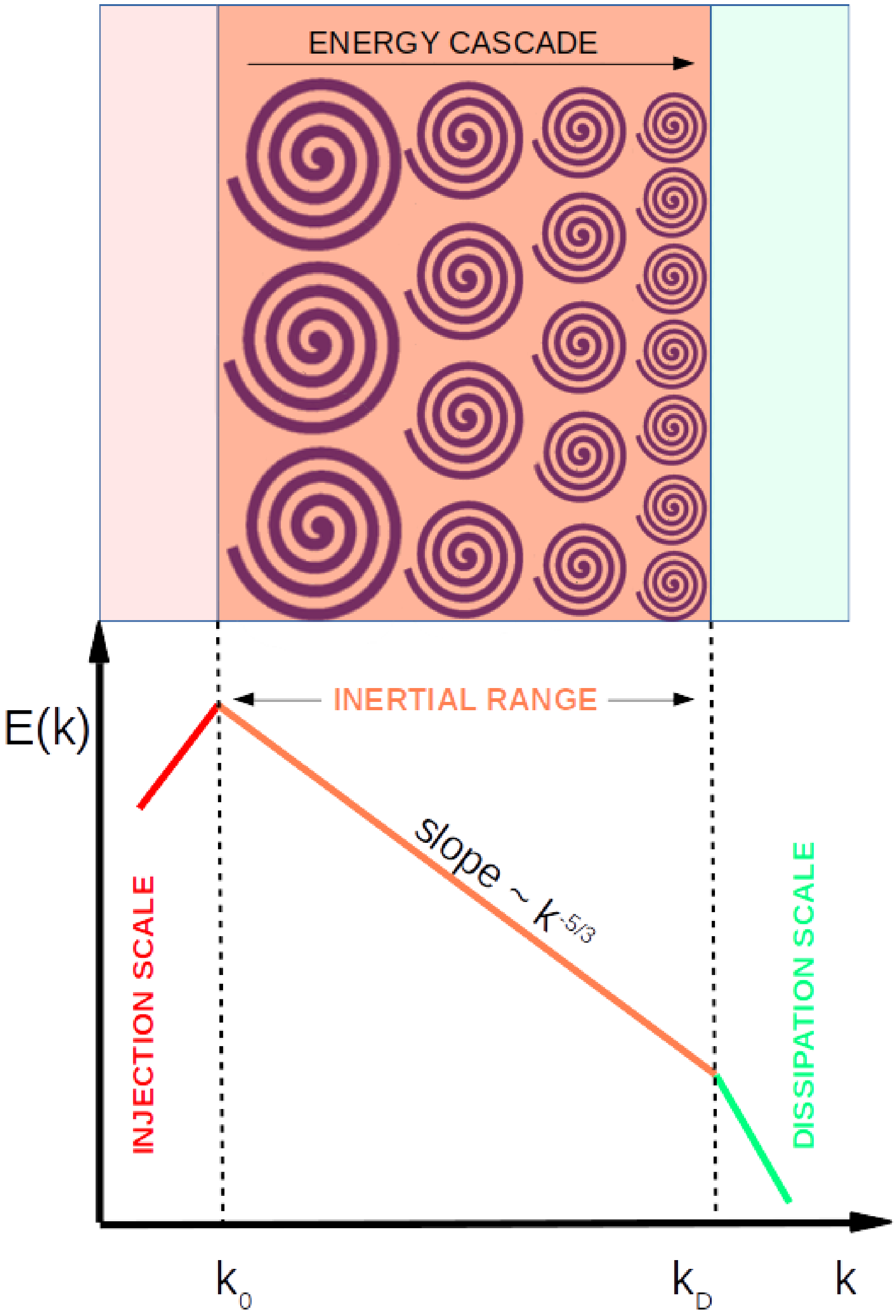

The turbulence cascade for Kolmogorov incompressible turbulence. After energy is injected at an injection scale k_0, the energy cascades from large scales to small scales at a constant rate. This gives a slope to the energy spectrum proportional to $k^{-5/3}$ up until the point (k_D) where energy can be dissipated by some process, such as viscosity.

7.4 Turbulence statistical analysis

Star formation is known to take place in the densest parts of molecular clouds within filaments that are governed by the complex interaction of gravity, magnetic fields, and turbulence (MCKEE; OSTRIKER, 2007). The distribution of the gas density within the cloud is thought to be dictated by turbulence (Figure 7.4) and, thus, is thought to regulate the properties of star formation, such as the star formation rate and the initial mass function (KRUMHOLZ; MCKEE, 2005; HENNEBELLE; CHABRIER, 2011; PADOAN et al., 2014). It is, therefore, vital that we find a way of describing turbulence. Kolmogorov was the first to suggest turbulence could be described in a statistical manner and, although the Kolmogorov theory does not apply directly to molecular clouds, this manner of depicting turbulence is the most used to date.

Figure 7.4 - Comparison: observations and simulations

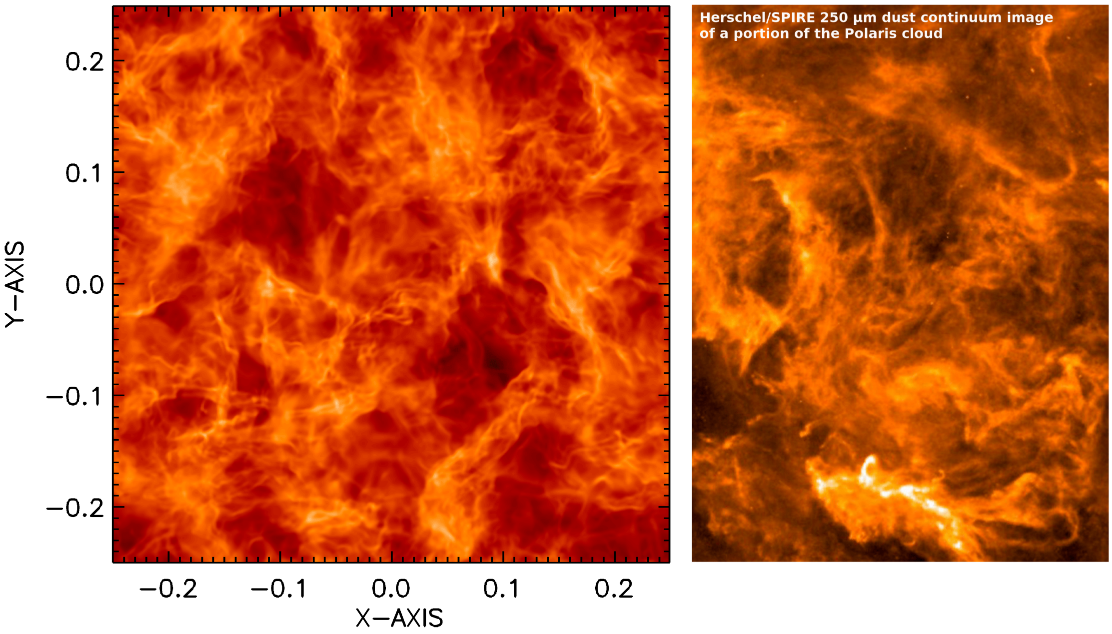

On the left one of our simulations of a turbulent molecular cloud and on the right the Herschel/SPIRE 250 μm dust continuum image of a portion of the Polaris flare cloud from André (2017). We can see that there is a striking resemblance between the two. Note that the real molecular cloud seems to have more darker regions representing the low density patches. This is probably due to the fact that the turbulent forcing used in this work is purely solenoidal and larger low density patches are more strongly present in compressive modes.

7.4.1 Power spectrum

One of the most fundamental quantities in turbulence statistical analysis is the power spectrum, which, put simply, answer the question “How much of this quantity is found at this frequency?". In turbulence analysis, it is often used to analyse the velocity field to deduce how energy is distributed across different scales. It was, in fact, the velocity power spectra that first hinted on the existence of a turbulent cascade across the many scales of the ISM (LARSON, 1981). The power spectrum may generally be defined by considering an auto-correlation function C for an observable $\mathcal{O}$:

$$C(\delta r) = < \mathcal{O}(r)\mathcal{O}(r+\delta r) > . \tag{7.11}$$

where r is a spatial location and δr an increment to r.

Then, the Power Spectrum is simply its Fourier transform:

$$P(k) = \hat{\mathcal{O}}(r)\hat{\mathcal{O}}(r+\delta r)* \tag{7.12}$$

where the ˆ represents the Fourier transform and $*$ the complex conjugate. We follow (ELMEGREEN; SCALO, 2004) using the convention where the energy spectrum $E(k)$ is one-dimensional (1D) and equals the average over all directions of the power spectrum, $E(k)dk = P(k)dk^D$ for a number of dimensions D. For incompressible turbulence, the Kolmogorov power spectrum in three-dimensions (3D) is $\propto k^{-11/3}$ and the energy spectrum is $E(k) \propto k^{-5/3}$.

As mentioned before, Kolmogorov’s theory applies to subsonic and incompressible flows, whereas interstellar turbulence is known to be both supersonic and compressible. In compressible fluids dominated by shocks (Burgers turbulence), the energy spectrum will be $E(k) \propto k^{-2}$. However, the works of Federrath et al. (2009), Federrath et al. (2010) encounter exponents for the energy spectrum in both observations and simulations between $-5/3$ and -2, that is, slightly steeper than the Kolmogorov one and lying between the cases for incompressible and shock-dominated turbulence (for Mach numbers between 5 and 6). This result is in agreement with values found by Heyer e Brunt (2004), Kritsuk et al. (2007), Schmidt et al. (2009). The exponent of the energy spectrum asymptotically approaches the Burgers limit as the Mach number increases. In addition, real molecular clouds are in fact not isothermal; thus a Kolmogorov-type energy cascade is only an approximation to the process that occurs in these clouds.

Many other models that describe turbulence have been developed over the years, in particular ones that take into account compressibility and the magnetic fields of molecular clouds which are thought to alter the power spectrum (see Falceta-Goncalves et al. (2014) for a review). The key idea, however, was that the turbulent energy distribution over scales could be analysed in terms of power spectrum.

7.4.2 The density PDF

The density probability distribution function, as mentioned on Chapter 4, gives the probability each density value has of occurring. Since star formation takes place in the densest parts of the ISM, we can set a critical value ρ_{crit} above which that star formation is likely to occur (KAINULAINEN et al., 2014). The PDF of the density can, then, give us the portion of the gas that is likely to be star-forming (Figure7.5).

Figure 7.5 - Star formation and turbulent statistics

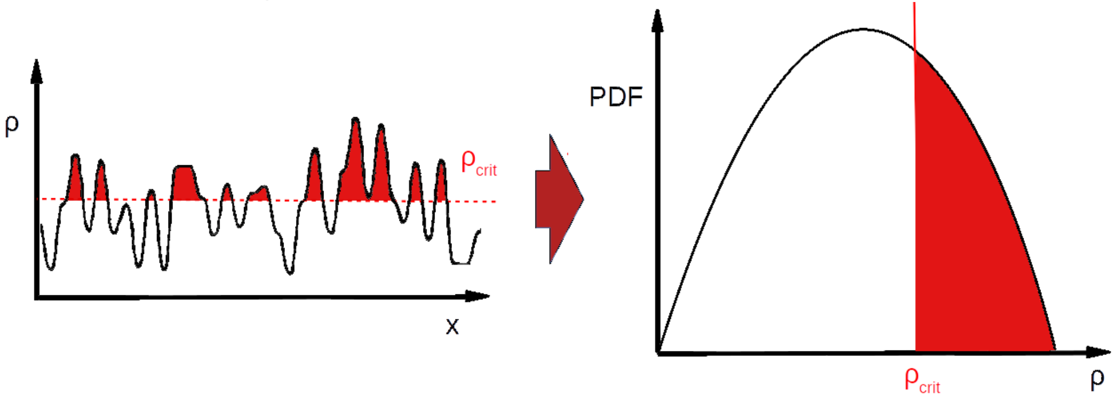

On the left an schematic of how the density may vary in space (x), showing in red the regions where the density is above the critical one, and thus, potentially star forming. On the right the PDF of the density highlighting the same portion of dense gas above the critical limit. If the density distribution were to change more/less gas would fall above ρ_{crit} and star formation would increase/descrease.

As turbulence results in many interacting shocks, we may think of the turbulence generated density distribution as a succession of multiplicative density perturbations (which are, therefore, additive in the logarithm). Given that the perturbations are independent events, from the central limit theorem, we can expect the logarithm of the density distribution to be a normal distribution (PASSOT; VÁZQUEZ-SEMADENI, 1998) or equivalently that the mass density probability distribution function (ρ PDF) is log-normal in shape (VAZQUEZ-SEMADENI, 1994; PADOAN et al., 1997).

The shape of the density PDF is also altered by how supersonic the ISM turbulence is. This can be quantified by the value of the sonic Mach number, defined as the ratio of the gas speed to the speed of sound $\mathcal{M} = \frac{u_{gas}}{c_s}$. In the simplest case of an isothermal compressible turbulence, the density and velocity across a shock is given by the Rankine-Hugoniot conditions:

$$\rho_1 u_1 = \rho_2 u_2 \tag{7.13}$$

$$\rho_1(u_1^2 + c_s^2) = \rho_2(u_2^2 + c_s^2). \tag{7.14}$$

It is easily seen that $\mathcal{M}_1 = (\rho_2/\rho_1)\mathcal{M}_2$ and, thus, that $\rho_2/\rho_1 \propto \mathcal{M}_1^2$. This implies that the compression factor in an isothermal shock can be arbitrarily high and that the density structure of the turbulence to be related to $\mathcal{M}^2$. The early works of (VAZQUEZ-SEMADENI, 1994) have shown that the standard deviation σ_ρ of the linear density PDF increases proportionally to the root mean square (RMS) of the Mach number of the turbulent flow.

We characterise the mass distribution by introducing a new variable s, defined as the natural logarithm of density divided by the mean density $s = ln(\rho/ < \rho >)$. The PDF can, then, be expressed as:

$$P(s) = \frac{1}{\sqrt{2\pi}\sigma_s} exp\left(\frac{-(s- < s >)^2}{2\sigma_s^2}\right), \tag{7.15}$$

The exact correlation between the sonic Mach number and the PDF's σ_ρ is not yet clear, but it is usually written as:

$$\sigma_s^2 = ln(1 + b^2\mathcal{M}^2) \tag{7.16}$$

where b is a dimensionless quantity related to the turbulent forcing mode and σ_s^2 is the variance. Thus we have a log-normal PDF whose width depends on the Mach number of the supersonic flow.

On the observational perspective, log-normal PDFs have, indeed, been observed in multiple molecular clouds (KAINULAINEN et al., 2009; GOODMAN et al., 2009; BURKHART et al., 2015), although in most scenarios they are also accompanied by a power-law tail, at high wave numbers, which is usually attributed to effect of gravity.

Interestingly, more lognormal PDFs are found in quiescent molecular clouds (which do not present star formation). Could, then, be the case that the log-normality of a cloud is linked to the fact of being star forming or not? If so, could the shape of the PDF be related not only to gravity but to a certain extent to the feedback from the forming stars? It was suggested by (BRUNT, 2015) that the tail of this PDF could be attributed to a bimodality and that we are actually tracing two PDFs: one of the warm gas and another from the cold gas (Figure7.6). The warm gas would naturally have higher sound speeds which, in contrast, lead to lower mach number, and thus to narrowing of the observed PDF.

Figure 7.6 - Tail of the PDF

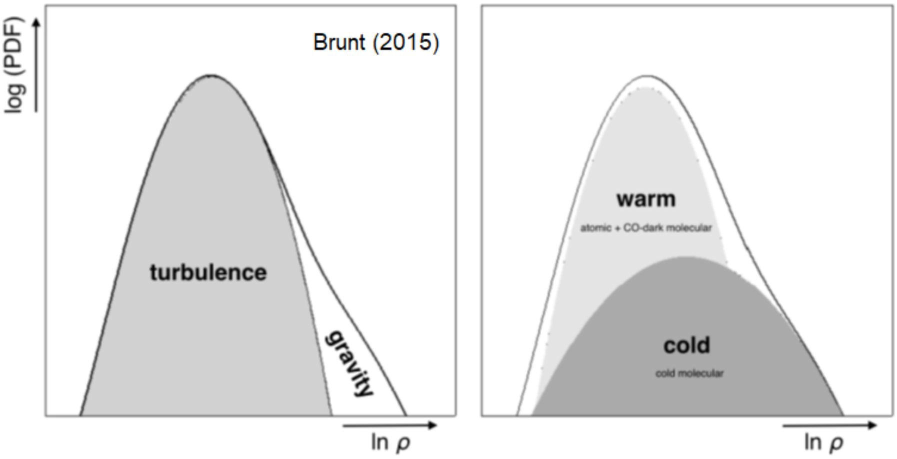

On the left the power law tail usually attributed to the effects of gravity. On the right an alternative explanation from Brunt (2015) (where this figure was obtained) showing how the tail could be formed by the superposition of two PDFs; one for the warm gas and one for the cold gas.

The density PDF and its dependence on turbulence properties have served as a basis for star formation theories, being regularly related to the initial mass function and the star formation rate and efficiency (KRUMHOLZ; MCKEE, 2005; HENNEBELLE; CHABRIER, 2011; HENNEBELLE; CHABRIER, 2013; PADOAN et al., 2014; RENAUD et al., 2012; GIRICHIDIS et al., 2014; MOCZ; BURKHART, 2018; BURKHART; MOCZ, 2019) as well as an aid to determine the dynamical state of molecular clouds from observational data (KAINULAINEN et al., 2009; BRUNT et al., 2010; BALLESTEROS-PAREDES et al., 2011; SCHNEIDER et al., 2012; KAINULAINEN; TAN, 2013).

7.5 Simulations of RHD turbulence

It is well established that turbulence regulates star formation in molecular clouds. Large Mach numbers result in dense structures, due to the shocks, which end up collapsing, fragmenting, and forming stars. However, what stars once formed can do to the turbulence itself? Does the stellar feedback change turbulent properties of its surrounding medium and impact further star formation?

In this section we are going to analyse, through simulations of turbulent media, if photoionization does have an impact in the statistical properties of hydrodynamical solenoidal turbulence.

7.5.1 Method

The simulations are performed using the AMUN code with the new Monte Carlo radiative transfer code, introduced in Chapter 4. Once more, we use a static 3D Cartesian grid of width 10 pc with resolutions 256^3 cells to model a turbulent molecular cloud. We also set the equation of state to be adiabatic, but with a polytropic index of $\gamma = 1.0001$, thus mimicking an isothermal equation of state. For simplicity, the material in the simulated molecular cloud is assumed to be composed solely by hydrogen, with no heavier elements or dust. Our aim is to determine the impact of photoionization alone, and assuming pure hydrogen is adequate for this purpose. Including heavy elements is important for cooling rates, but their low abundances make their opacities much lower than that of hydrogen and, consequently, they do not significantly influence the radiation transport and the resulting ionization structure of hydrogen, as seen in Chapter 3. Dust, on the other hand, would have a sizeable effect on the region, as radiation pressure on dust is going to affect the dynamics of the gas and, therefore, the region around the star. Here, however, we will ignore the effects of radiation pressure and concentrate on the effects of photoionization, keeping the inclusion of the former for a latter investigation.

In each simulation run, we place an ionizing point source within the cloud emitting isotropically. The ionizing luminosity of the point source is kept constant throughout each simulation. The ionizing packets are propagated through a discrete density grid until a randomly sampled optical depth is reached. At this point, two things can happen to the photon: either it is absorbed, thereby,“terminating the packet”, or it is re-emitted as another ionizing photon with probability $\alpha_1/\alpha_A \approx 0.36$ (where α_1 is the recombination rate to ground level and α_A is the recombination rate to all energy levels). For each Monte Carlo timestep, we iterate 10 times to guarantee the convergence of the ionized region. As in previous chapters, we still use the two-temperature approximation with the neutral temperature, T_n, set to 100K and the ionized temperature, T_i, set to 8000K, such that the temperature in each cell is given by $T_{cell} = T_i(1 - n_{frac}) + T_n n_{frac}$, where n_{frac} is the portion of cell that is still neutral. Given the temperatures in each cell, the pressure in the hydrodynamics code can be updated accordingly. The simulations are divided in two stages. In the first stage of the simulation, we run only the hydrodynamics module with the turbulence forcing. This is done so that the turbulence can evolve to a statistically stationary state before we introduce the radiative feedback. The second half of the simulations is identical to the first half, except that now we add one or more sources of radiation to probe the effect it has on the statistics of the turbulence.

7.5.2 Statistical results

In Figure 7.7 we show the density PDFs both of a run with photoionizing feedback from a point source emitting 10^{50} ionizing photons/s and another, otherwise identical, run without the feedback. We see that the PDF 7.7 gets marginally narrower once photoionization feedback is turned on. We can see from Figure7.8 that the RMS of the Mach number has reduced by about order unity, which is expected since the sound speed has considerably risen in a significant portion of the cloud.

Figure 7.7 - Evolution of the density PDF with ionization feedback

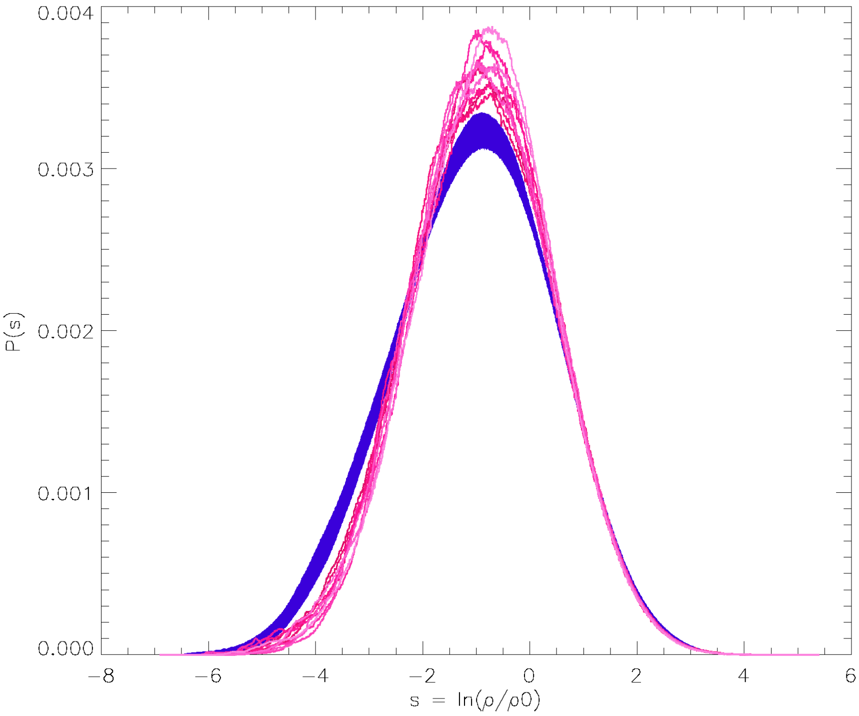

The probability density function (PDF) of the natural logarithm of the density. The blue region shows the values for a simulation run without photoionization feedback. Conversely, the pink to red lines show the PDF obtained for the run with photoionizing feedback with the lighter colours showing later timesteps.

Figure 7.8 - Evolution of the Mach number with ionization feedback

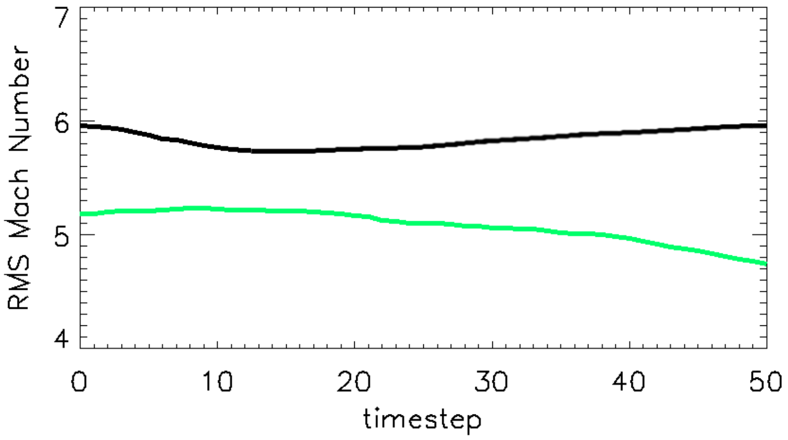

The black line shows the Mach number for the last 50 snapshots of the hydrodynamical simulation before photoionizing feedback was introduced. The green line shows the first 50 snapshots since the start of the photoionization effects. We can see that the RMS mach number is reduced due to the fact that the sound speed is higher for the ionized region.

The power spectrum of the density, illustrated in Figure 7.9, also shows almost no appreciable change, specially for the larger wave numbers (i.e. for the smallest scales).

Figure 7.9 - Evolution of the density PS with ionization feedback

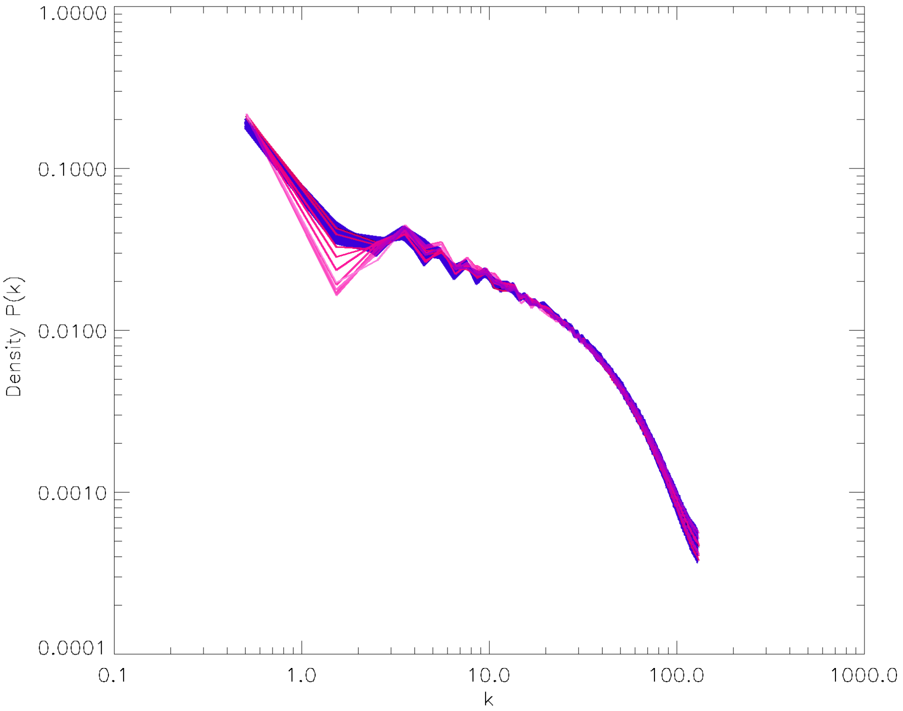

As in Figure7.7 but for the power spectrum on the density.

In relation to the velocity statistics, little difference is seen as well between the runs with and without photoionization feedback, with the power spectrum showing the same slope and with no significant change in the velocity PDF 7.10.

Figure 7.10 - Evolution of the velocity PDF and PS with ionization feedback

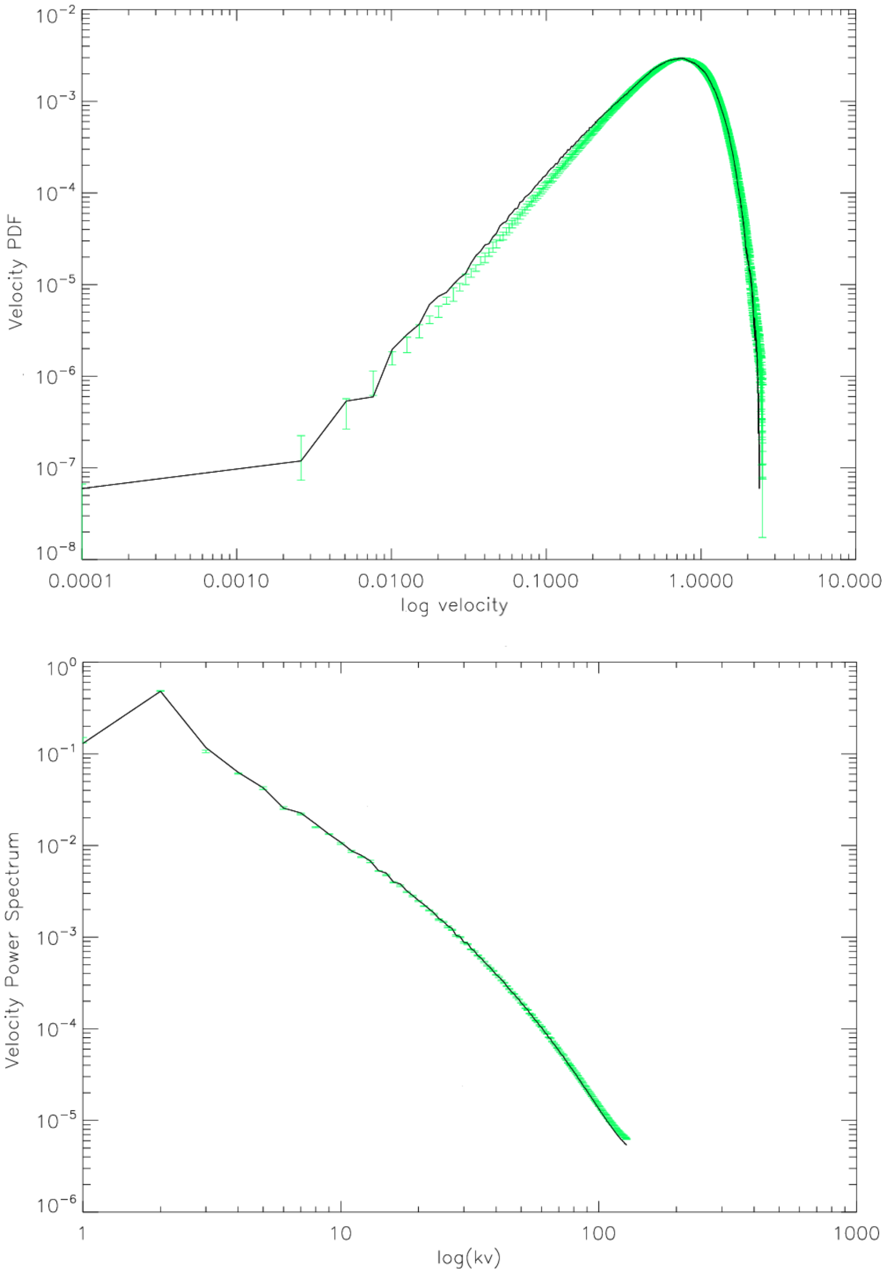

On the top, the probability distribution function for the velocity, and on the bottom, the velocity power spectrum. The green error bars show the maximum and minimum values that were reached for the same simulation, but without the introduction of the ionizing luminosity. We can see that the effect of the photoionization on the velocities is minimal, with values for the run with feedback usually lying within the error bars.

In fact, all that photoionization does is to ionize and heat the less dense regions of the molecular cloud. These pockets of low density material tend to be large and this makes the ionized region have a large filling factor. However, it is clear from the statistics above that this effect alone is not able to change the distribution of the gas or the manner in which the energy cascades from larger to smaller scales.

We also analyse if the impact of the photoionizing feedback is dependant on the location of the massive star. With this purpose, we have run a series of experiments with varying placement of the ionizing source: in the middle of a dense filament or in the middle of a low density region. Figure 7.11 shows different scenarios with distinct ionizing luminosities.

We see that, for luminosities of around 10^{49} ionizing photons per second, a star placed within a filament cannot escape the filament region; instead, it simply causes the filament to puff up. At a higher luminosity, $L = 10^{50}$ photons$/s$, the star manages to open a gap in the filament and, from then on, it ionizes only the low density structures. We can observe the existence of a large, diffuse H_{II} region, but we also notice that the dense structures are not overall altered in any of the cases studied. The column density, in particular, looks identical for every run.

Consequently, we may conclude that, as no significant change in the structure of the gas occurs, the photoionization alone will not alter the star formation in the molecular clouds since:

- there is no increase in high density regions that could boost star formation;

- there is no significant dissipation or ionization of the existing filaments, so the highest density regions remain cold and thus should not have any thermal support preventing their collapse into stars;

- the only region that gets significantly heated up is the low density regions which shouldn't be contributing to star formation anyhow.

This result also indicates that we are able to extract information from turbulent simulations which do not include photoionization effects, that is, simulations that consider only a cold isothermal ISM, and compare them directly with observations of the real multiphase ISM, as their turbulence statistics should still be equivalent.

Figure 7.11 - H_{ii} region expansion in different turbulent conditions

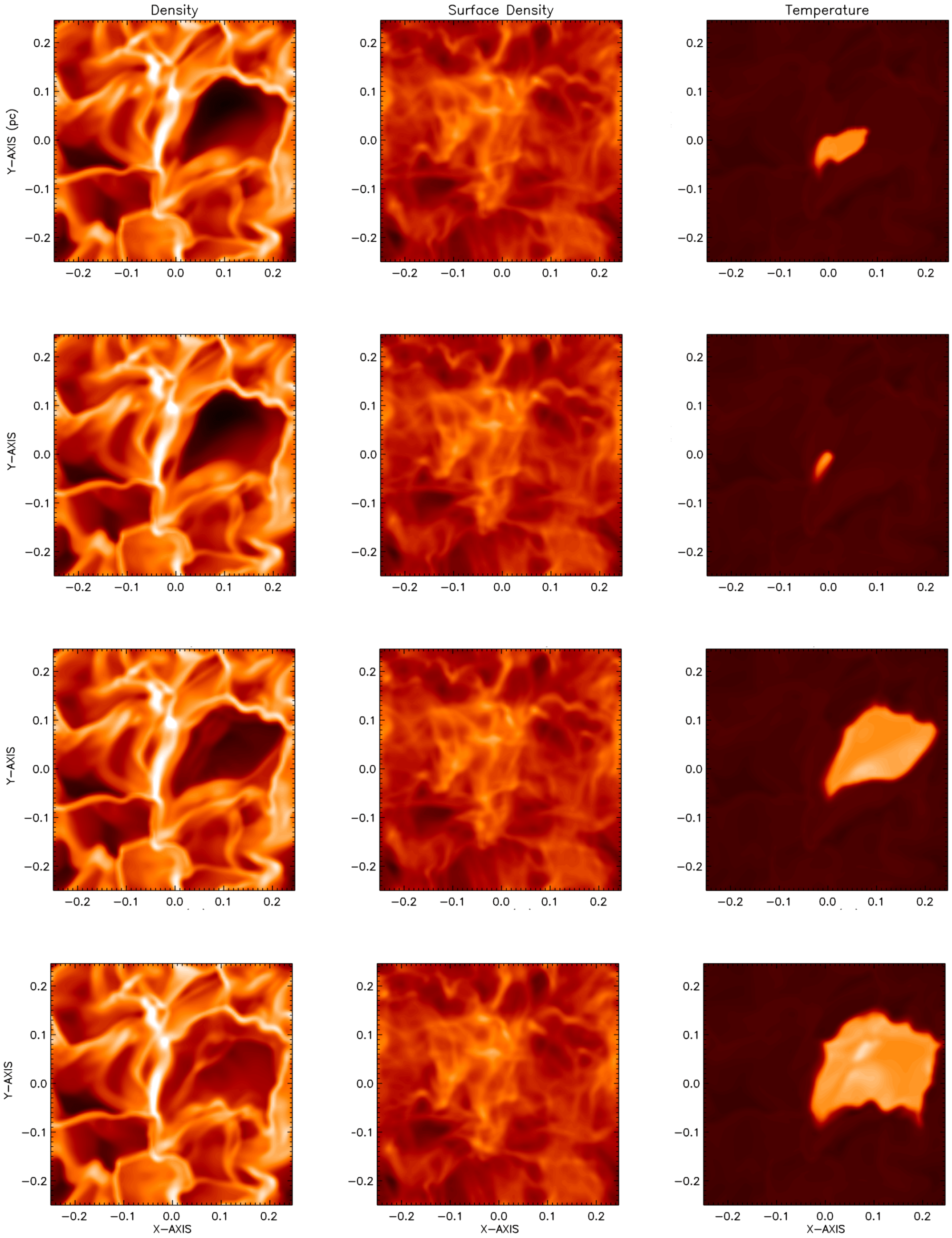

In each row from left to right we show the density, the column density and the temperature for a set of simulations. For the two top rows the star was initially placed on a filament, whereas for the two bottom rows the star was put in the middle of a low density region. Row 1 and 3 have ionizing luminosity of $L = 10^{49} s^{-1}$ and can be taken to represent a single star whereas rows 2 and 4, $L = 10^{50} s^{-1}$ representing a small cluster.

In addition, it is worth noticing that, in our simulations, the ionization effect from a single star is not sufficient to completely disperse the denser filaments or to cause the dissipation of the molecular cloud, unlike simulations from Dale et al. (2014), Ali et al. (2018) in which most of the molecular clouds mass is thrown away by the effect of photoionization. This difference is probably due to the fact they do not use “turbulence in a box” simulations and instead set the turbulence in the cloud by imposing a random Gaussian turbulent velocity field.

8 CONCLUSIONS

In this thesis, we have investigated the impact of photoionization feedback from massive stars on the molecular clouds that harbour these stars and on their own formation process. This involved simulations using radiation-hydrodynamics codes, such as CMacIonize and AMUN + MC, the development of the Monte Carlo radiation transfer code of the latter being part of the outcome of this work. This chapter summarises the main findings of each of the chapters presented in this thesis, along with future work that can be build upon this undertaking.

8.1 Numerical codes

We have successfully added turbulent forcing, following Alvelius (1999), to the radiation hydrodynamics code CMacIonize (VANDENBROUCKE; WOOD, 2018a). We have also presented the successful combination of the AMUN Hydrodynamics code (KOWAL, 2007–2016) with a Monte Carlo Radiative Transfer method, as a live radiation hydrodynamics scheme (AMUN + MC). At regular time intervals, the code would call the Monte Carlo radiation transfer code for computing the ionization of the simulated environment around the stars. The code was tested against the STARBENCH (BISBAS et al., 2015) benchmark and obtained results that fit well with the expected analytic solution and has comparable outcomes to other codes. We also tested other approximations, such as the two-temperature approximation for the ISM, which allow us to give a realistic temperature for molecular clouds, even though the heating and cooling effects are not computed. This approximation gave comparable results to a Monte Carlo radiation transfer which does calculate explicitly the cooling via a few heavier elements (WOOD et al., 2004).

8.2 Spherically symmetric accretion onto massive stars

We studied the stability of spherically symmetric Bondi accretion flows around young stellar objects surrounded by an H_{II} region. We derived an analytic expression for a two temperature steady state solution in which an ionization front is trapped in the highly supersonic accreting flow, consistent with the work of Keto (2003). We were able to accurately reproduce this analytic profile in a constrained 1D RHD simulation, using both the CMacIonize and the AMUN + MC codes. However, we also showed that this steady state solution is only marginally stable if ionization is treated self-consistently, leading to a collapse of the ionization front under small perturbations in density or ionizing luminosity. This semi-analytical result has been confirmed in Vandenbroucke et al. (2019) through 1D radiation-hydrodynamics simulations.

8.3 Disk accretion onto massive stars

We saw that massive stars may extend their accretion timescale by accreting through trapped H_{II} region. We show that we expect trapped H_{II} regions for dense accretion disks (simulations with initial density at the Bondi radius of $\rho_B = 10^{-21}$g cm^{-3} or higher), regardless of the central star's mass, as its luminosity will never be high enough to cause the destruction of the disk. Nevertheless, the inner accretion disks for these simulations are Toomre unstable, so it is possible that more than one stellar core would develop under this configuration.

For less dense disks (initial Bondi densities of $\rho_B = 10^{-23}$g cm^{-3}), we expect that – assuming a single central star as the source of radiation – the disk would be dispersed as soon as the star starts emitting significant amounts of ionizing radiation.

The simulations show that, if we consider multiple cores leading to the formation of two or more stars, the resulting disk is denser and more likely to be able to withstand the ionizing radiation coming from the stars without being dispersed. This indicates that massive stars may benefit from forming alongside one or more stars: a cooperative accretion. This is a compelling result, since the binary fraction is higher for O stars than for other stellar types.

These conclusions, however, have to be tested against more complete models which allow for possible effects of magnetic fields and self-gravity on the disk stability and density, as well as the impact of other feedback mechanisms such as outflows and jets, radiation pressure on dust and stellar winds.

8.4 Photoionization of turbulent molecular clouds

We have probed the effect of photoionizing radiation in the environment around a massive star. We have seen that the turbulence statistics is not significantly altered by the effect of photoionization. We do not, thus, expect a change in star formation due to solely photoionization feedback. We also concluded that the photoionization feedback from a single star is not enough to cause a filament to disperse; instead, the star will photoionize the lowest density regions confined by the denser filaments. We conclude that photoionization feedback has little effect on the star formation within the simulated molecular clouds and that, by modelling cold isothermal turbulence, we still should get the same overall turbulence statistics of the more complex multiphased ISM. However, in order to truly verify the validity of these assertions, it would be necessary to repeat this study considering full MHD turbulence in a molecular cloud and including self gravity.

8.5 Future work

This thesis offers many directions in which this work can be continued and here we will list some of them.

In massive star formation, there is much work to be done in both including better models of the accretion disk and in considering other feedback effects. Regarding the disk, it is essential that new simulations take into account the effects of self-gravity as, specially at the initial stages, the disk is of comparable mass of that of the star. Our simulations do not include an alpha viscosity parameter for the disk, such that the viscosity present owes itself only to numerical viscosity and, thus, is resolution dependant. New disk models should include this viscosity parameter as a new variable to be studied and it will most certainly affect accretion rates in the simulation. It is also important to analyse the effects of magnetic fields in the accretion disks around massive stars and see what effects they may have on the disk's shape and on the accretion rates. Magnetic fields are also important when modelling feedback from jets that have been observed on massive young stellar objects. To our knowledge, to date there hasn't been a study including the evolution of magnetic fields and the self-consistent launching of jets within the context of forming massive stars. There are, also, a number of other feedback processes that will have significant impact on the surrounding of the accreting star, such as line-driven winds, radiation pressure on dust and outflows. Most of these have been analysed individually by works in the past, but not in conjunction.

Finally, for the first time we are being able to image the formation of massive stars with high resolution with ALMA. Synthetic observations made from simulations will allow us to directly compare our models to what is truly happening, giving us deep insights on where we may improve in the future and on what is being missed or overlooked.

In the effects of photoionization within molecular clouds, it would be crucial to include better models for the turbulence. Using a more realistic forcing recipe that is able to include a combination of solenoidal and compressive forcing would be interesting, as an increase in the compressive modes would lead to a different distribution of gas and, thus, to a different photoionization. Again, the incorporation of magnetic fields and self gravity will change the statistics of the turbulence and the results have to be verified against more robust models. Simulations that automatically track the fragmentation of the densest parts of the molecular cloud and create stars that emit ionizing luminosity would give us a more faithful description of what is happening within a star forming molecular cloud. We can analyse, as well, if the impact of many massive stars placed at different locations gives a different result, as the multiple stars in this work were all concentrated at a single point.

In summary, as with most areas of research, there is a lot to be improved and worked upon. We have now excellent observational and computational tools that will allow us to probe the scenarios above more accurately than ever. Interesting times lie ahead and we hope to be part of it.

REFERENCES

AGERTZ, O.; KRAVTSOV, A. V.; LEITNER, S. N.; GNEDIN, N. Y. Toward a complete accounting of energy and momentum from stellar feedback in galaxy formation simulations. **Astrophysical Journal**, v. 770, n. 1, p. 25, Jun 2013. 8

AGERTZ, O.; MOORE, B.; STADEL, J.; POTTER, D.; MINIATI, F.; READ, J.; MAYER, L.; GAWRYSZCZAK, A.; KRAVTSOV, A.; NORDLUND, Å. Fundamental differences between SPH and grid methods. **Monthly Notices of the Royal Astronomical Society**, v. 380, n. 3, p. 963–978, Sep 2007. 17

ALI, A.; HARRIES, T. J.; DOUGLAS, T. A. Modelling massive star feedback with Monte Carlo radiation hydrodynamics: photoionization and radiation pressure in a turbulent cloud. **Monthly Notices of the Royal Astronomical Society**, v. 477, n. 4, p. 5422–5436, Jul 2018. 157

ALVELIUS, K. Random forcing of three-dimensional homogeneous turbulence. **Physics of Fluids**, v. 11, n. 7, p. 1880–1889, Jul 1999. 38, 39, 40, 159

ANDRÉ, P. Interstellar filaments and star formation. **Comptes Rendus Geoscience**, v. 349, n. 5, p. 187 – 197, 2017. ISSN 1631-0713. Disponível em: <`http://www.sciencedirect.com/science/article/pii/S1631071317300901`>. 144

ANDRE, P.; MEN'SHCHIKOV, A.; BONTEMPS, S.; KONYVES, V.; MOTTE, F.; SCHNEIDER, N.; DIDELON, P.; MINIER, V.; SARACENO, P.; WARD-THOMPSON, D.; FRANCESCO, J. di; WHITE, G.; MOLINARI, S.; TESTI, L.; ABERGEL, A.; GRIFFIN, M.; HENNING, T.; ROYER, P.; MERÍN, B.; VAVREK, R.; ATTARD, M.; ARZOUMANIAN, D.; WILSON, C. D.; ADE, P.; AUSSEL, H.; BALUTEAU, J. P.; BENEDETTINI, M.; BERNARD, J. P.; BLOMMAERT, J. A. D. L.; CAMBRÉSY, L.; COX, P.; GIORGIO, A. di; HARGRAVE, P.; HENNEMANN, M.; HUANG, M.; KIRK, J.; KRAUSE, O.; LAUNHARDT, R.; LEEKS, S.; PENNEC, J. L.; LI, J. Z.; MARTIN, P. G.; MAURY, A.; OLOFSSON, G.; OMONT, A.; PERETTO, N.; PEZZUTO, S.; PRUSTI, T.; ROUSSEL, H.; RUSSEIL, D.; SAUVAGE, M.; SIBTHORPE, B.; SICILIA-AGUILAR, A.; SPINOGLIO, L.; WAELKENS, C.; WOODCRAFT, A.; ZAVAGNO, A. From filamentary clouds to prestellar cores to the stellar IMF: initial highlights from the Herschel Gould Belt Survey. **Astronomy and Astrophysics**, v. 518, p. L102, Jul 2010. 5

BABA, J.; MOROKUMA-MATSUI, K.; SAITOH, T. R. Eventful evolution of giant molecular clouds in dynamically evolving spiral arms. **Monthly Notices of the Royal Astronomical Society**, v. 464, n. 1, p. 246–263, Jan 2017. 9

BALLESTEROS-PAREDES, J.; VÁZQUEZ-SEMADENI, E.; GAZOL, A.; HARTMANN, L. W.; HEITSCH, F.; COLÍN, P. Gravity or turbulence? - II. Evolving column density probability distribution functions in molecular clouds. **Monthly Notices of the Royal Astronomical Society**, v. 416, n. 2, p. 1436–1442, Sep 2011. 148

BASTIAN, N.; COVEY, K. R.; MEYER, M. R. A universal stellar initial mass function? A critical look at variations. **Annual Review of Astronomy and Astrophysics**, v. 48, p. 339–389, Sep 2010. 12

BEHREND, R.; MAEDER, A. Formation of massive stars by growing accretion rate. **Astronomy and Astrophysics**, v. 373, p. 190–198, Jul 2001. 98

BELTRÁN, M. T.; DEWIT, W. J. Accretion disks in luminous young stellar objects. **Astronomy and Astrophysics Review**, v. 24, p. 6, jan. 2016. 72, 101, 103

BEUTHER, H.; SCHILKE, P.; SRIDHARAN, T. K.; MENTEN, K. M.; WALMSLEY, C. M.; WYROWSKI, F. Massive molecular outflows. **Astronomy and Astrophysics**, v. 383, p. 892–904, mar. 2002. 101

BEUTHER, H.; WALSH, A. J.; JOHNSTON, K. G.; HENNING, T.; KUIPER, R.; LONGMORE, S. N.; WALMSLEY, C. M. Fragmentation and disk formation in high-mass star formation: the ALMA view of G351.77-0.54 at 0.06" resolution. **Astronomy and Astrophysics**, v. 603, p. A10, jun. 2017. 134

BIGIEL, F.; LEROY, A. K.; WALTER, F.; BRINKS, E.; BLOK, W. J. G. de; KRAMER, C.; RIX, H. W.; SCHRUBA, A.; SCHUSTER, K.-F.; USERO, A.; WIESEMEYER, H. W. A constant molecular gas depletion time in nearby disk galaxies. **Astrophysical Journal Letters**, v. 730, p. L13, abr. 2011. 8

BISBAS, T. G.; HAWORTH, T. J.; WILLIAMS, R. J. R.; MACKEY, J.; TREMBLIN, P.; RAGA, A. C.; ARTHUR, S. J.; BACZYNSKI, C.; DALE, J. E.; FROSTHOLM, T.; GEEN, S.; HAUGBØLLE, T.; HUBBER, D.; ILIEV, I. T.; KUIPER, R.; ROSDAH, J.; SULLIVAN, D.; WALCH, S.; WÜNSCH, R. STARBENCH: the D-type expansion of an H II region. **Monthly Notices of the Royal Astronomical Society**, v. 453, n. 2, p. 1324–1343, Oct 2015. 61, 66, 159

BONDI, H. On spherically symmetrical accretion. **Monthly Notices of the Royal Astronomical Society**, v. 112, p. 195, Jan 1952. 71, 72

BONNELL, I. A.; BATE, M. R. Accretion in stellar clusters and the collisional formation of massive stars. **Monthly Notices of the Royal Astronomical Society**, v. 336, n. 2, p. 659–669, Oct 2002. 99

______. Star formation through gravitational collapse and competitive accretion. **Monthly Notices of the Royal Astronomical Society**, v. 370, p. 488–494, jul. 2006. 101

BONNELL, I. A.; BATE, M. R.; CLARKE, C. J.; PRINGLE, J. E. Competitive accretion in embedded stellar clusters. **Monthly Notices of the Royal Astronomical Society**, v. 323, p. 785–794, maio 2001. 101

BRUNT, C. M. Power-law tails in probability density functions of molecular cloud column density. **Monthly Notices of the Royal Astronomical Society**, v. 449, n. 4, p. 4465–4475, Jun 2015. 148

BRUNT, C. M.; FEDERRATH, C.; PRICE, D. J. A method for reconstructing the variance of a 3D physical field from 2D observations: application to turbulence in the interstellar medium. **Monthly Notices of the Royal Astronomical Society**, v. 403, n. 3, p. 1507–1515, Apr 2010. 148

BURKHART, B.; LEE, M.-Y.; MURRAY, C. E.; STANIMIROVIĆ, S. The lognormal probability distribution function of the Perseus molecular cloud: a comparison of HI and dust. **Astrophysical Journal**, v. 811, n. 2, p. L28, Oct 2015. 147

BURKHART, B.; MOCZ, P. The self-gravitating gas fraction and the critical density for star formation. **Astrophysical Journal**, v. 879, n. 2, p. 129, Jul 2019. 148

CESARONI, R.; GALLI, D.; LODATO, G.; WALMSLEY, C. M.; ZHANG, Q. Disks around young O-B (proto)stars: observations and theory. **Protostars and planets V**, p. 197–212, 2007. 72

CESARONI, R.; GALLI, D.; NERI, R.; WALMSLEY, C. M. Imaging the disk around IRAS 20126+4104 at subarcsecond resolution. **Astronomy and Astrophysics**, v. 566, p. A73, Jun 2014. 101

CESARONI, R.; NERI, R.; OLMI, L.; TESTI, L.; WALMSLEY, C. M.; HOFNER, P. A study of the Keplerian accretion disk and precessing outflow in the massive protostar IRAS 20126+4104. **Astronomy and Astrophysics**, v. 434, n. 3, p. 1039–1054, May 2005. 101

CHURCHWELL, E. Ultra-compact HII regions and massive star formation. **Annual Review of Astronomy and Astrophysics**, v. 40, p. 27–62, Jan 2002. 72

CODELLA, C.; BELTRAN, M. T.; CESARONI, R.; MOSCADELLI, L.; NERI, R.; VASTA, M.; ZHANG, Q. Sio collimated outflows driven by high-mass ysos in g24.78+0.08. **Astronomy and Astrophysics**, v. 550, 12 2012. 101

COLELLA, P.; WOODWARD, P. R. The piecewise parabolic method (PPM) for gas-dynamical simulations. **Journal of Computational Physics**, v. 54, p. 174–201, Sep 1984. 30

COURANT, R.; FRIEDRICHS, K.; LEWY, H. Über die partiellen Differenzengleichungen der mathematischen Physik. **Mathematische Annalen**, v. 100, p. 32–74, Jan 1928. 27

CRUTCHER, R. M.; HAKOBIAN, N.; TROLAND, T. H. Testing magnetic star formation theory. **Astrophysical Journal**, v. 692, n. 1, p. 844–855, Feb 2009. 9

DALE, J. E.; NGOUMOU, J.; ERCOLANO, B.; BONNELL, I. A. Before the first supernova: combined effects of H II regions and winds on molecular clouds. **Monthly Notices of the Royal Astronomical Society**, v. 442, p. 694–712, jul. 2014. 157

DOBBS, C. L. The interstellar medium and star formation on kpc size scales. **Monthly Notices of the Royal Astronomical Society**, v. 447, n. 4, p. 3390–3401, Mar 2015. 9

DOBBS, C. L.; BURKERT, A.; PRINGLE, J. E. Why are most molecular clouds not gravitationally bound? **Monthly Notices of the Royal Astronomical Society**, v. 413, n. 4, p. 2935–2942, Jun 2011. 9

DOBBS, C. L.; PRINGLE, J. E. The exciting lives of giant molecular clouds. **Monthly Notices of the Royal Astronomical Society**, v. 432, n. 1, p. 653–667, Jun 2013. 9

DOLAG, K.; BORGANI, S.; SCHINDLER, S.; DIAFERIO, A.; BYKOV, A. M. Simulation techniques for cosmological simulations. **Space Science Reviews**, v. 134, n. 1-4, p. 229–268, Feb 2008. 30

ELMEGREEN, B. G.; SCALO, J. Interstellar turbulence I: observations and processes. **Annual Review of Astronomy and Astrophysics**, v. 42, n. 1, p. 211–273, Sep 2004. 139, 145

FALCETA-GONCALVES, D.; KOWAL, G.; FALGARONE, E.; CHIAN, A. C. L. Turbulence in the interstellar medium. **Nonlinear Processes in Geophysics**, 2014. 140, 146

FEDERRATH, C. The origin of physical variations in the star formation law. **Monthly Notices of the Royal Astronomical Society**, v. 436, n. 4, p. 3167–3172, Dec 2013. 8

FEDERRATH, C.; KLESSEN, R. S.; SCHMIDT, W. The fractal density structure in supersonic isothermal turbulence: solenoidal versus compressive energy injection. **Astrophysical Journal**, v. 692, n. 1, p. 364–374, Feb 2009. 145

FEDERRATH, C.; ROMAN-DUVAL, J.; KLESSEN, R. S.; SCHMIDT, W.; MACLOW, M. M. Comparing the statistics of interstellar turbulence in simulations and observations. Solenoidal versus compressive turbulence forcing. **Astronomy and Astrophysics**, v. 512, p. A81, Mar 2010. 38, 145

FERRIERE, K. M. The interstellar environment of our galaxy. **Reviews of Modern Physics**, v. 73, n. 4, p. 1031–1066, Oct 2001. 5

FRISCH, U.; KOLMOGOROV, A. Turbulence: the legacy of a. n. kolmogorov. Cambridge University Press, 1995. Disponível em: <`https://books.google.com.br/books?id=K-Pf7RuYkf0C`>. 140

FRYXELL, B.; OLSON, K.; RICKER, P.; TIMMES, F. X.; ZINGAL, M.; LAMB, D. Q.; MACNEICE, P.; ROSNER, R.; TRURAN, J. W.; TUFO, H. **FLASH: adaptive mesh hydrodynamics code for modeling astrophysical thermonuclear flashes**. Oct 2010. ascl:1010.082 p. 17

GENT, F. A.; MACLOW, M.-M.; KäPYLä, M. J.; SARSON, G. R.; HOLLINS, J. F. Modelling supernova-driven turbulence. **Geophysical & Astrophysical Fluid Dynamics**, p. 1–29, 2019. Disponível em: <`https://doi.org/10.1080/03091929.2019.1634705`>. 10

GINGOLD, R. A.; MONAGHAN, J. J. Smoothed particle hydrodynamics: theory and application to non-spherical stars. **Monthly Notices of the Royal Astronomical Society**, v. 181, p. 375–389, Nov 1977. 17

GIRICHIDIS, P.; KONSTANDIN, L.; WHITWORTH, A. P.; KLESSEN, R. S. On the evolution of the density probability density function in strongly self-gravitating systems. **Astrophysical Journal**, v. 781, n. 2, p. 91, Feb 2014. 148

GODUNOV, S. K. A difference method for numerical calculation of discontinuous solutions of the equations of hydrodynamics. **Matematicheskii Sbornik**, v. 47, n. 89, p. 271–306, 1959. 30

GOLDREICH, P.; KWAN, J. Molecular clouds. **Astrophysical Journal**, v. 189, p. 441–454, May 1974. 8

GOODMAN, A. A.; PINEDA, J. E.; SCHNEE, S. L. The "true" column density distribution in star-forming molecular clouds. **Astrophysical Journal**, v. 692, p. 91–103, fev. 2009. 147

HABART, E.; WALMSLEY, M.; VERSTRAETE, L.; CAZAUX, S.; MAIOLINO, R.; COX, P.; BOULANGER, F.; PINEAUDESFORÊTS, G. Molecular hydrogen. **Space Science Reviews**, v. 119, n. 1-4, p. 71–91, Aug 2005. 5

HAEMMERLÉ, L.; EGGENBERGER, P.; MEYNET, G.; MAEDER, A.; CHARBONNEL, C. Star formation with disc accretion and rotation. I. Stars between 2 and 22 $M_\odot$ at solar metallicity. **Astronomy and Astrophysics**, v. 557, p. A112, Sep 2013. 98

______. Massive star formation by accretion. I. Disc accretion. **Astronomy and Astrophysics**, v. 585, p. A65, jan. 2016. 98

HARRIES, T. J.; DOUGLAS, T. A.; ALI, A. Radiation-hydrodynamical simulations of massive star formation using Monte Carlo radiative transfer - II. The formation of a 25 solar-mass star. **Monthly Notices of the Royal Astronomical Society**, v. 471, p. 4111–4120, nov. 2017. 11, 101

HARTEN, A.; LAX, S. D.; VANLEER, B. On upstream differencing and Godunov–type schemes for hyperbolic conservation laws. **SIAM Review**, v. 25, n. 1, p. 35–61, Feb 1983. 36

HAYWARD, C. C.; HOPKINS, P. F. How stellar feedback simultaneously regulates star formation and drives outflows. **Monthly Notices of the Royal Astronomical Society**, v. 465, n. 2, p. 1682–1698, Feb 2017. 2, 11

HENNEBELLE, P.; CHABRIER, G. Analytical star formation rate from gravoturbulent fragmentation. **Astrophysical Journal Letters**, v. 743, n. 2, p. L29, Dec 2011. 144, 148

______. Analytical theory for the initial mass function. III. time dependence and star formation rate. **Astrophysical Journal**, v. 770, n. 2, p. 150, Jun 2013. 148

HENNEBELLE, P.; FALGARONE, E. Turbulent molecular clouds. **Astronomy and Astrophysics Review**, v. 20, p. 55, Nov 2012. 5

HEYER, M.; DAME, T. M. Molecular clouds in the milky way. **Annual Review of Astronomy and Astrophysics**, v. 53, p. 583–629, Aug 2015. 10

HEYER, M. H.; BRUNT, C. M. The universality of turbulence in galactic molecular clouds. **Astrophysical Journal Letters**, v. 615, n. 1, p. L45–L48, Nov 2004. 145

HOPKINS, P. F. A general theory of turbulent fragmentation. **Monthly Notices of the Royal Astronomical Society**, v. 430, n. 3, p. 1653–1693, Apr 2013. 1

HOSOKAWA, T.; INUTSUKA, S. Dynamical expansion of ionization and dissociation front around a massive star: a starburst mechanism. **The Astrophysical Journal**, v. 648, n. 2, p. L131–L134, aug 2006. Disponível em: <https://doi.org/10.10862F507887>. 63

HOSOKAWA, T.; OMUKAI, K. Evolution of massive protostars with high accretion rates. **Astrophysical Journal**, v. 691, n. 1, p. 823–846, Jan 2009. 98

HOSOKAWA, T.; YORKE, H. W.; OMUKAI, K. Evolution of massive protostars via disk accretion. **Astrophysical Journal**, v. 721, n. 1, p. 478–492, Sep 2010. 98

ILEE, J. D.; CYGANOWSKI, C. J.; BROGAN, C. L.; HUNTER, T. R.; FORGAN, D. H.; HAWORTH, T. J.; CLARKE, C. J.; HARRIES, T. J. G11.92-0.61 MM 1: A fragmented Keplerian disk surrounding a proto-O star. **Astrophysical Journal Letters**, v. 869, n. 2, p. L24, Dec 2018. 101

ILEE, J. D.; CYGANOWSKI, C. J.; NAZARI, P.; HUNTER, T. R.; BROGAN, C. L.; FORGAN, D. H.; ZHANG, Q. G11.92-0.61 MM1: a Keplerian disc around a massive young proto-O star. **Monthly Notices of the Royal Astronomical Society**, v. 462, n. 4, p. 4386–4401, Nov 2016. 72, 101

JOHNSTON, K. G.; ROBITAILLE, T. P.; BEUTHER, H.; LINZ, H.; BOLEY, P.; KUIPER, R.; KETO, E.; HOARE, M. G.; VANBOEKEL, R. A Keplerian-like disk around the forming O-type star AFGL 4176. **Astrophysical Journal Letters**, v. 813, n. 1, p. L19, Nov 2015. 101

KAHN, F. D. Cocoons around early-type stars. **Astronomy and Astrophysics**, v. 37, p. 149–162, dez. 1974. 99

KAINULAINEN, J.; BEUTHER, H.; HENNING, T.; PLUME, R. Probing the evolution of molecular cloud structure. From quiescence to birth. **Astronomy and Astrophysics**, v. 508, p. L35–L38, dez. 2009. 147, 148

KAINULAINEN, J.; FEDERRATH, C.; HENNING, T. Unfolding the laws of star formation: the density distribution of molecular clouds. **Science**, v. 344, n. 6180, p. 183–185, Apr 2014. 146

KAINULAINEN, J.; TAN, J. C. High-dynamic-range extinction mapping of infrared dark clouds. Dependence of density variance with sonic Mach number in molecular clouds. **Astronomy and Astrophysics**, v. 549, p. A53, Jan 2013. 148

KEE, N. D.; OWOCKI, S.; KUIPER, R.; SUNDQVIST, J. Line-driven ablation of circumstellar disks. In: Eldridge, J. J.; Bray, J. C.; McClelland, L. A. S.; Xiao, L. (Ed.). **The Lives and Death-Throes of Massive Stars**. [S.l.: s.n.], 2017. (IAU Symposium, v. 329), p. 412–412. 135

KENNICUTT, R. C. J. Star formation in galaxies along the Hubble sequence. **Annual Review of Astronomy and Astrophysics**, v. 36, p. 189–232, 1998. 6, 71

KETO, E. On the evolution of ultracompact H II regions. **Astrophysical Journal**, v. 580, p. 980–986, dez. 2002. 72

______. The formation of massive stars by accretion through trapped hypercompact H II regions. **Astrophysical Journal**, v. 599, n. 2, p. 1196–1206, Dec 2003. 72, 159

______. The formation of massive stars: accretion, disks, and the development of hypercompact H II regions. **Astrophysical Journal**, v. 666, p. 976–981, set. 2007. 102

KLASSEN, M.; PUDRITZ, R. E.; KUIPER, R.; PETERS, T.; BANERJEE, R. Simulating the formation of massive protostars. I. Radiative feedback and accretion disks. **Astrophysical Journal**, v. 823, p. 28, maio 2016. 134

KLESSEN, R. S. Star formation in molecular clouds. In: CHARBONNEL, C.; MONTMERLE, T. (Ed.). **EAS publications series**. [S.l.: s.n.], 2011. (EAS publications series, v. 51), p. 133–167. 10

KOLMOGOROV, A. The local structure of turbulence in incompressible viscous fluid for very large Reynolds' numbers. **Akademiia Nauk SSSR Doklady**, v. 30, p. 301–305, Jan 1941. 137, 140

KOWAL, G. **AMUN Code**. 2007–2016. Available at: `https://bitbucket.org/amunteam/godunov-code`. 3, 159

KRITSUK, A. G.; NORMAN, M. L.; PADOAN, P.; WAGNER, R. The statistics of supersonic isothermal turbulence. **Astrophysical Journal**, v. 665, n. 1, p. 416–431, Aug 2007. 145

KRUMHOLZ, M. R. The big problems in star formation: the star formation rate, stellar clustering, and the initial mass function. **Physics Reports**, v. 539, p. 49–134, Jun 2014. 1

KRUMHOLZ, M. R.; BATE, M. R.; ARCE, H. G.; DALE, J. E.; GUTERMUTH, R.; KLEIN, R. I.; LI, Z. Y.; NAKAMURA, F.; ZHANG, Q. Star cluster formation and feedback. In: BEUTHER, H.; KLESSEN, R. S.; DULLEMOND, C. P.; HENNING, T. (Ed.). **Protostars and planets VI**. [S.l.: s.n.], 2014. p. 243. 11

KRUMHOLZ, M. R.; BURKHART, B. Is turbulence in the interstellar medium driven by feedback or gravity? An observational test. **Monthly Notices of the Royal Astronomical Society**, v. 458, n. 2, p. 1671–1677, May 2016. 10

KRUMHOLZ, M. R.; KLEIN, R. I.; MCKEE, C. F. Molecular line emission from massive protostellar disks: predictions for ALMA and EVLA. **Astrophysical Journal**, v. 665, p. 478–491, ago. 2007. 134

KRUMHOLZ, M. R.; MCKEE, C. F. A general theory of turbulence-regulated star formation, from spirals to ultraluminous infrared galaxies. **Astrophysical Journal**, v. 630, n. 1, p. 250–268, Sep 2005. 10, 144, 148

KRUMHOLZ, M. R.; STONE, J. M.; GARDINER, T. A. Magnetohydrodynamic evolution of H II regions in molecular clouds: simulations methodology, tests and uniform media. **Astrophysical Journal**, v. 671, n. 1, p. 518–535, Dec 2007. 135

KRUMHOLZ, M. R.; TAN, J. C. Slow star formation in dense gas: evidence and implications. **Astrophysical Journal**, v. 654, p. 304–315, jan. 2007. 8

KUIPER, R.; HOSOKAWA, T. First hydrodynamics simulations of radiation forces and photoionization feedback in massive star formation. **Astronomy and Astrophysics**, v. 616, p. A101, ago. 2018. 11, 101, 134

KUIPER, R.; KLAHR, H.; BEUTHER, H.; HENNING, T. Circumventing the radiation pressure barrier in the formation of massive stars via disk accretion. **Astrophysical Journal**, v. 722, n. 2, p. 1556–1576, Oct 2010. 99, 100

LARSON, R. B. Turbulence and star formation in molecular clouds. **Monthly Notices of the Royal Astronomical Society**, v. 194, p. 809–826, Mar 1981. 6, 7, 145

LEROY, A. K.; WALTER, F.; SANDSTROM, K.; SCHRUBA, A.; MUNOZ-MATEOS, J.-C.; BIGIEL, F.; BOLATTO, A.; BRINKS, E.; BLOK, W. J. G. de; MEIDT, S.; RIX, H.-W.; ROSOLOWSKY, E.; SCHINNERER, E.; SCHUSTER, K.-F.; USERO, A. Molecular gas and star formation in nearby disk galaxies. **Astronomical Journal**, v. 146, p. 19, ago. 2013. 8

LUCAS, W. E.; BONNELL, I. A.; FORGAN, D. H. Can the removal of molecular cloud envelopes by external feedback affect the efficiency of star formation? **Monthly Notices of the Royal Astronomical Society**, v. 466, n. 4, p. 5011–5019, Apr 2017. 2

LUCY, L. B. A numerical approach to the testing of the fission hypothesis. **Astronomical Journal**, v. 82, p. 1013–1024, Dec 1977. 17

______. Computing radiative equilibria with Monte Carlo techniques. **Astronomy and Astrophysics**, v. 344, p. 282–288, Apr 1999. 48

LUND, K.; WOOD, K.; FALCETA-GONÇALVES, D.; VANDENBROUCKE, B.; SARTORIO, N. S.; BONNELL, I. A.; JOHNSTON, K. G.; KETO, E. Radiation hydrodynamic simulations of massive star formation via gravitationally trapped HII regions - Spherically symmetric ionised accretion flows. **Monthly Notices of the Royal Astronomical Society**, mar. 2019. 71, 90, 104

MACLOW, M.-M.; KLESSEN, R. S. Control of star formation by supersonic turbulence. **Reviews of Modern Physics**, v. 76, n. 1, p. 125–194, Jan 2004. 1, 2

MASSEY, P. Massive stars in the local group: implications for stellar evolution and star formation. **Annual Review of Astronomy and Astrophysics**, v. 41, p. 15–56, 2003. 11, 71

MAUND, J. R.; CROWTHER, P. A.; JANKA, H.-T.; LANGER, N. Bridging the gap: from massive stars to supernovae. **Philosophical Transactions of the Royal Society of London Series A**, v. 375, n. 2105, p. 20170025, Sep 2017. 11

MCKEE, C. F.; OSTRIKER, E. C. Theory of star formation. **Annual Review of Astronomy and Astrophysics**, v. 45, n. 1, p. 565–687, Sep 2007. 1, 9, 144

MCKEE, C. F.; TAN, J. C. The formation of massive stars from turbulent cores. **Astrophysical Journal**, v. 585, p. 850–871, mar. 2003. 101

MESTEL, L. The influence of stellar radiation on the rate of accretion. **Monthly Notices of the Royal Astronomical Society**, v. 114, p. 437, 1954. 72

MESTEL, L.; SPITZER L., J. Star formation in magnetic dust clouds. **Monthly Notices of the Royal Astronomical Society**, v. 116, p. 503, Jan 1956. 9

MEYER, D. M. A.; VOROBYOV, E. I.; KUIPER, R.; KLEY, W. On the existence of accretion-driven bursts in massive star formation. **Monthly Notices of the Royal Astronomical Society**, v. 464, n. 1, p. L90–L94, Jan 2017. 98

MOCZ, P.; BURKHART, B. Star formation from dense shocked regions in supersonic isothermal magnetoturbulence. **Monthly Notices of the Royal Astronomical Society**, v. 480, n. 3, p. 3916–3927, Nov 2018. 148

MOLINARI, S.; SWINYARD, B.; BALLY, J.; BARLOW, M.; BERNARD, J. P.; MARTIN, P.; MOORE, T.; NORIEGA-CRESPO, A.; PLUME, R.; TESTI, L.; ZAVAGNO, A.; ABERGEL, A.; ALI, B.; ANDERSON, L.; ANDRÉ, P.; BALUTEAU, J. P.; BATTERSBY, C.; BELTRÁN, M. T.; BENEDETTINI, M.; BILLOT, N.; BLOMMAERT, J.; BONTEMPS, S.; BOULANGER, F.; BRAND, J.; BRUNT, C.; BURTON, M.; CALZOLETTI, L.; CAREY, S.; CASELLI, P.; CESARONI, R.; CERNICHARO, J.; CHAKRABARTI, S.; CHRYSOSTOMOU, A.; COHEN, M.; COMPIEGNE, M.; BERNARDIS, P. de; GASPERIS, G. de; GIORGIO, A. M. di; ELIA, D.; FAUSTINI, F.; FLAGEY, N.; FUKUI, Y.; FULLER, G. A.; GANGA, K.; GARCIA-LARIO, P.; GLENN, J.; GOLDSMITH, P. F.; GRIFFIN, M.; HOARE, M.; HUANG, M.; IKHENAODE, D.; JOBLIN, C.; JONCAS, G.; JUVELA, M.; KIRK, J. M.; LAGACHE, G.; LI, J. Z.; LIM, T. L.; LORD, S. D.; MARENGO, M.; MARSHALL, D. J.; MASI, S.; MASSI, F.; MATSUURA, M.; MINIER, V.; MIVILLE-DESCHÊNES, M. A.; MONTIER, L. A.; MORGAN, L.; MOTTE, F.; MOTTRAM, J. C.; MÜLLER, T. G.; NATOLI, P.; NEVES, J.; OLMI, L.; PALADINI, R.; PARADIS, D.; PARSONS, H.; PERETTO, N.; PESTALOZZI, M.; PEZZUTO, S.; PIACENTINI, F.;

PIAZZO, L.; POLYCHRONI, D.; POMARÈS, M.; POPESCU, C. C.; REACH, W. T.; RISTORCELLI, I.; ROBITAILLE, J. F.; ROBITAILLE, T.; RODÓN, J. A.; ROY, A.; ROYER, P.; RUSSEIL, D.; SARACENO, P.; SAUVAGE, M.; SCHILKE, P.; SCHISANO, E.; SCHNEIDER, N.; SCHULLER, F.; SCHULZ, B.; SIBTHORPE, B.; SMITH, H. A.; SMITH, M. D.; SPINOGLIO, L.; STAMATELLOS, D.; STRAFELLA, F.; STRINGFELLOW, G. S.; STURM, E.; TAYLOR, R.; THOMPSON, M. A.; TRAFICANTE, A.; TUFFS, R. J.; UMANA, G.; VALENZIANO, L.; VAVREK, R.; VENEZIANI, M.; VITI, S.; WAELKENS, C.; WARD-THOMPSON, D.; WHITE, G.; WILCOCK, L. A.; WYROWSKI, F.; YORKE, H. W.; ZHANG, Q. Clouds, filaments, and protostars: The Herschel Hi-GAL Milky Way. **Astronomy and Astrophysics**, v. 518, p. L100, Jul 2010. 5

MOUSCHOVIAS, T. C. Nonhomologous contraction and equilibria of self-gravitating, magnetic interstellar clouds embedded in an intercloud medium: star formation. II. Results. **Astrophysical Journal**, v. 207, p. 141–158, Jul 1976. 9

MURRAY, N.; RAHMAN, M. Star formation in massive clusters via the Wilkinson microwave anisotropy probe and the Spitzer glimpse survey. **Astrophysical Journal**, v. 709, n. 1, p. 424–435, Jan 2010. 8

NAKANO, T. Conditions for the formation of massive stars through nonspherical accretion. **Astrophysical Journal**, v. 345, p. 464, Oct 1989. 99

NAVIER, C. Mémoire sur les lois du mouvement des fluides. **Mémoires de l'Académie Royale des Sciences de l'Institut de France**, v. 6, n. 1823, p. 389–440, 1823. 138

NGUYEN-LUONG, Q.; NGUYEN, H. V. V.; MOTTE, F.; SCHNEIDER, N.; FUJII, M.; LOUVET, F.; HILL, T.; SANHUEZA, P.; CHIBUEZE, J. O.; DIDELON, P. The scaling relations and star formation laws of mini-starburst complexes. **Astrophysical Journal**, v. 833, n. 1, p. 23, Dec 2016. 10

OFFNER, S. S. R.; LIU, Y. Turbulent action at a distance due to stellar feedback in magnetized clouds. **Nature Astronomy**, v. 2, p. 896–900, Sep 2018. 11

PADOAN, P.; FEDERRATH, C.; CHABRIER, G.; EVANS N. J., I.; JOHNSTONE, D.; JØRGENSEN, J. K.; MCKEE, C. F.; NORDLUND, Å. The star formation rate of molecular clouds. In: BEUTHER, H.; KLESSEN, R. S.; DULLEMOND, C. P.; HENNING, T. (Ed.). **Protostars and planets VI**. [S.l.: s.n.], 2014. p. 77. 144, 148

PADOAN, P.; NORDLUND, A. A super-alfvénic model of dark clouds. **Astrophysical Journal**, v. 526, n. 1, p. 279–294, Nov 1999. 9

PADOAN, P.; NORDLUND, A.; JONES, B. J. T. The universality of the stellar initial mass function. **Monthly Notices of the Royal Astronomical Society**, v. 288, n. 1, p. 145–152, Jun 1997. 147

PADOAN, P.; PAN, L.; HAUGBØLLE, T.; NORDLUND, Å. Supernova driving. I. The origin of molecular cloud turbulence. **Astrophysical Journal**, v. 822, n. 1, p. 11, May 2016. 10

PALLA, F.; STAHLER, S. W. The pre-main-sequence evolution of intermediate-mass stars. **Astrophysical Journal**, v. 418, p. 414, Nov 1993. 97

PASSOT, T.; VÁZQUEZ-SEMADENI, E. Density probability distribution in one-dimensional polytropic gas dynamics. **Physical Review E**, v. 58, n. 4, p. 4501–4510, Oct 1998. 146

PATEL, N. A.; CURIEL, S.; SRIDHARAN, T. K.; ZHANG, Q.; HUNTER, T. R.; HO, P. T. P.; TORRELLES, J. M.; MORAN, J. M.; GÓMEZ, J. F.; ANGLADA, G. A disk of dust and molecular gas around a high-mass protostar. **Nature**, v. 437, n. 7055, p. 109–111, Sep 2005. 101

PETERS, T.; KLESSEN, R. S.; MACLOW, M.-M.; BANERJEE, R. Limiting accretion onto massive stars by fragmentation-induced starvation. **Astrophysical Journal**, v. 725, p. 134–145, Dec 2010. 134

POPE, S. B. Turbulent flows. **Measurement Science and Technology**, v. 12, n. 11, p. 2020–2021, oct 2001. 140

PREDEHL, P.; SCHMITT, J. H. M. M. X-raying the interstellar medium: ROSAT observations of dust scattering halos. **Astronomy and Astrophysics**, v. 500, p. 459–475, Jan 1995. 5

PRICE, D. J.; FEDERRATH, C. A comparison between grid and particle methods on the statistics of driven, supersonic, isothermal turbulence. **Monthly Notices of the Royal Astronomical Society**, v. 406, p. 1659–1674, ago. 2010. 17

RAGA, A. C.; CANTÓ, J.; RODRÍGUEZ, L. F. Analytic and numerical models for the expansion of a compact H II region. **Monthly Notices of the Royal Astronomical Society**, v. 419, n. 1, p. L39–L43, Jan 2012. 63

RENAUD, F.; KRALJIC, K.; BOURNAUD, F. Star formation laws and thresholds from interstellar medium structure and turbulence. **Astrophysical Journal Letters**, v. 760, n. 1, p. L16, Nov 2012. 148

REY-RAPOSO, R.; DOBBS, C.; AGERTZ, O.; ALIG, C. The roles of stellar feedback and galactic environment in star-forming molecular clouds. **Monthly Notices of the Royal Astronomical Society**, v. 464, n. 3, p. 3536–3551, Jan 2017. 2

REYNOLDS, O. An experimental investigation of the circumstances which determine whether the motion of water shall be direct or sinuous, and of the law of resistance in parallel channels. **Philosophical Transactions of the Royal Society of London**, v. 174, p. 935–982, 1883. ISSN 02610523. Disponível em: <`http://www.jstor.org/stable/109431`>. 137, 138, 139

RICHARDSON, L. **Weather prediction by numerical process**. Cambridge University Press, 1922. (Cambridge Mathematical Library). ISBN 9780521680448. Disponível em: <`https://books.google.com.br/books?id=D52d3_bbgg8C`>. 137, 139

ROMAN-DUVAL, J.; JACKSON, J. M.; HEYER, M.; RATHBORNE, J.; SIMON, R. Physical properties and galactic distribution of molecular clouds identified in the Galactic Ring Survey. **Astrophysical Journal**, v. 723, n. 1, p. 492–507, Nov 2010. 10

ROSEN, A. L.; KRUMHOLZ, M. R.; MCKEE, C. F.; KLEIN, R. I. An unstable truth: how massive stars get their mass. **Monthly Notices of the Royal Astronomical Society**, v. 463, n. 3, p. 2553–2573, Dec 2016. 101

SANA, H.; DEMINK, S. E.; DEKOTER, A.; LANGER, N.; EVANS, C. J.; GIELES, M.; GOSSET, E.; IZZARD, R. G.; BOUQUIN, J.-B. L.; SCHNEIDER, F. R. N. Binary interaction dominates the evolution of massive stars. **Science**, v. 337, p. 444, jul. 2012. 131

SARTORIO, N. S.; VANDENBROUCKE, B.; FALCETA-GONCALVES, D.; WOOD, K.; KETO, E. Massive star formation via torus accretion: the effect of photoionization feedback. **Monthly Notices of the Royal Astronomical Society**, v. 486, n. 4, p. 5171–5183, Jul 2019. 95

SCALO, J.; ELMEGREEN, B. G. Interstellar turbulence II: implications and effects. **Annual Review of Astronomy and Astrophysics**, v. 42, n. 1, p. 275–316, Sep 2004. 2

SCHMIDT, W.; FEDERRATH, C.; HUPP, M.; KERN, S.; NIEMEYER, J. C. Numerical simulations of compressively driven interstellar turbulence. I. Isothermal gas. **Astronomy and Astrophysics**, v. 494, n. 1, p. 127–145, Jan 2009. 145

SCHNEIDER, N.; CSENGERI, T.; HENNEMANN, M.; MOTTE, F.; DIDELON, P.; FEDERRATH, C.; BONTEMPS, S.; FRANCESCO, J. D.; ARZOUMANIAN, D.; MINIER, V.; ANDRÉ, P.; HILL, T.; ZAVAGNO, A.; NGUYEN-LUONG, Q.; ATTARD, M.; BERNARD, J. P.; ELIA, D.; FALLSCHEER, C.; GRIFFIN, M.; KIRK, J.; KLESSEN, R.; KÖNYVES, V.; MARTIN, P.; MEN'SHCHIKOV, A.; PALMEIRIM, P.; PERETTO, N.; PESTALOZZI, M.; RUSSEIL, D.; SADAVOY, S.; SOUSBIE, T.; TESTI, L.; TREMBLIN, P.; WARD-THOMPSON, D.; WHITE, G. Cluster-formation in the Rosette molecular cloud at the junctions of filaments. **Astronomy and Astrophysics**, v. 540, p. L11, Apr 2012. 148

SEIFRIED, D.; BANERJEE, R.; KLESSEN, R. S. Turbulence and its effect on protostellar disk formation. **arXiv e-prints**, p. arXiv:1509.04467, Sep 2015. 135

SEIFRIED, D.; BANERJEE, R.; KLESSEN, R. S.; DUFFIN, D.; PUDRITZ, R. E. Magnetic fields during the early stages of massive star formation - I. Accretion and disc evolution. **Monthly Notices of the Royal Astronomical Society**, v. 417, n. 2, p. 1054–1073, Oct 2011. 135

SEIFRIED, D.; WALCH, S.; HAID, S.; GIRICHIDIS, P.; NAAB, T. Is molecular cloud turbulence driven by external supernova explosions? **Astrophysical Journal**, v. 855, n. 2, p. 81, Mar 2018. 10

SHAKURA, N. I.; SUNYAEV, R. A.; ZILITINKEVICH, S. S. On the turbulent energy transport in accretion. **Astronomy and Astrophysics**, v. 62, n. 1-2, p. 179–187, Jan 1978. 135

SPITZER, L. **Physical processes in the interstellar medium**. [S.l.: s.n.], 1978. 62

STERNBERG, A. The excitation of molecular hydrogen and its significance. In: BÖHM-VITENSE, E. (Ed.). **Infrared spectroscopy in astronomy**. [S.l.: s.n.], 1989. p. 269. 5

STERNBERG, A.; HOFFMANN, T. L.; PAULDRACH, A. W. A. Ionizing photon emission rates from O- and early B-type stars and clusters. **Astrophysical Journal**, v. 599, p. 1333–1343, dez. 2003. 128, 129, 132

STONE, J. M.; OSTRIKER, E. C.; GAMMIE, C. F. Dissipation in compressible magnetohydrodynamic turbulence. **Astrophysical Journal Letters**, v. 508, n. 1, p. L99–L102, Nov 1998. 11

STRÖMGREN, B. The physical state of interstellar hydrogen. **Astrophysical Journal**, v. 89, p. 526, May 1939. 62

SUNDQVIST, J. O.; OWOCKI, S. P. Clumping in the inner winds of hot, massive stars from hydrodynamical line-driven instability simulations. **Monthly Notices of the Royal Astronomical Society**, v. 428, n. 2, p. 1837–1844, Jan 2013. 135

TAN, J. C.; BELTRÁN, M. T.; CASELLI, P.; FONTANI, F.; FUENTE, A.; KRUMHOLZ, M. R.; MCKEE, C. F.; STOLTE, A. Massive star formation. **Protostars and planets VI**, p. 149–172, 2014. 72, 101

TAN, J. C.; MCKEE, C. F. The formation of the first stars. I. Mass infall rates, accretion disk structure, and protostellar evolution. **Astrophysical Journal**, v. 603, n. 2, p. 383–400, Mar 2004. 13

TEYSSIER, R. Cosmological hydrodynamics with adaptive mesh refinement. A new high resolution code called RAMSES. **Astronomy and Astrophysics**, v. 385, p. 337–364, Apr 2002. 17

TOOMRE, A. On the gravitational stability of a disk of stars. **Astrophysical Journal**, v. 139, p. 1217–1238, maio 1964. 112

TORO, E. **Riemann solvers and numerical methods for fluid dynamics: a practical introduction**. [S.l.]: Springer, 1997. ISBN 9783540616764. 36

TORO, E. F.; SPRUCE, M.; SPEARES, W. Restoration of the contact surface in the HLL-Riemann solver. **Shock Waves**, v. 4, p. 25–34, jul. 1994. 36

VANDENBROUCKE, B.; SARTORIO, N. S.; WOOD, K.; LUND, K.; FALCETA-GONÇALVES, D.; HAWORTH, T. J.; BONNELL, I.; KETO, E.; Tootill, D. Testing the stability of supersonic ionized Bondi accretion flows with radiation hydrodynamics. **Monthly Notices of the Royal Astronomical Society**, v. 485, n. 3, p. 3771–3782, May 2019. 71, 84, 90, 94, 159

VANDENBROUCKE, B.; WOOD, K. The Monte Carlo photoionization and moving-mesh radiation hydrodynamics code CMacIonize. **arXiv e-prints**, p. arXiv:1802.09528, Feb 2018. 3, 159

______. The Monte Carlo photoionization and moving-mesh radiation hydrodynamics code CMACIONIZE. **Astronomy and Computing**, v. 23, p. 40–59, abr. 2018. 103, 104

VANLEER, B. Towards the ultimate conservative difference Scheme. IV. A new approach to numerical convection. **Journal of Computational Physics**, v. 23, p. 276, Mar 1977. 30

VAZQUEZ-SEMADENI, E. Hierarchical structure in nearly pressureless flows as a consequence of self-similar statistics. **Astrophysical Journal**, v. 423, p. 681, Mar 1994. 147

VERNER, D. A.; FERLAND, G. J. Atomic data for astrophysics. I. radiative recombination rates for H-like, He-like, Li-like, and Na-like ions over a broad range of temperature. **Astrophysical Journal**, v. 103, p. 467, abr. 1996. 107

VONWEIZSÄCKER, C. F. The evolution of galaxies and stars. **Astrophysical Journal**, v. 114, p. 165, Sep 1951. 7

WADA, K.; MEURER, G.; NORMAN, C. A. Gravity-driven turbulence in galactic disks. **Astrophysical Journal**, v. 577, n. 1, p. 197–205, Sep 2002. 10

WILLIAMS, J. P.; MCKEE, C. F. The galactic distribution of OB associations in molecular clouds. **Astrophysical Journal**, v. 476, n. 1, p. 166–183, Feb 1997. 8

WOLFIRE, M. G.; CASSINELLI, J. P. Conditions for the formation of massive stars. **Astrophysical Journal**, v. 319, p. 850–867, ago. 1987. 99

WOLFIRE, M. G.; MCKEE, C. F.; HOLLENBACH, D.; TIELENS, A. G. G. M. Neutral atomic phases of the interstellar medium in the galaxy. **Astrophysical Journal**, v. 587, n. 1, p. 278–311, Apr 2003. 5

WOOD, K.; BARNES, J. E.; ERCOLANO, B.; HAFFNER, L. M.; REYNOLDS, R. J.; DALE, J. Three-dimensional geometries and the analysis of H II regions. **Astrophysical Journal**, v. 770, p. 152, jun. 2013. 130

WOOD, K.; MATHIS, J. S.; ERCOLANO, B. A three-dimensional Monte Carlo photoionization code for modelling diffuse ionized gas. **Monthly Notices of the Royal Astronomical Society**, v. 348, n. 4, p. 1337–1347, Mar 2004. 66, 67, 103, 159

YORKE, H. W.; SONNHALTER, C. On the formation of massive stars. **Astrophysical Journal**, v. 569, n. 2, p. 846–862, Apr 2002. 99

ZHANG, Q.; HUNTER, T. R.; BRAND, J.; SRIDHARAN, T. K.; CESARONI, R.; MOLINARI, S.; WANG, J.; KRAMER, M. Search for CO outflows toward a sample of 69 high-mass protostellar candidates. II. Outflow properties. **Astrophysical Journal**, v. 625, p. 864–882, jun. 2005. 101

ZINNECKER, H.; YORKE, H. W. Toward understanding massive star formation. **Annual Review of Astronomy and Astrophysics**, v. 45, p. 481–563, set. 2007. 72, 98

ZUCKERMAN, B.; EVANS, N. J. Models of massive molecular clouds. **Astrophysical Journal Letters**, v. 192, p. L149, Sep 1974. 6, 8

ZUCKERMAN, B.; PALMER, P. Radio radiation from interstellar molecules. **Annual Review of Astronomy and Astrophysics**, v. 12, p. 279–313, Jan 1974. 8

PUBLICAÇÕES TÉCNICO-CIENTÍFICAS EDITADAS PELO INPE

Teses e Dissertações (TDI)

Teses e Dissertações apresentadas nos Cursos de Pós-Graduação do INPE.

Notas Técnico-Científicas (NTC)

Incluem resultados preliminares de pesquisa, descrição de equipamentos, descrição e ou documentação de programas de computador, descrição de sistemas e experimentos, apresentação de testes, dados, atlas, e documentação de projetos de engenharia.

Propostas e Relatórios de Projetos (PRP)

São propostas de projetos técnico-científicos e relatórios de acompanhamento de projetos, atividades e convênios.

Publicações Seriadas

São os seriados técnico-científicos: boletins, periódicos, anuários e anais de eventos (simpósios e congressos). Constam destas publicações o Internacional Standard Serial Number (ISSN), que é um código único e definitivo para identificação de títulos de seriados.

Pré-publicações (PRE)

Todos os artigos publicados em periódicos, anais e como capítulos de livros.

Manuais Técnicos (MAN)

São publicações de caráter técnico que incluem normas, procedimentos, instruções e orientações.

Relatórios de Pesquisa (RPQ)

Reportam resultados ou progressos de pesquisas tanto de natureza técnica quanto científica, cujo nível seja compatível com o de uma publicação em periódico nacional ou internacional.

Publicações Didáticas (PUD)

Incluem apostilas, notas de aula e manuais didáticos.

Programas de Computador (PDC)

São a seqüência de instruções ou códigos, expressos em uma linguagem de programação compilada ou interpretada, a ser executada por um computador para alcançar um determinado objetivo. Aceitam-se tanto programas fonte quanto os executáveis.